Seismic Performance of Corroded RC Bridge Piers

Development of a Multi-Mechanical Nonlinear Fibre Beam-Column Model

By

MOHAMMAD MEHDI KASHANI

BSc (Hons) MSc

Department of Civil Engineering

UNIVERSITY OF BRISTOL

A dissertation submitted to the University of Bristol in accordance with the requirements for award of the degree of Doctor of Philosophy in the Faculty of Engineering

May 2014

Word Count: fifty nine thousands

To my parents *Nasser Kashani* and *Azam Khalighi* and my sisters *Farzaneh* and *Afsaneh*

ABSTRACT

The impact of corrosion on the nonlinear stress-strain behaviour of reinforcing bars under monotonic and cyclic loading was explored experimentally. The corrosion procedure was simulated in a laboratory environment using an accelerated corrosion procedure. A total of 132 corroded test specimens were produced and tested under monotonic and cyclic loading. 23 corroded bars from the tests specimens were taken for further statistical analysis of their corrosion patterns. An advanced 3D optical measurement technique was employed to scan the surface of corroded bars. A novel stochastic signal processing technique was used for corrosion pattern analysis and subsequent development of probabilistic distribution models for the geometrical properties of corroded bars (cross section area, second moment of area etc.). Finally the scanned bars were tested under monotonic buckling and cyclic loading. The impact of the corrosion patterns on the nonlinear stress-strain behaviour of corroded bars was then investigated using nonlinear finite element modelling of the tested bars which was compared with the experimental results.

Using the experimental and numerical data a new phenomenological uniaxial material model is also developed for reinforcing bars. The new material model accounts for the influence of corrosion damage, inelastic buckling and low-cycle fatigue degradation. This model is then implemented into the OpenSees platform as a new uniaxial material class known as *CorrodedReinforcingSteel*. Finally the material model is validated against 10 buckling critical flexural RC columns from the UW-PEER experimental RC column database. In addition, a new modelling technique is developed for modelling the flexural behaviour of buckling critical RC bridge piers using a distributed plasticity fibre beam-column model.

These new models for the assessment of corrosion damaged RC columns have significantly improved the accuracy of previous models. This will help bridge managers and owners to develop a rigorous maintenance strategy to evaluate and predict the performance of their bridge network so that repairs can be prioritised and targeted at the most critical structures.

ACKNOWLEDGEMENT

One of the joys of completion is to look over the journey and remember all the friends and family who have helped and supported me along this long but fulfilling road.

I would like to express my heartfelt gratitude to Dr Adam Crewe and Dr Nicholas Alexander, who are not only supervisors but dear friends. I would like to thank them for their guidance and advice over the course of this research. I could not have asked for better inspirational, supportive, and patient.

I would also like to thank my former employer URS (previously known as Scott Wilson and Benaim) for their partial financial support to my research. I would like to thank my managers Colin McKenna, Darren Kimberly, Simon Bourne and James Rowe for their supports throughout my part-time working and studying. It would not be possible to progress with my PhD without their help and support.

I would like to thank the Institute for Advance Studies (IAS) of the University of Bristol for providing me with financial support to spend eight months at the University of Washington for research collaboration.

It was a great privilege to work with academics of the University of Washington. I would like to express my very special thanks to Dr Laura Lowes of the University of Washington for her invaluable advice and guidance during our collaboration. Her input to my research had a great impact on my thesis and changed my thinking direction. Her knowledge, her friendly personality and her openness to transfer her knowledge made the collaboration flourish. I would also like to thank Professors John Stanton and Marc Eberhard for their kind and expert guidance to me during my visit. I would like to thank all my friends in Seattle and graduate students at the University of Washington for their support to me and helping me to have a fantastic and enjoyable time in the Seattle.

I'm very grateful to have been helped along the way with good friends and colleagues. Their help and support made this journey to go smoothly. Special thanks to David Ward and Ed Skuse, our technicians in the earthquake laboratory, for their support for specimen preparation of the experimental study. I would also like to thank Pete Whereat and Guy Pearn, our technicians in the heavy structures laboratory, for their support in calibration and preparation of the Instron machines and instrumentations for material testing.

I could not have done this without the love and support of my family. It was the toughest few years of my life and your ongoing support, patience and love helped more than you know. I would like to thank my parents for always providing the perfect blend of encouragement, high expectations and love.

Mohammad Mehdi Kashani
Bristol, UK
January 2014

AUTHOR'S DECLARATION

I declare that the work in this dissertation was carried out in accordance with the requirements of the University's Regulations and Code of Practice for Research Degree Programmes and that it has not been submitted for any other academic award. Except where indicated by specific reference in the text, the work is the candidate's own work. Work done in collaboration with, or with the assistance of, others, is indicated as such. Any views expressed in the dissertation are those of the author.

SIGNED: ..... DATE: .....

LIST OF PUBLICATIONS AND AWARDS

This thesis is based on the work published in the following papers. The publication list includes the peer reviewed journal papers, conference papers and author's contribution to a chapter in book.

Peer Reviewed Journal Papers:

[1] *Mohammad M. Kashani*, Adam J. Crewe, Nicholas A. Alexander (2013), Nonlinear stress-strain behavior of corrosion-damaged reinforcing bars including inelastic buckling, ***Engineering Structures***, (48) 417– 429.

[2] *Mohammad M. Kashani*, Adam J. Crewe, Nicholas A. Alexander (2013), Nonlinear cyclic response of corrosion-damaged reinforcing bars with the effect of buckling, ***Construction and Building Materials***, (41) 388– 400.

[3] *Mohammad M. Kashani*, Adam J. Crewe, Nicholas A. Alexander (2013), Use of a 3D optical measurement technique for stochastic corrosion pattern analysis of reinforcing bars subjected to accelerated corrosion, ***Corrosion Science***, (73) 208–221.

[4] *Mohammad M. Kashani* (2011), Seismic performance of corrosion damaged RC bridges in earthquake regions, ***The Structural Engineer***, 89 (14) 16 – 19.

[5] *Mohammad M. Kashani*, Laura N. Lowes, Adam J. Crewe, Nicholas A. Alexander (2014), Finite element investigation of the influence of corrosion pattern on inelastic buckling and cyclic response of corroded reinforcing bars, ***Engineering Structures***. Under Review.

[6] *Mohammad M. Kashani*, Laura N. Lowes, Adam J. Crewe, Nicholas A. Alexander (2014), Phenomenological hysteretic model for corroded reinforcing bars including inelastic buckling and low-cycle fatigue degradation, ***Computers and Structures***. Under Review.

[7] *Mohammad M. Kashani*, Laura N. Lowes, Adam J. Crewe, Nicholas A. Alexander (2014), Nonlinear fiber element modeling of RC bridge piers considering inelastic buckling of reinforcement, ***Journal of Structural Engineering***. Under Review.

[8] *Mohammad M. Kashani*, Laura N. Lowes, Adam J. Crewe, Nicholas A. Alexander (2014), Nonlinear fibre element modelling of corrosion damaged RC bridge piers, ***Earthquake Engineering and Structural Dynamics***. Under Review.

Peer Reviewed Conference Papers:

[1] *Mohammad M. Kashani*, Laura N. Lowes, Adam J. Crewe, Nicholas A. Alexander, (2014), Implementation of Corrosion Damage Models in Nonlinear Fibre Beam-Column Element, Submitted to *10th U.S. National Conference on Earthquake Engineering, Alaska.*

[2] *Mohammad M. Kashani*, Laura N. Lowes, Adam J. Crewe, Nicholas A. Alexander, (2014), Modelling Nonlinear Behaviour of Corrosion Damaged RC Bridge Piers subject to Cyclic Loading, Submitted to *4th International Symposium on Life-Cycle Civil Engineering, Tokyo.*

[3] *Mohammad M. Kashani*, Adam J. Crewe, Nicholas A. Alexander, Laura N. Lowes, (2013), Experimental investigation and computational modelling of corrosion induced mechanical-geometrical degradation of reinforcing bars, *11th International Conference on Structural Safety and Reliability, New York.*

[4] *Mohammad M. Kashani*, Adam J. Crewe, Nicholas A. Alexander (2012), Stress-strain response of corroded reinforcing bars under monotonic and cyclic loading, *15th World Conference on Earthquake Engineering, Lisbon, Portugal.*

[5] *Mohammad M. Kashani*, Adam J. Crewe, Nicholas A. Alexander, (2012), Durability considerations in performance-based seismic assessment of deteriorated RC bridges, *15th World Conference on Earthquake Engineering, Lisbon, Portugal.*

[6] *Mohammad M. Kashani*, (2012), Seismic Performance Evaluation of RC Bridge Piers Subject to Combined Earthquake Loading and Material Deterioration in Aggressive Environment, *The 9th fib International PhD Symposium in Civil Engineering*, Karlsruhe Institute of Technology (KIT), Germany.

[7] *Mohammad M. Kashani*, Adam J. Crewe, (2010), Curvature ductility and displacement-based assessment of corrosion damaged RC bridge piers in seismic zones, *Proceeding of SECED Young Engineers Conference, London, CD-ROM Proceeding.*

[8] *Mohammad M. Kashani*, Adam J. Crewe, T.D.G. Canisius, (2010), Ductility of corrosion damage RC bridges in seismic assessment, T*he 5th International ASRANet Conference, Edinburgh, CD-ROM Proceeding.*

[9] *Mohammad M. Kashani*, Adam J. Crewe, (2009), Modelling chloride induced corrosion service life of concrete bridge half-joints, *Proceeding of the fib Conference, Concrete 21st Century Super Hero, London, CD-ROM Proceeding.*

Chapter in Book:

[1] Matt Dietz, Luiza Dihoru, Olafur Oddbjornsson, Mateusz Bocian, ***Mohammad M. Kashani***, James A.P. Norman, Adam J. Crewe, John H.G. Macdonald, and Colin A. Taylor (2011), Earthquake and Large Structures Testing at the Bristol Laboratory for Advanced Dynamics Engineering, *M.N. Fardis and Z.T. Rakicevic (eds.), Role of Seismic Testing Facilities in Performance-Based Earthquake Engineering: SERIES Workshop, Geotechnical,Geological and Earthquake Engineering (22),* DOI :10.1007/978-94-007-1977-4_2.

Awards:

Worldwide University Network - Research Mobility Programme, University of Bristol (2012)

Funding grant for research collaboration with the Department of Civil and Environmental Engineering of the University of Washington.
Title: *Development of modelling strategies for nonlinear seismic performance analysis of corrosion damaged RC bridge piers.*

Runner-up, Young Researchers Conference, Institution of Structural Engineers, UK (2010)

Title: *Seismic performance of corrosion damaged RC bridges in earthquake region.*

This page is intentionally left blank.

TABLE OF CONTENTS

CHAPTER 5. A New Phenomenological Material Model for Reinforcing Bars

LIST OF TABLES

LIST OF FIGURES

“Scientists investigate that which already is; Engineers create that which has never been”

Albert Einstein

This page is intentionally left blank.

CHAPTER 1

Introduction

1.1. Motivation for the study

Reinforced concrete (RC) structures are subject to a variety of deterioration mechanisms including chloride-induced corrosion, alkali-silica reaction and carbonation. Significant research has been done on these various mechanisms, especially in the past two decades or so (Mattues 2009). This has led researchers to develop mathematical models to model and predict the long-term behaviour of RC structures. Moreover, this has enabled researchers and engineers to develop techniques that enhance the resistance of RC structures to deterioration e.g. cathodic protection, saline treatment, desalination etc. (Chryssanthopoulos and Sterritt 2002). The deterioration of concrete structures can be categorised in three main groups as shown in Fig. 1.1.

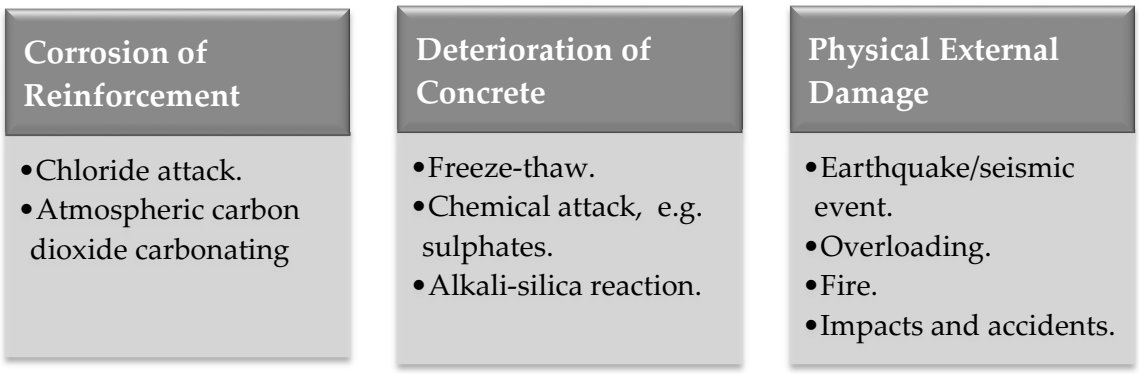

Fig. 1.1 Deterioration mechanisms of RC bridges

Deterioration of concrete bridges, a major part of transport infrastructure artefacts, is recognised as one of the major challenges facing bridge owners and managers. Reinforced and prestressed concrete structures are vulnerable to the damaging effects of corrosion induced primarily by chlorides (from de-icing salts and seawater) and to a lesser extent by carbonation (Gaal et al. 2004) as shown in Fig. 1.2.

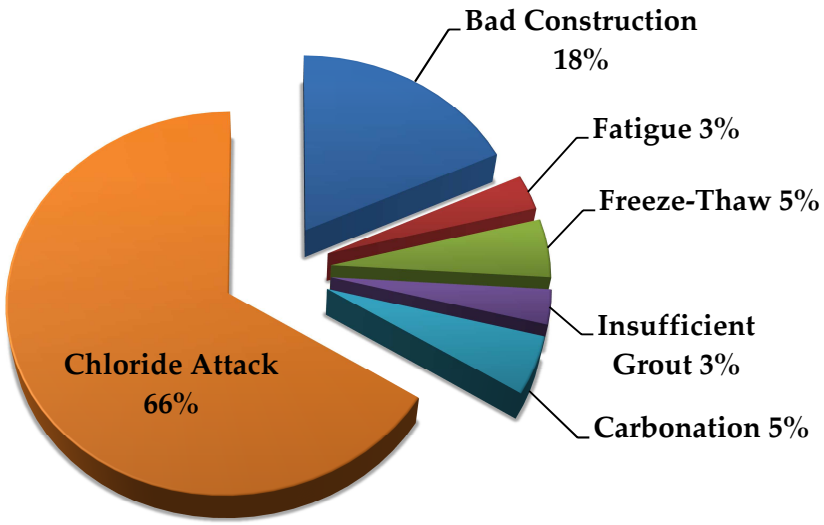

Fig. 1.2 Significance of chloride-induced corrosion of concrete bridges (Gaal et al. 2004)

The corrosion of reinforcing steel in RC structures is a major issue that bridge owners and managers are facing. This is one of the most important sources of engineering and economic problems in developed countries. In the UK, the Department of Transport (DoT) estimated that salt-induced corrosion damage on motorway and trunk road bridges totalled £616.5 million in England and Wales alone (Wallbank 1989) and these bridges represent only about 10% of the total bridge inventory in the country. By one American estimate there is $150 billion worth of corrosion damage on their interstate highway bridges caused by de-icing and sea salt induced corrosion (Transportation Research Board 1991). Indeed, severe corrosion of reinforcement has caused the complete collapse of one structure under live loading as reported in Broomfield (2007). The corrosion of the steel reinforcement leads to concrete fracture through cracking, delamination and spalling of the concrete cover, reduction in strength (flexural, shear, etc.) and a reduction in ductility (Fig. 1.3). As a result, the safety and serviceability of concrete structures are reduced. Therefore their useful service lives are shortened and the probability of failure under extreme loading (e.g. earthquake) is increased.

Fig. 1.3 Corrosion damaged RC bridge pier (Lambert and Atkins 2007)

Furthermore, there are a significant number of older major infrastructure artefacts that are located in earthquake prone regions and are suffering from the material aging and deterioration. In order to provide a durable and reliable solution, the functionality, safety and the service life of various infrastructure artefacts must be estimated based on scientific and engineering knowledge. Climate change, sustainability issues and limited funding in recent years means there is a need for a new bridge management system that can capture all this complexity in a single comprehensive framework. This has led researchers around the world to consider extending existing performance based earthquake engineering frameworks to include long term material performance. In

addition, the deterioration of RC structures due to corrosion increases the risk of failure of aging structures in major earthquakes and can also result in significant permanent damage in smaller earthquakes. This will increase the whole life cycle cost (WLCC) of the structures, and methods for assessment of WLCC and ways to reduce these WLCCs are urgently needed by bridge owners around the world.

Moreover, one of the most common observed collapse mechanisms of RC structures in past earthquakes (e.g. Kobe 1998 and Chile 2010) is buckling of the vertical reinforcement together with crushing of core concrete in RC elements (columns and shear walls). This is due to the lack of confinement reinforcement in older RC columns and shear walls. Fig. 1.4 shows an example of bridge collapse in Kobe earthquake due to this problem.

Fig. 1.4 Collapse of a RC bridge in Kobe earthquake due to lack of confinement and buckling of vertical reinforcement (Arscott 1995)

Accordingly, in recent decades the nonlinear analysis of RC framed structures subject to seismic loading has received a lot of attention. This has been focused on the development of the fibre element technique (Taucer et al. 1991, Spacone et al. 1996). In this approach the member cross section is decomposed into a number of steel and concrete fibres at selected integration points. The material nonlinearity is represented through a uniaxial constitutive material model of steel (tension and compression) and concrete (confined core concrete and unconfined cover concrete). Therefore, the accuracy of the model is greatly influenced by the accuracy of uniaxial material models at cross section level.

Previous research resulted in calibration and validation of fibre models for circular flexural RC bridge piers against extensive experimental dataset (Berry and Eberhard 2006). However, these models are only capable of predicting the nonlinear response without any degradation effect due to inelastic buckling of reinforcement and low-cycle fatigue. There is currently no numerical fibre model available that is able to predict the

nonlinear response of bridge columns accounting for combined effect of inelastic buckling and low-cycle fatigue degradation.

This problem is more critical in corrosion damaged bridge piers where corrosion has a significant impact on the stress-strain response of reinforcement. Ou et al. (2011) and Ma et al. (2012) have investigated, experimentally, the effect of corrosion on the nonlinear response of cantilever RC beams and columns subject to cyclic loading. The results from these experimental studies showed that non-uniform corrosion (also known as pitting corrosion) significantly affects the global response of corroded RC elements subject to cyclic loading. This is mainly due to the influence of corrosion on the cyclic behaviour and inelastic buckling of the corroded bars as well as premature concrete crushing due to corrosion induced cracking of the cover concrete and degradation of the confinement reinforcement.

Choe et al. (2008), Berto et al. (2009), Ghosh and Padgett (2010), Alipour et al. (2011) have investigated the effect of reinforcement corrosion on the behaviour and response of RC bridges subject to seismic loading using a nonlinear fibre-based finite element analysis. However, due to the significant paucity of experimental data and uniaxial material models in the literature, all of these models are based on a simple averaged reduction in the cross section are of the corroded reinforcing bars and ignoring other damage parameters.

Therefore, there is a need for experimental studies to explore the impact of corrosion on nonlinear behaviour of reinforcement so that more advanced uniaxial material models can be developed to improve the accuracy of the existing fibre models. These material models should be implemented to the existing fibre models and be validated against experimental dataset at component level (e.g. column and beams).

This thesis is addressing these issues. The detailed objectives and contribution of the thesis to the state of the art are discussed in the following sections.

1.2. Research objectives and scope

The primary objectives of the research presented in this thesis are:

1) To explore the impact of pitting corrosion on the nonlinear stress-strain behaviour of corroded reinforcing bars under monotonic loading with the effect of inelastic buckling.
2) To explore the impact of pitting corrosion on the nonlinear cyclic stress-strain behaviour of corroded reinforcing bars with the combined effects of inelastic buckling and low-cycle fatigue degradation.

3) To study the influence of corrosion pattern on the mechanical-geometrical degradation of reinforcing bars under monotonic and cyclic loading.
4) To develop a new phenomenological uniaxial hysteretic model to model the nonlinear cyclic stress-strain behaviour of reinforcing bars including the effect of corrosion, inelastic buckling and low-cycle fatigue degradation.
5) To develop modelling recommendations that provide accurate simulation of the cyclic response, including loss of lateral strength and cyclic degradation for flexurally governed RC bridge piers. This objective has two parts: *i*) calibration and validation of a basic uncorroded model for simulation of uncorroded RC bridge piers and *ii*) Implementation of the corrosion damage models in a calibrated numerical model to investigate the impact of material deterioration on the cyclic behaviour (including loss of lateral strength and cyclic degradation) of two hypothetical RC bridge piers.

1.3. Overview of the thesis and contribution to the state of the art

The research presented in this thesis focuses on the development of a new uniaxial material model for accurately simulating cyclic response of corrosion damaged reinforcing bars which includes the effect of inelastic buckling and low-cycle fatigue degradation. Moreover, a methodology is developed for simulation of the cyclic response of corrosion damaged flexurally governed RC bridge piers to evaluate and advance current assessment procedures in practice. The research comprises:

Chapter 2 outlines the existing mathematical models for corrosion damage and service life prediction of bridges. Previous experimental testing on the impact of corrosion on nonlinear cyclic behaviour of beams and columns is reviewed and critical issues are also discussed.

Chapter 3 presents a detailed discussion on the experimental programme which investigated the influence of corrosion on the nonlinear monotonic and cyclic behaviour of reinforcing bars. The corrosion was simulated in the laboratory environment using an accelerated corrosion procedure. A total of 12 monotonic tension tests, 57 monotonic compression (buckling) tests and 40 cyclic tests with various corrosion levels and slenderness ratios were conducted. Using the experimental data a set of simple empirical equations are developed and incorporated into existing material models to simulate the buckling and post-buckling behaviour of corroded reinforcing bars.

Chapter 4 discusses the spatial variability of corrosion and its impact on the nonlinear stress-strain behaviour of corroded reinforcing bars. 15 corroded bars from the monotonic buckling tests specimens and 8 corroded bars from the cyclic test specimens

were taken for further statistical analysis of the corrosion patterns. An advanced 3D optical measurement technique was employed to scan the surface of the corroded bars. A novel stochastic signal processing technique was used for the corrosion pattern analysis and to develop the probabilistic distribution models for geometrical properties of corroded bars. Finally the scanned bars were tested under monotonic buckling and cyclic loading. The impact of corrosion patterns on the nonlinear stress-strain behaviour of corroded bars was then investigated using nonlinear finite element modelling of the tested bars the results of which were compared with the experimental results.

In **Chapter 5**, a new phenomenological uniaxial material model is developed for reinforcing bars. The new material model accounts for the influence of corrosion damage, inelastic buckling and low-cycle fatigue degradation. The material parameters are calibrated based on experimental and numerical simulation data of uncorroded and corroded bars. The new material model is then implemented in the OpenSees platform as a new uniaxial material class known as *CorrodedReinforcingSteel*. Finally the material model is validated against a UW-PEER experimental RC column dataset. The model parameters are also calibrated for RC columns using a comprehensive parametric study of pinching parameters to account for the influence of horizontal tie reinforcement. Moreover, a new modelling technique is developed for modelling the flexural behaviour of buckling critical RC bridge piers using a distributed plasticity fibre beam-column element. The new technique avoids localisation issues due to the softening behaviour of critical sections following the buckling of the vertical reinforcement.

In **Chapter 6**, a computational platform is developed to implement the calibrated corrosion damage uniaxial material models developed in Chapters 3 to 5 into the optimum fibre model also developed in Chapter 5. The impact of the modelling assumptions and different corrosion damage models on the response of corroded RC columns are explored. Two hypothetical corroded columns are considered with different confinement levels. Using monotonic pushover analyses and cyclic analyses the impact of corrosion on the drift capacity, ductility, energy dissipation capacity and cyclic degradation are explored. Chapter 6 provides an insight into a new detailed modelling technique that is able to capture the combined effect of inelastic buckling, low cycle fatigue and corrosion on the cyclic degradation of RC columns. A limitation of earlier fibre models is that the corrosion damage is assumed to be uniform along the reinforcing bars. The modelling technique developed in Chapter 6 accounts for the impact of pitting corrosion on cross section area, buckling length, yield strength and ductility loss in tension, buckling behaviour in compression and reduced low-cycle fatigue life of the corroded vertical reinforcement. The model also accounts for the impact of corrosion on the cracked cover concrete and the reduced strength and ductility of the core confined concrete due to the corrosion of the confinement reinforcement. Chapter 6 advances the

existing modelling techniques that are not able to capture any degradation in the nonlinear behaviour of RC columns caused by the combination of corrosion and cyclic loading.

Chapter 7 summarises the main conclusions and findings of this research and provides recommendations for future research.

An overview of the thesis outline is shown in the Fig. 1.5.

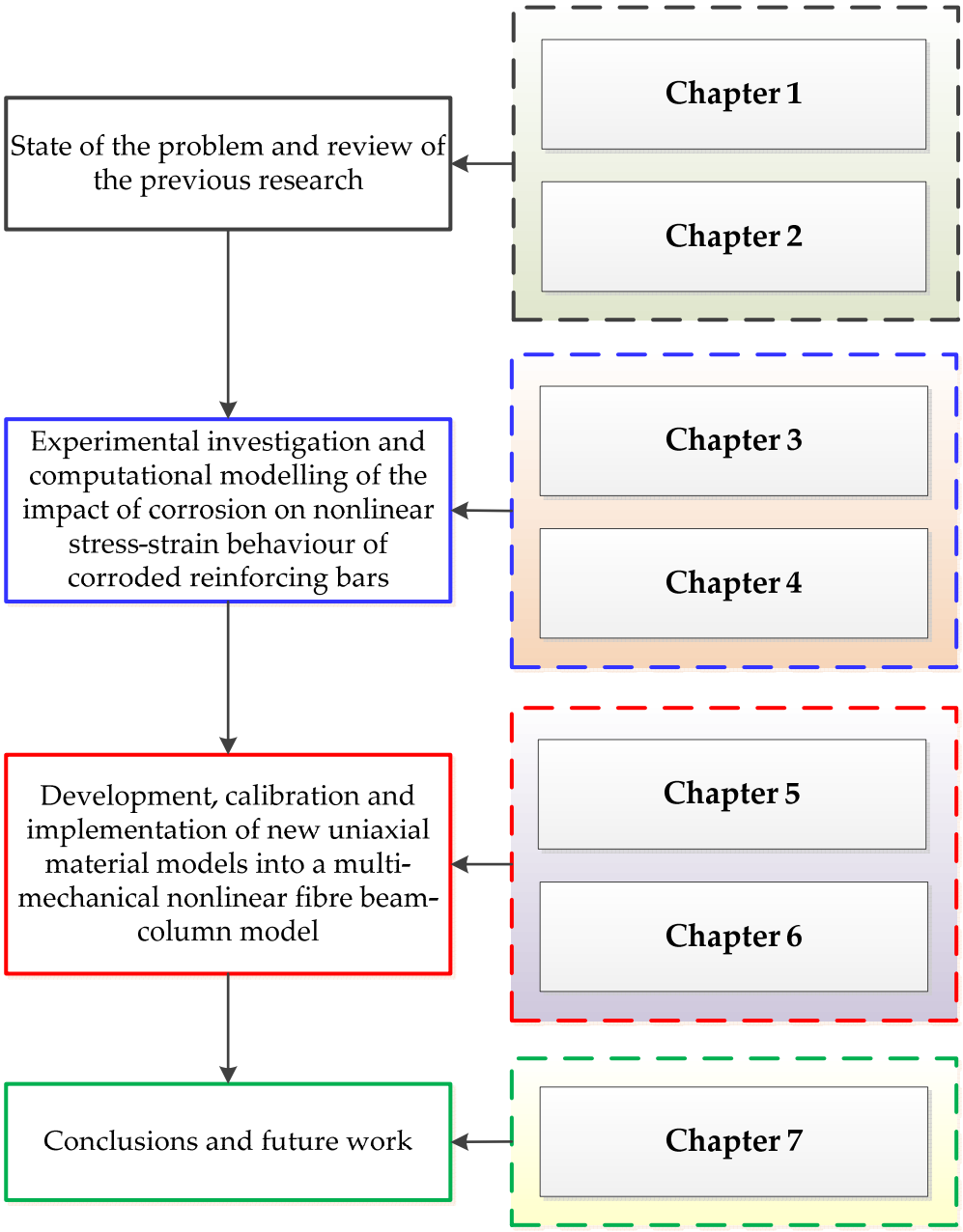

Fig. 1.5 Overview of the thesis outline

CHAPTER 2

Corrosion–Induced Structural Degradation (Literature Review)

2.1. Deterioration of RC structures due to chloride induced corrosion

In existing models of chloride induced deterioration of RC (reinforced concrete) structures, the performance degradation is directly related to the cross section loss of reinforcing steel due to corrosion. Deterioration of a bridge or its components is not considered until the initiation of corrosion at reinforcement level, as it is shown by the horizontal line on the curve in Fig. 2.1. This model was initially proposed by Tuutti (1982) and can be used to predict the service life of a bridge structure or its components. Based on this model the performance and service life of RC structures/bridges exposed to chloride can be idealised in two phases which are (a) *Initiation phase* and (b) *propagation phase* (Lounis and Amleh 2003) as shown in Fig. 2.1.

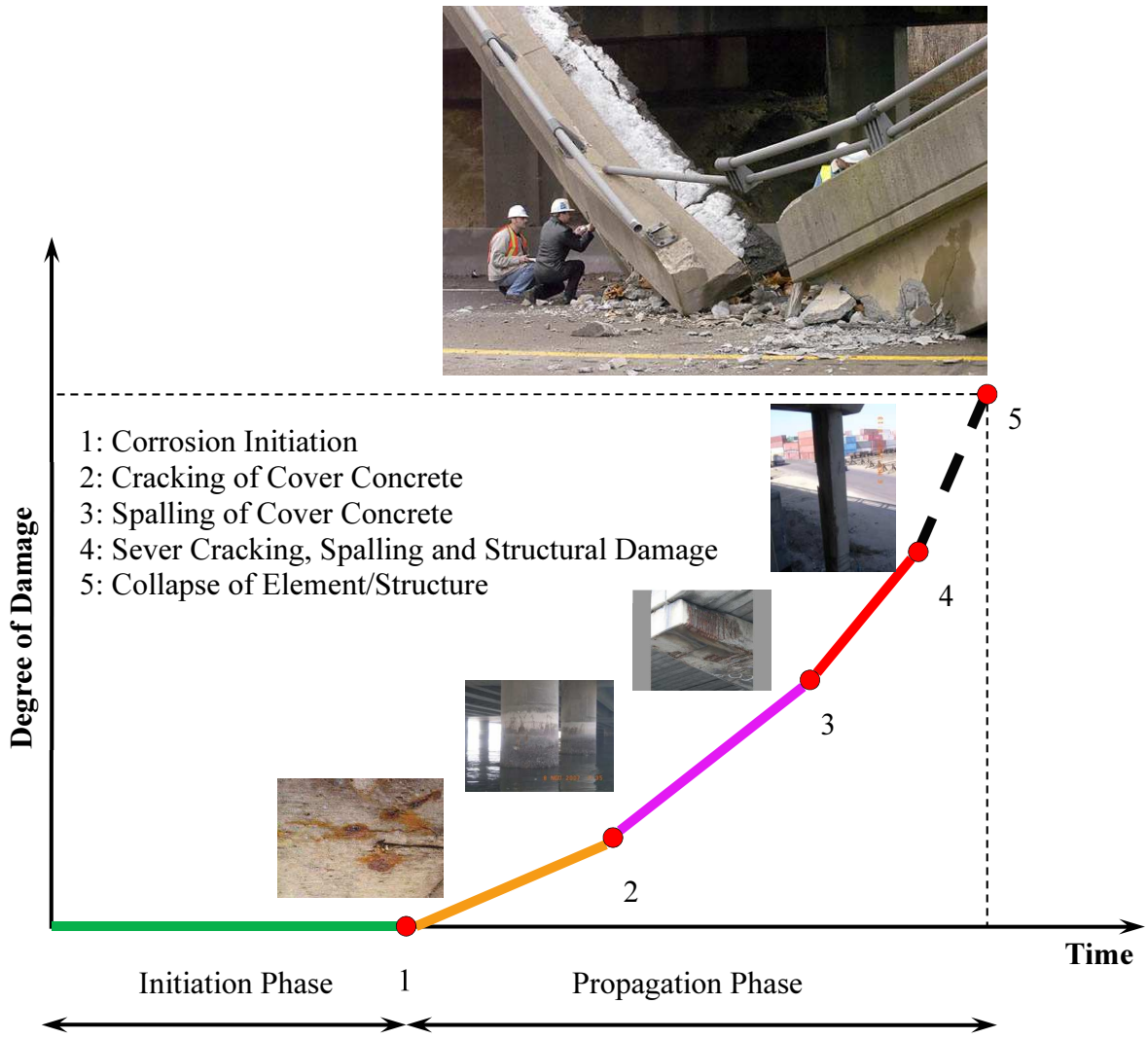

Fig. 2.1 Phases of corrosion induced deterioration of RC structures

a) Initiation phase: During this phase chloride ions penetrate through the cover concrete. Once the chloride ions reach the first layer of reinforcing steel, they accumulate over the time. Corrosion will initiate once the amount of chloride ions at the reinforcement level reaches the so-called *threshold level*. At this stage the chloride ions at the reinforcement level break the passive layer at the interface of reinforcement and concrete and initiate the corrosion depending on the availability of water and oxygen (Fig. 2.2). Chloride ions are not consumed in the corrosion process but they help to breakdown the passive layer and therefore they accelerate the process (Broomfield 2007). The corrosion initiation time is a function of several parameters, including the depth of cover concrete, the concentration of chloride at the surface of RC section, the quality concrete and the type of reinforcing steel (epoxy-coated black steel, galvanised steel, etc.).

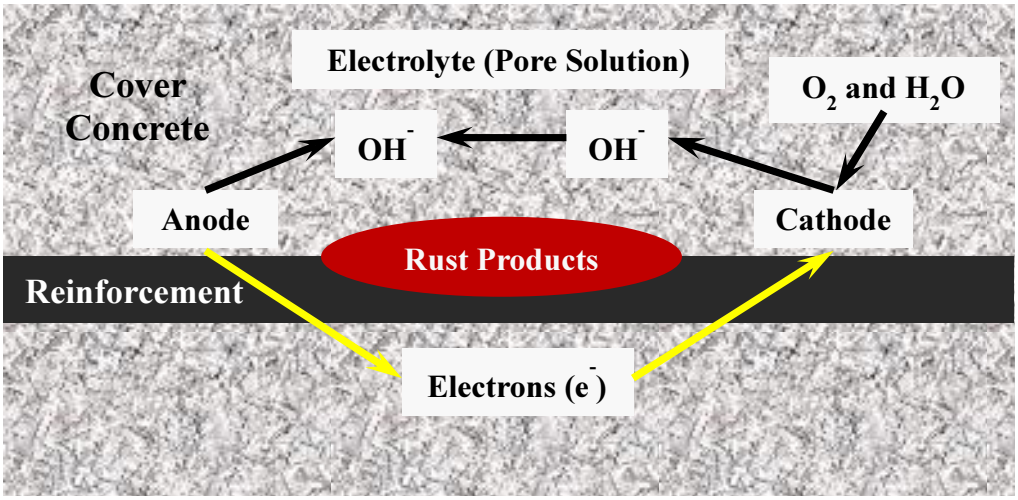

Fig. 2.2 Corrosion mechanism of steel reinforcement inside concrete

Once the passive layer around the reinforcement breaks down, rust formation process will start at the surface of steel. This process is progressing by dissolving reinforcing steel in the concrete pore water. At this stage reinforcement starts giving up electrons which is known as *anodic* reaction as described in Eq. (2.1):

$$Fe \rightarrow Fe2 + 2e^- \quad (2.1)$$

In order to preserve the electrical neutrality, the $2e^-$ created in the anodic reaction has to be consumed on the reinforcement surface. Therefore, another chemical reaction is required to consume the electrons. This reaction is known as *cathodic* reaction which takes place by consumption of water and oxygen as described in Eq. (2.2):

$$2e^- + H2O + 1/2\ O2 \rightarrow 2OH^- \quad (2.2)$$

b) Propagation Phase: Once corrosion initiates the rust product around the reinforcement starts expanding. Therefore, the stresses induced by this expansion generate tensile stress in cover concrete which subsequently leads to fracture of cover concrete (cracking, delamination, spalling). This will result in the loss of ultimate strength, loss of bond between steel and concrete and ultimately failure of the section (Fig. 2.3). The failure of a structure depends on several parameters including the corrosion rate, environmental condition, natural hazards i.e. earthquake loading, quality of construction etc.

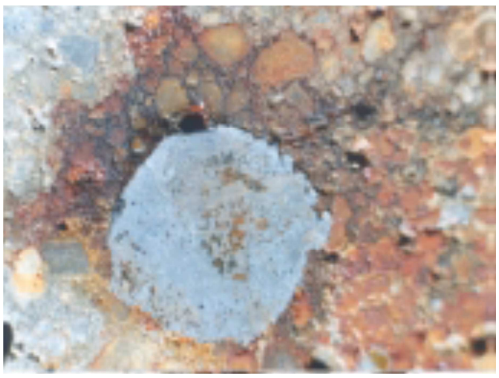

(a)

(b)

(c)

Fig. 2.3 Examples of corrosion propagation stage: (a) crack initiation period (b) crack propagation period (c) spalling of cover concrete

In the past decades several researchers have put significant efforts to develop a mathematical model to predict the service life of RC bridges. This is an important part of the modern bridge management systems. In this chapter the existing material models that have been developed by other researchers to predict the corrosion initiation time, corrosion induced crack initiation time and crack propagation are reviewed and discussed.

2.2. Importance of deterioration modelling in a bridge management system

Organising a Bridge Management System (BMS) is a challenging task that involves the prioritisation of an optimum maintenance strategy for bridge structures. This requires the determination of a distinct optimum rehabilitation strategy for individual parts of a structure in a given bridge or in the entire bridge network. This optimisation mainetance

strategy should consider the minimisation of failure risk and rehabilitation costs over the service life of the structures. Therefore, there is a need to develop a reliable and effective decision support models that include condition assessment models, deterioration prediction models, risk assessment models and maintenance optimisation models (Lounis 2003). This is shown schematically in Fig. 2.4.

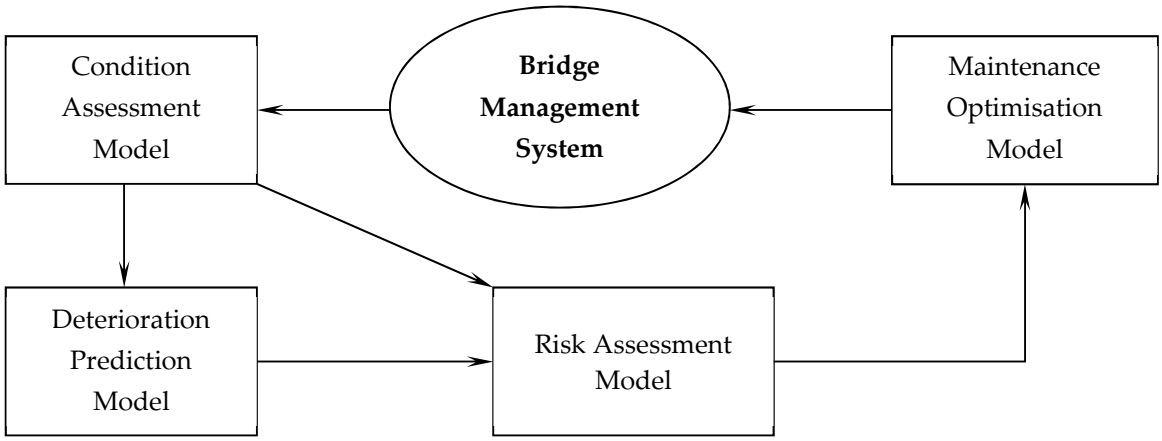

Fig. 2.4 Decision Model for Bridge Management System (Lounis 2003)

2.3. Modelling chloride induced corrosion

There are several models available in the literature for predicting the corrosion initiation time for reinforcing steel in concrete exposed to chloride ions (Andrade et al. 1993, Bamforth 2004, Rafiq et al. 2004 and Val 2007). As explained previously in Section 2.1, corrosion has two stages, defined as initiation and propagation (Fig. 2.1) which was first proposed by Tuutti (1982). The rate of chloride ingress is normally modelled using the Fick's 2nd law of diffusion. The initial mechanism is suction by capillary action, especially when the surface of concrete is dry which is then followed by 'true' diffusion (Broomfield 2007).

Given that concrete is not a homogeneous material and is aging over time, the diffusion of chloride into the concrete is affected by the environment. Therefore, it is possible to describe the time variation of chloride concentration at the depth of concrete using the Fick's 2nd law of diffusion for a one dimensional flow as shown in Eq. (2.3) (Crank 1975):

$$\frac{\partial C}{\partial t} = \frac{\partial}{\partial x}\left[D \frac{\partial C}{\partial x} \right] \tag{2.3}$$

where C is chloride concentration at a distance x from the surface of concrete at time t and D is corresponding diffusion coefficient.

Assuming a constant diffusion coefficient, C = C_s and C = 0 for x > 0 at t = 0, Crank's solution to Eq. (2.3) yields (Crank 1975):

$$C(x,t) = C_s\left(1 - erf\left(\frac{x}{2\sqrt{Dt}}\right)\right) \tag{2.4}$$

where $C(x,t)$ is chloride level at depth x at time t, *erf* is the error function, C_s is the surface chloride (% weight of cement) and D is the diffusion coefficient (mm²/year).

From Eq. (2.4) it is possible to estimate the apparent diffusion coefficient, D and the time for corrosion initiation by setting $C(x,t)$ equal to critical chloride threshold C_{cr}. The following assumptions are made in this calculation (Chryssanthopoulos and Sterritt 2002):

- The chloride ingress process in RC structures can be modelled by one dimensional diffusion law in a homogeneous body.
- The surface chloride concentration, Cs, is not time dependant.
- The diffusion coefficient, D is constant.

The Eq. (2.4) represents the very basic diffusion model based on the Fick's law. However, in real world the chloride diffusion parameters are affected by environmental conditions i.e. moisture, temperature etc. More recently other researches have extended the Eq. (2.4) to account for these parameters. This has been included in the CEB-FIP *fib* (*fib* Bulletin 34 2006) model code for service life design.

2.3.1. CEB-FIP fib approach for modelling depassivation of the reinforcement

In the early 1990s several parallel efforts took place that improved the original Fickian model (Crank 1975). A full probabilistic platform has been developed for modelling chloride induced corrosion within the research project DuraCrete (DuraCrete 2000). This has slightly been revised in the research project DARTS, both funded by the European Union. The *fib* (Fédération Internationale du Béton - International Federation for Structural Concrete) model code is based on DuraCrete model which is in accordance with basic Fick's second law of diffusion (Eq. (2.4)) with some modifications (*fib* bulletin 34 2006). The limit state equation in which the chloride concentration C_{crit} is compared to the actual chloride concentration at the depth of the reinforcement at time t is described in Eq. (2.5):

$$C_{crit} = C(x,t) = C_0 + \left(C_{S,\Delta x} - C_0\right)\left(1 - erf\left(\frac{a-\Delta x}{2\sqrt{D_{app,C}\,t}}\right)\right) \quad (2.5)$$

where, C_{crit} is the critical chloride threshold content (% weight of cement), $C(x,t)$ is chloride concentration at depth x at time t (% weight of cement), *erf* is the error function, C_0 is the initial chloride content of the concrete that can be taken as 2.78% of cement weight in standard concrete mixes, $C_{S,\Delta x}$ is chloride content at depth Δx at a certain point of time t (% weight of cement), x is the depth with a corresponding chloride content (mm), a is the thickness of cover concrete (mm), Δx is the depth of the convection zone (concrete layer, up to which the process of chloride penetration differs from Fick's second law of diffusion), and $D_{app,c}$ is the apparent diffusion coefficient through concrete (mm^2/year).

Usually $D_{app,c}$ is calculated using a chloride profiling method with back calculation of the state equation shown in Eq. (2.5). The chloride profiling method is usually implemented via material testing using drilled concrete cores which are tested in a laboratory. Therefore, the calculated $D_{app,c}$ using this method is a constant average value representing the period between the start of exposure and the time of inspection/material testing. In the absence of any material testing or real data, the method suggested by *fib* (*fib* bulletin 34 2006) can be used to calculate the $D_{app,c}$ which is described in Eq. (2.6).

$$D_{app,C} = k_e\, D_{RCM,0}\, k_t\, A(t) \quad (2.6)$$

where k_e is the environmental transfer variable as described in Eq. (2.7)

$$k_e = \exp\left(b_e\left(\frac{1}{T_{ref}} - \frac{1}{T_{real}}\right)\right) \quad (2.7)$$

b_e is the regression variable with mean value and standard deviation of 4800K and 700K respectively, T_{ref} is the standard test temperature that can be taken as 293K, T_{real} is the temperature of the structural element or the ambient air that can be determined using the available data from the nearest weather station, K_t is the transfer variable equal to 1 and $A(t)$ is the ageing parameter as described in Eq. (2.8)

$$A(t) = \left(\frac{t_0}{t}\right)^a \quad (2.8)$$

a is the ageing exponent. The *fib* recommended values for a are summarised in Table 2.1. t_0 is the reference point of time that can be taken as 0.0767yrs (t_0 = 28 days) and $D_{RCM,0}$ is chloride migration coefficient. The *fib* recommended values for $D_{RCM,0}$ are summarised in Table 2.2.

Table 2.1 Probabilistic distribution parameters of the ageing variable *a* (*fib* Bulletin 34 2006)

Concrete Type	Ageing Exponent *a*
Portland cement concrete CEM I; 0.40 ≤ w/c ≤ 0.60	Beta[1] (m[2]= −0.3; s[3]= −0.12; a[4] = 0.0; b[5] = −1.0)
Portland fly ash cement concrete f ≥0.2z; k = 0.50 CEM I; 0.40 ≤ w/c ≤ 0.62	Beta[1] (m[2]= −0.6; s[3]= −0.15; a[4] = 0.0; b[5] = −1.0)
Portland cement concrete CEM III/B; 0.40 ≤ w/c ≤ 0.60	Beta[1] (m[2]= −0.45; s[3]= −0.20; a[4] = 0.0; b[5] = −1.0)

[1]Beta distribution; [2]m: mean value; [3]s: standard deviation; [4]a: lower bound; [5]b: upper bound

Table 2.2 Quantification of the $D_{RCM,0}$ for different concrete mixtures (*fib* Bulletin 34 2006)

$D_{RCM,0}$ (m²/S) Cement Type	w/c					
	0.35	**0.40**	**0.45**	**0.50**	**0.55**	**0.60**
CEM I 42.5 R	n.d.[1]	8.9×10^{-12}	10.0×10^{-12}	15.8×10^{-12}	19.7×10^{-12}	25.0×10^{-12}
CEM I 42.5 R + FA (k = 0.5)	n.d.[1]	5.6×10^{-12}	6.9×10^{-12}	9.0×10^{-12}	10.9×10^{-12}	14.9×10^{-12}
CEM I 42.5 R + SF (k = 2.0)	4.4×10^{-12}	4.8×10^{-12}	n.d.[1]	n.d.[1]	5.3×10^{-12}	n.d.[1]
CEM III/B 42.5	n.d.[1]	1.4×10^{-12}	1.9×10^{-12}	2.8×10^{-12}	3.0×10^{-12}	3.4×10^{-12}

n.d. – chloride migration coefficient $D_{RCM,0}$ has not been determined for these concrete mixes. FA is fly ash and SF is silica fume with their respective k-value (efficiency factor).

If the structural element is exposed to wet and dry cyclic chloride concentration i.e. bridge piers adjacent to a highway; the water in the concrete close to the surface evaporates, therefore any subsequent rewetting provokes capillary suction. The capillary action leads to a rapid chloride transport and accumulation in the concrete up to a depth Δx until the saturation condition where $C_{S,\Delta x} = C_{S,0}$. The mean and standard deviation of Δx for the splash zone condition are 8.9mm and 5.6mm respectively. For the spray condition, where the distance of the structural element is larger than 1.5m from the road surface, and the submerged condition in marine structures $\Delta x = 0$.

The chloride contamination of a structural element $C_{S,\Delta x}$ in the splash zone or in the spray zone increases with a decreasing distance to the chloride source. $C_{S,\Delta x}(t)$ is a time-dependent variable, however for simplicity the *fib* recommendation is to consider it as a time-independent variable. Eq. (2.9) can be used to calculate the maximum chloride content of chloride profile in the concrete (C_{max}).

$$C_{\max}\left(x_a, x_h\right) = 0.465 - 0.051\ln\left(x_a + 1\right) - \left(0.00065\left(x_a + 1\right)^{-0.187}\right)x_h \tag{2.9}$$

where, x_a is the horizontal distance from the roadside (cm) and the x_h is the height above the road surface (cm). For structural elements in a splash zone condition $C_{S,\Delta x}$ is defined as C_{max} and for structural elements in the spray zone condition (the height is more than 1.5m above the road surface) C_{max} equals the chloride content at the concrete surface C_S. It

should be noted that Eq. (2.9) is calibrated based on the conditions on German roads. Therefore, this model must be used with caution elsewhere in the world.

2.3.2. Estimation of the critical corrosion initiation time T_{corr}

From the chloride profile and draw back calculation of the error function the chloride parameters can be estimated. If we substitute $C_{s,\Delta x}$ with C_{crit} as the critical chloride threshold at depth Δx of concrete, then the corrosion initiation period T_{corr} can easily be calculated from equation (2.10) as shown below:

$$T_{corr} = \frac{(a-\Delta x)^2}{4\,D_{app,C}}\left(1-erf^{-1}\left(\frac{C_{crit}}{C_{S,\Delta x}-C_0}\right)\right)^{-2} \tag{2.10}$$

The *fib* recommended mean and standard deviation values for C_{crit} are 0.6% and 0.15% of the cement weight in the concrete mix respectively.

Based on the procedure explained in this section, the time at which corrosion initiates can be estimated. Further detail and discussions of other model parameters regarding the diffusion procedure and other environmental effects are available in CEB-FIP *fib* (*fib* Bulletin 34 2006).

2.4. Modelling corrosion induced cracking of cover concrete

Cover cracking due to corrosion is a well-known problem. There are numerous models that have been developed for prediction of the corrosion induced cover cracking during the past decades.

The first model was introduced by Bazant (1979). His model was based on the thick-wall cylinder model to determine the internal pressure induced by corrosion. He considered that the cover fails once the first crack appears on the internal radius. Some researchers have used finite element simulation to model cover cracking (Molina et al. 1993 and Du et al. 2007) and others used analytical formulations based on experimental testing to predict the crack initiation and crack propagation in reinforced concrete specimens (Liu and Weyer 1998, Vu et al. 2005, Bhargava et al. 2006, El Maaddaay and Soudki 2007). Some of the researchers used fracture mechanics theory to predict the time to cover cracking and crack propagation (Ohtsu and Yoshimura 1997 and Williamson and Clark 2000). In this research a simplified thick-wall theory that was developed by Liu and Weyers (1998) is used to predict the time of crack initiation and propagation crack in cover concrete due to accumulation of corrosion products.

2.4.1. Modelling of the amount of corrosion product needed to fill the porous zone

Concrete has some porosity at the reinforcement interface. The porosity decreases with increasing the distance from the reinforcement interface. The porosity is typically of the order of 0.5 at about 10-20μm from the reinforcement interface. If t_{pore} is considered to be the thickness of an equivalent zone with the porosity of one around a reinforcing bar, the W_{porous}, the mass of rust products that is necessary to fill the porous zone can be written as Eq. (2.11) (Thoft-Christensen 2003).

$$W_{porous} = t_{pore} \times \pi \rho_{rust} D_0 \tag{2.11}$$

Where ρ_{rust} is the density rust products and D_0 is the diameter of the original uncorroded reinforcement. A schematic representation of the corroded bar configuration in shown in Fig. (2.5).

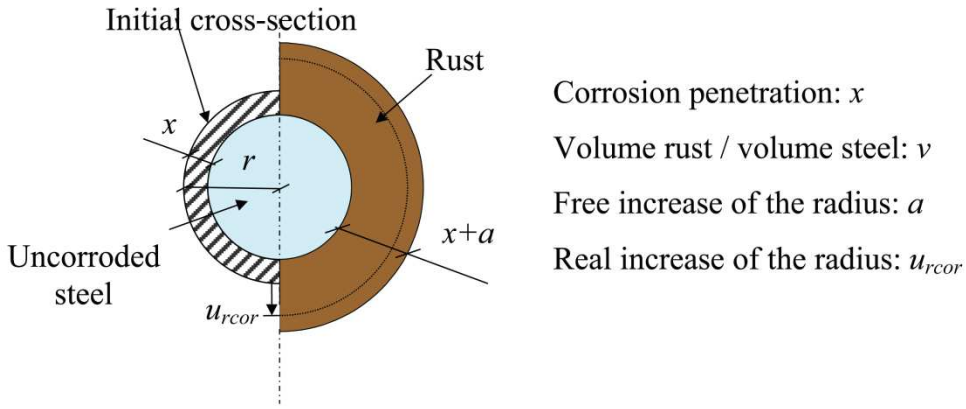

Fig. 2.5 Configuration of corroding reinforcement (Schlune 2006)

2.4.2. Modelling of the critical amount of corrosion products

Once corrosion process starts, the corrosion products will initially fill the porous zone which then results in an expansion in the concrete surrounding the reinforcement. This mechanism generates tension stress in the concrete. Given the concrete is a weak material in tension, with increasing the corrosion the tensile stresses will quickly reach the maximum tension capacity of concrete which results in cracking of cover concrete (Thoft-Christensen 2003).

At the initial stage of cover concrete cracking the corrosion products should fill three volumes, namely the porous zone, the expansion of concrete due to rust pressure, and

the space of the consumed corroded steel. The corresponding total mass of corrosion products at time T_{crit} that requires filling these volumes is defined in Eq. (2.12).

$$W_{crit} = W_{porous} + W_{expan} + W_{steel} \tag{2.12}$$

W_{expan} is the mass of corrosion product needed to fill the space due to the expansion of the concrete around the reinforcement and W_{steel} is the mass of rust products at time T_{crack} of cracking.

The W_{expan} can be written as follows (Eq. (2.13)):

$$W_{expan} = \rho_{rust}\pi(D + 2t_{por})t_{crit} \tag{2.13}$$

where, t_{crit} is the thickness of the expansion at crack initiation. Other researchers (Liu and Weyers 1998) have estimated t_{crit} by assuming that the concrete is a homogeneous elastic material and can be approximated by a thick-walled concrete cylinder with inner radius $a = (D+2t_{pore})/2$ and outer radius $b = c+(D+2t_{pore})/2$ where c is the cover depth as shown in Fig. 2.6.

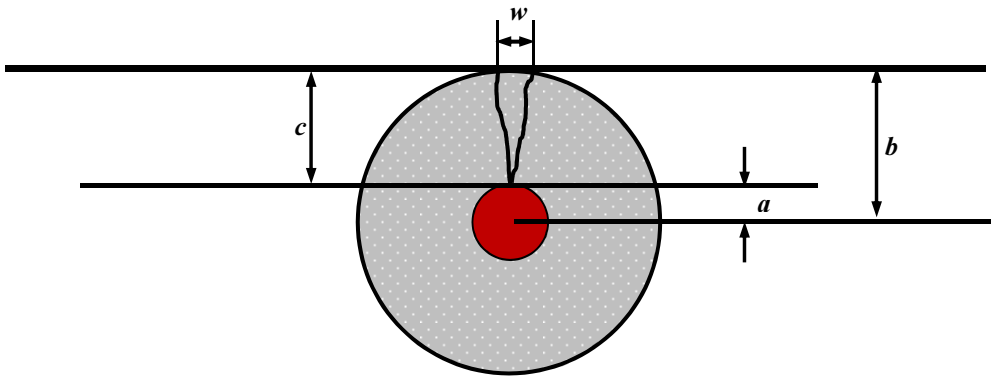

Fig. 2.6 Idealisation of the concrete around the reinforcement by a thick-walled cylinder

Then the approximate value of the critical expansion t_{crit} is defined in Eq. (2.14).

$$t_{crit} = \frac{c\, f_t'}{E_{eff}}\left(\frac{a^2 + b^2}{b^2 + a^2} + \nu_c\right) \tag{2.14}$$

Where v_c is Poisson's ratio of concrete, f_t' is the tensile strength of concrete and E_{eff} is the effective elastic modulus of concrete. The effective elastic modulus of the concrete can be estimated as $E_{eff} = E_c / (1+\varphi_{cr})$, where E_c is the elastic modulus of concrete and φ_{cr} is creep coefficient of concrete (Val 2007). Finally, W_{steel} can be written in the form of Eq. (2.15)

$$W_{steel} = \frac{\rho_{rust}}{\rho_{steel}} M_{steel} \tag{2.15}$$

Where, ρ_{steel} is steel density and M_{steel} is the mass of the corroded steel. M_{steel} is proportional to W_{crit}, in this thesis the value of proportionality is considered to be $M_{steel} = 0.57W_{crit}$. Therefore, Eq. (2.12) can be rewritten as below (Eq. (2.16)).

$$W_{crit} = \frac{\rho_{steel}}{\rho_{steel} - 0.57\rho_{rust}}(W_{porous} + W_{expan}) \tag{2.16}$$

The model assumes that the rate of production of corrosion products is inversely proportional to their thickness because an increase in the thickness of corrosion products leads to an increase in the steel ionic diffusion distance. The time to crack initiation (time needed for formation of W_{crit} of corrosion products) can then be defined in Eq. (2.17).

$$t_{cr} = \frac{W_{crit}^2}{2k_p} \tag{2.17}$$

where, k_p is the rate of production of corrosion products given by the following empirical formula suggested by Val (2007):

$$k_p = 9.8\times10^{-5}\frac{\pi D i_{corr}(t)}{\alpha} \tag{2.18}$$

where, $i_{corr}(t)$ is the corrosion current density at time t after corrosion initiation in μA/cm². The time dependent corrosion current density can be estimated using Eq. (2.19) and (2.20):

$$i_{corr}(t) = 0.85\, i_{corr0}\left(t - T_{corr}\right)^{-0.3} \tag{2.19}$$

$$i_{corr0} = \frac{27\left(1 - w/c\right)^{-1.64}}{C} \tag{2.20}$$

where, i_{corr0} is the corrosion current density at corrosion initiation time T_{corr}, w/c is the water cement ratio of concrete and C is the thickness of cover concrete. Eq. (2.19) shows that corrosion current density decreases after corrosion initiation time. This is due to the formation of corrosion products around the surface of the reinforcement. This reduces the diffusion of the iron ions away from the reinforcement surface which will result in reduction of corrosion rate with time (Vu and Stewart 2000).

The end of service life of a corroded structure is defined as excessive cracking, i.e., when the width of a crack due to corrosion, w, exceeds a limit value, w_{lim} (*e.g.* w_{lim} = 0.5mm Val (2007)). Existing models describing crack propagation due to corrosion of reinforcing steel are empirical models obtained by regression analysis of experimental data. The following empirical equation (Eq. (2.21)) may be used to describe the crack propagation (Vidal 2004).

$$w = K(\Delta A_s - \Delta A_{s0}) \tag{2.21}$$

Where ΔA_s is the steel loss of the reinforcing bar cross section in mm^2, ΔA_{s0} is the steel cross section loss needed for crack initiation in mm^2 and K = 0.0575 is an empirical coefficient. To evaluate ($\Delta A_s - \Delta A_{s0}$) it is assumed, for simplicity, that after crack initiation the corrosion rate does not change with time (for $t > t_{cr}$, i_{corr} is given by Eq. (2.19)). Additional penetration of corrosion Δp, at time t after crack initiation can then be calculated as (Val 2007).

$$\Delta p(t) = 0.0116 i_{corr}(t - t_{cr} - t_i) \tag{2.22}$$

$$\Delta A_s - \Delta A_{s0} = \pi \Delta p\left(D - 2p_0 - \Delta p(t)\right) \tag{2.23}$$

where, p_0 is the corrosion penetration corresponding to ΔA_{s0} which is defined in Eq. (2.24).

$$p_0 = \frac{\alpha W_{crit}}{(\pi D \rho_{st})} \tag{2.24}$$

Thus, the additional corrosion penetration, Δp_{lim} corresponding to the limit crack width, w_{lim} can be estimated as

$$\Delta p_{\lim} = \frac{D - 2p_0}{2} - \sqrt{\left(\frac{D - 2p_0}{2}\right)^2 - \frac{w_{\lim}}{\pi K}} \tag{2.25}$$

Given Δp_{lim}, the time of failure, t_f (when $\Delta p(t_f) = \Delta p_{lim}$) can be easily evaluated from Eq. (2.25) (Val 2007).

The procedure of service life prediction described in sections 2.3 to 2.4 is summarised in a flowchart that is shown in Fig. 2.7.

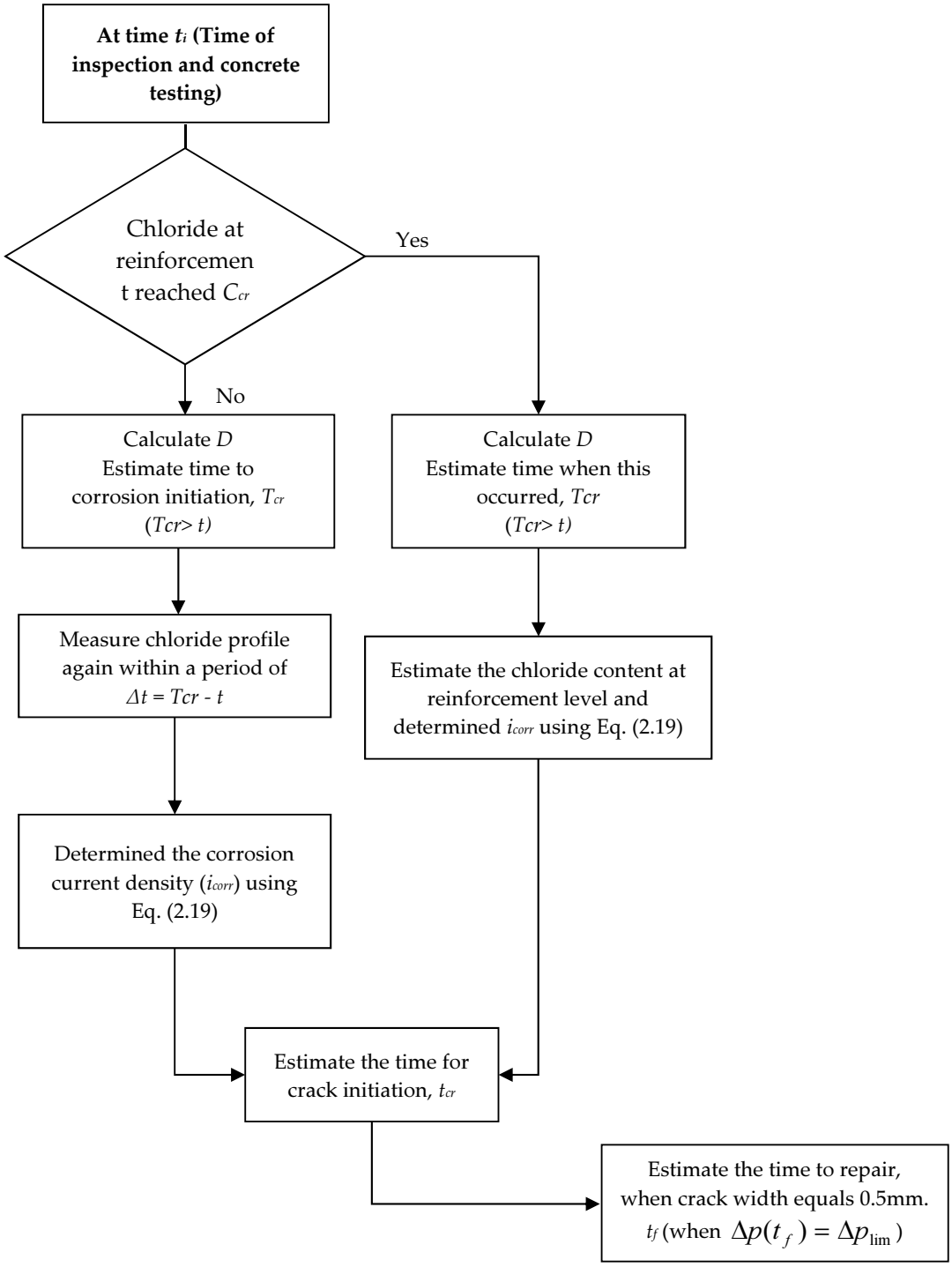

Fig. 2.7 Procedure of modelling chloride induced corrosion and service life prediction of deteriorating RC structures

2.5. Corrosion effect on structural performance of RC structures

As discussed in the previous sections, the problem associated with the deterioration of RC structures due to corrosion is not only limited to the reinforcing steel. The corrosion products exert stresses within the cover concrete that cannot be supported by the limited tension capacity of the concrete which results in concrete cracking. This leads to weakening of the bond and anchorage between concrete and reinforcement which directly affects the structural performance of concrete elements within a structure.

Over the past few decades several researchers have put a significant effort into studying the effect of corrosion on the mechanical behaviour of corroded structural elements (beams, slabs and columns) using an accelerated corrosion procedure in the laboratory (Cairns and Zhao 1993, Rodriguez et al. 1996, Rodriguez et al. 1997, Razak and Choi 2001, Cairns et al. 2005, Rodriguez et al. 2005, Du et al 2007, Azad et al. 2007). The principal effects of corrosion on structural elements are:

- Loss of bar cross section.
- Changing the mechanical properties and ductility of steel reinforcement.
- Reduced compressive capacity of the cracked cover concrete.
- Reduction of bond strength at the steel and concrete interface.

The consequences of each of these effects and their interrelationships on load-carrying capacity are summarised in Fig. 2.8 (Cairns et al. 2008).
The progressive expansion of rust at the steel and concrete interface induces splitting stresses in concrete and eventually leads to cover cracking and spalling. This will result in deterioration of the bond between steel and concrete, which will influence the bending stiffness and the shear capacity of the structural element (Rodriguez et al. 1996a, Yoon et al. 2000, Chung et al. 2008a, Malumbela et al. 2009). Moreover, pitting corrosion causes localised cross section loss, which results in a reduction in strength and ductility of the corroded reinforcing bar. Therefore, corrosion induced mechanical damage at a material level (concrete, steel and bond) will lead to diminished structural performance of RC elements and will subsequently affect the global response of the structural system.

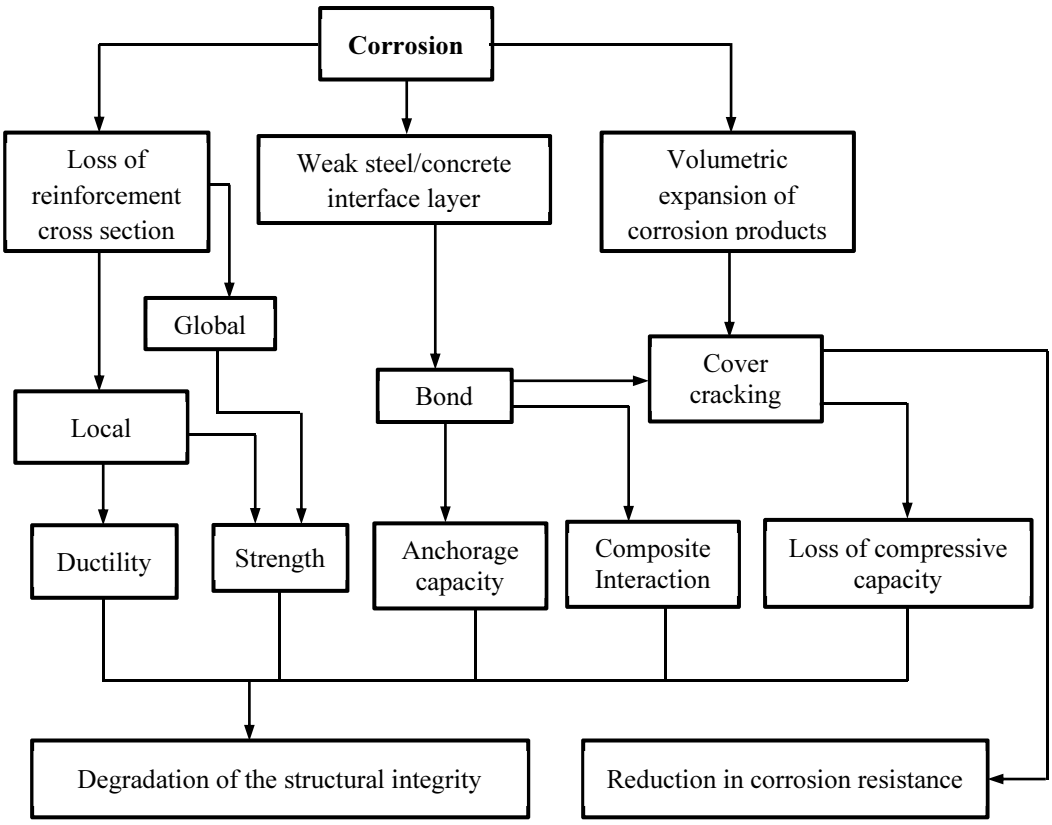

Fig. 2.8 Effect of corrosion on structural integrity of deteriorating RC structures (Cairns et al 2008).

2.6. Non-uniform cross section loss due to pitting corrosion

Chloride induced corrosion results in irregular loss of the cross section of reinforcing steel known as pitting corrosion. Gonzalez et al. (1995) studied the influence of corrosion on the maximum and minimum pitted section in bars corroded experimentally. They developed the first pitting coefficient R_{pit}, based on their experimental results, which is the ratio of the maximum pitting depth P_{max} (or the minimum cross section) to average cross section loss assuming average corrosion P_{ave}. They observed that the value of pitting coefficient varied from 4 to 8. An example of corroded reinforcement with pitted cross sections is shown in Fig 2.9.

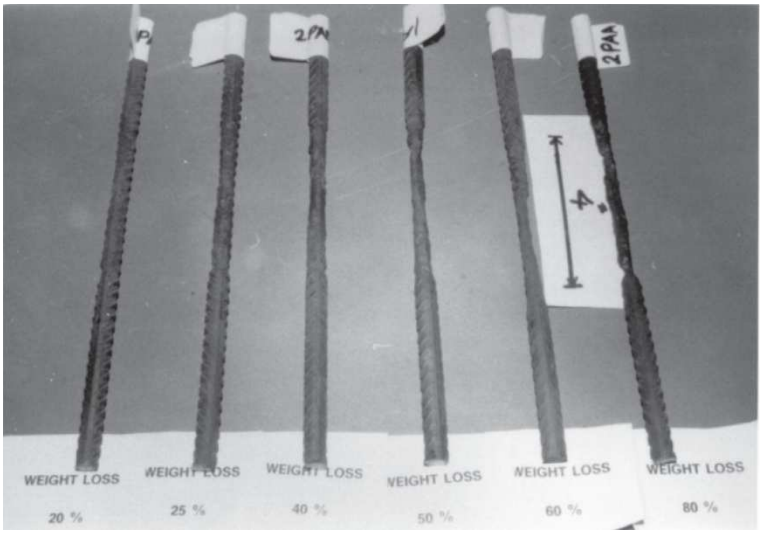

Fig. 2.9 Non-uniform pitting corrosion of reinforcement after accelerated corrosion procedure in the Lab (Almusallam 2001)

The reduction in the diameter of a corroding reinforcing bar at time t, after corrosion initiation can be computed as:

$$\phi(t) = \phi_0 - \alpha P_{ave} \tag{2.26}$$

Where $\phi(t)$ is the residual bar diameter at time t after corrosion initiation, ϕ_0 is the initial bar diameter, $P_{ave}(t)$ is the corrosion penetration (described in Eq. 2.22 where $\Delta p(t) = P_{ave}(t)$) and α is the ratio of the maximum pitting depth to the average reduced area known as the pitting coefficient (Vidal et al. 2004 and Gonzalez et al. 1995); α is 2 for homogeneous corrosion and 4 to 8 for pitting corrosion as shown in Fig. 2.9. Finally, the residual cross section area of reinforcement can be written as Eq. (2.27)

$$A_s(t) = \frac{n\pi\phi(t)^2}{4} \tag{2.27}$$

Where n is the number of reinforcement bars in the given RC section and $A_s(t)$ is the residual cross section area at time t after corrosion initiation. In this model the pit depth is equal to $\alpha P_{ave}(t)$ as defined in Eq. (2.26), as shown in Fig. (2.10).

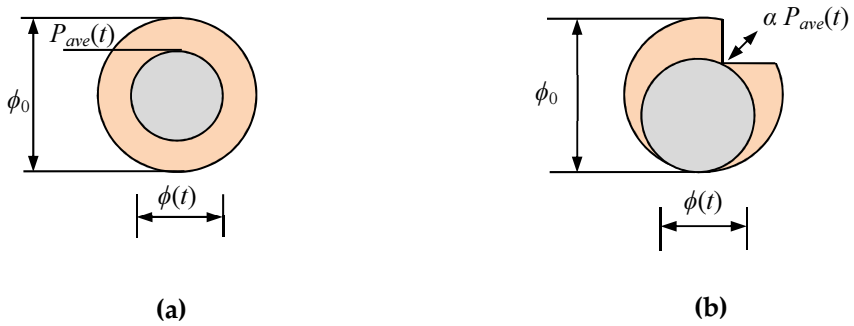

Fig. 2.10 Residual cross section of reinforcing bars: (a) homogeneous (b) pitting

In another model that was initially proposed by Val and Melchers (1997), the pitted section in idealised to a hemispherical shape as shown in Fig 2.11.

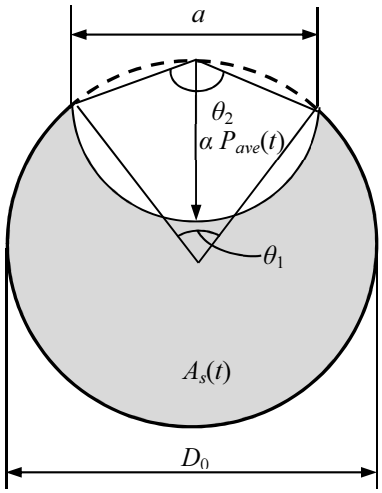

Fig. 2.11 Configuration of pitted section

The net cross section area of the corroded reinforcement $A_s(t)$ is the shaded area that is defined in the following Eq. (2.28) to Eq. (2.33).

$$A_s(t) = \begin{cases} \dfrac{\pi D_0^2}{4} - A_1 - A_2 & P_{ave}(t) \le \dfrac{\sqrt{2}}{2} D_0 \\ A_1 - A_2 & \dfrac{\sqrt{2}}{2} D_0 \le P_{ave}(t) \le D_0 \\ 0 & P_{ave}(t) > D_0 \end{cases} \tag{2.28}$$

$$A_1 = \frac{1}{2}\left[\theta_1\left(\frac{D_0}{2}\right)^2 - a\left|\frac{D_0}{2} - \frac{P_{ave}(t)^2}{D_0}\right|\right] \tag{2.29}$$

$$A_2 = \frac{1}{2}\left[\theta_2 P_{ave}(a)^2 - a\frac{P_{ave}(a)^2}{D_0}\right] \tag{2.30}$$

$$a = 2P_{ave}(a)\sqrt{1-\left(\frac{P_{ave}(t)}{D_0}\right)^2} \tag{2.31}$$

$$\theta_1 = 2\sin^{-1}\left(\frac{2a}{D_0}\right) \tag{2.32}$$

$$\theta_2 = 2\sin^{-1}\left(\frac{P_{ave}(t)}{D_0}\right) \tag{2.33}$$

Further detailed discussion about the influence of pitting corrosion on the geometrical properties of corroded reinforcement and the spatial variability of pitted areas can be found in Chapter 4.

Apostolopoulos et al. (2013) conducted an experimental comparison between corroded bare bars that were corroded using salt spray and corroded embedded bars that were corroded inside concrete. In both methods an accelerated corrosion procedure was employed. The mechanical properties and pitting effect were compared and they employed a 3D image processing technique to analyse the pits. Fig. 2.12 shows a schematic representation of the image processing technique.

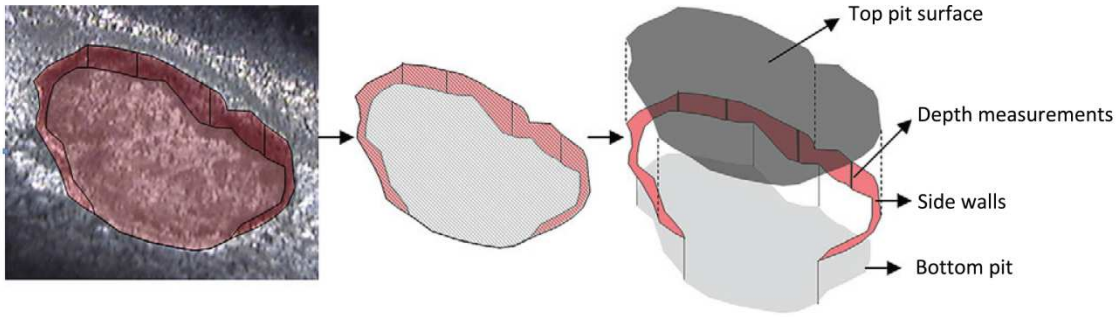

Fig. 2.12 Schematic representation of pit depth and area measurement (Apostolopoulos et al. 2013)

The results of the analysis showed that corroded bars that were embedded in concrete displayed more nonuniform pitting corrosion compared to the corresponding bare bars with a similar average mass loss ratio. This is shown in Fig. 2.13 where two corroded bars with the same average mass loss ratio are compared.

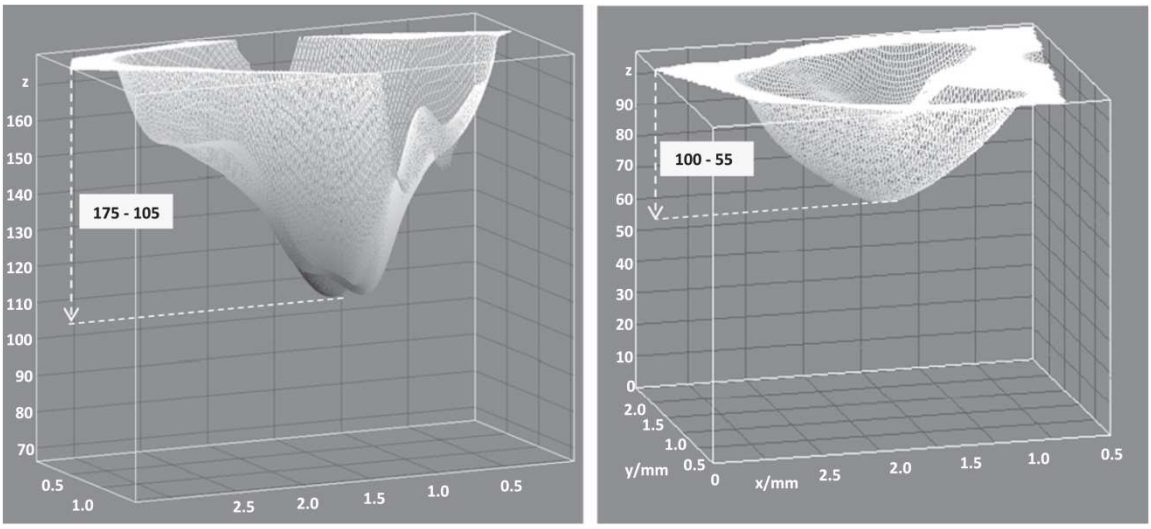

(a) **(b)**

Fig. 2.13 3D surface plots of pits (Apostolopoulos et al. 2013): (a) embedded bar and (b) bare bar 20 days salt spray samples (vertical axis in pixel units, horizontal axes in mm)

In general the embedded corroded bars had larger pit depths (Fig. 2.13 (a)). They found that the majority of embedded corroded bars had pit depths in the range of 0.6mm – 0.8mm with high occurrences of pit depths 0.8 mm and above. In contrast, the bare corroded bars which were exposed for 20 days, had pit depths in the range of 0.4mm – 0.6mm (Apostolopoulos et al. 2013). They also conducted a statistical analysis of pit depths. Further details and discussion is available in Apostolopoulos et al. (2013).

2.7. Influence of corrosion on mechanical properties of corroded reinforcing bars in tension

There is a large amount of literature on the corrosion of reinforcement inside concrete focusing on the mechanism of corrosion, service life prediction and corrosion prevention methods. However, in recent years researchers have conducted several experimental studies exploring the impact of pitting corrosion on residual capacity and ductility of corroded reinforcement (Almusallam 2001, Palsson and Mirza 2002, Du et al. 2005a, b, Cairns et al. 2005, Apostolopoulos et al. 2006, Alexopoulos et al. 2007, Apostolopoulos and Michalopoulos 2007, Papadopoulos et al. 2007, Apostolopoulos and Papadopoulos 2007, Apostolopoulos and Pasialis 2008, Apostolopoulos and Koutsoukos 2008, Apostolopoulos and Papadakis 2008, Apostolopoulos 2009, Lee and Cho 2009). Kallias

(2011) provided a summary of recent experimental testing on corroded bars which is reproduced in Table 2.3 at the end of this section.

Almusallam (2001) conducted experimental testing on 6 and 12mm diameter reinforcing bars. The test specimens were corroded inside concrete using an accelerated corrosion procedure. Almusallam (2001) reported that the corrosion did not influence the yield strength of the reinforcement when the tensile strength was calculated considering the actual cross section area of the corroded bars. The tensile strength calculated using the actual cross-section area is reported to be more than 600MPa for bars with as much as 70% to 80% corrosion. However, the tensile strength was less than the ASTM A 615 requirement of 600 MPa when the level of corrosion was 12% or more in 6mm diameter bars, and 24% or more in 12mm diameter bars when considering the nominal cross section area.

The experiments showed that with increasing levels of mass loss most of the test specimens had a low level of ductility compared to uncorroded bars which demonstrated a large ductility before failure. Furthermore, test specimens with 12.6% mass loss or more showed a brittle failure mode. An example load-elongation response of corroded bars with original diameter of 6 mm reported by Almusallam (2001) is shown in Fig. (2.14).

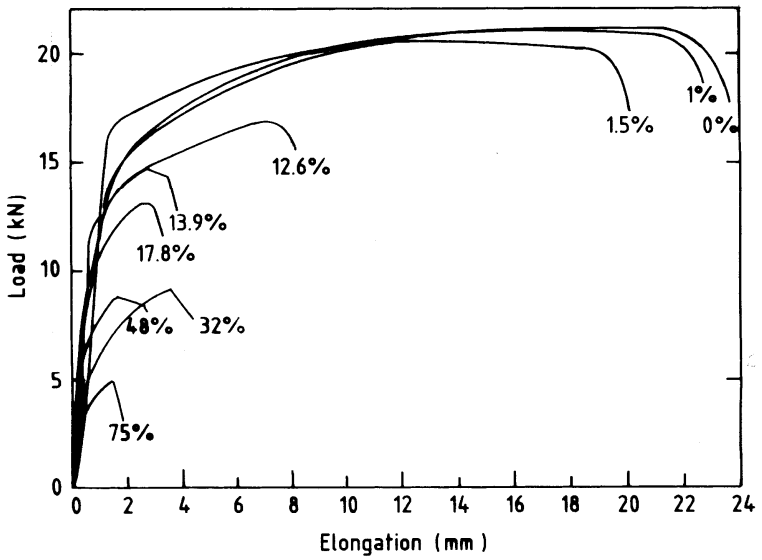

Fig. 2.14 Load-elongation curves for corroded bars with varying corrosion levels (Almusallam 2001)

Du et al. (2005a) conducted a comprehensive set of experimental testing on corroded reinforcing bars using an accelerated corrosion procedure on both bare bars and bars embedded inside concrete. They reported that for up to 16% mass loss, corrosion does not substantially influence the force-extension response of corroded reinforcement. In general, corroded specimens with mass loss ratios below 16% had a significant yield plateau (Fig. 2.15).

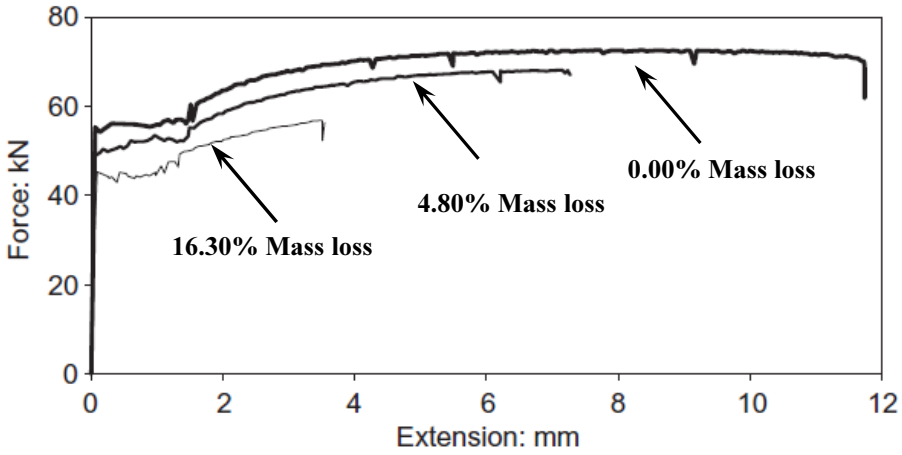

Fig. 2.15 Force - extension plot of corroded bars

Following the experimental study, Du et al. (2005a) derived the empirical Eq. (2.34) which suggests that the yield and ultimate strength of steel reinforcement has a linear relationship with the mass loss ratio.

$$f(t) = \left(1 - \beta_s \psi(t)\right) f_0 \tag{2.34}$$

Where f_0 is either the yield or ultimate strength of uncorroded steel, β_s is an empirical coefficient equal to 0.005, $\psi(t)$ is the percentage mass loss at time t, and $f(t)$ is either the residual yield or ultimate strength of corroded reinforcement. Therefore the Eq. (2.34) can be written in the form of Eq. (2.35).

$$f(t) = \left(1 - \beta_s \left(\frac{A_s(t)}{A_{s0}}\right)100\right) f_0 \tag{2.35}$$

where, $A_s(t)$ and A_{s0} are the cross section area of pitted section at time t and uncorroded and corroded reinforcement respectively.

Du et al. (2005b) also studied the effect of corrosion on the ductility of reinforcing bars. They have reported that the strength ratio, hardening strain and elastic modulus of reinforcement are not significantly affected by corrosion. Therefore the corresponding values for uncorroded bars can be adopted in practice. However, pitting corrosion creates a non-uniform distribution of cross sections along the length of a bar. This results in a significant reduction in ultimate strain, the ductile area under the stress-strain curve and elongation. The reductions in these measures of ductility are much greater than those related to yield and ultimate strengths which have been reported previously by Du et al. (2005b).

Based on the experimental data, empirical Eq. (2.36) is derived by Du et al. (2005b) to modify the ultimate strain of reinforcing steel.

$$\varepsilon_u(t) = \left(1 - \beta_{eps}\left(\frac{A_s(t)}{A_{s0}}\right)100\right)\varepsilon_{u0} \tag{2.36}$$

where, ε_{u0} is the ultimate strain of the uncorroded steel and $\varepsilon_u(t)$ is the ultimate strain of the corroded reinforcement at time t after corrosion initiation.

Further discussion and detailed comparison of the previous experimental studies and the current research is available in Chapter 3.

Table 2.3 Summary of previous experimental studies on corroded bars (Kallias 2011)

Reference	Bar type	Specimen type	Exposure type	Bar diameter (mm)	Mass loss (%)	Summary
Almusallam (2001)	Ribbed	Embedded in concrete	Accelerated corrosion	6,12	Up to 75%	Significant loss of strength and ductility for mass loss ratio greater than 12.6%
Palsson and Mirza (2002)	Ribbed	Taken from a corroded bridge	Natural corrosion	16	Up to 80% (minimum area)	Small loss of yield/ultimate strength, loss of ductility
Du et al. (2005a)	Plain, Ribbed	Bare, embedded in concrete	Accelerated corrosion	8, 16, 32	Up to 25%	Significant loss of strength and ductility for mass loss ratio greater than 16% mass loss
Du et al. (2005b)	Plain, Ribbed	Bare, embedded in concrete	Accelerated corrosion	8, 16, 32	Up to 25%	Significant loss of ductility of mass loss ratio gre16% mass loss
Cairns et al. (2005)	Plain, Ribbed	Bare, embedded in concrete	Accelerated corrosion, machined	12, 14, 20, 24	Up to 72%	Small change in strength but significant ductility loss
Apostolopoulos et al. (2006)	Ribbed	Bare	Accelerated corrosion using salt spray	8	Up to 32%	Small change in strength but significant ductility loss
Alexopoulos et al. (2007)	Ribbed	Bare	Accelerated corrosion using salt spray	12	Up to 3%	Small change in strength but significant ductility loss
Apostolopoulos and Michalopoulos (2007a)	Ribbed	Bare	Accelerated corrosion using salt spray	8	Up to 26%	Bars with pre-existing plastic deformations had more significant change in their mechanical properties.
Apostolopoulos and Michalopoulos (2007b)	Ribbed	Bare	Accelerated corrosion using salt spray	12	Up to 10.4%	Significant change in low-cycle fatigue life
Papadopoulos et al. (2007)	Ribbed	Bare	Accelerated corrosion using salt spray	12	Up to 9%	Mechanical properties of two type of steel are compared
Apostolopoulos and Papadopoulos (2007)	Ribbed	Bare	Accelerated corrosion using salt spray	10	Up to 9%	Significant change in low-cycle fatigue life
Apostolopoulos and Pasialis (2008)	Ribbed	Bare	Accelerated corrosion using salt spray	12	Up to 9%	Mechanical properties of two type of steel are compared
Apostolopoulos and Koutsoukos (2008)	Ribbed	Bare	Accelerated corrosion using salt spray	8	Up to 32%	Loss of strength and ductility
Apostolopoulos and Papadakis (2008)	Ribbed	Bare	Accelerated corrosion using salt spray	10	Up to 11%	Small change in strength but significant ductility loss
Apostolopoulos (2009)	Ribbed	Bare	Accelerated corrosion using salt spray	8, 10, 12, 16, 18	Up to 14%	More significant change in stress-strain behaviour of bars with small diameter
Lee and Cho (2009)	Ribbed	Embedded in concrete	Accelerated corrosion, wet and dry cycles	10, 13	Up to 35%	Loss of strength and ductility, change in elastic modulus also observed

2.8. Influence of corrosion on low-cycle fatigue behaviour of corroded reinforcing bars

One of the important parameters that limit the seismic performance and ductile behaviour of RC structures is the premature fracture of reinforcing bars under cyclic loading due to low-cycle fatigue. As shown in Table 2.3, corrosion has a significant adverse influence on the low-cycle fatigue life of longitudinal reinforcing bars in structural elements.

Apostolopoulos (2007) conducted an experimental study on the effect of corrosion on the low-cycle fatigue behaviour of 12mm diameter S500s tempcore reinforcing bars. The experimental programme included an accelerated corrosion procedure using a salt-spray approach and low-cycle fatigue testing at constant strain amplitude. The corroded bars were subjected to a uniaxial sinusoidal force with 1 Hz frequency at constant strain amplitude of ±1%, ±2.5% and ±4%. A summary of the experimental results is provided in Tables 2.4 and 2.5.

Table 2.4 Percentage mass loss and reduced nominal diameter (Apostolopoulos (2007))

Exposure time	0	10	20	30	45	60	90
Mass loss (%)	0	1.35	2	3.03	4.89	6.65	10.4
Diameter (mm)	12	11.92	11.88	11.82	11.70	11.59	11.36

Table 2.5 Summary of low-cycle fatigue tests (Apostolopoulos (2007))

Mass loss (%)	**ε = ±1%**		**ε = ±2.5%**		**ε = ±4%**	
	Cycles	**Std. Dev.**	**Cycles**	**Std. Dev.**	**Cycles**	**Std. Dev.**
0	529	10.71	28	1.63	10	1.70
1.35	429	73.25	27	1.7	9	2.49
2	414	73.83	27	0.47	9	0.82
3.03	403	23.34	27	2.16	9	0.82
4.89	335	45.22	26	1.89	9	0.47
6.65	317	38.26	25	7.76	8	1.63
10.4	263	23.75	23	2.87	8	2.16

The fatigue life can be predicated using Coffin-Manson equations (Eq. 2.37 and 2.38) as given below (Apostolopoulos 2007):

$$\Delta_{\varepsilon t} = \Delta_{\varepsilon e} + \Delta_{\varepsilon p}$$

(2.37)

$$\frac{\Delta_{\varepsilon t}}{2} = \frac{\Delta_{\varepsilon e}}{2} + \frac{\Delta_{\varepsilon p}}{2} = \frac{\sigma'_f}{E}\left(2N_f\right)^{\beta} + \varepsilon'_f\left(2N_f\right)^{\alpha} \tag{2.38}$$

where, $\Delta_{\varepsilon t}/2$ is the total strain amplitude, $\Delta_e/2$ is the elastic strain amplitude, $\Delta_p/2$ is the plastic strain amplitude, ε'_f is the fatigue ductility, α is the fatigue ductility exponent, σ'_f is the fatigue strength coefficient, β is the fatigue strength exponent and E is the elastic modulus (Fig. (2.16)).

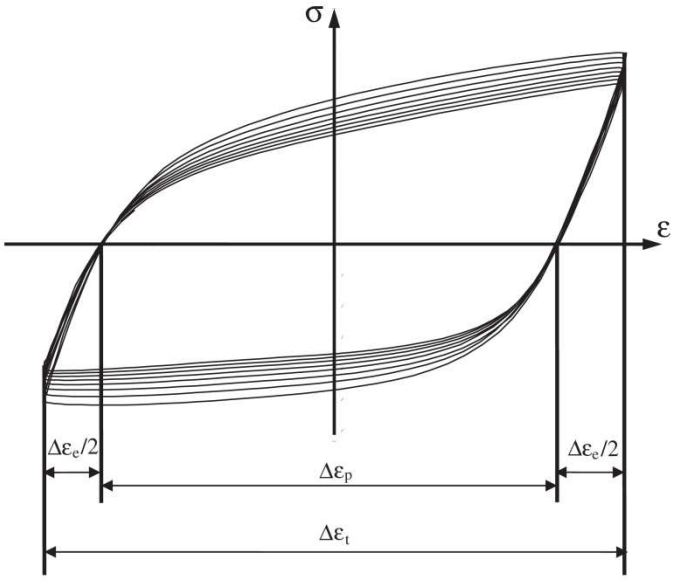

Fig. 2.16 Graphical representation of Coffin-Manson low-cycle fatigue life model (Apostolopoulos 2007)

Fig. 2.17 (a-e) shows a comparison between the results of the low-cycle fatigue tests of specimens with 10.4% mass loss and the corresponding uncorroded specimens for 1%, 2.5% and 4% strain amplitudes. The calculated stress in Fig. 2.14 is based on the average reduced cross sectional area of each corroded bar.

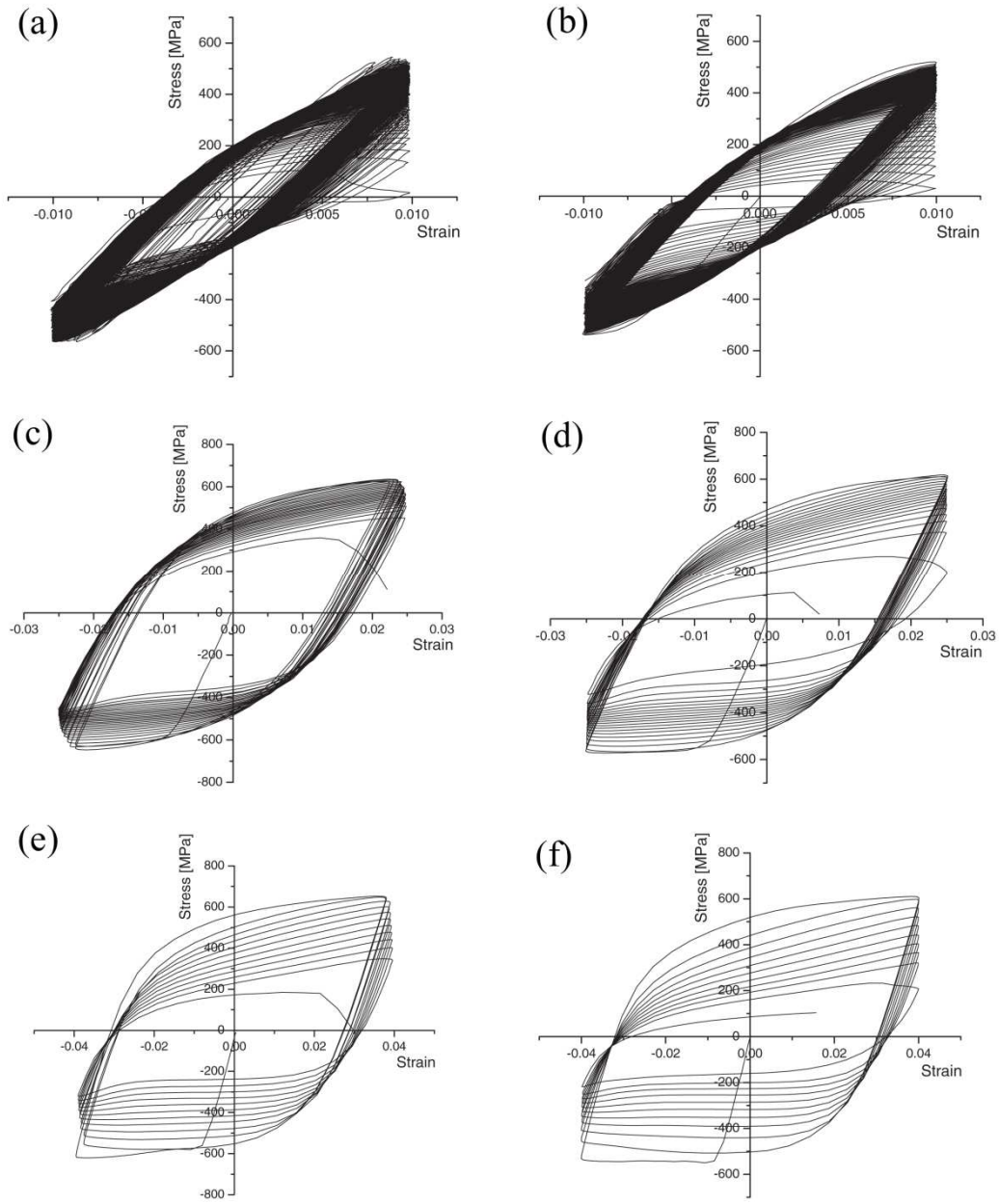

Fig. 2.17 Comparison of the stress-strain curves of uncorroded (a, c, e) and corroded bars (b, d, f) (Apostolopoulos 2007)

As shown in Fig. 2.17, corrosion causes a rapid degradation of the stress-strain curves of corroded bars in these low-cycle fatigue tests. It should be noted that corrosion simulation in the lab using the salt spray method produces relatively more uniform corrosion compared to corroded bars in the real world or bars corroded inside concrete in a laboratory environment. Further discussion about the experimental techniques is available in Chapter 3. Although further research is required for better understanding of the influence of corrosion on low-cycle fatigue life of reinforcing bars these results,

nevertheless, indicate that corrosion can reduce the effective service life of RC structures significantly. Fig. 2.18 shows that as the level of corrosion damage increases the number of cycles for which the material can sustain the applied force greatly reduces.

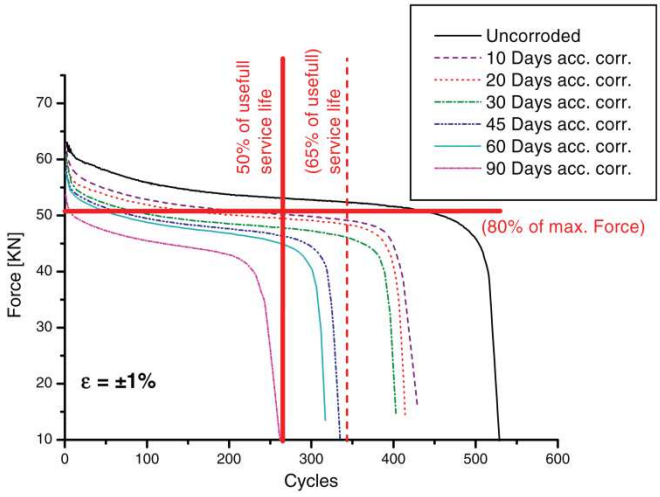

Fig. 2.18 Cycles before load capacity drops below 80% of the maximum value for 1% strain amplitude (Apostolopoulos 2007)

In another experiment Zhang et al. (2012) compared the tensile behaviour and high-cycle fatigue life of naturally corroded bars and bars corroded inside the concrete using an accelerated corrosion procedure in the laboratory. The naturally corroded bars were corroded by carbonation-induced corrosion mechanisms but the bars artificially corroded in the laboratory were corroded using chloride-induced corrosion mechanisms. The overall results showed that naturally corroding bars produced a slightly more significant influence on the tensile and fatigue behaviour of the reinforcing bars. Fig. 2.19 shows a comparison between the force-extension behaviour of 6.5mm diameter naturally corroded bars and 12mm diameter artificially corroded bars. The mass loss ratio (η_s) is used as a measure of corrosion damage in Fig 2.19.

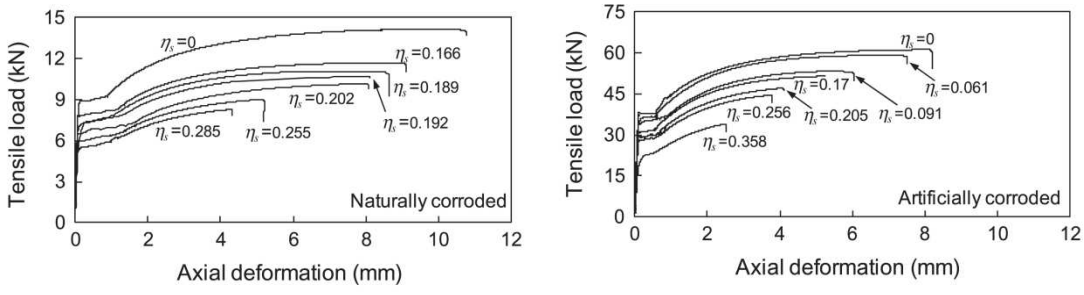

(a) **(b)**

Fig. 2.19 Typical force-extension response of artificially and naturally corroded bars: (a) naturally corroded (b) artificially corroded

Fig. 2.20 shows a comparison on the influence of corrosion on high-cycle fatigue life of naturally and accelerated corroded reinforcing bars under various stress range.

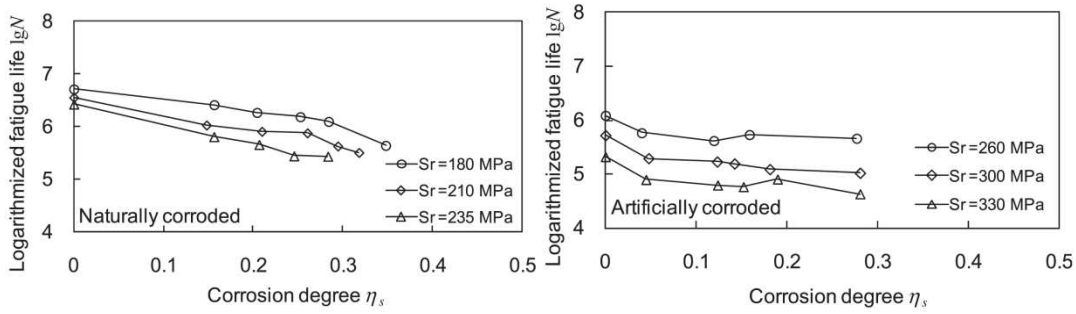

(a) **(b)**

Fig. 2.20 Influence of corrosion on fatigue life of corroded bars: (a) naturally corroded bars (b) accelerated corroded bars

Further discussion about the influence of corrosion on cyclic behaviour of corroded bars and fatigue life modelling are available in Chapters 3 and 4.

2.9. Influence of corrosion damage on behaviour of concrete in compression

As explained in previous sections the volume of corrosion products is bigger than that of the original uncorroded steel. This produces a radial pressure on the concrete surrounding the reinforcement that eventually will result in fracture of the cover concrete. The reduction in reinforcement diameter and reduced bond on the steel and concrete interface will influence the tension zone of the RC section in flexure. However, the impact of the corrosion damage on concrete is not only limited to the tension zone and the microcracking of the concrete will also result in loss of compressive strength of the concrete in the compressive zone of RC sections.

Capozucca and Cerri (2003) conducted a set of experimental tests on RC beams with corrosion damage in the compression zone. Fig. 2.21 shows that corrosion of compressive zone changes the failure mode of the test specimens. Fig. 2.21(a) shows that the failure mode of the uncorroded specimen is caused by yielding of the tension reinforcement. However, as shown in Fig 2.21(b) the failure mode of the corroded specimen is by concrete crushing in compression together with a change in crack pattern and widths due to the impact of corrosion on the bond-slip behaviour of the reinforcement in tension.

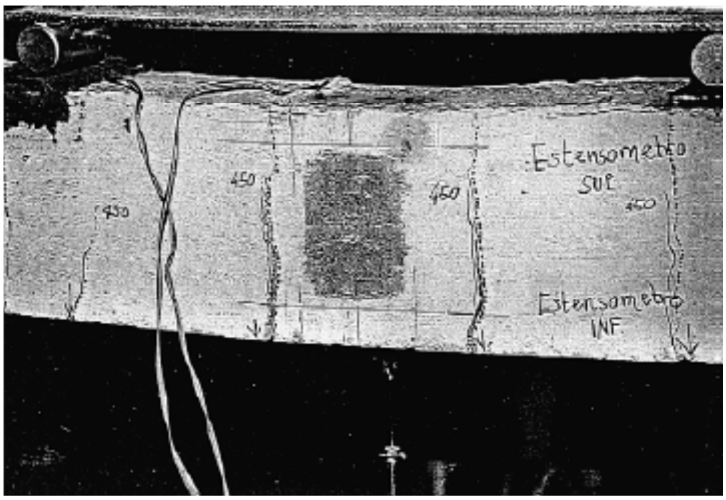

(a)

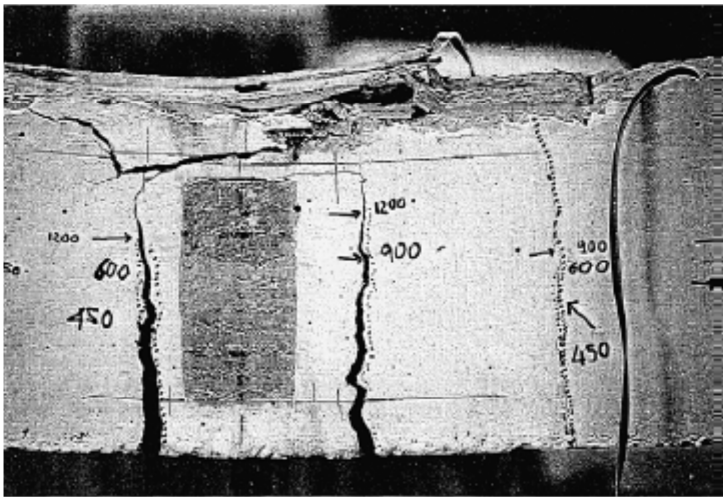

(b)

Fig. 2.21 Failure of RC beam in compression zone due to corrosion damage (Capozucca and Cerri 2003): (a) uncorroded beam ductile failure (b) corroded beam concrete crushing and brittle failure

Lee et al. (2000) conducted a set of experimental studies on short columns to investigate the effectiveness of strengthening using CFRP sheets. Fig. 2.22 shows an example load-displacement response of a corroded column with its corresponding uncorroded and repaired test specimens.

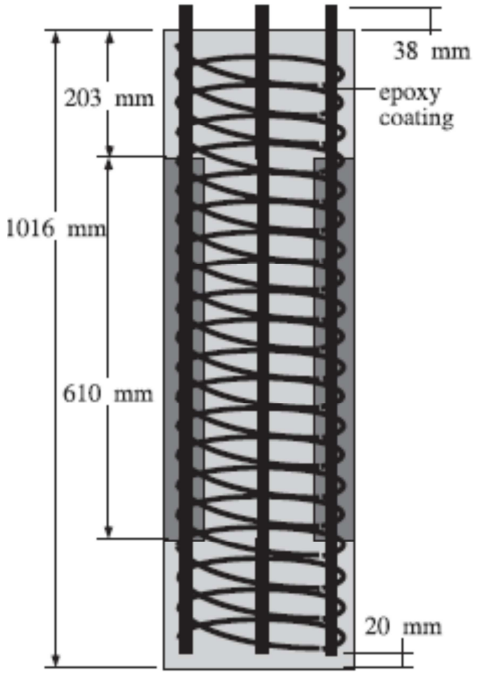

(a)

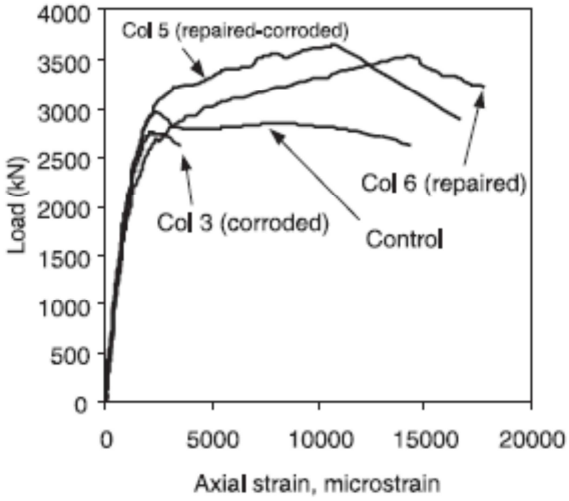

(b)

Fig. 2.22 Load-deformation plot of Lee et al. (2000) specimens: (a) test specimen (b) load-deformation response

Comparing the uncorroded control specimen with corroded unrepaired column (Col 3) and repaired corroded column (Col 6) in Fig. 2.22, it is evident that corrosion has a significant impact on the load-displacement behaviour of RC columns in compression. The test results show that the corrosion significantly reduced the ductility and crushing strain of concrete in compression and to a lesser extent reduced the compressive strength. Lee et al. (2000) reported that the ductility ratio of the uncorroded specimen

was 9.9 whereas the ductility of Col 3 was 2.7. Lee et al. (2000) also took physical cross sections through the thickness of the unrepaired corroded column (Col 1) to investigate the internal damage due to corrosion. Fig. 2.23 shows a schematic of the internal damage in the corroded column (Lee et al. 2000).

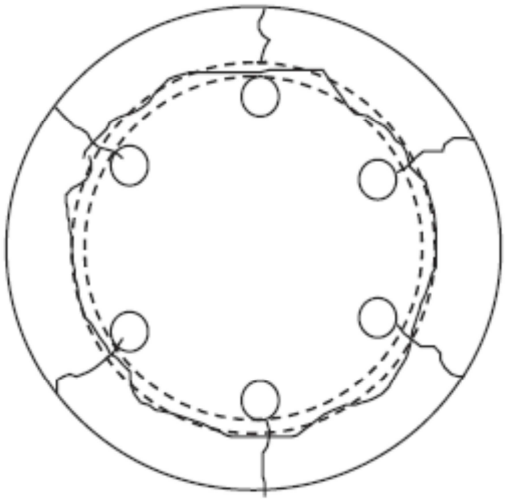

Fig. 2.23 Schematic internal damage as reported in Lee et al. (2000)

As expected, the cross section cuts showed that corrosion resulted in radial cracks in the cover concrete aligned with the vertical reinforcement. Moreover, they observed that a single crack had formed a continuous ring around the spiral reinforcement which resulted in complete delamination of the cover concrete. This is a very important observation that explains the significant influence of corrosion on the crushing strain of RC columns.

It is known to researchers that the compressive behaviour of confined concrete is a function of volumetric ratio, yield strength and fracture strain of tie reinforcement (i.e. spiral or hoop reinforcement) (Park et al. 1982, Mander et al. 1988a,b, Penelis and Kappos 1997). Since tie reinforcement is the outmost reinforcement to be exposed to chloride attack it starts corroding prior to the corrosion initiation of the vertical reinforcement. As a result the volumetric ratio of confinement reinforcement, yield strength and fracture strain are reduced. Therefore, the tie reinforcement fractures much earlier than the uncorroded columns under compression.

To date there have not been any experimental studies exploring the effect of corrosion on the nonlinear behaviour of confined concrete either under pure compression or under cyclic loading. This is an area for further research. However a simplified methodology has been developed in this research that can be used to modify the constitutive model of the existing confined concrete model to account for the effect of corrosion damage.

Further discussion on the constitutive modelling of corrosion damaged unconfined cover concrete and confined core concrete is available in Chapter 6.

2.10. Influence of corrosion on bond-slip behaviour of embedded corroded bars in concrete

When a reinforced concrete element is loaded, the transfer of load between the reinforcement and the concrete occurs through the development of shear stresses at the steel-concrete interface. It is the presence of these stresses that prevents excessive slip between the reinforcement and the concrete and ensures that the average strain in the embedded reinforcing bars is equal to that of the surrounding concrete. In the absence of sufficient bond strength the effective beam action, as required by the codes of practice, cannot be achieved and hence the specified design equations are no longer valid. Loss of strain compatibility at the depth of reinforcement leads to redistribution of stresses in the reinforced concrete element which may lead to excessive service deflections and altered load capacity (Karimi and Benfield 2007).

The use of deformed bars greatly enhances the steel-concrete bond capacity. Park and Pauley (1975), identified three main components which contribute to the development of bond strength between adjacent ribs of a reinforcement bar. These are the shear stress v_a developed by adhesion along the bar surface, the longitudinal bearing stress f_{bl} against the face of rib and the shear stress v_c acting on the cylindrical concrete surface between adjacent ribs. Due to the inclination of the ribs, the bearing stresses are separated in two components, a longitudinal (f_{bl}) and a radial (f_{br}) component as shown in Fig. 2.24.

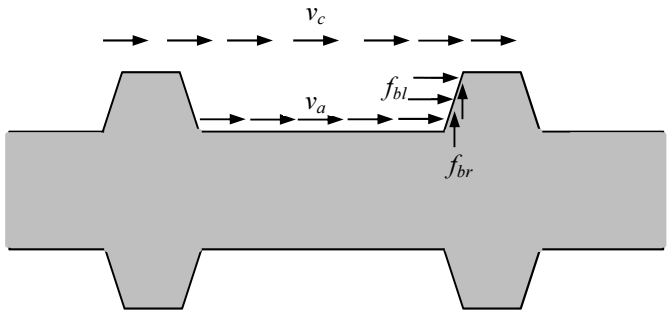

Fig. 2.24 Stresses between the two ribs of a deformed reinforcing bar

The radial stress f_{br} generates a tension force in cover concrete which results in cracking of cover concrete (Fig. 2.25).

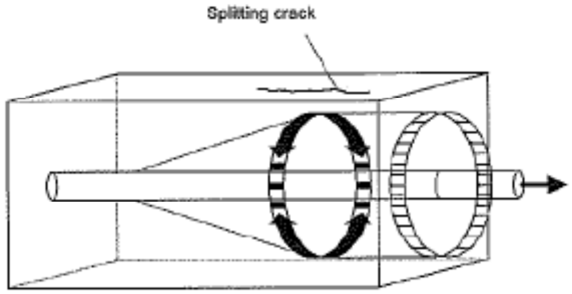

Fig. 2.25 Tensile radial stresses in the anchorage zone (Tepfers 1973)

The cover cracking can be caused by either corrosion or by slip or by some combination of both. Previous studies by experimental testing and analytical modelling of the bond behaviour of corroded embedded reinforcement in concrete are discussed in the following sections.

2.10.1. Experimental investigation of the bond-slip behaviour of embedded corroded bars

Al-Sulaimani et al.(1990a), Rodriguez et al. (1994), Cabrera (1996), Almusallam et al. (1996), Fu and Chung (1997), Amleh and Mirza (1999), Auyeung et al. (2000), Lee et al. (2002), Fang et al. (2004) have conducted a series of pull-out tests on corroded specimens under monotonic loading. Al-Sulaimani et al. (1990b), Stanish et al. (1999) and Chung et al. (2004) have conducted flexural tests on beams to investigate the bond-slip behaviour of corroded bars under flexural loading. In all these experiments an accelerated corrosion procedure has been used to corrode the test specimens. The following is a summary of the observations that are reported in the literature:

- At the early stage of corrosion (mainly before cover cracking) the bond strength between the reinforcement and concrete is improved. This is due to the radial pressure caused by the expansion of the corrosion products around the reinforcement which increases the friction between the reinforcement and concrete. However once cover concrete cracks due to corrosion the bond strength drops (Fig. 2.26).

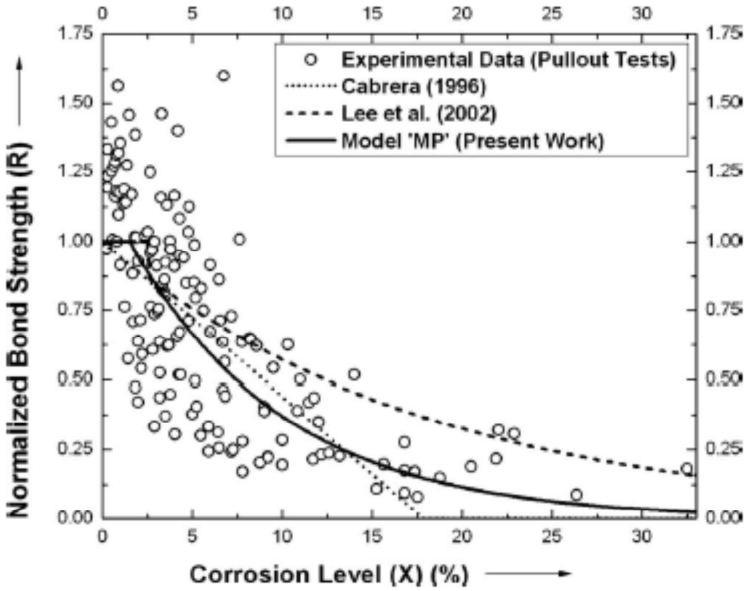

Fig. 2.26 Normalised bond strength as a function of mass loss ratio for various experimental data from pull-out tests (Bhargava et al. 2008)

- The main parameters influencing the bond strength of corroded bars are the level of confinement and ribs on the bars. By increasing the level of corrosion the height of the ribs reduces, and the expansion of corrosion products reduces the interaction between the rib and concrete. This phenomenon results in a significant reduction in bond strength (Fig. 2.27).

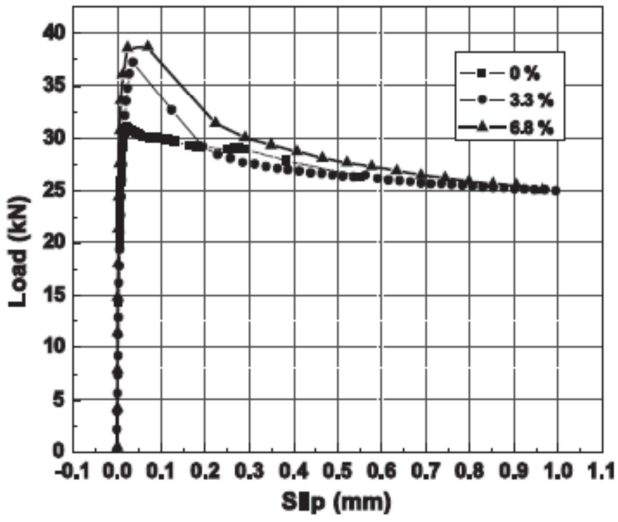

(a)

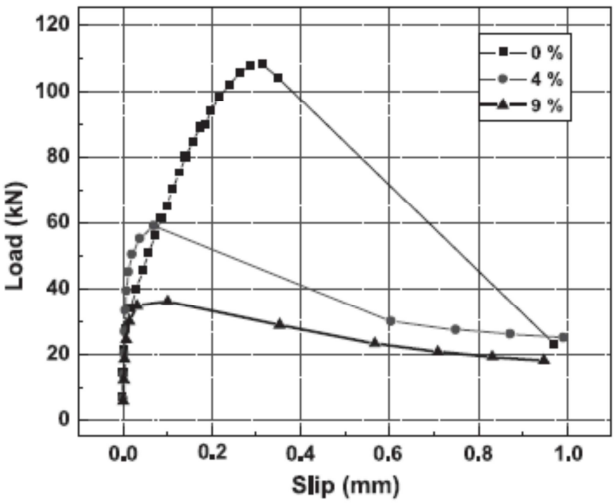

(b)

Fig. 2.27 Influence of corrosion on bon behaviour of bars (Fang et al. 2004): (a) smooth bars and (b) bars with ribs

- Fang et al. (2004) reported that if the corroded specimen is well confined the bond strength of the corroded bars may not drop below the bond strength of corresponding uncorroded bars (Fig. 2.28).

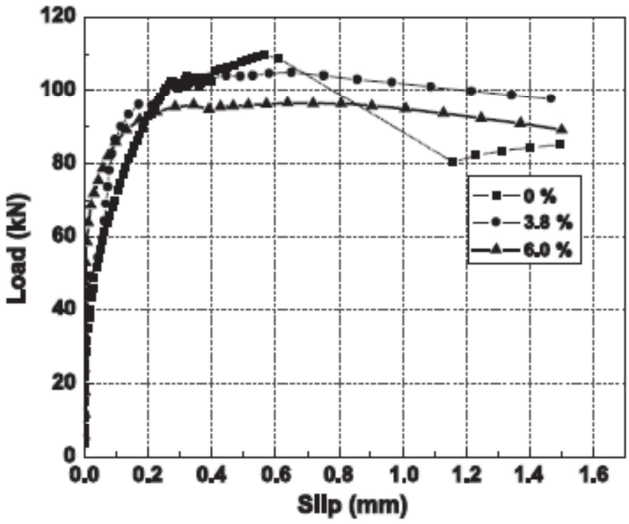

Fig. 2.28 Influence of confinement on bond behaviour of corroded bars (Fang et al. 2004)

- Fang et al. (2006) conducted a series of pull-out tests on corroded specimens under cyclic loading. They reported that splitting failure was observed (Fig. 2.29) for the unconfined corroded bars with ribs. Following the splitting crack the bond stress reached its maximum strength and then followed by a sharp softening of bond stress to a very low level.

Fig. 2.29 Splitting failure of corroded specimens (Fang et al. 2006)

However, a pull-out type failure was observed for the confined specimens. Fig. 2.30 shows an example of the bond-slip response of corroded and uncorroded test specimen as reported by Fang et al. (2006).

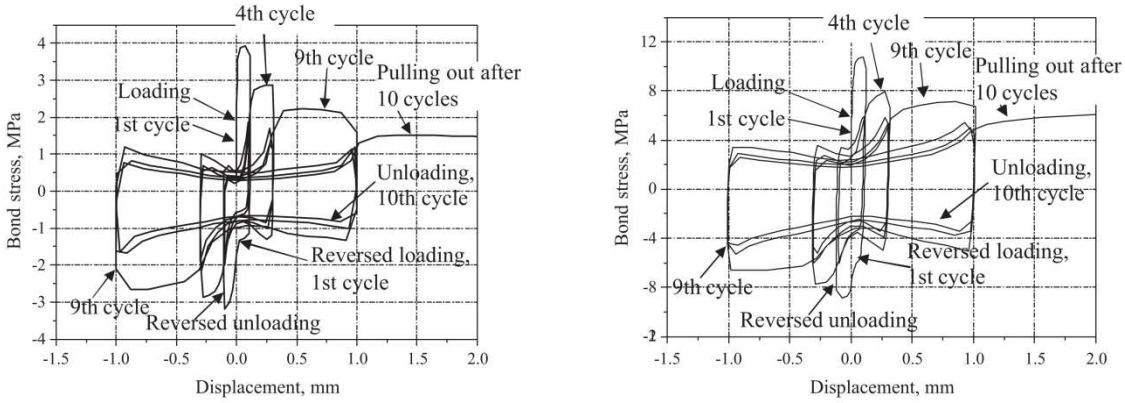

(a) **(b)**

Fig. 2.30 Bond-slip response of smooth bars tests under cyclic pull-out test (Fang et al. 2006): (a) uncorroded control specimens (b) corroded specimens with 1% mass loss ratio

Fang et al. (2006) used a degradation parameter to indicate the reduction of the maximum bond stress at the *N*th cycle. This is defined in Eq. (2.39)

$$\lambda_N = 1-\kappa = 1-\frac{\tau_{\max}(N)}{\tau_{\max}(1)} \tag{2.39}$$

where, λ_N is the degradation parameter of the *N*th cycle, $\tau_{max}(1)$ is the maximum bond stress in the first cycle, $\tau_{max}(N)$ is the maximum bond stress in the *N*th cycle, and κ the ratio of the maximum bond stress to that of the first cycle. The test results showed that

the influence of corrosion on the bond degradation parameter for test specimens with confinement is less significant than for those without confinement. Fig. 2.31 shows the influence of corrosion on the bond degradation parameter.

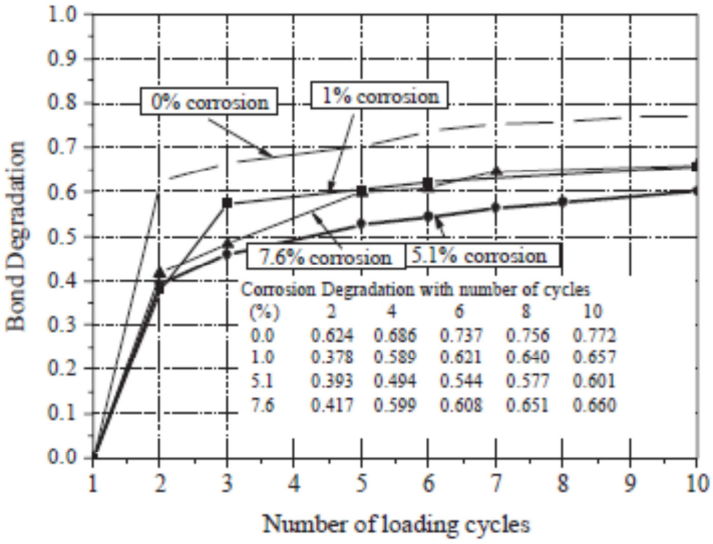

Fig. 2.31 Bond degradation parameter of confined ribbed reinforcement with varied corrosion levels (Fang et al. 2006)

2.10.2. Analytical models to predict the bond strength and to model the bond-slip behaviour of embedded corroded bars

Lee et al. 2002 investigated the relationship between the degree of reinforcement corrosion and the maximum bond stress (τ_{max}) and the bond rigidity (D_s), as a function of mass loss percentage (ψ).

Based on the results of pull-out tests and finite element analysis of test specimens they developed a set of empirical equations to calculate the maximum bond strength and the bond rigidity as a function of percentage mass loss. These quantities are very important in nonlinear finite element analysis of corroded RC members. Table 2 summarises the empirical equations developed Lee et al. (2002).

Table 2. 6 Equations for bond properties of reinforcement as function of mass loss

Corrosion Percentage (%)	Maximum Bond Strength (τ_{max}) (MPa)	Bond Rigidity (D_s) (MPa)
$\psi < \psi_c$	$\tau_{\max} = 0.34\sigma_B - 1.93$	$D_s = 16.5\sigma_B - 160$
$\psi \geq \psi_c$	$\tau_{\max} = 5.21e^{-0.056\,\psi}$	$D_s = 1160\psi - 1.014$

σ_B: Compressive strength of concrete.
ψ: Mass loss percentage (%).
ψ_c: Mass loss percentage at cracking (%).

Coronelli and Gambarova (2004) employed the bond stress–slip model proposed in CEB-FIP Model Code 90 (1993) with modified bond properties to account for corrosion effects (Fig. 2.32). The bond strength τ_{max}, the slip s_1 at the maximum bond stress and the softening branch are modified as a function of mass loss. The model (Eq. (2.40)) considers a cover splitting failure mode in the post-peak branch. The empirical model proposed by Rodriguez et al. (1996) is used to predict the loss of bond in corroded bars.

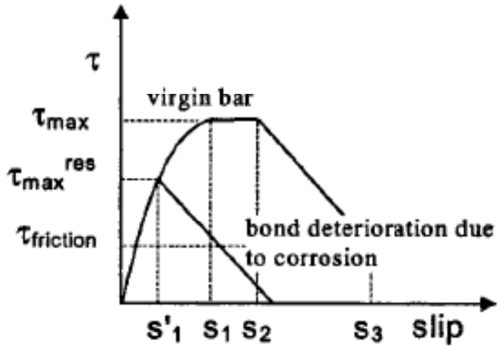

Fig. 2.32 Bond-slip model of corroded bars proposed by Coronelli and Gambarova (2004)

The same bond-slip relationship is considered for the entire reinforcement. In other words it is assumed that corrosion is uniformly distributed along the length of the longitudinal bars.

$$\tau_{\max}^{res} = \tau_{concrete} + \tau_{tie} = 0.6(0.5 + \frac{C}{d_b}) f_{ct}(1 - \beta\psi^{\mu}) + \frac{kA_{tr} f_y}{sd_b} \tag{2.40}$$

where, $\tau_{\max}^{res}$ is the residual bond strength, f_{ct} is the concrete tensile strength, $\tau_{concrete}$ is the concrete contribution to bond, ψ is the corrosion attack penetration, τ_{tie} is the contribution to the bond from transverse reinforcement (ties), C/d_b is the cover to diameter ratio, A_{tr} is the cross section area of a tie, f_y is the yield stress of a tie, s is the tie spacing, and β, μ, k are empirical constants.

El Maaddawy et al. (2005) developed an analytical formulation for nonlinear analysis of corroded RC beams. In this formulation they used a bond stress-slip model that is based on the CEB-FIP Model Code 90 (1993) for monotonic loading with the modified maximum bond stress τ_{max} as a function of mass loss (Fig. 2.33).

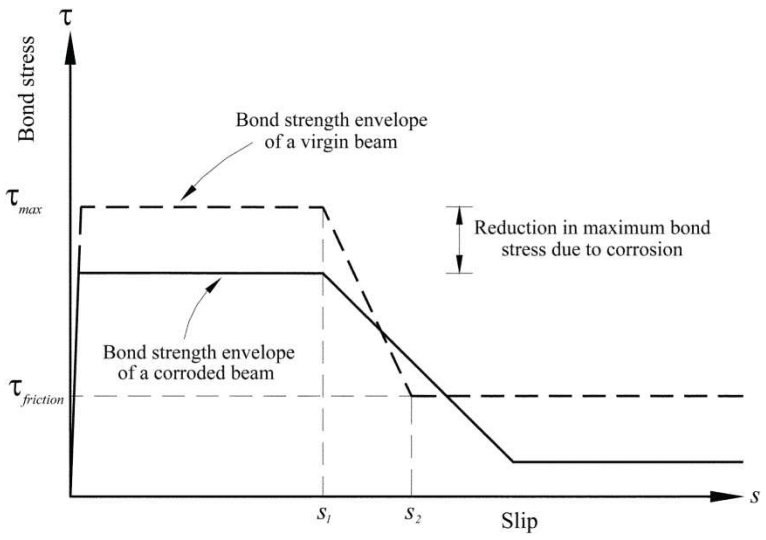

Fig. 2.33 Proposed bond-slip model (El Maaddawy et al. 2005)

The maximum bond stress of uncorroded reinforcement is based on the experimental work by Kemp and Wilhelm (1979) who proposed Eq. (2.41) to determine the maximum bond stress of concrete beams with deformed steel bars. The maximum bond stress of an uncorroded beam τ_{maxv} consists of two components: the contribution of the concrete to the bond strength τ_{conc} and the contribution of the stirrups to the bond strength τ_{st}.

$$\tau_{maxv} = \left(0.55 + 0.24\frac{C}{d_b}\right)\sqrt{f_c} + 0.191\frac{A_t f_{yt}}{s_s d_b} \tag{2.41}$$

The maximum bond stress calculated from Eq. (2.41) is then modified based on the experimental results reported by Saifulah and Clark (1994). The empirical factor R (Eq. (2.42)) is used to predict the reduction in the bond strength caused by corrosion. This factor predicts an initial increase in bond before corrosion cracking and a reduction in bond as the percentage mass loss of the reinforcing steel (m_l) increases.

$$R = A_1 + A_2 m_l \tag{2.42}$$

The values of A_1 and A_2 are dependent on the current density used to induce corrosion that are summarised in Table 2.7. Generally, the contribution of the stirrups to the bond strength is independent of the corrosion level within the flexural reinforcement. This means that the contribution of the stirrups, if uncorroded, to the bond strength will not be influenced by corrosion of the flexural reinforcement. Hence, the maximum bond stress of a corroded part of the beam τ_{maxc} is given by Eq. (34).

$$\tau_{maxv} = (A_1 + A_2 m_l)\left(0.55 + 0.24\frac{C}{d_b}\right)\sqrt{f_c} + 0.191\frac{A_t f_{yt}}{s_s d_b} \tag{2.43}$$

where, f_c is the concrete compression strength, C/d_b is the cover to diameter ratio, A_t is the cross section area of a tie, f_{yt} is the yield stress of a tie and s_s is the spacing of the tie.

Table 2.7 Values of A1 and A2 (El Maaddawy et al 2005)

Current Density μA/cm²	A1	A2
40	1.003	-0.037
90	1.104	-0.024
150	1.152	-0.021
250	1.163	-0.011
500	0.953	-0.014
1000	0.861	-0.014
2000	0.677	-0.009
4000	0.551	-0.01

The slope of ascending branch of the bond stress-slip curve is calculated assuming that the value of the steel stress at the end of the element occurs just as a new crack is about to form, that is, f_s at the end of the element is equal to $n_r f_r$, where n_r is the modular ratio of steel to the concrete and f_r is the rupture strength of the concrete. The ascending branch of the El Maaddawy et al.'s model can be calculated using the Eq. (2.44).

$$\tau = \begin{cases} \dfrac{d_b}{2S_m}\left(f_{max} - n_r f_r\right) & \tau \le \tau_{max} \\ \tau_{max} & S \le S_1 \\ \tau_{max} - \left(\tau_{max} - \tau_{frinction}\right) & S_1 \le S \le S_2 \\ \tau_{frinction} & S \ge S_2 \end{cases} \tag{2.44}$$

where S_1, S_2, $\tau_{friction}$ are defined in CEB-FIP Model Code 90 and are presented in Table 4 and S_m is the mean crack spacing. Further detail is available in El Maaddawy et al. (2005).

Table 2.8 Parameters to define the bond-slip relationship (El Maaddawy et al 2005)

Parameter	Unconfined Concrete		Confined Concrete	
	Good Bond Conditions	All other Bond Conditions	Good Bond Conditions	All other Bond Conditions
S_1	0.6mm	0.6mm	3.0mm	3.0mm
S_2	1.0mm	2.5mm	Clear Rib Spacing	Clear Rib Spacing
$\tau_{friction}$	$0.15\tau_{max}$	$0.15\tau_{max}$	$0.4\tau_{max}$	$0.4\tau_{max}$

More recently Kivell (2012) conducted a comprehensive set of experimental pull-out tests to investigate the influence of corrosion on bond-slip behaviour of corroded bars under both monotonic and cyclic loading. Fig. 2.34 shows the response of an uncorroded bar and a corroded bar with 18.6% mass loss subject to cyclic pull-out test.

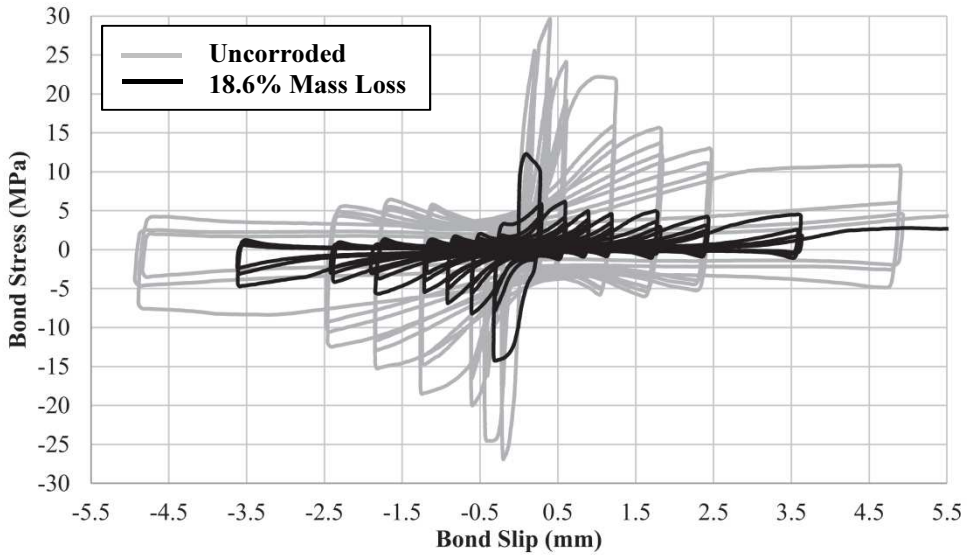

Fig. 2.34 Bond-slip slip reponse of corroded and uncorroded test specimens under cyclic pull-out test (Kivell 2012)

Based on the experimental results Kivell (2012) developed an analytical model to model the bond-slip behaviour of corroded bars under cyclic loading. The monotonic envelope curve of this model follows the same concept as the CEB-FIP Model Code 90 (1990). They have adopted a set of cyclic rules to model the unloading/reloading branches as well as the cyclic deterioration of bond-slip. The enveloped curve is adjusted as a function of percentage mass loss to account for the effect of corrosion damage. The description of the cyclic branches is available in Kivell (2012) in greater detail. Only a general overview of Kivell's model and a comparison of the model and the experimental results are shown in Fig 2.35 and Fig 2.36.

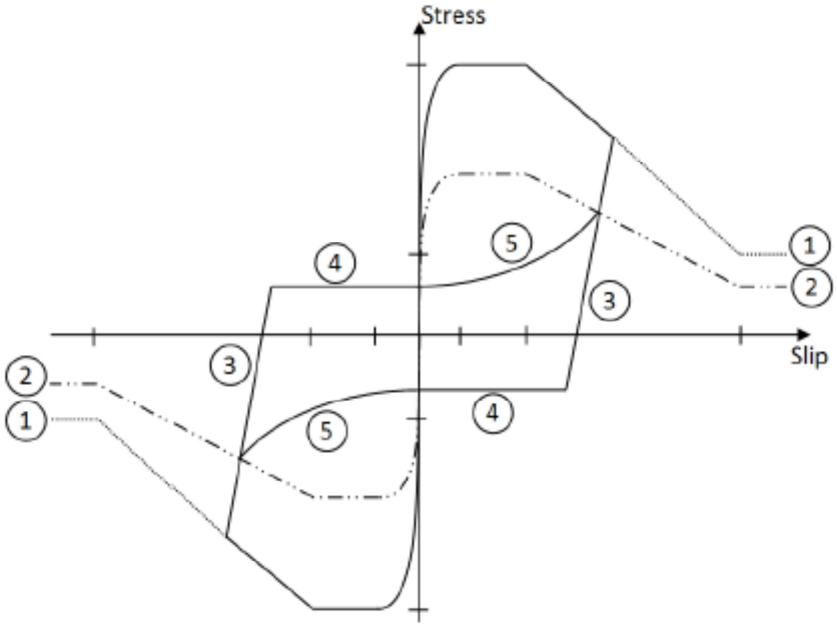

Fig. 2.35 General overview of the Kivell's model (Kivell 2012)

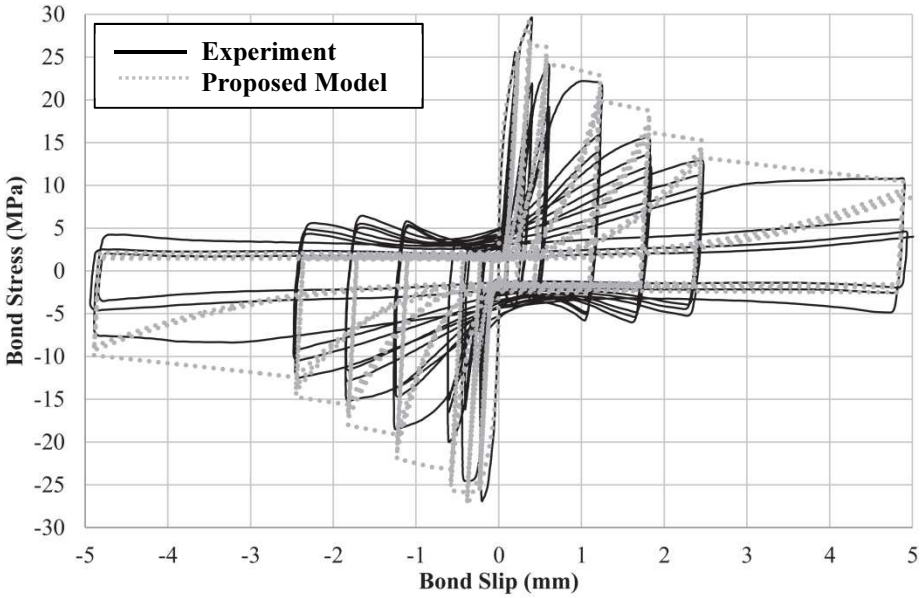

(a)

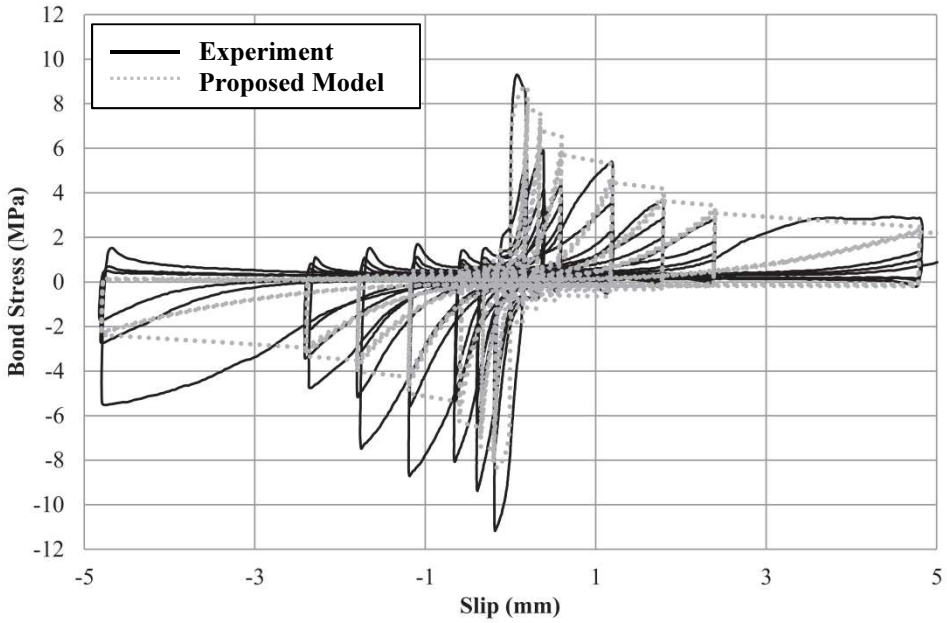

(b)

Fig. 2.36 Kivel's model verification with experimental data (Kivell 2012): (a) uncorroded (b) 18.6% mass loss

The proposed bond-slip model has been used in a multi-spring model to investigate the influence of corrosion on moment-curvature of RC sections. Further detail is available in Kivell (2012).

Kallias (2011) conducted a comprehensive nonlinear finite element analysis of corroded beams using a two dimensional continuum model. They validated their numerical model against the experimental data set reported by Rodriguez (1997) and Mangat (19997). After validation of the numerical model they investigated the influence of different deterioration parameters on the ultimate and serviceability limit state behaviour of corroded beams. They found that the main parameters influencing the load-displacement behaviour and the flexural capacity of corroded beams are the loss of steel cross section, the yield strength of steel and the concrete cracking. They also investigated the partial loss of bond and loss of bond over the entire length of the beam. The outcome of the analysis showed that the loss of bond has almost no influence of the ultimate capacity and the load-displacement behaviour of corroded beams. However, they reported that change in bond-slip behaviour has a significant influence in crack pattern and crack widths in tension. Therefore modelling the bond-slip behaviour is very important in performance assessment of corroded beams at serviceability limit state.

2.11. Influence of corrosion on the nonlinear flexural behaviour of corroded RC beams and columns under cyclic loading

As discussed in the previous sections, corrosion has a significant influence on the mechanical properties and the nonlinear response of RC structures at material level. However it is also very important to understand that how these changes in material response affect the component response. Therefore, several researchers have put significant effort into exploring the nonlinear behaviour of corrosion damaged RC beams and slabs under vertical loading (Cairns J and Zhao 1993, Rodriguez et al. 1996, Rodriguez et al. 1997, Razak and Choi 2001, Cairns et al. 2005, Rodriguez et al. 2005, Du et al 2007, Azad et al. 2007). In recent years several researchers have also employed nonlinear finite element analysis for parametric study of the influence of corrosion on the structural response of RC beams (Coronelli and Gambarova 2004, El Maaddawy et al. 2005, Kallias 2011). Almost all of the previous experimental and numerical studies have been focused on the structural response of RC beams and slabs under monotonic loading. However, there are a large number of RC bridges and structures that are located in environmentally aggressive and high seismicity regions. Therefore, some researchers have started to investigate the influence of corrosion on the cyclic behaviour of RC beams and columns and the effectiveness of using advanced composite materials to retrofit the deficient structural elements (Pantazopoulou et al. 2001, Aquino 2002, Tastani et al. 2004, Bousias et al. 2004, Belarbi and Bae 2007). Given the paucity in the literature in experimental study of the performance of corroded RC columns under cyclic loading, in this section, a comprehensive review of the very few available experimental studies is provided and the critical issues are identified.

Aquino (2002) conducted a set of experimental tests on six RC columns. One column was used as the control uncorroded specimen, one column was used as a control corroded specimen without strengthening and the other four columns were strengthened using CPRP sheets. The columns were corroded using an accelerated corrosion procedure. Because the columns were to be tested under lateral load after corrosion, the critical section would be immediately above the base. Therefore only 1200mm immediately above the base was corroded. Fig. 2.37 shows three columns after accelerated corrosion procedure.

(a) **(b)** **(c)**

Fig. 2.37 Columns after corrosion (Aquino 2002): (a) column 1 (b) column 3 and (c) column 5

In these columns (Fig. 2.37) a heavy accumulation of rust product on the surface of the concrete and a uniform staining of the corrosion along the length of longitudinal reinforcement is observed. Of these three columns (1, 3 and 5), Column 1 presented the most severe cracking and rust accumulation on the surface of concrete (Aquino 2002).

The geometrical properties of columns and the foundation are shown in Fig 2.38. Further details about the experiment and the test setup for this study are available in Aquino (2002).

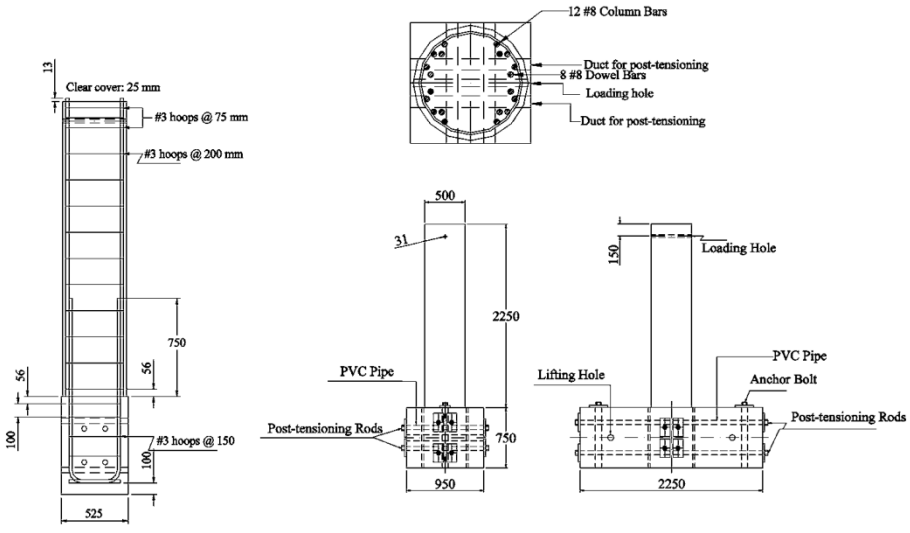

Fig. 2.38 Geometry of columns and foundation (Aquino and Hawkins 2007)

The observed damage in the uncorroded specimen was mainly due to the opening of a large crack at the connection between the column and the base due to slippage of the bars in the base. A few small flexural horizontal cracks were observed in the column

along with major cracks running parallel to the longitudinal reinforcement, which appeared close to the maximum load and opened up significantly when this load was attained. This is the typical failure mode of columns with insufficient lap splice lengths which does not allow the full strength and straining capacity of the reinforcing steel to be developed (Aquino 2002). Fig 2.39 shows the crack pattern of the uncorroded specimen after cyclic test and its corresponding load-displacement response.

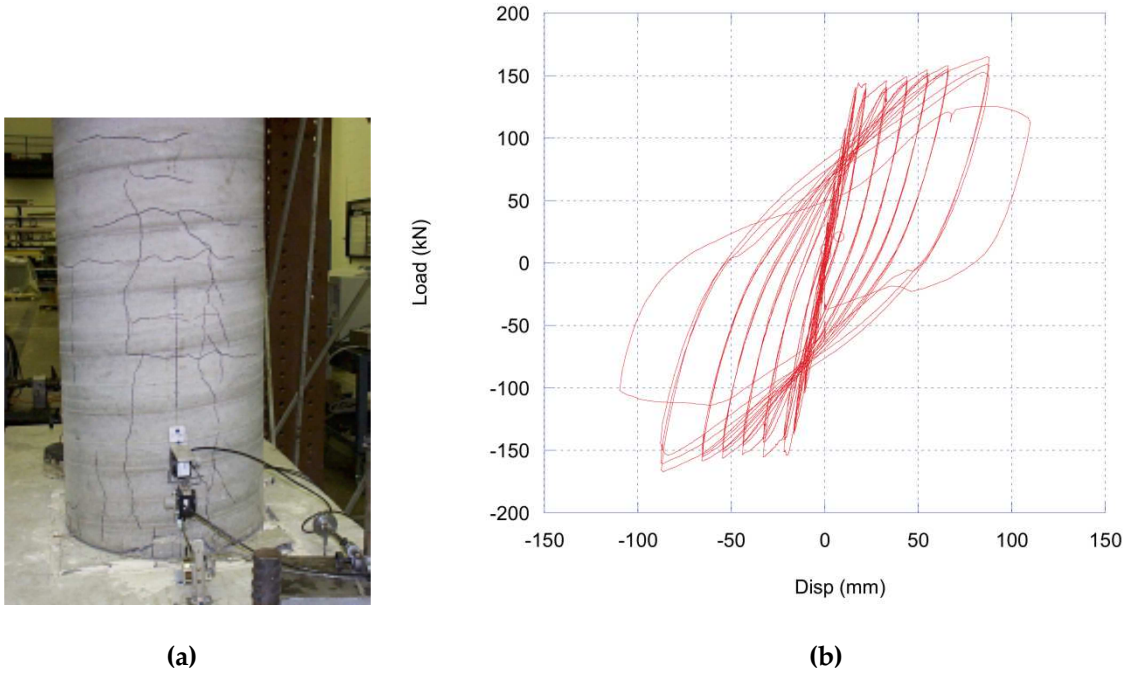

(a) **(b)**

Fig. 2.39 Response of uncorroded control specimen (Aquino 2002): (a) crack pattern (b) load-displacement resposne

Fig. 2.40 (a) shows a plot of the load-displacement response of the corroded column. As it can be seen in Fig. 2.40 (a), the load–displacement response of this column was symmetric, until a load of 133kN and a corresponding displacement of 21 mm were reached. After this point, a significant reduction in load in the positive direction was observed, while the load in negative direction remained unchanged. The cracks parallel to the reinforcing steel that were originally caused by the corrosion opened significantly. Because it was observed that load in the negative direction was still increasing, it was decided to further investigate the residual capacity of the column in this direction. Therefore, the rest of the experiment was conducted by applying increments in displacement in the negative direction only as shown in Fig 2.40 (b) (Aquino 2002).

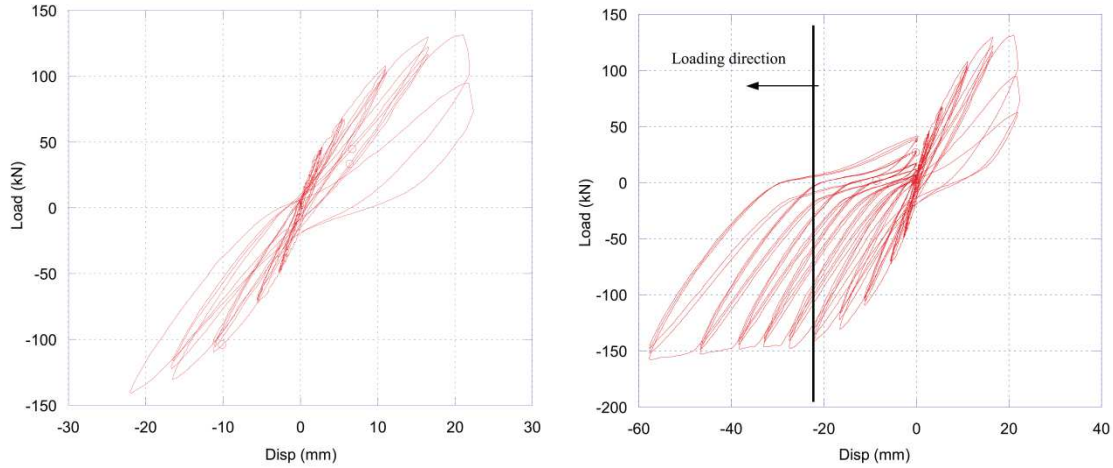

Fig. 2.40 Response of corroded control specimen (Aquino 2002): (a) initial full-cycle displacement history (b) continued half-cycle displacement history

During negative loading, the more deteriorated side of the column was under compression. Failure during cycling in the negative direction was due to buckling of the vertical reinforcement on the compression side of the column. It was observed that most of the tie reinforcement (hoops) had fractured due to pitting corrosion and they had experienced a significant loss of cross section during the corrosion process. The rupture of the tie reinforcement resulted in a significant loss of confinement and subsequently premature buckling of the corroded vertical reinforcement in compression as shown in Fig. 2.41 (Aquino 2002).

Fig. 2.41 Fracture of cover concrete induced by buckling of vertical reinforcement in compression (Aquino 2002)

Ou et al. (2012) conducted a series of cyclic test on large scale cantilever beams. The geometrical dimensions and the reinforcement details of test specimens are shown in Fig. 2.42 (a). The experimental test set up is also shown in Fig. 2.42 (b).

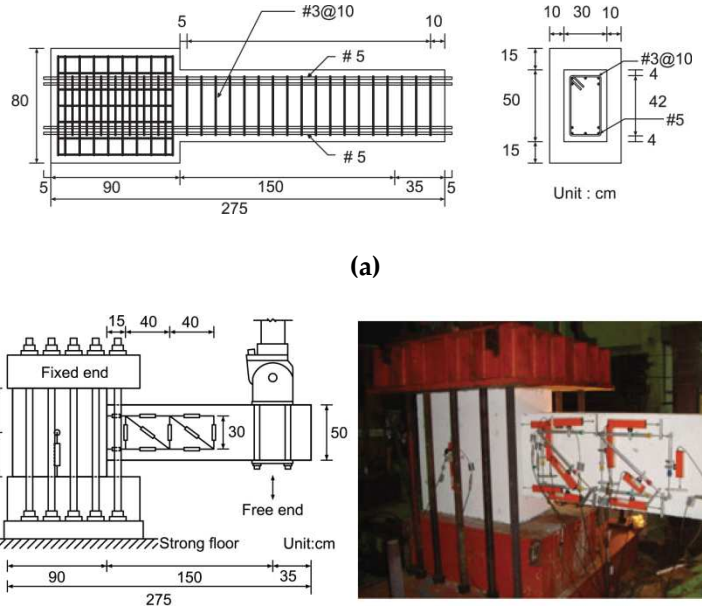

Fig. 2.42 Experimental test Specimens (Ou et al. 2012): (a) dimensions and reinforcement details (b) test setup

One of the specimens was used as a uncorroded control specimen and other four specimens were corroded with varied percentage mass losses which were 1.7%, 3.08%, 4.08% and 8.03%. Fig. 2.43 shows the crack pattern of all the specimens at 4% drift. The control specimen and the specimens with corrosion durations of 12.5, 25, and 50 days (specimens with 1.7%, 3.08% and 4.08% mass loss respectively) showed a typical flexural failure mode. The flexural cracks developed initially on the top and bottom faces of the specimens and, as the drift level increased, propagated through the thickness of the section. The cover concrete spalled off at about 3% drift. The longitudinal reinforcing bars started to show a significant inelastic buckling at 5% drift and subsequently resulted in crushing of core concrete which eventually led to beam failure.

Fig. 2.44 shows the hysteretic and envelope response curves of all specimens. The positive and negative drifts are considered by pulling up and pushing down the beam respectively. For the specimens with low level corrosion from 0% to 4.08% mass loss, the maximum applied force reached at about 4% drift. The combined effects of buckling of longitudinal reinforcement and crushing of core concrete resulted in a significant reduction in load capacity beyond the 4% drift. No fracture of the reinforcement was observed. However, as the level corrosion increased to 8.03%, the failure mode changed from flexural failure to flexural-shear failure. Fig. 2.44(e) shows the locations when

fracture of shear reinforcement occurred, indicated by black circles on the graph. The envelope response of this specimen in Fig. 2.44(f) shows that the maximum capacity was reached at 0.8% drift. Significant softening type behaviour observed once the third hoop fractured at about 2.5% drift.

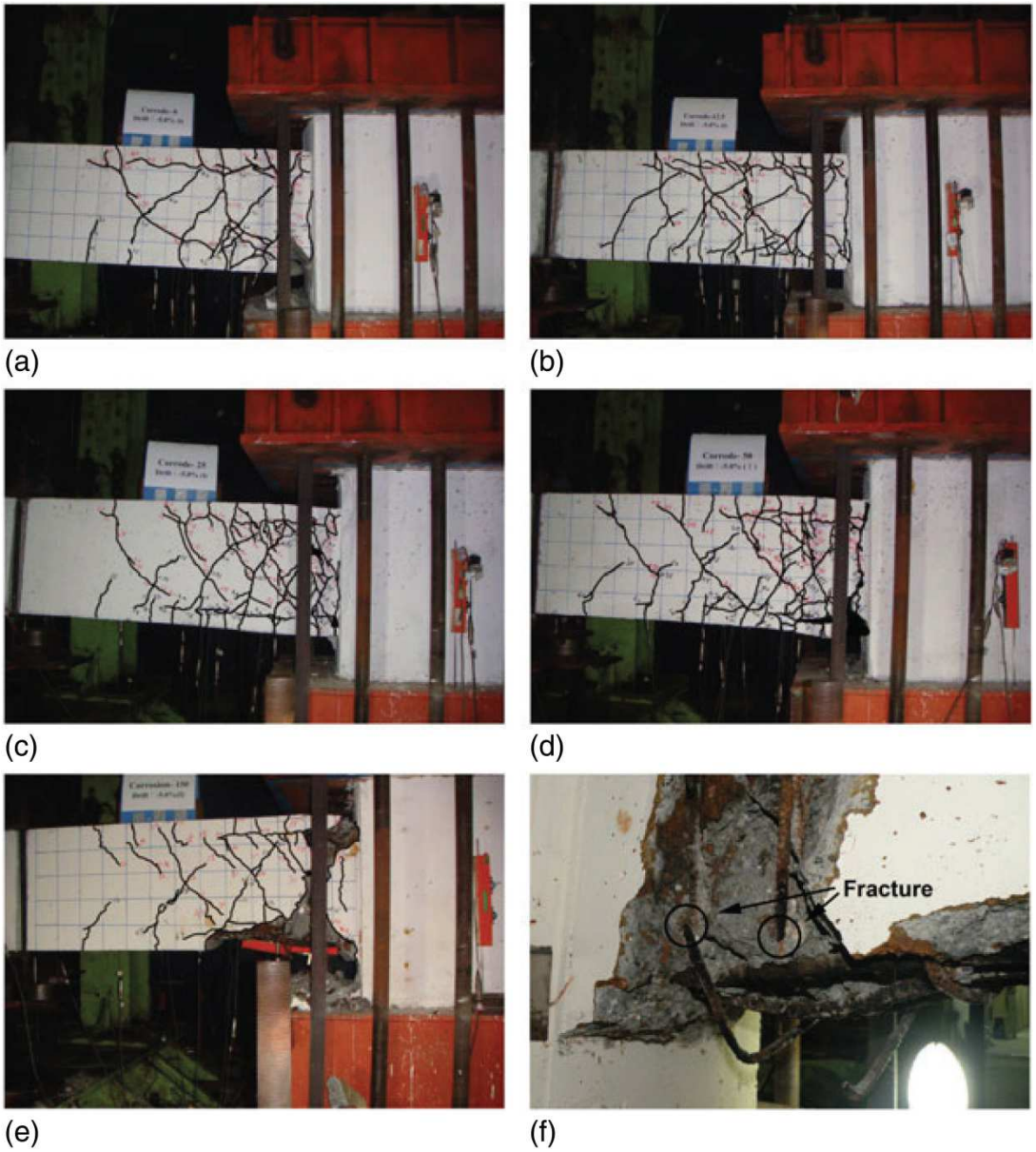

Fig. 2.43 Cracks pattern at 4% drift (Ou et al. 2012): (a) control specimen, (b) 1.7% mass loss, (c) 3.08% mass loss, (d) 4.08% mass loss, (e) 8.03% mass loss and (f) close view of fracture of transverse reinforcement for the test specimen in (e)

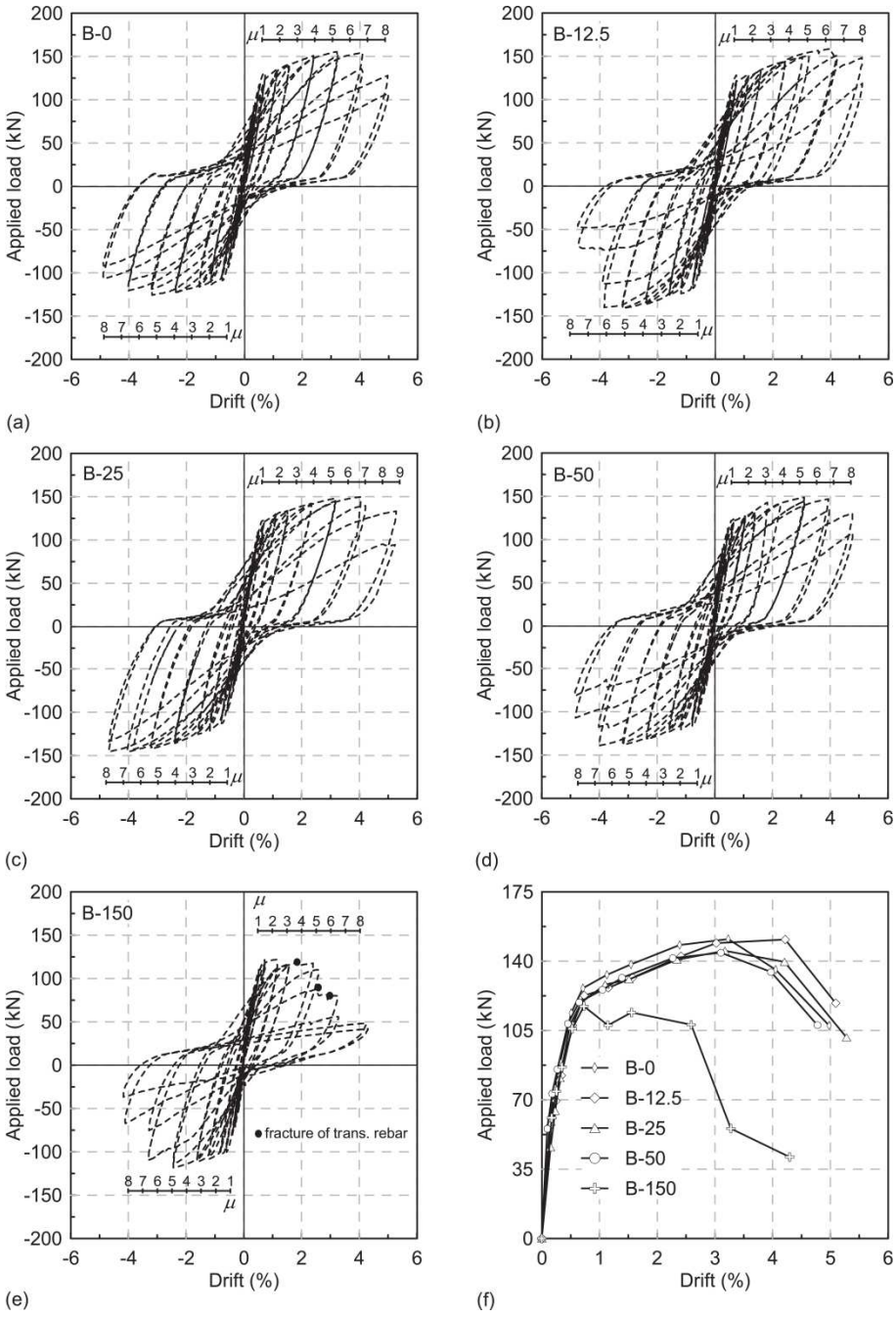

Fig. 2.44 Hysteretic response (Ou et al. 2012): (a) control specimen, (b) B-12.5 = 1.7% mass loss, (c) B-25 = 3.08% mass loss, (d) B-50 = 4.08% mass loss, (e) B-150 = 8.03% mass loss and (f) envelope curves of all specimens

Ma et al. (2012) conducted a series of experimental testing on thirteen columns with varied corrosion levels and axial force ratios. Similar to the previous experiments they also used an accelerated corrosion procedure to corrode the test specimens. The dimensions and reinforcement details are shown in Fig. 2.45. Each specimen consisted of a 260 mm diameter and 1000 mm long column cast into a 1300 mm×360 mm×400 mm

base. The clear cover to the spirals was 30 mm. The columns had an effective length of 820 mm and a span to depth ratio of 3.15. Six 16mm diameter reinforcing bars were used as longitudinal reinforcement and 8mm diameter reinforcing bars at 100mm spacing were used as the tie reinforcement (Ma et al. 2012). Eight out of thirteen columns had axial force ratios ($P/A_g f_c$) between 0.15 and 0.4 and five of them had axial force ratios between 0.60 and 0.90 which are rather high compared to normal bridge columns. Therefore, only the results of eight columns with axial force ratios below 0.5 are discussed in this section. A summary of the test matrix is also provided in Table 2.9.

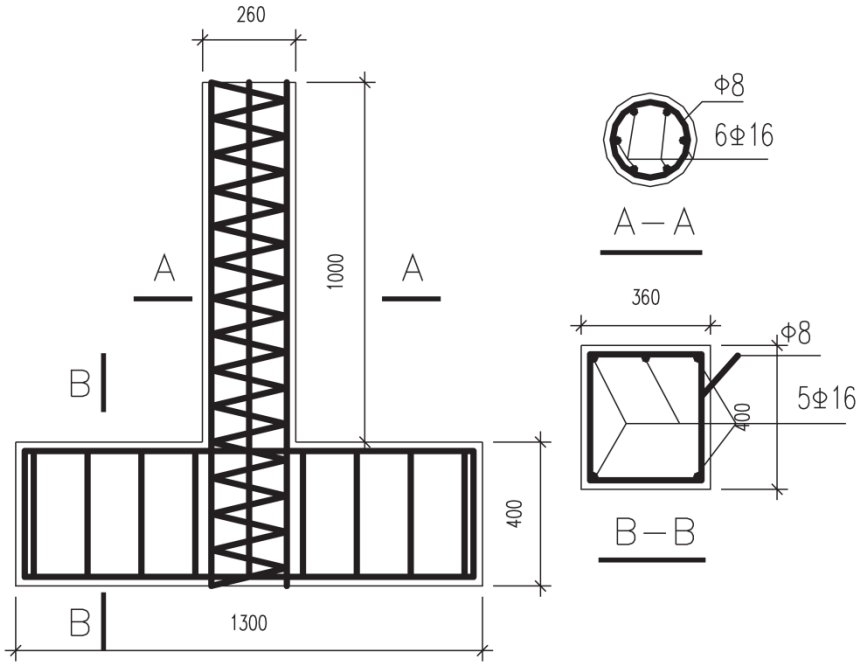

Fig.2.45 Test specimens details (Ma et al. 2012)

Table 2.9 Test matrix

Specimen	C0-15	C0-25	C0-40	C9-15	C4-25	C9-25	C9-40	C14-32
Mass loss (%)	0	0	0	9.5	4.1	9.7	9.3	14.7
Axial load ratio	0.15	0.25	0.4	0.15	0.4	0.25	0.4	0.32

In the three control specimens (with different axial force ratios), the first flexural crack formed perpendicular to the column axis in the bottom of column where the plastic hinge region occurred. These cracks propagated and with the increasing lateral load diagonal cracks appeared. In the last cycle, the core concrete crushed indicating the failure of these specimens (Ma et al. 2012).

The five corroded specimens C9–15, C4–25, C9–25, C9–40 and C14–32, showed a flexural failure mode similar to the uncorroded specimens. However, the failure of these corroded specimens was very brittle. The crack spacing of corroded specimens at failure

was greater than for the corresponding control specimens. As the displacement demand increased spalling of cover concrete occurred at the bottom of the column (plastic hinge region) which was then followed by severe buckling of the longitudinal bars and crushing of the core concrete. Fig. 2.46 shows the buckling and spalling of the cover concrete in the specimen C15–90 at failure (Ma et al. 2012).

Fig. 2.46 buckling of vertical reinforcement in specimen C14-32 with 14.7% mass loss and axial force ratio of 0.32 (Ma et al. 2012)

The load–displacement hysteretic responses for each specimen are shown in Fig. 2.47. As expected the energy dissipation capacity and ductility of specimens decreased with an increasing reinforcement corrosion and axial load ratio. Specimens C0–25, C4–25 and C9–25 had the same axial load ratio, however a smaller hysteretic area was observed in severely corroded specimen C9–25. Specimen C9–15, C9–25 and C9–40 had almost the same corrosion level, but severe degradation in the hysteretic responses was observed with increasing the axial force ratio.

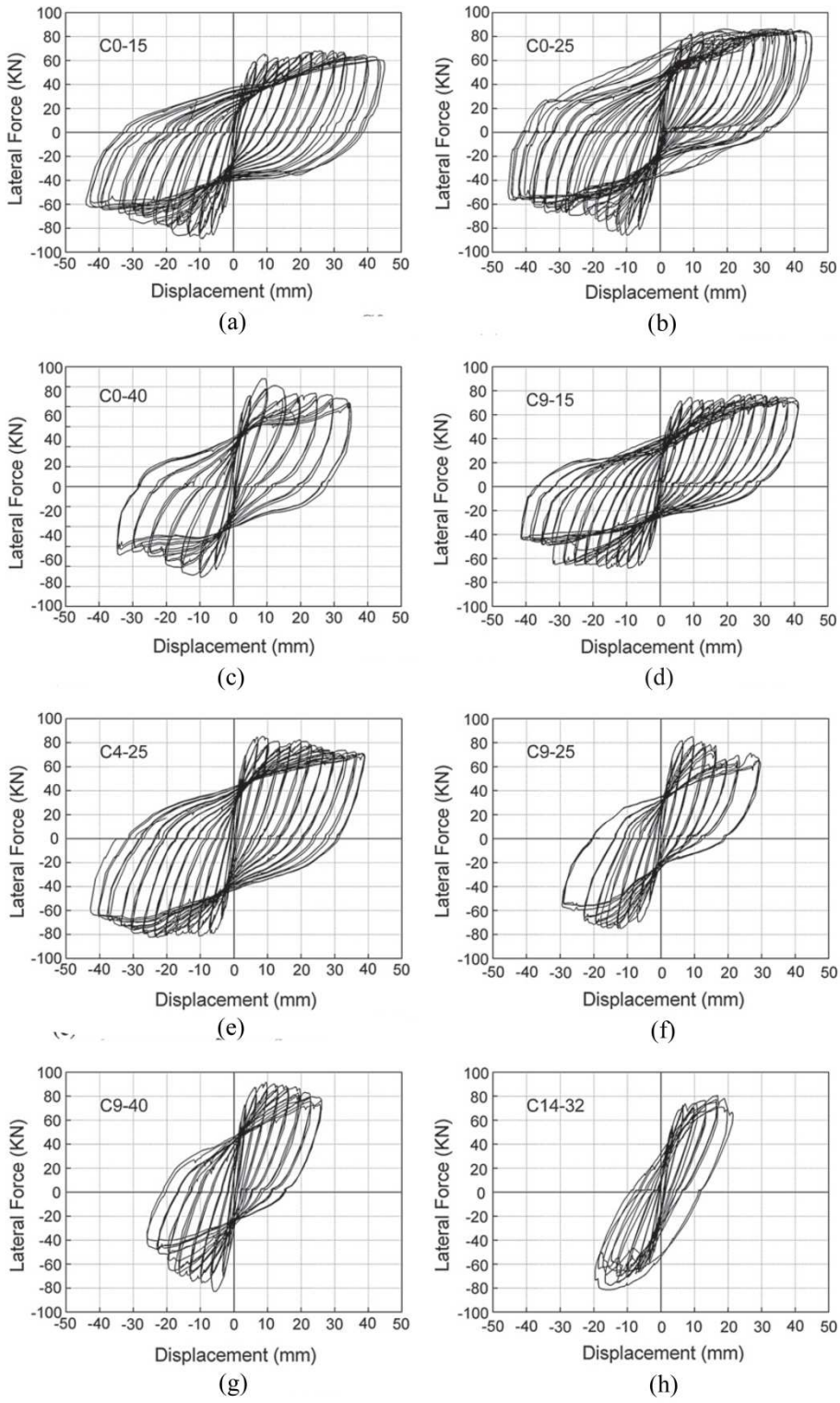

Fig. 2.47 Force-displacement response of columns under cyclic loading (Ma et al. 2012): (a) uncorroded, (b) uncorroded, (c) uncorroded, (d) 9.5% mass loss, (e) 4.1% mass loss, (f) 9.7% mass loss, (g) 9.3% mass loss, (h) 14.7% mass loss

Comparing the axial force and corrosion level, it was found that the corrosion level is the dominating factor that affects the hysteretic behaviour. For example, specimen C14–32

which was subjected to slightly lower axial load than specimen C4-25, but which had more severe corrosion damage, showed very poor energy dissipation capacity and failed in a brittle manner (Ma et al. 2012). This was mainly due to the buckling of vertical reinforcement which resulted in crushing of the cover concrete.

2.12. Influence of corrosion on the seismic vulnerability of RC bridges

In recent years several researchers have studied the influence of corrosion on seismic performance, fragility and the life-cycle cost analysis of deteriorating structures and bridges (Choe et al. 2008, Berto et al. 2009, Choe et al. 2009, Simoni 2009, Simon et al. 2010, Ghosh and Padgett 2010, Akiyama et al. 2011, Alipour et al. 2011, Akiyama and Frangopol 2013, Biondini 2013 and Ou et al. 2013). The results of these studies showed that corrosion has a significant impact on the seismic vulnerability of RC structures and bridges. In all of these studies a fibre-based type of nonlinear finite element programme, such as OpenSees, has been used for the analysis. A detailed discussion about OpenSees and fibre-based finite element method is given in Chapters 5 and 6. Here only a critical review of the previous numerical analysis methods is presented and the gaps are identified.

Fig. 2.48 shows the monotonic and cyclic moment-curvature analysis examples of a corroded bridge pier reported by Ghosh and Padgett (2010). In this analysis the only factor considered is a uniform loss of cross section area of corroded bar. All other damage parameters are not considered.

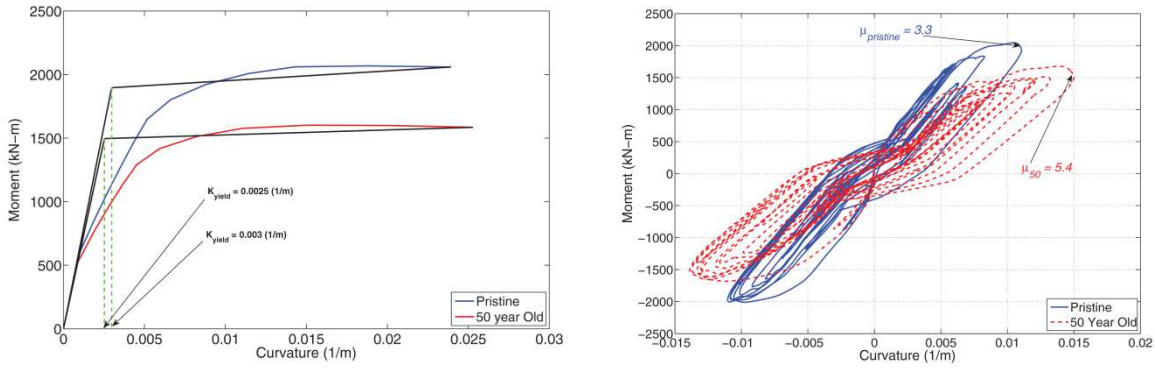

(a) **(b)**

Fig. 2.48 Influence of corrosion on moment-curvature behaviour of RC section (Gosh and Padgett 2010): (a) monotonic, (b) cyclic

Fig. 2.48 (a) shows that corrosion resulted in a 16.6% reduction in yield curvature and a 21% reduction in the yield moment for a 50 year old corroded column as compared to the uncorroded condition. This has a significant impact on the ultimate curvature

ductility as is shown in Fig. 2.48 (b). The ultimate curvature ductility demand is defined in Eq. (2.45).

$$\mu_u = \frac{\phi_u}{\phi_y} \tag{2.45}$$

where, μ_u is the ultimate curvature ductility, ϕ_u is the maximum curvature and ϕ_y is the curvature at first yield of the outmost reinforcement in tension.

In another study, Alipour et al. (2013) conducted a pushover analysis of a corroded RC column. Fig. 2.49 shows the significance of corrosion on the capacity loss of corroded columns. Unlike Gosh and Padgett (2010) they have considered the influence of corrosion on the yield strength of the corroded bars based on the model suggested by Du et al. (2005). However, they did not consider the other damage parameters in the analysis (Alipour et al. 2013).

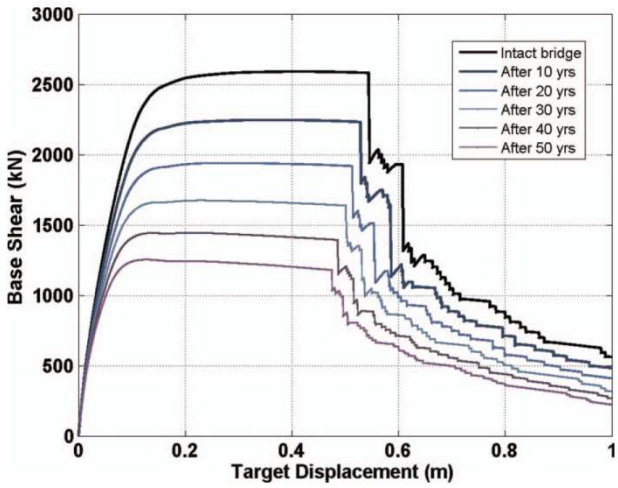

Fig. 2.49 Influence of corrosion on nonlinear behaviour of RC column under monotonic loading (Alipour et al. 2013)

Alipour et al. (2011) also conducted a comprehensive nonlinear time-history analysis of eighteen bridges including nine two-span and nine three-span bridges. The time-dependent fragility curves of the two-span bridges with a medium span length and column height of 10 m are shown in Fig. 2.50. It can be seen in Fig. 2.50 that, for a specific PGA value, the probability of exceeding any damage state increases over time owing to the level of corrosion. This increases the seismic damageability of the bridge and makes it more vulnerable to natural hazards (Alipour 2011).

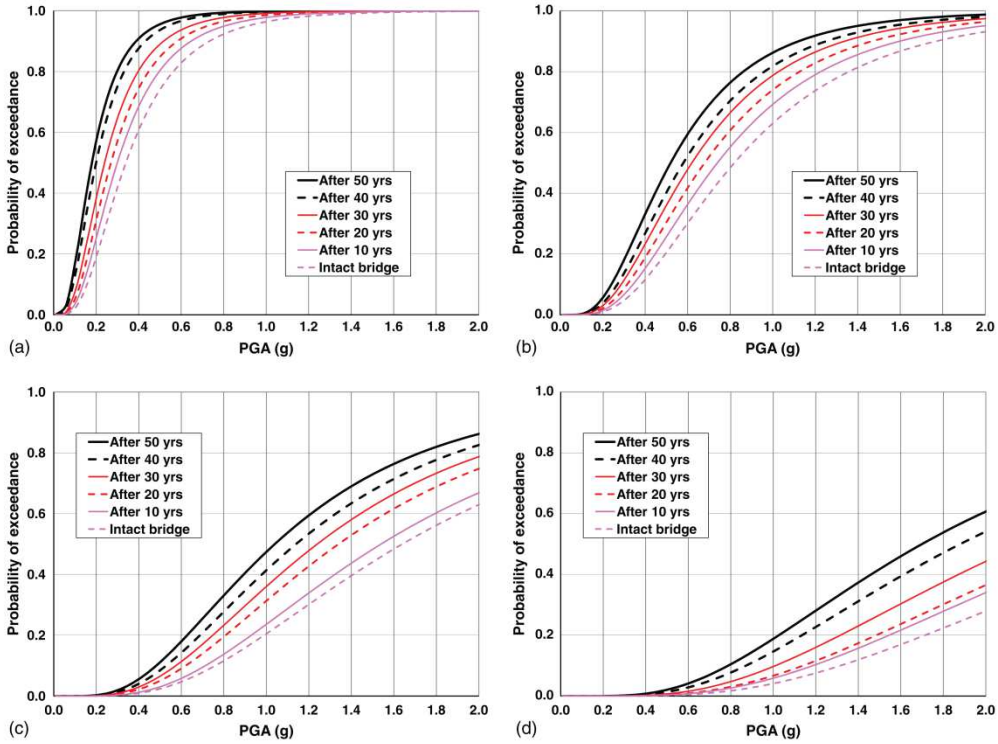

Fig. 2.50 Time-dependent fragility curves for two-span bridge with medium span length and column height of 10 m (Alipour et al. 2011): (a) at least slight damage state, (b) at least moderate damage state, (c) at least extensive damage state, and (d) complete damage state

It is quite clear that in recent years several researchers around the world have put significant effort into investigating the influence of corrosion on the seismic vulnerability of RC bridges. However, in all of the previous studies, simplified damage models have been used in the analyses. Despite these simplifications, the results of these studies show that corrosion has a significant influence on seismic vulnerability of RC bridges and structures. Therefore, more attention needs to be given to performance modelling strategies and methodologies to improve the existing models.

2.13. Conclusions

A comprehensive review of the existing mathematical models for modelling the deterioration process and service life prediction is provided. The results of previous experimental tests and analytical modelling of the influence of corrosion on structural integrity at material level have also been discussed. Examples of experimental testing on the impact of corrosion on nonlinear cyclic behaviour of beams and columns (component level) are also reviewed and the critical issues are discussed. Finally, the previous research on the impact of corrosion on the seismic fragility, vulnerability and life cycle cost of RC bridges is reviewed and the critical points are highlighted. The conclusions of

the literature review and the gaps in the existing models that have been addressed in this thesis can be summarised as below:

1. Pitting corrosion creates a nonuniform variation in the cross sectional area along the length of reinforcing bars. This results in a change in stiffness of corroded bars when they are subject to tensile force. This causes a premature yielding of the minimum section (the section with maximum pitting) while other sections are still elastic. Once other sections start yielding the minimum section will already be in the strain hardening region and will eventually fracture before other sections can completely harden. This results in a significant reduction in the plastic deformation capacity and ductility of corroded reinforcing bars. This is an important phenomenon that needs to be considered in numerical modelling of corroded RC structures and bridges.
2. The impact of corrosion is not only limited to the reinforcing bars. The expansion of corrosion products results in fracture and spalling of cover concrete. This will reduce the compressive capacity of corrosion damaged members. This effect can also change the failure mode from ductile flexural failure to brittle concrete crushing in pure flexural members. Moreover, the corrosion of horizontal ties also affects the behaviour of the core confined concrete under compressive loading. This issue is very critical in RC column sections where the confinement of concrete is essential for columns to reach the desired drift capacity in order to dissipate energy during big earthquakes. This needs to be considered in the numerical models for seismic performance assessment and evaluation of corroded bridges.
3. Corrosion has an impact on bond strength and bond-slip behaviour of embedded reinforcing bars. This has an impact on structural behaviour corroded RC element at serviceability limit state and affects the crack pattern. However, experimental investigation and numerical parametric studies conducted by other researchers showed that bond-slip behaviour of corroded bars does not have a big impact on the ultimate capacity of corroded RC elements. The failure modes observed in previous experimental studies have been fracture of bars in tension due to limited ductility and reduced low-cycle fatigue life of longitudinal reinforcement, inelastic buckling of longitudinal reinforcement and crushing of confined concrete due to corrosion of confinement reinforcement.
4. Inelastic buckling of vertical reinforcement in RC columns and beams subject to cyclic loading is well known to researchers. There has been a significant effort to investigate and model the buckling and post-buckling behaviour of reinforcing bars. However, there has not been comprehensive validation and calibration of any the existing models against an experimental data set. Moreover, recent experimental studies showed that corrosion results in a significant reduction in the buckling capacity of longitudinal reinforcing bars. This will result in a severe degradation in the cyclic behaviour of RC components which then limits the energy dissipation of corroded

elements during big earthquakes. This is a very important and fundamental issue which has not been explored to date. Furthermore, when the longitudinal bars are corroding, the low-cycle fatigue life of these bars is also affected. Therefore there is a need for a comprehensive model that can capture all this complexity in a nonlinear finite element formulation. The main contribution of this thesis is development of a buckling model for uncorroded and corroded bars as well as a consistent and reliable modelling approach that can be used to model the nonlinear behaviour of RC columns under cyclic loading considering the damage degradation due to corrosion and cyclic loading effect.

This page is intentionally left blank.

CHAPTER 3

Nonlinear Stress-Strain Behaviour of Corroded Reinforcing Bars

3.1 Introduction

As was discussed in the previous chapter, corrosion of reinforcing steel is the most common reason for the premature deterioration of RC structures in chloride laden environments. Many of these bridges are also located in high seismicity regions and will be subjected to cyclic dynamic loading during an earthquake. Therefore consideration needs to be given to the effect of material deterioration on the nonlinear response of these structures under seismic loading. In recent decades the nonlinear analysis of RC framed structures subject to seismic loading has received a lot of attention. This has been focused on the development of the fibre element technique (Spacone and Filippou 1996a, b, SeismoStruct 2011 and OpenSees 2011). In this approach the member cross section is decomposed into a number of steel and concrete fibres at selected integration points. The material nonlinearity is represented through a uniaxial constitutive material model of steel (tension and compression) and concrete (confined core concrete and unconfined cover concrete).

More recently, Choe et al. (2008), Berto et al. (2009), Ghosh and Padgett (2010) and Alipour et al. (2011) have investigated the effect of reinforcement corrosion on the behaviour and response of RC bridges subject to seismic loading through nonlinear fibre-based finite element analysis. Ou et al. (2011), Akiyama et al. (2011), and Ma et al. (2012) have investigated the effect of corrosion on the nonlinear response of RC beams and columns subject to cyclic loading experimentally. The results from these experimental studies showed that non-uniform pitting corrosion affects the global response of corroded RC elements subject to cyclic loading. This is mainly due to the influence of corrosion on cyclic behaviour and premature buckling of corroded bars.

Previous work on the corrosion of RC structures has focused mainly on corrosion induced cover cracking, corrosion prevention and repair of corrosion damaged structures. In recent years researchers have studied the effect of corrosion on the residual tension capacity and mechanical properties of reinforcing bars (Almusallam 2001, Palssom and Mirza 2002, Du et al. 2005a,b, Cairns et al. 2005, Apostolopoulos et al 2006 and Apostolopoulos 2007). In most previous studies researchers have used accelerated corrosion techniques on bare bars and bars embedded in concrete to simulate the corrosion process in a laboratory environment (Du et al. 2005a,b). Some studies have also used reinforcing bar samples from real corroded bridges (Palssom and Mirza 2002). A key aspect that almost all these researchers agree on is that the non-uniform cross section loss due to pitting corrosion along the bar has a significant influence on the force-extension response of reinforcement in tension tests.

As mentioned, all of the previous studies have focused on the effect of corrosion on residual capacity and ductility of reinforcement in tension and there have been no studies on the effect of corrosion on the inelastic buckling of bars in compression. Buckling of reinforcement is a very important damage state (performance criteria) in seismic assessment of RC structures in earthquake regions. Therefore, there is a need for research to understand the effect of corrosion damage on the nonlinear behaviour of reinforcing bars under both monotonic compressive and cyclic loading. There are a number of analytical models available in the literature for monotonic and cyclic stress-strain response of uncorroded reinforcing steel in tension and compression, with and without buckling (Menegotto and Pinto 1973, Monti and Nuti 1992, Chang and Mander 1994, Dodd and Restrepo 1995, Gomes and Appleton 1997, Balan et al. 1998, Rodriguez 1999, Dhakal and Maekawa 2002a,b, Bae et al. 2005, Hoehler and Stanton 2006 and Kunnath et al. 2009). The effect of corrosion on the behaviour of reinforcing bars subject to low-cycle fatigue loading has also been studied (Apostolopoulos 2007, Apostolopoulos and Papadopoulos 2007, Zhang et al. 2012). However, currently there is no experimental data available showing the extent of corrosion damage on the buckling response of reinforcing bars with large compressive strain demand. Moreover, the effect

of corrosion damage on the nonlinear stress-strain response of corroded bars subject to cyclic loading with high strain demand in compression including the effect of buckling has not been explicitly studied to date. In this research a comprehensive experimental study is conducted to explore these issues. Furthermore, an analytical methodology has been developed to describe the post-buckling behaviour and low-cycle high amplitude fatigue degradation of corroded bars.

3.2 Specimen preparation and corrosion simulation

3.2.1 Test specimens

In order to simulate the corrosion of steel reinforcement embedded in concrete a total of ten reinforced concrete specimens were cast. Two specimens dimensioned 200×150×500mm incorporated the 8mm and 12mm diameter reinforcing bars which would be used in the tension tests, and eight specimens dimensioned 250×250×700mm incorporated the 12mm diameter reinforcing bars which would be used in the buckling and cyclic tests. The RC specimens are shown in Fig. 3.1. The concrete mix was designed to have a mean compressive strength of 30MPa at 28 days with a maximum aggregate size of 12mm. The specimens were cast with nominal cover of 25mm.

The reinforcing bars used were typical B500B British standard reinforcing bars. For each bar size a set of three tension tests were used as control specimens to identify the mechanical properties of the original uncorroded reinforcement.

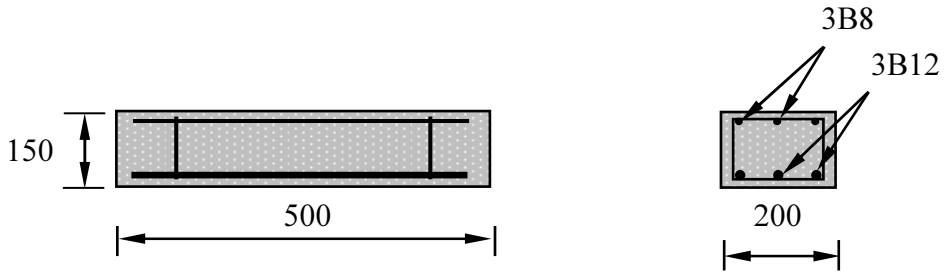

(a)

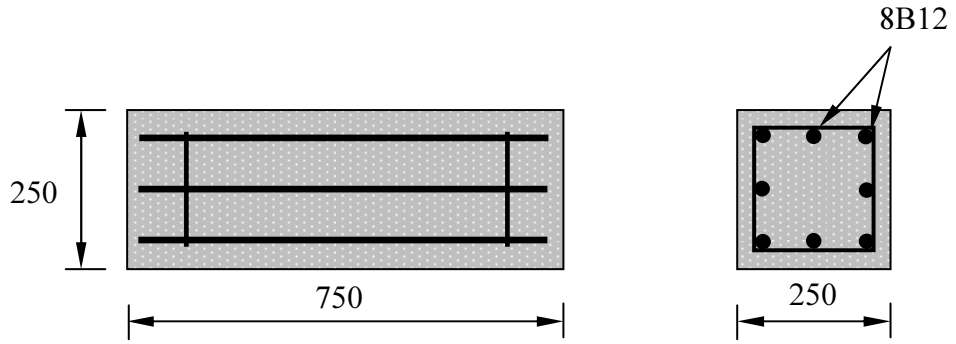

(b)

Fig. 3.1 Reinforced concrete test specimens: (a) for tension tests (b) for compression and cyclic tests

3.2.2 Accelerated corrosion procedure

Even in a very severe and aggressive environment, where the corrosion rate is quite fast, it takes years to get moderate to heavy corrosion of reinforcing bars. Therefore, it is necessary to use artificial techniques to accelerate the corrosion process in the laboratory when extended time testing is not practical. However, it is important to ensure that these techniques realistically simulate the deterioration process in the natural environment.

Previously, researchers have successfully used external current methods to induce accelerated corrosion in reinforcing bars (Almusallam 2001 and Du et al. 2005). The concept of using external currents is very simple and consists of forming an electrochemical circuit using an external power supply. The reinforcing bars act as an anode in the cell and an external material acts as the cathode. Fig. 2(a-c) shows a schematic arrangement of the test setup for inducing accelerated corrosion, a typical test specimen during accelerated corrosion, and some cleaned corroded reinforcement after removal from the concrete. Common materials that can be used as external cathodes are copper, stainless steel, and regular carbon steel. A saline solution is commonly used to function as an electrolyte to carry the ionic current from the interior of the concrete to the external cathode. In this experiment a stainless steel plate was used as the external cathode along with a 3% *NaCl* (sodium chloride) saline solution. To improve the conductivity 5% of cement weight sodium chloride was added to the concrete mix.

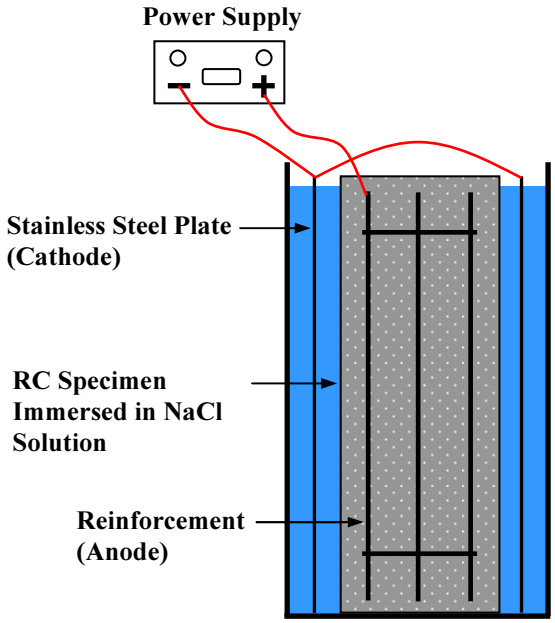
Power Supply
Stainless Steel Plate
(Cathode)
RC Specimen
Immersed in NaCl
Solution
Reinforcement
(Anode)

(a)

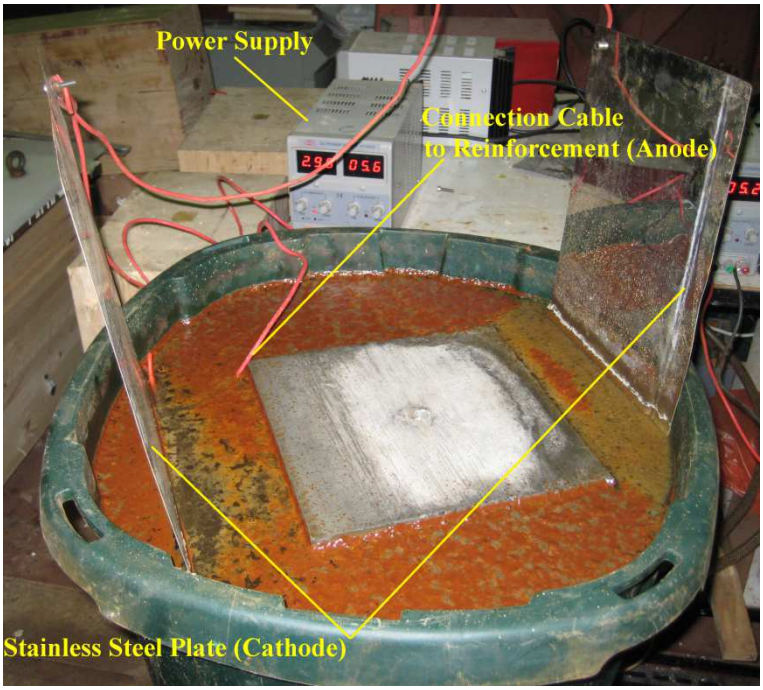
Power Supply
Connection Cable
to Reinforcement (Anode)
Stainless Steel Plate (Cathode)

(b)

(c)

(d)

Fig. 3.2 Corrosion simulation procedure: (a) schematic representation of accelerated corrosion test setup (b) accelerated corrosion procedure in the laboratory (c) corroded test specimen after accelerated corrosion process and (d) corroded bars after corrosion removal

Eq. (3.1) is Faraday's 2nd Law of Electrolysis which was used to estimate the duration of the corrosion process in relation to mass loss (Δm) due to corrosion (Almusallam 2001 and Du et al. 2005):

$$\Delta m = \left(\frac{Q}{F}\right)\left(\frac{M}{z}\right) \tag{3.1}$$

where, Q is the total electric charge passed through the substance, M is the molar mass of the substance (55.847g for steel), z is the ionic charge (electrons transferred per ion=2), F is the Faraday's constant (96500 A/s) and Q can be calculated as below (Eq. (3.2)):

$$Q = \int_0^T I \, \mathrm{d}t = IT \tag{3.2}$$

where, I is the magnitude of the electric current (A) and T is the duration of exposure (s).

Eq. (3.1) was used to estimate the corrosion duration for desired mass loss. However, the actual mass loss ratio was calculated by measuring the mass loss of the steel bar relative to the mass of the bar before corrosion.

After corrosion simulation, the concrete specimens (shown in Fig. 3.1) were broken open and the corroded bars (for both tension and compression testing) were carefully removed from the concrete. To ensure that the concrete was completely removed from the corroded bars, a mechanical cleaning process using a bristle brush was used, in accordance with ASTM G1-03 (ASTM G1-03 2011). The corroded bars were then washed with tap water and dried. The brushing and washing process was then repeated a second time. It should be noted that the same brushing process was applied to the uncorroded control specimens and it was found that the effect of brushing on the mass loss of base material is negligible. This method has been successfully used by other researchers (Apostolopoulos et al. 2006 and Apostolopoulos 2007).

The following Eq. (3.3) was used to determine the actual mean mass loss ratio (γ):

$$\gamma = \frac{m_0 - m}{m_0} \tag{3.3}$$

where, m_0 is the mass per unit length of the original steel bar, m is the mass per unit length of the steel bar after removal of the corrosion products. Eq. (3.3) gives an average corrosion level (mass loss) along the bar length.

Table 3.1 (a-c) summarises the predicted and measured mass loss the six test specimens. The results show that the values of predicted mass loss, based on Faraday's law, are much higher than the measured values. El-Maaddawy and Soudki (2003) studied the

effectiveness of the external current approach experimentally. They found that for mass losses ranging from 4% to 7.27% at current density levels ranging from 0.1 to 0.5 mA/cm^2, the predicted mass loss based on Faraday's law was in a good agreement with the measured mass loss of the steel reinforcement. However, the current density levels used in this experiment were 2.4 mA/cm^2 and 1.1 mA/cm^2 for the tension and compression specimens respectively. In addition, at higher degrees of corrosion the amount of corrosion products around the steel bars may have prevented the diffusion of OH^- and/or Fe^{2+} ions through the rust layer. This can have an influence on the ability of Faraday's law to predict the real mass loss (El-Maaddawy and Soudki 2003). It should be noted that for the buckling test specimens the average mass loss was calculated relative to the buckling length used in each test. Similarly, for tension test specimens the mass loss was calculated relative to the length of each individual bar used in the tension test.

Table 3.1(a) Summary of corrosion durations of tension test specimens

Tension specimens				
Specimen no.	**Corrosion current density (mA/cm^2)**	**Corrosion duration (days)**	**Estimated mass loss Eq. 3.3**	**Measured mass loss**
T1	2.4	5	15%	6.5%
T2	2.4	14	25%	10.5%

Table 3.1 (b) Summary of corrosion durations of compression buckling test specimens

Compression buckling specimens				
Specimen no.	**Corrosion current density (mA/cm^2)**	**Corrosion duration (days)**	**Estimated mass loss Eq. 3.3**	**Measured mass loss**
CB1	1.1	28	30%	19.1%
CB2	1.1	35	38%	26.5%
CB3	1.1	43	50%	32.0%
CB4	1.1	35	38%	25.0%

Table 3.1 (c) Summary of corrosion durations of cyclic test specimens

Cyclic specimens				
Specimen no.	**Corrosion current density (mA/cm^2)**	**Corrosion duration (days)**	**Estimated mass loss Eq. 3.3**	**Measured mass loss**
CC1	1.1	28	30%	18.5%
CC2	1.1	28	38%	25.0%
CC3	1.1	56	60%	40.0%
CC4	1.1	42	50%	30.0%

3.3 Investigation of the spatial variability of corrosion

The general variation of corrosion along the length of the reinforcing bars was investigated by cutting a corroded bar with 23% average weight loss into 35 No. slices and measuring the mass of each slice individually. This captured the general distribution of corrosion along the length of the bar, but shorter slices would be needed to capture the variability of bars with highly localised corrosion pitting. The effective cross sectional area of each slice was calculated based on the average density of a reinforcing bar. This average density was calculated using three uncorroded 80mm long B12 bars. The mass of each corroded slice was measured and its volume was found by determining the change in volume of water in a measuring cylinder. The nominal length of each cut slice was 11mm ±1mm, the deviation being a result of the cutting process. The exact length of slices was measured with a digital Vernier Calliper. The corroded bars varied in diameter in a similar manner to that found by other researchers (Du et al. 2005a,b). Fig. 3.3(a) shows the variation of average diameter along the corroded bar (for each 11mm slice) and the nominal bar diameter before corrosion. Fig. 3.3(b) shows the mass loss variation in percentage ($\psi = 100\gamma$) along the bar as well as the mean ($\mu = 23.63$) and standard deviation ($\sigma = 8.88$).

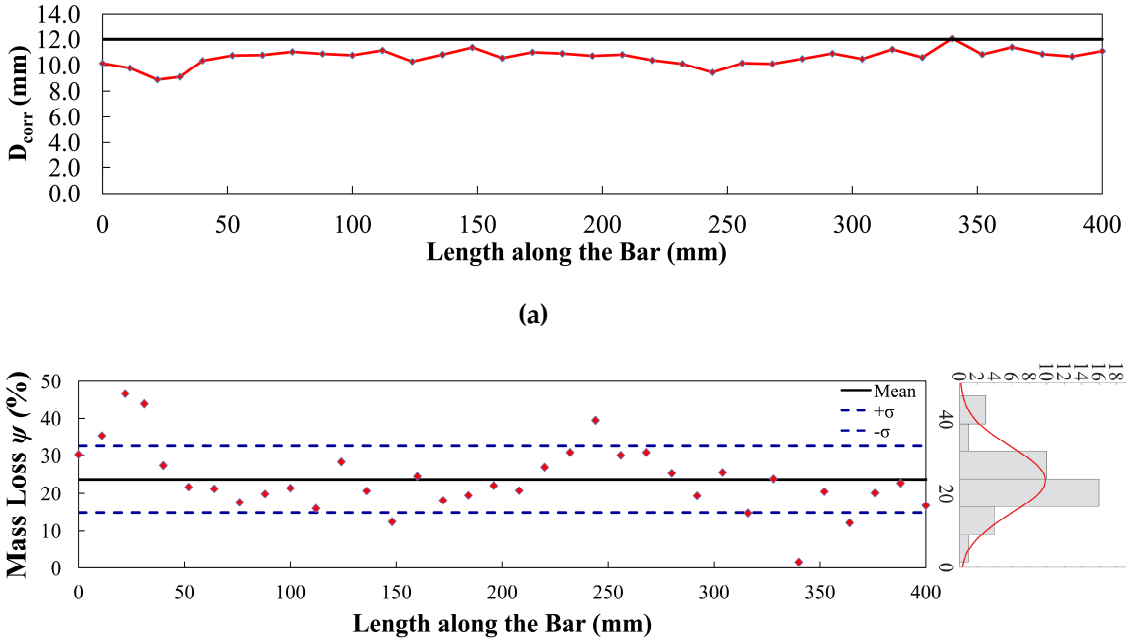

Fig. 3.3 Spatial variability of corrosion along the bar: (a) residual diameter of corroded bar (b) mass loss variation along the bar

This analysis shows that it is impossible to predict the exact location of pitting on reinforcement in a real structure. However, using currently available technology it is

possible to measure the corrosion rate of reinforcement in existing corroded RC structures using non-destructive corrosion monitoring systems (Broomfield 2007). Accordingly the total mass loss of reinforcement due to corrosion can be estimated in relation to the measured corrosion rate. The mean reduced diameter (D_{corr}) of reinforcement for a specific mass loss can be calculated using Eq.(3.4) [8,17]:

$$D_{corr} = D_0\sqrt{1-\gamma} \tag{3.4}$$

where, D_0 is the initial diameter of uncorroded bar and γ is defined in Eq. (3.3).

3.4 Uniaxial tension tests of reinforcing bars

For the tension testing of the bars a universal testing machine with 600kN capacity, instrumented with an internal LVDT and having V-groove jaws with coarse tooth pattern was used. The speed of testing was set to 2mm/min (Palssom and Mirza 2002). A 100mm gauge length extensometer with maximum stroke of ±25mm used to measure the bar extension to failure.

3.4.1 Observed stress-strain response in tension

The mechanical properties of the original reinforcing bars were calculated using the results of the tension tests on uncorroded bars. A summary of properties of the original reinforcement and the relevant code requirements (BS 4449 2005 and BS-EN 10080 2005) are shown in Table 3.2 and Table 3.3 respectively. It should be noted that the unit mass specified in BS4449 only represents a nominal unit mass based on nominal diameter. In reality this value can vary slightly because the unit mass is function of the pattern of ribs and is not solely dependent on the actual bar diameter. The unit mass value of 12mm diameter bars in Table 3.2 is the average unit mass of all the bars before corrosion and the difference between this value and the nominal value in the code is only 1.57% which is considered insignificant.

Table 3.2 Mechanical properties of uncorroded reinforcement

Reinforcement type		8mm (B8)	12mm (B12)
Yield Strength	f_y (MPa)	510	520
Modulus of Elasticity	E_s (MPa)	194881	212099
Yield Strain	$\varepsilon_y = f_y/E_s$	0.00261	0.00247
Ultimate Strength	f_u (MPa)	645	616
Ultimate Strain	ε_u	0.04660	0.06033
Strain Ratio	$\varepsilon_u/\varepsilon_y$	17.85	24.42
Strength Ratio	f_u/f_y	1.27	1.18
Total Elongation at Maximum Force	λ (%)	4.66%	6.03%
Unit Mass	m (kg/m)	0.396	0.874

Table 3.3 The minimum values of tensile properties of B500B reinforcement (BS 4449-2009)

Reinforcement type		8mm (B8)	12mm (B12)
Yield Strength	f_y (MPa)	485	485
Strength Ratio	f_u/f_y	1.06	1.06
Total Elongation at Maximum Force	λ (%)	4%	4%
Nominal Unit Mass	m (kg/m)	0.395	0.888

Fig. 3.4 shows the mean stress-strain responses for the 8mm diameter bars tested. The mean stress is the calculated stress based on the average reduced cross section area and the mean strain is the average strain over the entire length of the bar. The boundaries for the minimum code requirements are also shown on this graph. These boundaries indicate the significance of corrosion on the residual capacity and ductility of corroded bars. In some cases the rebar fracture occurred within the gauged section but, because the point of fracture depended on the pitting corrosion, the fracture often occurred outside the gauge. This issue is also reported by other researchers who did tension tests on corroded bars (Du et al. 2005a,b , Cairns et al. 2005, Apostolopoulos et al. 2006, Apostolopoulos 2007 and Palssom and Mirza 2002). Therefore, the data reading from the internal LVDT in the test machine was used to calculate the average strain over the entire length of bars.

The results show that, for corroded specimens, the mean strain at failure reduces quickly even with small amounts of corrosion. For the bar with a mass loss of 6.44% the mean strain at failure reduced by approximately 35%. A significant variation in the mean strain at failure for the more highly corroded bars was also observed. For example, one bar with a 15% mass loss showed a 78% reduction in the mean strain at failure, while another with 17% mass loss only showed a 62% reduction. These changes to the mean strain at failure are similar to the results of previous studies which used British manufactured reinforcement (Du et al. 2005 a,b).

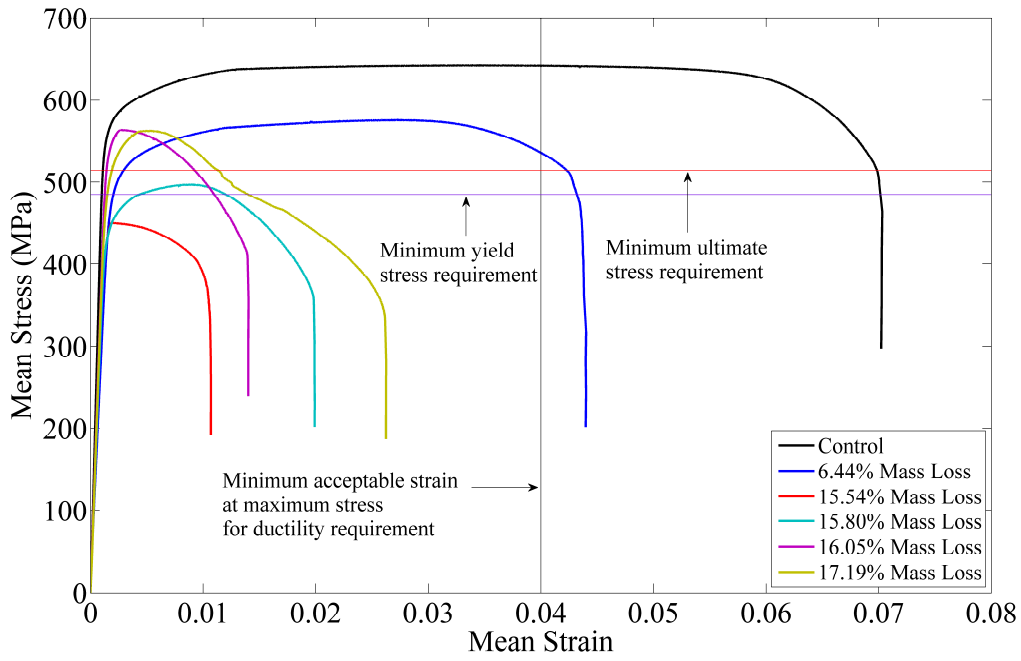

Fig. 3.4 Mean stress-strain curves of tension tests for the 8mm diameter bars

However these results contrast with results reported by researchers from other countries. Some of these results indicate that corrosion doesn't have significant effect on the stress-strain curve of bars in tension (Andrade 1991). In contrast Zhang et al (1995) reported that up to 21% mass loss shortened the yield plateau on the force–extension response of corroded reinforcement. In another study Almusallam (2001) reported that reinforcing steel bars with 12.6% or more mass loss indicated a brittle behaviour. They also reported that the elongation limit of bars with more than 12% mass loss was less than the 9% specified by ASTM A 615. Palssom and Mirza (2002) reported that due to non-uniform loss in cross sectional area, a 20% difference between the greatest and smallest cross section area along the bar can cause a 50% reduction in ultimate strain at failure. These variations in the experimental results are due the random nature of corrosion and may also be related to the differences in steel grades used in each test. There is need for further analytical work based on stochastic methods to model the uncertainties associated with corrosion and their influences on the material response.

Nevertheless most researchers agree that if the corrosion induced mass loss was uniform along the length of the corroded bars it would not have a significant effect on the mean stress-strain response of the bar in tension (where mean stress is the calculated stress based on the mean reduced diameter of corroded bar). Therefore, the change in the mean stress-strain response is caused by non-uniform distribution of pits along the length of corroded bars (Du et al. 2005a,b, Cairns et al. 2005 and Palssom and Mirza 2002). This change in response occurs because the corroded reinforcement starts yielding at the location of the smallest cross section while other parts of the bar remain elastic. As the

section that reached yield first starts to strain harden there is the possibility that next weakest section along the bar will start to yield. This process results in a non-uniform stiffness distribution along the bar and subsequently affects the yield and ultimate strength and ductility of corroded bars.

3.4.2 Effect of corrosion on reduction of yield and ultimate stress

In Fig. 3.5 the normalised ratios of yield and ultimate stress (f_y and f_u respectively) of corroded bars to the corresponding values for uncorroded bars are plotted relative to the percentage mass loss. A linear trend line was fitted to the test data to estimate the strength reduction due to pitting corrosion. Trend lines were fitted to the combined scatter plot including the two groups of reinforcement tested in this experiment (8mm and 12mm diameter bars). It should be noted that the original uncorroded cross section area was considered in this analysis. The calculated regression factors of the current tests were then compared to the equations proposed by Du et al. (2005a) as follows (Eq. (3.5) and (3.6)):

$$f_{yt} = f_y(1-0.015\psi) \tag{3.5}$$

$$f_{ut} = f_u(1-0.015\psi) \tag{3.6}$$

where, f_y and f_u are yield and ultimate stresses of uncorroded bar, f_{yt} and f_{ut} are the corresponding yield and ultimate stresses of corroded bar based on the original cross section area, and ψ is the mass loss in percentage ($\psi=100\gamma$). The best fit of the experimental data and the Upper Bound and Lower Bound of predicted values at 95% confidence together with the Eqs. (3.5) and (3.6) are shown in Fig. 3.5(a) and (b). It is clear from Fig. 3.5 that the outcome of both experiments are similar, with these tests giving values of 0.017 and 0.018 for the regression factors for yield and ultimate stress respectively.

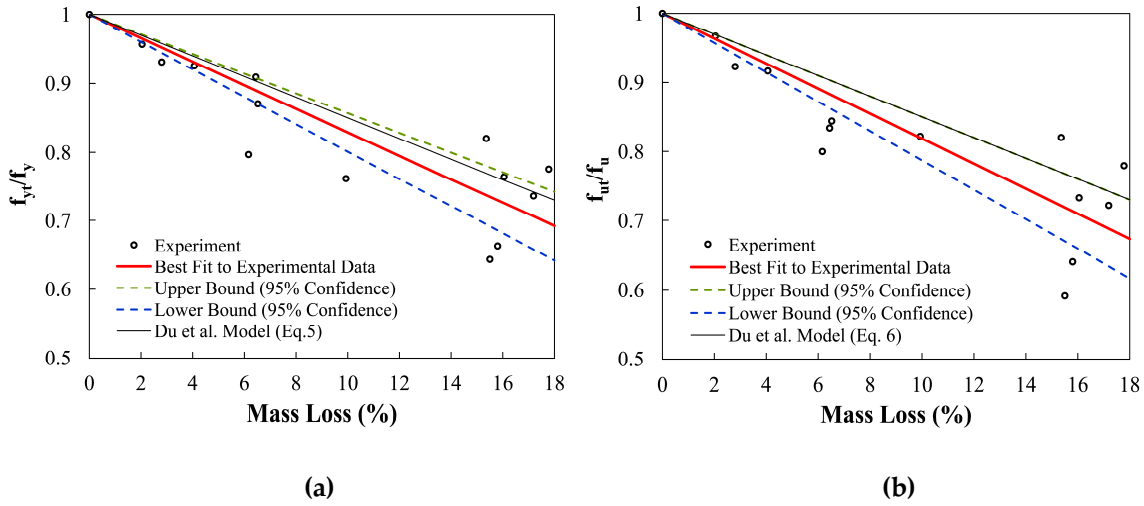

Fig. 3.5 Trend lines of test experiments of all groups of bars: (a) Yield Stress (b) Ultimate Stress

The regression factors, affecting the yield and ultimate stresses and ultimate strain of corroded bars, obtained by other researchers (Clark and Saifullah 1994, Zhang et al. 1995, Du et al. 2005a,b, Cairns et al. 2005 and Kim et al. 2009) range from 0.01 to 0.017. This indicates a consistent trend between the results of this study and results obtained by other researchers. This shows that it is a fair assumption to consider a pseudo stress-strain curve for corroded bars based on the mean reduced area. The effect of non-uniform pitting corrosion along the length of the bar can then be included by modifying f_y and f_u using Eqs. (3.5) and (3.6) to calculate the strength reduction of corroded bars as proposed by Du et al. (2005a).

3.5 Uniaxial compression testing of reinforcing bars

A total of 57 monotonic compression tests were carried out on corroded bars with different effective lengths. The buckling lengths of the bars were chosen based on the ratio of spacing of horizontal ties (L) in the common construction of RC columns to the bar diameter (D) known as the L/D ratio. The L/D ratios used in these tests were 5, 8, 10, 15 and 20. A 250kN universal testing machine with hydraulic grips was used for the compression tests of the reinforcing bars. The machine used an internal LVDT to measure the displacement of the grips. A 50mm extensometer with maximum stroke of ±5mm was used to measure the average axial strain over the middle section of the reinforcement over the linear range. An additional external LVDT with maximum stroke of ±10mm was connected to the grips to measure the average displacement over the entire length of the bar, in both linear and non-linear test phases, as shown in Fig. 3.6. As the extensometer could not capture the post buckling behaviour, the data from the external LVDT has been used throughout this chapter to provide an average strain over the entire length of the bar throughout the test. Before the main experiment some sample tests were carried out on reinforcement with different diameters and lengths to make

sure that there would be no slippage within the grips during the main tests. Any slippage would have been seen as an increase in the external LVDT reading accompanied by a reduction in the applied force. This effect would not be seen in the force-displacement data from the extensometer. It was found that no slip occurred during the sample tests.

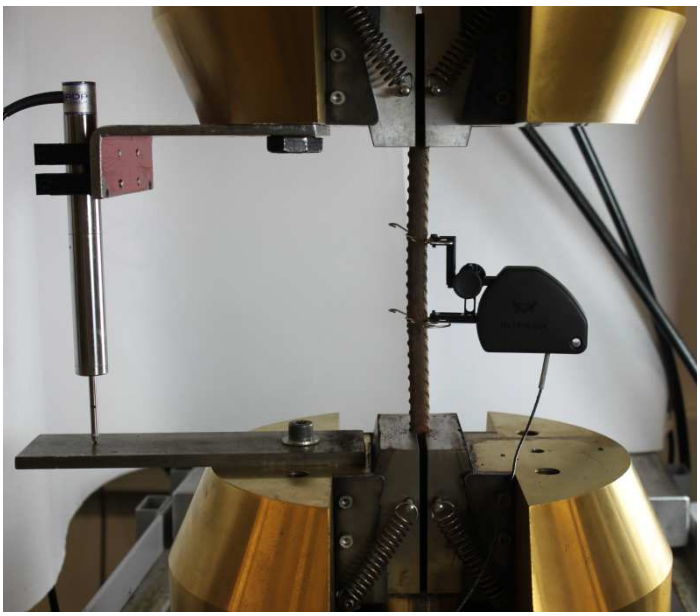

Fig. 3.6 Buckling test setup

3.5.1 Effect of corrosion on the buckling mechanism of corroded bars

The buckling behaviour of reinforcing bars has been studied both using experimental tests on reinforcement and using theoretical modelling employing nonlinear finite element analysis (Bresler and Gilbert 1961, Scribner 1986, Papia and Russo 1989, Mau and El-Mabsout 1990, Mau 1990, Monti and Nuti1992, Restrepo et al. 1994, Dodd and Restrepo 1995, Gomes and Appleton 1997, Pantazopoulou 1998, Rodriguez et al. 1999, Bayrak and Sheikh 2001, Dhakal and Maekawa 2002a,b, Bae et al. 2005, and Cosenza and Prota 2006). All these researchers agree that the slenderness ratio of the bars and the yield stress are the most critical parameters governing the buckling load of bars.

As explained previously, in sections 3.3 and 3.4, pitting corrosion results in a localised reduction of the cross section area along the corroded bar. The results of these tests show that this phenomenon has a significant influence on the buckling mechanism of corroded bars.

that this phenomenon has a significant influence on the buckling mechanism of corroded bars.

The classical inelastic buckling of an encastré uncorroded bar starts with the formation of plastic hinges at mid-height and supports. However, this behaviour changes significantly when there is non-uniform corrosion along the buckling length of corroded bars. The classical inelastic buckling mechanism of uncorroded reinforcing bars and the observed buckling mechanisms of corroded bars are illustrated schematically in Fig. 3.7. A photo, after the buckling tests, of the group of bars with L/D = 10, 15 and 20 is shown in Fig. 3.8.

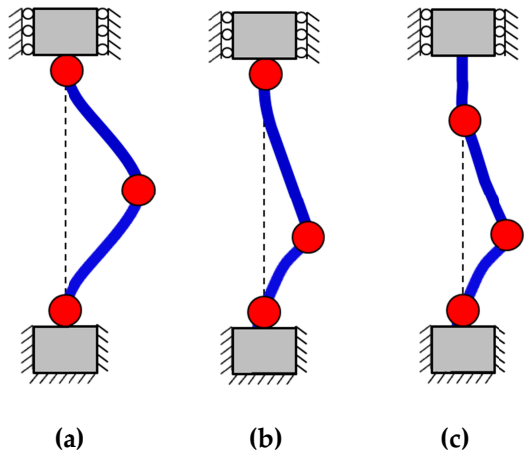

Fig. 3.7 Observed buckling mechanisms: (a) classical inelastic buckling of uncorroded bars, (b) inelastic buckling of corroded bars with unsymmetrical plastic hinges, (c) inelastic buckling of corroded bars with multiple intermediate plastic hinges

(a)

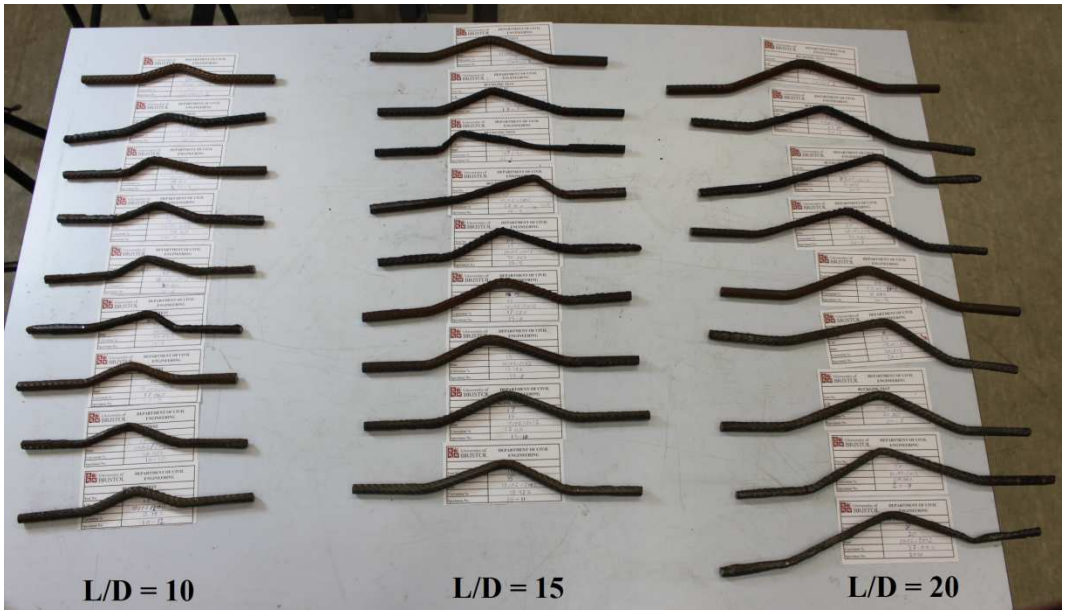

(b)

Fig. 3.8 Inelastic buckling of uncorroded and corroded bars: (a) classical inelastic buckling of uncorroded bars with L/D = 15, (b) inelastic buckling of corroded bars

In order to understand the parameters affecting the buckling mechanism of corroded bars one of the corroded bars which experienced an unsymmetrical buckling mechanism was sliced into small sections. The cross sectional slices for this bar (with L/D = 15 and 49.24% mass loss) are shown in Fig. 3.9. It was generally observed that the corrosion modified the cross sectional shape of the corroded bars. In other words, the cross section of corroded bars was no longer circular after corrosion. This has been reported by other researchers who investigated the variability of corrosion along bars taken from a real corroded bridge (Palssom and Mirza 2002).

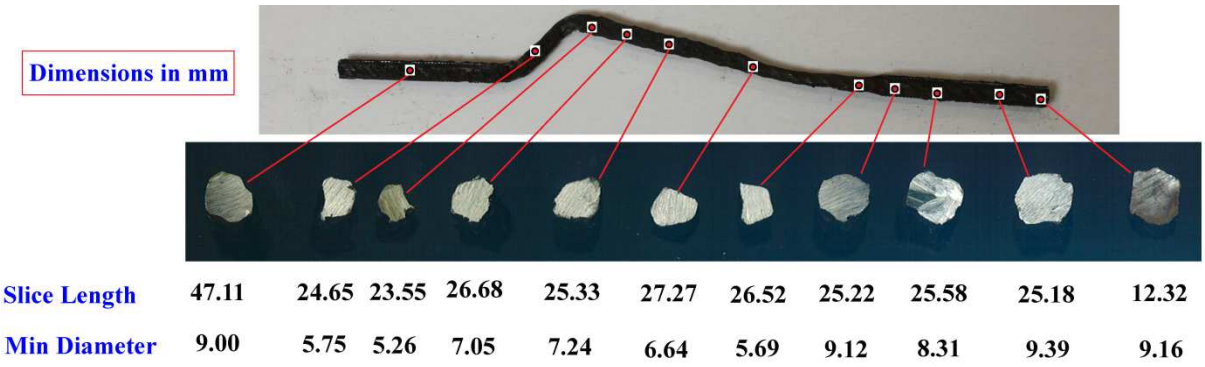

Fig. 3.9 Variation of non-uniform cross sections along the length of a buckled corroded bar

The unsymmetrical shapes of the cross sections create strong and weak axes in the reinforcement and change the radius of gyration in different axis. This directly affects the theoretical buckling load of corroded bars.

Other researchers have shown that the inelastic buckling of uncorroded bars can be explained by the theory of inelastic buckling (Timoshenko and Gere 1963 and Galambos and Surovek 2008). This theory relies on the *reduced modulus* concept which depends on both the material property and geometrical shape of bar cross section (Timoshenko and Gere 1963, Papia et al. 1988, Gomes and Appleton 1997 and Galambos and Surovek 2008). Given that the cross sections of corroded bars vary in shape and the shapes also vary along the buckling length, it is almost impossible to directly use this method to calculate the buckling stress of corroded bars. In addition, unsymmetrical pitting corrosion generates an imperfection along the bar which will result in an additional bending moment in the bar due to the load eccentricity. This load eccentricity will increase the local stress at critical sections.

3.5.2 Observed stress-strain response of corroded bars in compression

3.5.2.1 Yield and post-yield behaviour of the group of bars with $L/D = 5$

As expected the bars with L/D ratios of 5 were not prone to buckling and generally displayed stable behaviour under compression loading. The shape of the observed stress-strain response was almost identical to the shape of the stress-strain response in tension. Other researchers who carried out buckling tests on uncorroded bars observed similar behaviour (Bae at al. 2005 and Monti and Nuti 1992). In a similar manner to the tension tests, the corrosion resulted in a reduction in yield stress (mean stress based on mean reduced area) in these bars. For most bars the post-yield behaviour was also similar to the tension envelope. Only some of the most heavily corroded bars or bars with highly localised pits experienced limited buckling which resulted in a slight change in post-yield behaviour. Fig. 3.10 shows the observed stress-strain curves for bars with $L/D = 5$.

To show the significance of non-uniform pitting corrosion along the length of the bars the stress-strain responses considering the original uncorroded cross section and the averaged reduced cross section are provided in Fig. 3.10 (a) and (b) respectively. It should be noted that calculated stresses based on the original uncorroded cross section area are called Notional Stress and the calculated stresses based on the average reduced

cross section area are called Mean Stress. The Mean Strain is the average strain over the entire length of the bar.

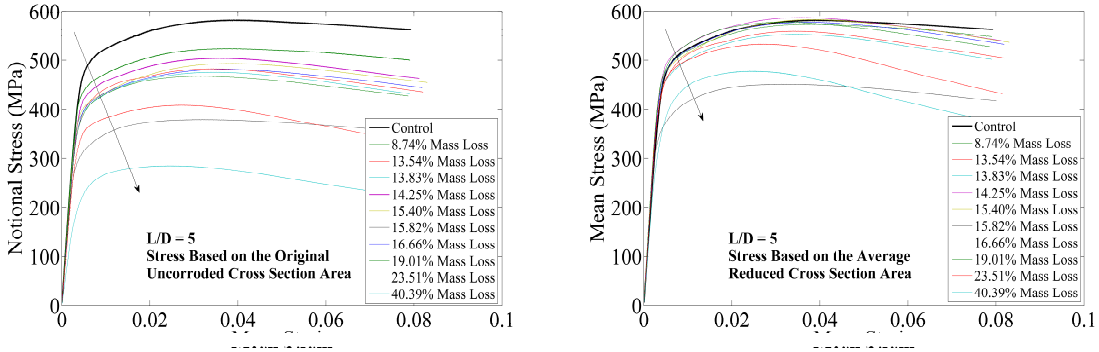

(a) (b)

Fig. 3.10 Observed stress-strain response of corroded reinforcement in compression with *L*/*D*=5

As shown in Fig. 3.10 (b), use of the average reduced cross section area reduces the apparent strength loss caused by the corrosion. In theory, if the corrosion was completely homogeneous and uniform along the bar the mean stress-strain response should be identical to the uncorroded bars. The remaining residual strength loss is caused by the effects of pitting corrosion. Based on these observed results, bars with $L/D \leq 5$ can be treated in a similar manner to tension bars and the effects of buckling can be ignored.

3.5.2.2 Yield and post-yield behaviour of the group of bars with *L*/*D* = 8 and 10

The uncorroded control specimens in this group of bars had a stable behaviour up to a stress close to the yield stress. They then showed a smooth transition from linear elastic to nonlinear plastic behaviour. Once the bars had yielded, instability and buckling started and a post-yield softening behaviour was then observed. Therefore, the maximum compressive stress prior to post-yield softening is defined as the buckling stress.

Corrosion changed this behaviour significantly as a result of the mass loss and distribution of pitting along the bar. Fig. 3.11 shows the observed notional and mean stress-strain responses of bars with $L/D = 8$ and 10. Three types of behaviour can be seen in Fig. 3.11. Those bars with highly localised pitting corrosion showed a smooth transition from linear elastic to nonlinear plastic, the transition taking longer compared to the uncorroded bars, and subsequently a post-yield softening (e.g. Fig 3.11 (c) 39.16% mass loss). This behaviour was due to the premature yielding and squashing of the weakest section before buckling started. The post-buckling softening of these bars generally showed a similar trend to the original uncorroded bar but with a significant

reduction in the buckling stress. Those bars with more uniformly distributed corrosion and a relatively small mass loss showed a similar behaviour to the original uncorroded bars but displayed a small reduction in their buckling stress. However, the bars with a high percentage of mass loss and relatively uniformly distributed corrosion showed a quicker transition from linear elastic to nonlinear plastic behaviour. The buckling stress in these bars was significantly lower and the bars displayed a steeper post-yield softening behaviour. This indicates that more uniform corrosion effectively results in a change to the overall slenderness ratio of the bars (e.g. Fig. 3.11(b) 46.38% mass loss).

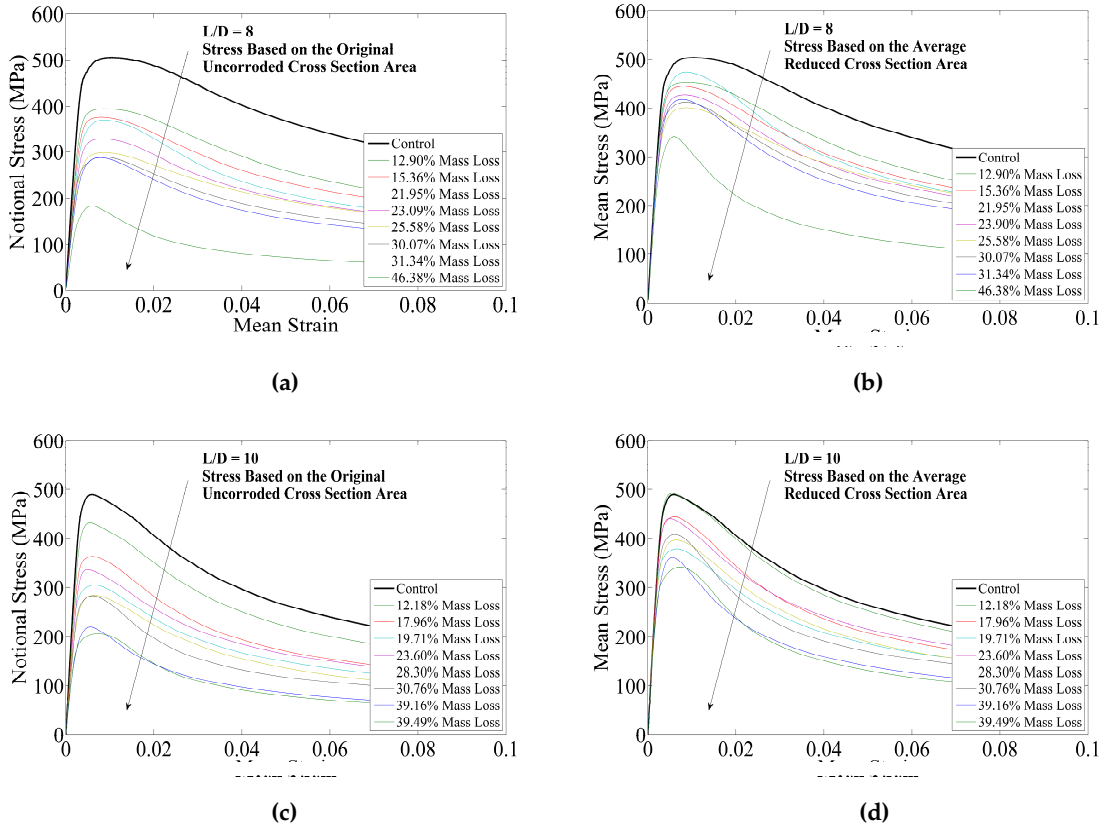

Fig. 3.11 Observed stress-strain response of corroded reinforcement in compression with *L*/*D* = 8 and 10

3.5.2.3 Yield and post-yield behaviour of the group of bars with *L*/*D* = 15 and 20

The observed mean and notional stress-strain responses of bars with *L*/*D*=15 and 20 are shown in Fig. 3.12. The uncorroded control specimens for this group of bars showed relatively stable behaviour up to a stress close to yield stress but then displayed a sharp and steep post-yield softening branch. The corroded bars with *L*/*D*=15 and 20 generally displayed a quick transition from linear elastic to post-yield softening compared to the shorter bars. The bars also showed a very sharp transition from linear elastic at the point

of buckling to a very steep post-yield softening branch. This is primarily due to effect of corrosion on the slenderness ratio of the corroded bars. In addition, corrosion induced imperfections had a more significant effect on the longer bars which resulted in a significant reduction in the buckling stress of corroded bars. The observed buckling mechanisms for these corroded bars were also more variable as reported in section 3.5.1.1.

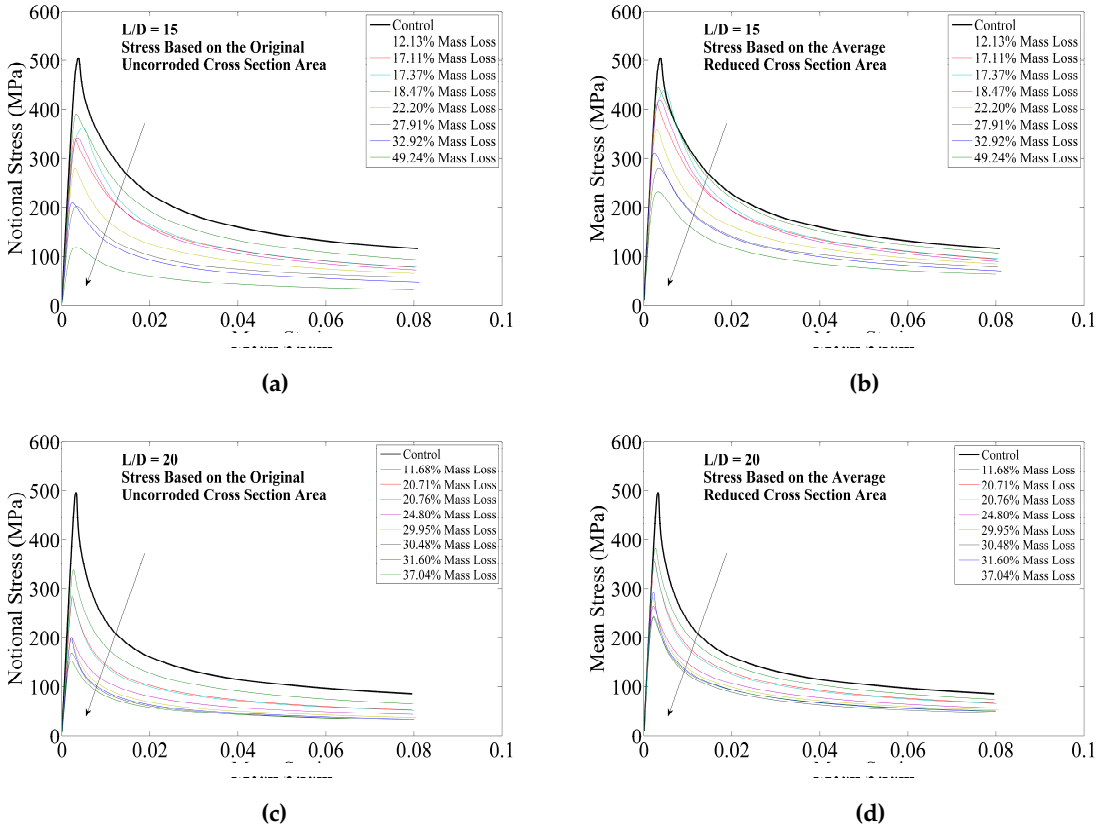

Fig. 3.12 Observed stress-strain response of corroded reinforcement in compression with *L*/*D*=15 and 20

3.5.3 Impact of corrosion on reduction of buckling stress of corroded bars

The effect of corrosion on the buckling stress of corroded bars was investigated by linear regression analysis of the normalised values of maximum compressive stress in the corroded bars at buckling to the corresponding values in uncorroded bars at buckling. The effects of using the original cross section compared to the average reduced cross section in stress calculation were considered separately. The physical tests were divided into two groups of (a) *L*/*D* = 8 and 10 and (b) *L*/*D* = 15 and 20. Fig. 3.13 (a-d) shows the results of the linear regression analysis of buckling stress of corroded bars for both groups.

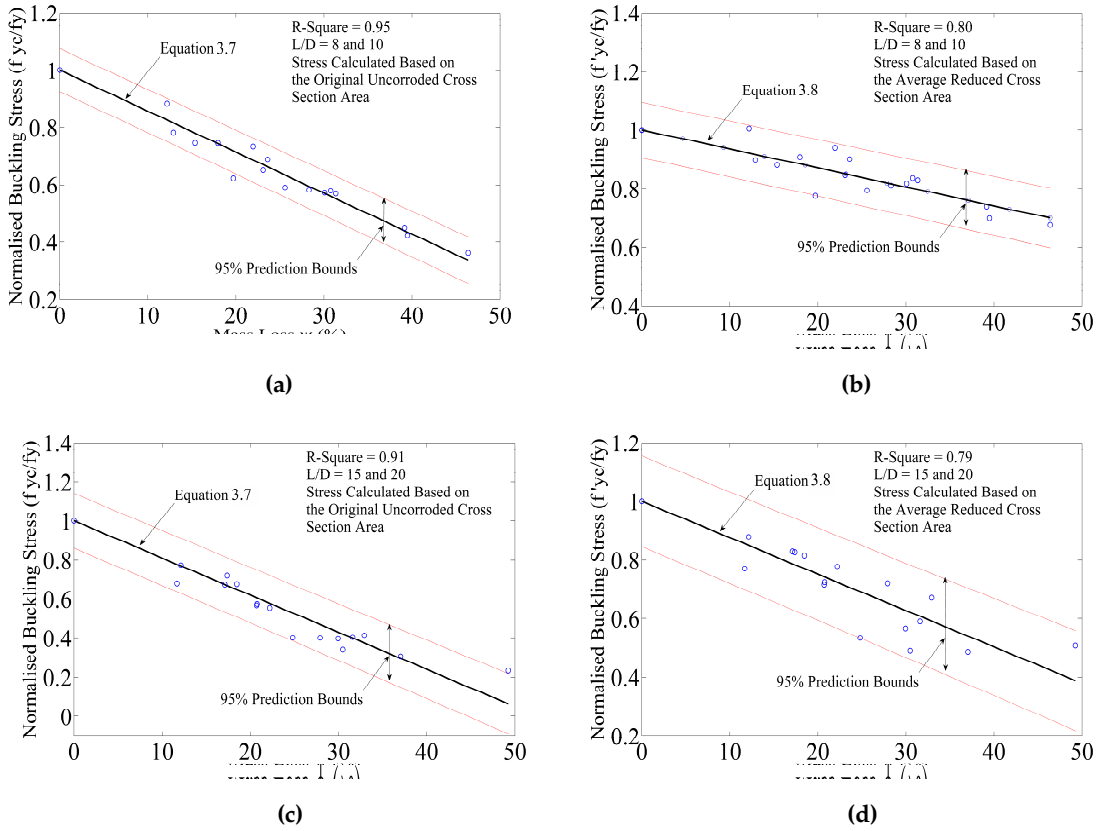

Fig. 3.13 Impact of corrosion on the reduction of buckling stress

The linear regression analysis for data in Fig. 3.13 is in the form shown in Eq. (3.7) and (3.8).

$$f_{yc} = f_y(1-\alpha\psi) \tag{3.7}$$

$$f'_{yc} = f_y(1-\beta\psi) \tag{3.8}$$

where, f_{yc} is the buckling stress of the corroded bars considering the original cross section of the uncorroded reinforcement, f'_{yc} is buckling stress of the corroded bars considering the average reduced cross section of the corroded reinforcement relative to mass loss (Eq. (3.3)), f_y is the yield stress of the uncorroded reinforcement and ψ is the mass loss in percentage ($\psi=100\gamma$). α and β are the regression analysis coefficients which are summarised in the Table 4. The α factor represents the effect cross section loss and non-uniform pitting corrosion on buckling capacity of corroded bars and the β factor represents the influence of non-uniform pitting corrosion. These empirical coefficients provide very important estimate of loss of buckling capacity which will be used in constitutive modelling of corroded bars as is described in the section 3.6 of this chapter.

Table 3.4 Regression coefficients

Slenderness ratio	α (Area loss and pitting coefficient)	β (Pitting coefficient)
L/D = 8 and 10	0.016	0.0065
L/D = 15 and 20	0.020	0.0124

3.6 Proposed analytical model of post-yield buckling response of corroded bars

Mau and El-Mabsout (1989) developed a special beam-column element for nonlinear finite element analysis of the inelastic buckling of reinforcing bars. This model can correctly simulate the inelastic buckling of a single reinforcement bar but it is computationally expensive for use in nonlinear analysis of RC structures. Monti and Nuti (1992) developed an analytical model based on experimental tests on reinforcing bars. This model is simple and suitable for incorporation into the computational section analysis that is found within a nonlinear analysis of RC structures and it uses a fibre-based section decomposition method. Bae et al. (2005) also developed an analytical model for inelastic buckling of reinforcing bars based on an experimental study of a number of single reinforcing bars with different L/D ratios and load eccentricities. In this model the post-yield buckling behaviour of the reinforcement is governed by the L/D ratio, the transverse displacement (horizontal displacement due to buckling) and yield stress σ_y. Dhakal and Maekawa (2002a) conducted a nonlinear finite element analysis on single reinforcement bars with different L/D ratios using a fibre-based technique. Based on the results of the nonlinear analysis, they developed a new analytical model that can model the post-yield buckling of a single reinforcing steel bar. The main feature of this model is that the behaviour of reinforcement buckling is governed by the L/D ratio and the yield stress σ_y of the reinforcement. In this model, the compression response of reinforcement is defined as a function of a single compound variable called the non-dimensional bar buckling parameter λ_p as defiend in Eq. (3.9) below:

$$\lambda_p = \sqrt{\frac{\sigma_y}{100}}\frac{L}{D} \tag{3.9}$$

It should be noted that σ_y in Eq. (3.9) is in MPa.

Given non-dimensional stress $\eta = \sigma/\sigma_y$ and strain $\xi = \varepsilon/\varepsilon_y$ (where σ_y is the yield stress and ε_y is the yield strain) the following equations define the stress-strain envelope shown in the Fig. 3.14.

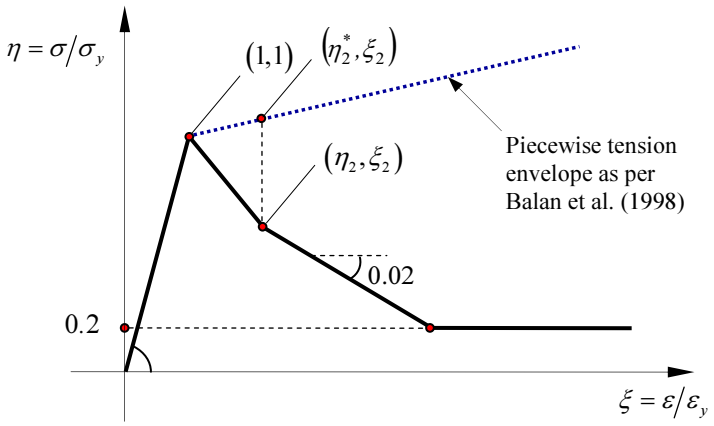

Fig. 3.14 Proposed Dhakal-Maekawa buckling model

$$\eta = \begin{cases} \xi; & \xi \le 1 \\ \dfrac{(\eta_2 - 1)}{(\xi_2 - 1)}(\xi - 1) + 1; & 1 < \xi \le \xi_2 \\ \eta_2 - 0.02(\xi - \xi_2); & \xi_2 \le \xi \;\&\; \eta \ge 0.2 \\ 0.2; & otherwise \end{cases} \tag{3.10}$$

where, the empirical relationships for (η_2,ξ_2) are given below:

$$\xi_2 = 55 - 2.3\lambda_p; \qquad \xi_2 \ge 7 \tag{3.11}$$

$$\eta_2 = \alpha\left(1.1 - 0.016\lambda_p\right)\eta_2^*; \qquad \eta_2 \ge 0.2 \tag{3.12}$$

where, η^*_2 is the non-dimensional piecewise stress corresponding to the ξ_2 . The value of α is a softening coefficient and depends on the strain hardening of reinforcement. Dhakal and Maekawa found that for elastic-perfectly plastic reinforcement α=*0.75* and for reinforcement with linear hardening α=*1.0*. The detailed description on the derivation of Eq. (3.11) and (3.12) is available in Dhakal and Maekawa (200a,b). Further detailed discussion regarding the calculation of the effective buckling length of bars to be considered in the model is also available in a companion paper by Dhakal and Maekawa (2002c). The detailed discussion about calculation of the effective buckling length of vertical bars in RC columns is available in Chapter 5 of this thesis.

The reinforcing bars used in this experiment were high strength reinforcing bars without a yield plateau. As explained previously, these bars have a smooth transition from linear elastic to the post-yield buckling softening branch. Accordingly, the tension model for high-strength steel developed by Balan et al. (1998) is used here as tension envelope. This

model is a bilinear continuous function based on two asymptotes that intersect at point (1,1) with a smooth transition from linear elastic to a strain hardening region in tension. This model provides a smooth transition from linear elastic to post-yield softening branch after buckling which agrees with the experimental responses.

The proposed buckling model has been verified by comparing the analytical response with the experimental results from the uncorroded reinforcing bars. Fig. 3.15 (a-d) shows the qualitative comparison of analytical buckling model and the experimental response together with the experimental tension envelope. It was found that the value of α=1.0 for bars with L/D<10 and α=0.75 for bars with L/D≥10 gives a good qualitative fit to the experimental results.

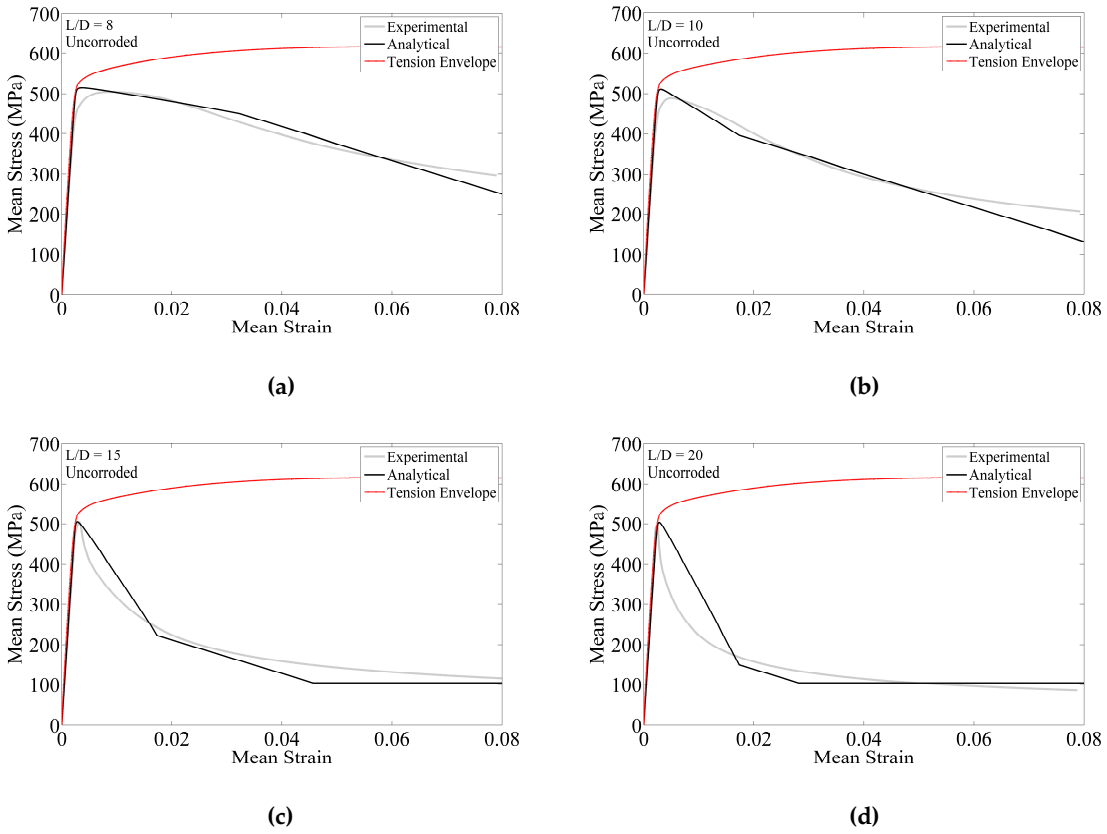

Fig. 3.15 Comparison of Dhakal-Maekawa model with the experimental results of uncorroded bars with different slenderness ratios

3.6.1 Modelling the effect of corrosion

As noted previously, the governing parameters of the buckling model are the L/D ratio and the yield stress σ_y. The analytical model assumes that the bar in compression first yields and then starts buckling which agrees with results of this experiment and results recorded by other researchers (Monti and Nuti 1992, Rodriguez et al. 1999, Dhakal and Maekawa 2002a, Bae et al. 2005 and Cosenza and Prota 2006). In order to extend the

Dhakal-Maekawa buckling model to include the effect of corrosion, the yield stress in compression and the non-dimensional bar buckling parameter λ_p are modified as below:

$$\lambda'_p = \sqrt{\frac{\sigma'_{yc}}{100}} \frac{L}{D_{corr}} \tag{3.13}$$

$$\sigma'_{yc} = \sigma_y(1 - \beta\psi) \tag{3.14}$$

where, λ'_p is the non-dimensional bar buckling parameter of corroded bars, σ'_{yc} is the yield stress of corroded bars in compression according to the regression analysis of the physical test data shown in Eq. (3.8). The regression coefficients considered are β=0.005 for $L/D \leq 5$, β=0.0065 for $5 < L/D \leq 10$ and β=0.0125 for $L/D > 10$. To include the effect of corrosion on the geometrical slenderness ratio of the corroded bars the L/D of the uncorroded bars is replaced with L/D_{corr} where, D_{corr} is defined in Eq. (3.4). ψ is defined in section 3.5.1.3.

Fig. 3.16 (a-h) shows examples of the corrosion extended Dhakal-Maekawa model compared to the test results for corroded bars with different percentages of mass loss and slenderness ratios.

It is clear from the qualitative comparison of analytical and experimental responses in Fig. 3.16 that the proposed corrosion extended Dhakal-Maekawa analytical model is able to model the average post-yield buckling behaviour of corroded bars. However, it was found that in some cases the value of η_2 underestimates the stress at ξ_2 by approximately 5% to 10%. This requires further experimental research and numerical modelling effort for further model calibration. Nevertheless, given the paucity of available experimental data and analytical models in the literature, this model is currently the only available analytical model which is able to predict the post-yield buckling behaviour of corroded reinforcing bars.

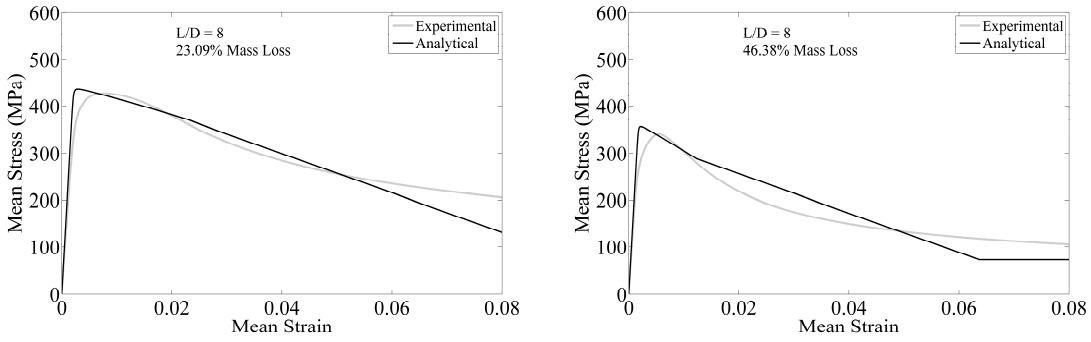

(a) **(b)**

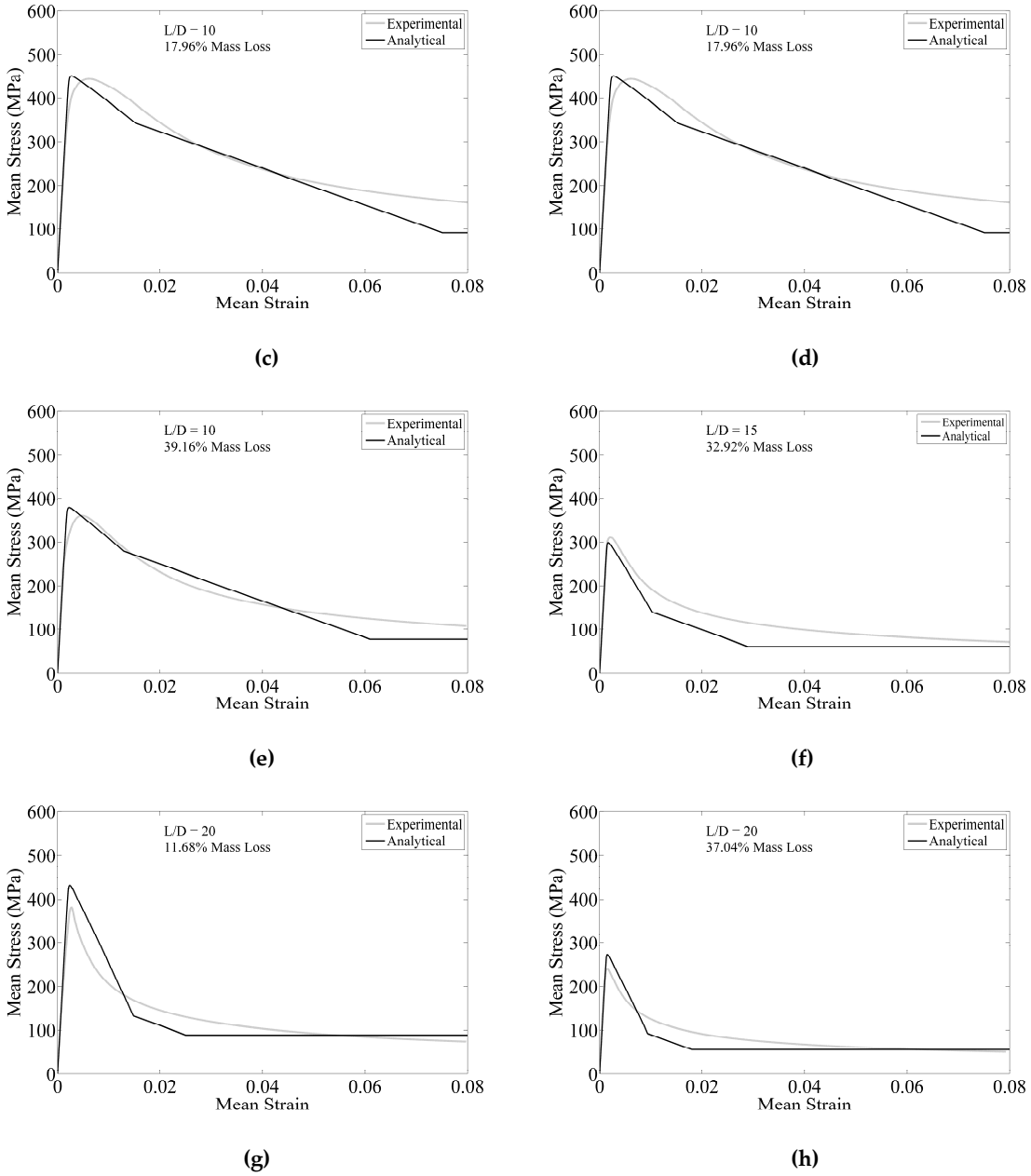

Fig. 3.16 Comparison of the corrosion extended Dhakal-Maekawa analytical buckling model and the experimental results

3.7 Cyclic test setup and loading protocol

A 250kN universal testing machine with hydraulic grips was used for the cyclic testing of the reinforcing bars. The machine used an integral Linear Variable Displacement Transducer (LVDT) to measure the displacement of the grips. A 50mm extensometer with a maximum stroke of ±5mm was used to measure the average axial strain in the reinforcement over the linear range. An additional external LVDT with maximum stroke of ±10mm was connected to the grips to measure the displacement over the entire length of the bar. As the extensometer could not capture the post buckling behaviour, the data

from the external LVDT has been used throughout this thesis to provide an average strain over the entire length of the bar throughout the test. A two cycle reversed symmetrical strain history was used in these experiments. This loading protocol was similar to the strain histories used by Rodriguez et al. (1999) but had a higher strain demand in compression and incorporated additional cycles at small strain demand levels. The additional small strain cycles were added because it was expected that heavily corroded bars might fracture at significantly lower strain levels compared to the corresponding uncorroded or lightly corroded bars. The machine was set to displacement control with a constant strain rate of 0.0003strain/sec. The cyclic loading protocol is shown in Fig. 3.17.

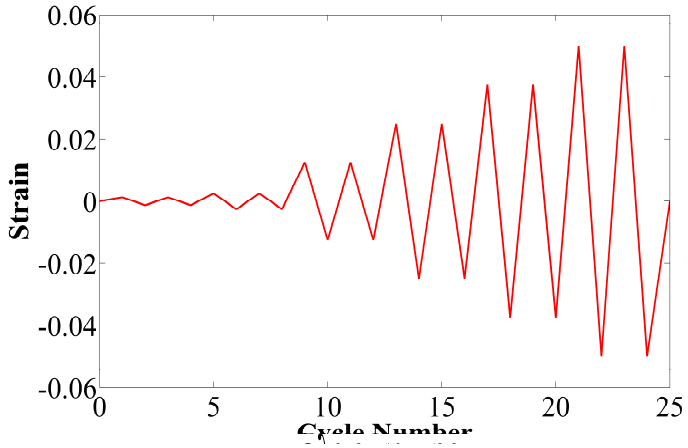

Fig. 3.17 Cyclic loading protocol

A total of 40 cyclic tests were carried out on corroded bars with different effective lengths. The slenderness ratios for the experiment were chosen based on the ratios of horizontal tie spacing in the common types of construction of RC columns (L) to bar diameter (D) known as the L/D ratio. The L/D ratios tested in this experiment were 5, 10, and 15. Three control (uncorroded) specimens were also tested for each slenderness ratio.

3.7.1 Experimental results and discussion

3.7.1.1 Qualitative summary of the experimental results of uncorroded bars

Typical stress-strain responses for the uncorroded reinforcement are shown in Fig. 3.18 (a-c). It should be noted that tension is positive and compression is negative in all the graphs presented in this chapter. As expected no buckling was observed for the reinforcement with L/D = 5. The stress-strain response was symmetrical in tension and compression and the tension envelope under cyclic loading is similar to the monotonic tension test envelope. When the strain demand increased beyond the yield strain the

Bauschinger effect (Bauschinger 1887) with kinematic hardening was observed. The second cycle at each strain demand level did not result in a significant cyclic degradation and the response was almost identical to the first cycle and to the monotonic envelope.

However for bars with L/D = 10 and 15, significant changes in the hysteresis curves were observed due to the effect of buckling. Two types of behaviour were observed in compression. At small strain demands the reloading branch after buckling was convex in shape. However as strain demand increased a complex pinching effect was seen in the hysteresis response of these bars. Similar behaviour was observed by Higai et al. (2006). The observed buckling stresses for the reinforcement in these cyclic tests were smaller than the buckling stresses observed during equivalent monotonic compression tests. This reduction is due to the effect of the tension strain history in the previous half cycle and the Bauschinger effect as shown in Fig. 3.18. This phenomenon has been reported by other researchers who carried out cyclic tests on single reinforcement bars (Higai et al. 2006) and in tests measuring the strain in reinforcement during cyclic reaction wall tests on RC bridge piers (Moyer and Kowalsky 2003). The hysteresis responses of reinforcing bars with L/D = 10 and 15 are more similar to the responses of slender beam-column elements (e.g. steel braces) than to typical material tests. This change in the response is due to the effects of the large displacement and geometrical nonlinearity. In addition, the second repeating cycle caused a reduction in the buckling stress and the corresponding tensile stress at the peak strain demand in tension. This is due to the effect of inelastic buckling that produces a residual plastic deformation in the bar. As a result, the tension stress does not completely straighten the bar in the second cycle and the buckling capacity reduces due to the effect of this residual imperfection. Crack initiation was observed on the inner side (compression face) of the buckled uncorroded bars due to low-cycle high amplitude fatigue as shown in Fig. 3.18 (d). This is because the local strain amplitude of the extreme fibre on the compression face is larger than in tension fibre which agrees with the results that reported by Higai et al (2006). The crack widths observed in bars with L/D = 10 and 15 were larger than in bars with L/D = 5. This is due to the effect of large deformations and second order effects in the longer bars that locally increased the compressive strain.

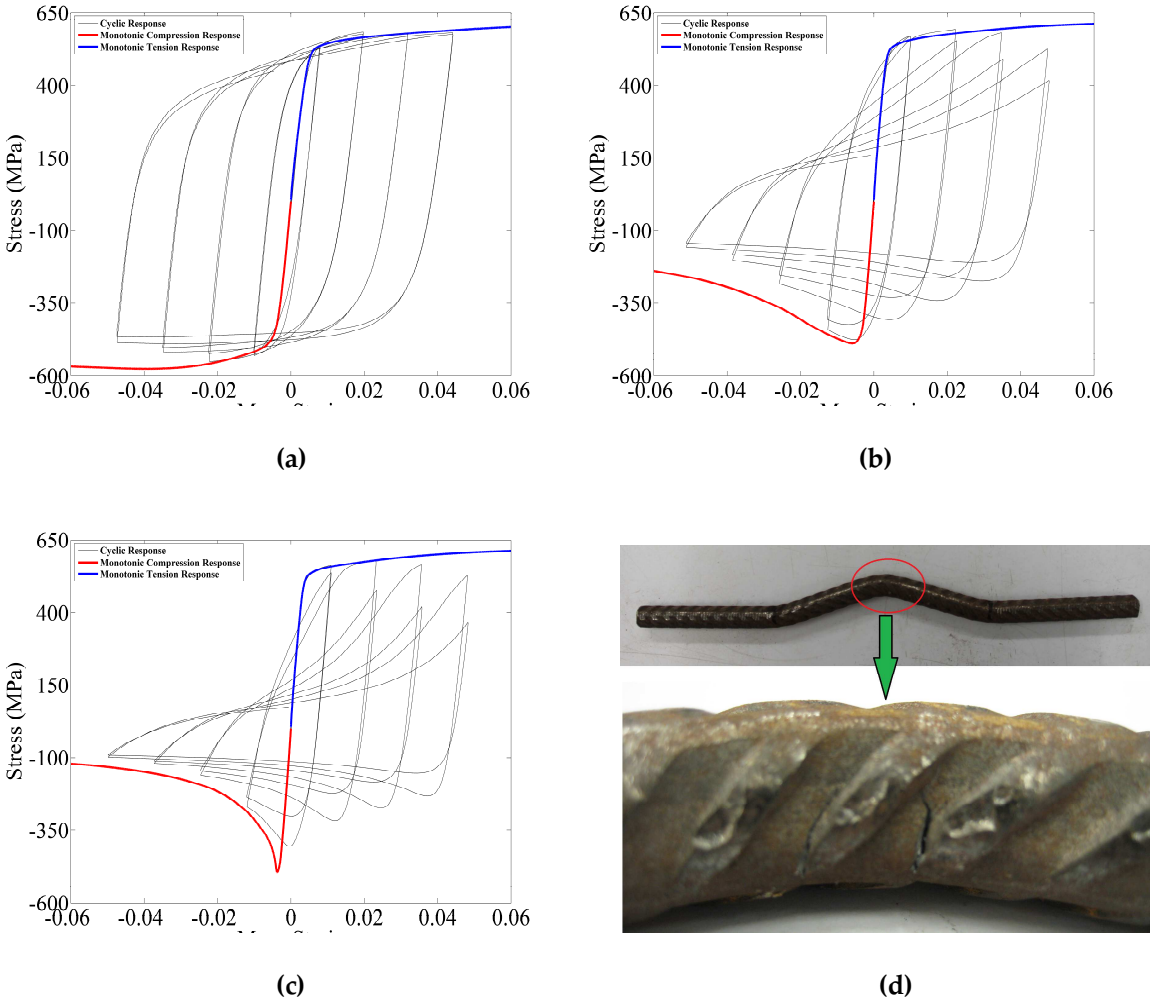

Fig. 3.18 Hysteresis response of uncorroded reinforcing steel bars: (a) L/D = 5, (b) L/D = 10, (c) L/D = 15, and (d) crack propagation in a bar with L/D = 10

3.7.1.2 Influence of non-uniform pitting corrosion on the buckling behaviour of corroded bars under cyclic loading

In the monotonic compression tests (discussed in Section 3.5.1.2) on corroded bars different buckling collapse mechanisms were observed. In general the buckling behaviour of corroded bars was governed by the variation of pitting corrosion along the bar which directly affected the plastic hinging mechanism. A similar behaviour was observed in these cyclic tests, but, due to the effect of the previous strain history and premature yielding of the corroded bars in tension, lower buckling capacity was observed compared to the monotonic tests. A comparison between the hysteresis response of corroded and uncorroded bars with L/D = 10 and 15 is shown in Fig. 3.19. The calculated stress in Fig. 3.19 is based on the original diameter of the uncorroded reinforcement and no adjustment to the diameter of corroded bars has been made, therefore it is called Notional Stress.

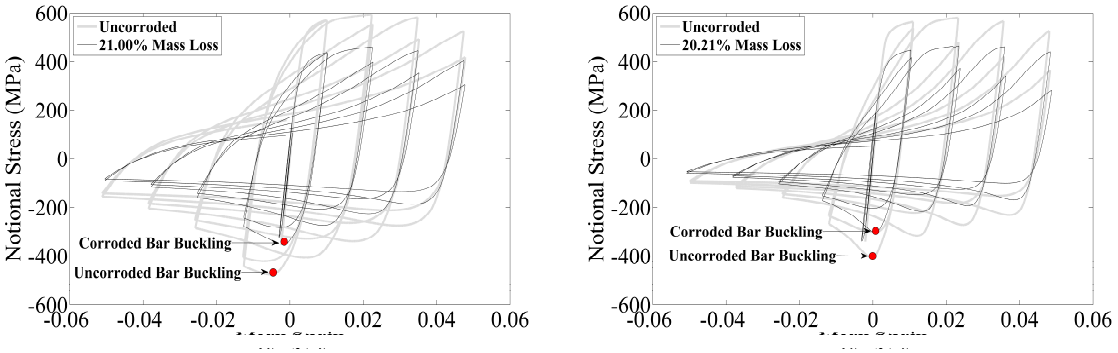

(a) **(b)**

Fig. 3.19 Significance of corrosion on buckling behaviour of reinforcing bars: (a) *L*/*D* =10, and (b) *L*/*D* =15

It was also observed that the Bauschinger effect (Bauschinger 1887) in the corroded bars starts at smaller strain demands compared to corresponding uncorroded bars. This is because the non-uniform corrosion along the bar and premature local yielding of the weak sections changes the response of the corroded bars in tension (Du et al. 2005a, Cairns et al. 2005, Apostolopoulos 2006).

The non-uniform corrosion along the bar produces imperfections in the bar which will result in stress concentration and increases the stress amplitude at the pit locations due to load eccentricity and the reduced section. In addition, pitting corrosion creates an irregular cross sectional shape for the corroded bars. This creates varying strong and weak bending axes along the bar which directly affects the buckling behaviour of corroded bars. As a result, corrosion significantly reduces the buckling capacity of corroded bars. This variation in the cross section shape is shown in Fig. 3.20 where a corroded bar with 27.13% mass loss and *L*/*D* = 10 has been cut into five slices after cyclic tests. The location and the minimum diameter of each sliced section are also shown in Fig. 3.20.

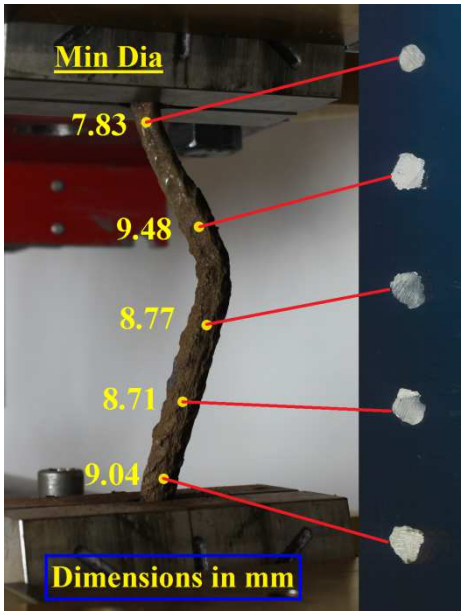

Fig. 3.20 shows that premature yielding in tension and plastic hinging in compression of the section with smallest diameter (7.83mm) at the top resulted in a change in the buckling mechanism of the bar (unsymmetrical buckling). This behaviour is in good agreement with the observed buckling mechanisms in the monotonic tests.

3.7.1.3 Effect of corrosion on the fracture mechanism of corroded bars in tension

As might be expected, corrosion significantly reduced the ductility of the bars in tension. In the cyclic tests the hysteresis cycles for the corroded bars were degraded because of the loss of cross section. Fig. 3.21 (a-c) compares the stress-strain curves for corroded bars (with different levels of corrosion and slenderness ratios) to the corresponding uncorroded bars. As seen in Fig. 3.21 localised pitting corrosion resulted in fracture of these bars in tension. A summary of all the observed 39 experimental tests are tabulated in Tables 3.5 to 3.7 which include the 13 bars that failed in tension along with the number of cycles before their failure.

In general, it was observed that for bars with higher slenderness ratios the amount of corrosion needed to cause tension fracture reduced. However where corrosion was particularly uniform along the bars they did not fracture in tension under the applied loading regime. The combined effect of the unsymmetrical plastic hinging mechanism and geometrical nonlinearity increased the stress amplitude at the location where the bar cross section was smallest. As a result, the heavily corroded bars started fracturing in tension at the plastic hinge location where they had buckled significantly in the previous compression strain cycle. Fig. 3.21 (d) shows the fracture mechanism for a heavily corroded bar along with the observed hysteresis response in Fig. 3.21 (c).

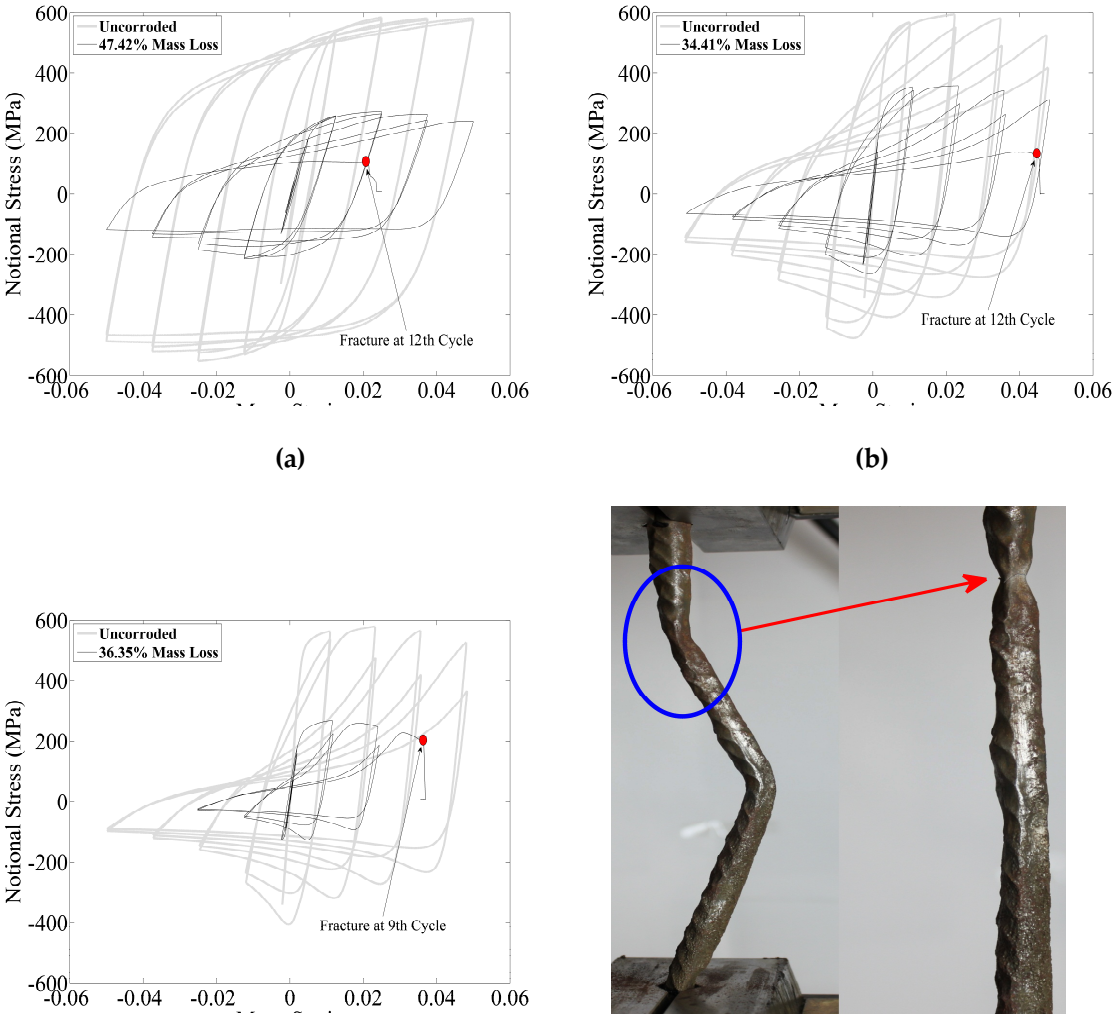

Fig. 3.21 Effect of corrosion on fracture of bars in tension: (a) L/D = 5, (b) L/D = 10, (c) L/D = 15, and (d) fracture of corroded bar in (c) at the pitting location after buckling in the previous compression strain history cycle

Table 3.5 Summary of the experimental results (L/D = 5)

Specimen ID	Mass Loss (%)	Average Diameter (mm)	Max Tensile Force (kN)	Max Tensile Stress (MPa)		Max Compressive Force (kN)	Max Compressive Stress (MPa)		Cycle Number at Fracture	Normalised Energy Dissipated (E_t/E_y)*
				Notional	Mean		Notional	Mean		
Control	0.00	12.00	66.43	587.35	587.35	63.08	557.75	557.75	NA	32.89
5-1	10.36	11.36	61.66	545.23	608.24	57.35	507.07	565.67	NA	30.80
5-7	12.94	11.20	54.76	484.20	556.17	51.88	458.68	526.86	NA	28.12
5-17	13.67	11.15	57.57	509.00	589.60	50.54	446.87	517.63	NA	28.62
5-6	14.64	11.09	55.38	489.71	573.69	48.91	432.46	506.63	NA	26.18
5-4	16.43	10.97	53.71	474.87	568.23	49.55	438.09	524.21	NA	27.06
5-19	17.34	10.91	51.90	458.86	555.12	48.43	428.22	518.05	NA	24.96
5-8	17.89	10.87	54.93	485.65	591.46	48.45	428.44	521.78	NA	24.96
5-2	20.46	10.70	50.51	446.57	561.44	44.86	396.62	498.65	NA	25.01
5-13	21.03	10.66	25.20	222.82	282.16	20.64	182.53	231.14	10	6.00
5-15	27.43	10.22	45.11	398.88	549.65	40.09	354.49	488.48	NA	20.31
5-12	31.12	9.96	25.82	228.33	331.49	29.88	264.18	383.53	8	4.15
5-3	31.42	9.94	7.99	70.62	102.97	6.55	57.93	84.47	7	0.58
5-11	32.35	9.87	40.45	357.69	528.74	33.86	299.35	442.50	NA	16.44
5-20	40.75	9.24	32.98	291.64	492.21	27.19	240.42	405.78	NA	11.80
5-5	42.05	9.13	35.72	315.86	545.06	31.89	282.01	486.64	NA	13.61
5-9	47.42	8.70	30.67	271.21	515.80	24.29	214.78	408.48	12	9.71

* E_t is based on the original bar diameter.

Table 3.6 Summary of the experimental results (L/D = 10)

Specimen ID	Mass Loss (%)	Average Diameter (mm)	Max Tensile Force (kN)	Max Tensile Stress (MPa)		Max Compressive Force (kN)	Max Compressive Stress (MPa)		Cycle Number at Fracture	Normalised Energy Dissipated (E_t/E_y)*
				Notional	Mean		Notional	Mean		
Control	0.00	12.00	66.95	591.99	591.99	54.61	482.86	482.86	NA	21.95
10-5	8.59	11.47	60.90	538.44	589.04	48.87	432.09	472.69	NA	18.58
10-4	10.40	11.36	61.27	541.74	604.63	46.05	407.20	454.47	NA	18.12
10-17	16.27	10.98	53.65	474.39	566.58	41.97	371.09	443.19	NA	14.88
10-16	16.42	10.97	51.21	452.80	541.76	39.66	350.64	419.52	NA	13.59
10-6	16.59	10.96	53.14	469.86	563.32	39.37	348.10	417.34	NA	14.62
10-11	21.00	10.67	51.85	458.48	580.35	40.14	354.90	449.24	NA	13.82
10-2	21.01	10.67	50.13	443.22	561.10	36.39	321.74	407.32	NA	13.86
10-18	21.49	10.65	52.67	465.67	591.63	41.13	363.63	461.98	NA	12.69
10-10	22.22	10.58	48.06	424.90	546.29	35.69	315.59	405.75	NA	12.08
10-19	22.30	10.58	47.56	420.53	541.22	35.55	314.36	404.58	12	10.98
10-16	23.36	10.51	50.76	448.80	585.60	37.91	335.17	437.34	12	11.70
10-1	24.65	10.42	48.31	427.12	566.84	33.62	297.23	394.47	12	11.53
10-13	26.88	10.26	46.43	410.55	561.48	33.47	295.93	404.72	13	10.76
10-8	27.13	10.24	38.33	338.88	465.05	29.65	262.13	359.72	NA	9.54
10-12	34.41	9.73	40.51	358.20	545.28	29.76	263.10	400.52	12	9.13
10-9	36.31	9.72	7.46	65.98	103.60	6.27	55.43	87.03	6	0.26

* E_t is based on the original bar diameter.

Table 3.7 Summary of the experimental results (L/D = 15)

Specimen ID	Mass Loss (%)	Average Diameter (mm)	Max Tensile Force (kN)	Max Tensile Stress (MPa)		Max Compressive Force (kN)	Max Compressive Stress (MPa)		Cycle Number at Fracture	Normalised Energy Dissipated (E_t/E_y)*
				Notional	Mean		Notional	Mean		
Control	0.00	12.00	65.57	579.77	579.77	45.89	405.77	405.77	NA	14.13
15-1	10.07	11.38	57.15	505.36	561.94	43.74	386.73	430.04	NA	12.34
15-6	20.21	10.72	52.30	462.44	579.57	38.55	340.85	427.18	NA	10.50
15-4	24.24	10.44	49.19	434.94	574.10	29.07	257.01	339.25	NA	8.47
15-2	24.33	10.44	48.95	432.83	572.00	34.26	302.96	400.36	NA	8.56
15-3	25.12	10.38	46.23	408.80	545.94	31.99	282.82	377.70	12	7.06
15-7	28.43	10.15	45.48	402.15	561.89	29.08	257.16	359.31	10	4.57
15-5	36.35	9.57	30.29	267.81	420.76	14.31	126.49	198.73	9	2.24

* E_t is based on the original bar diameter.

3.7.1.4 Effect of corrosion on slenderness ratio, hysteresis cycles and energy dissipation

As previously shown in Fig. 3.19 and Fig. 3.21 the slenderness ratio has a significant effect on the hysteresis response of reinforcing bars. A pinching effect was seen in the stress-strain graphs of bars with *L*/*D* = 10 and 15 which was the result of geometrical nonlinearity due to buckling. As the level of corrosion increased, the pinching effect in corroded bars also increased. This effect results in significant reductions in the areas of the hysteresis curves and subsequently a reduction in energy dissipation capacity. The corrosion can also lead to premature fracture of bars in tension as shown previously in Fig. 3.21.

The total hysteretic energy dissipated in the cyclic tests (E_t) has been calculated using Green's theorem and normalised to the yield/elastic energy (E_y) of the tension envelope (the area under the linear branch of stress-strain curve). Using Green's theorem, the area of the region *D* bound by a piecewise smooth closed curve *C* can be estimated. In this case, the region *D* is the hysteretic area bound by cyclic stress-strain curve as per Eq. (3.15) and (3.16) below:

$$E_t = \iint_D dA = \tfrac{1}{2}\oint_C \left(-\sigma\, d\varepsilon + \varepsilon\, d\sigma\right) \tag{3.15}$$

$$E_y = \tfrac{1}{2}\int_0^{\varepsilon_y} \sigma\, d\varepsilon = \tfrac{1}{2}\sigma_y\, \varepsilon_y \tag{3.16}$$

where, σ is the stress, ε is the strain and σ_y and ε_y are the yield stress and strain respectively. The influence of corrosion on energy dissipation capacity of corroded bars is shown in Fig. 3.22. For instance, considering the average reduced cross section area, 20% mass loss results in 30%, 34% and 36% reduction in the total energy dissipation capacity of bars with *L*/*D* = 5, 10 and 15 respectively. It should be noted that there were three corroded bars with severe localised pitting corrosion in the group of bars with *L*/*D* = 5. These bars had a premature fracture in tension; therefore they were considered as outliers and were not included in the best fit of energy loss calculation.

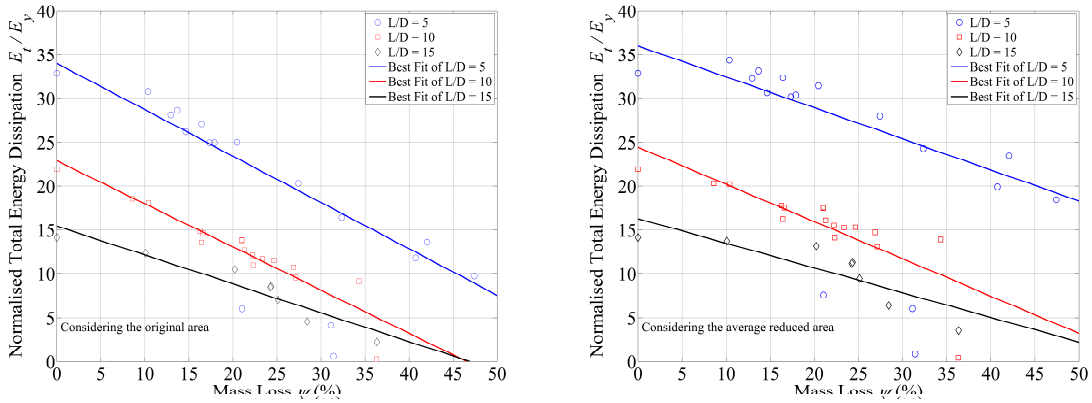

(a) **(b)**

Fig. 3.22 Reduction of total energy dissipation capacity of corroded bars: (a) considering the original cross section area (b) considering the averaged reduced cross section area

The uncorroded bars with L/D = 5 displayed a symmetric hysteresis response with a kinematic hardening. As the level of corrosion increased the hysteresis response of this group of bars showed a pinching effect similar to the bars with higher slenderness ratios. In other words, corrosion increases the effective slenderness ratio of the bars. As a result the heavily corroded bars with L/D = 5 buckled and geometrical nonlinearity resulted in a significant change to their hysteresis response.

An example of the hysteresis response of a corroded bar with L/D = 5 and 40% mass loss and the corresponding uncorroded test specimen response is shown in Fig. 3.23 (a). The deformed shapes for these bars, at the end of the cyclic tests, are shown in Fig. 3.23 (b, c). Although the bar with a 40% mass loss did not fracture in tension the corrosion significantly changed the cyclic hysteresis response.

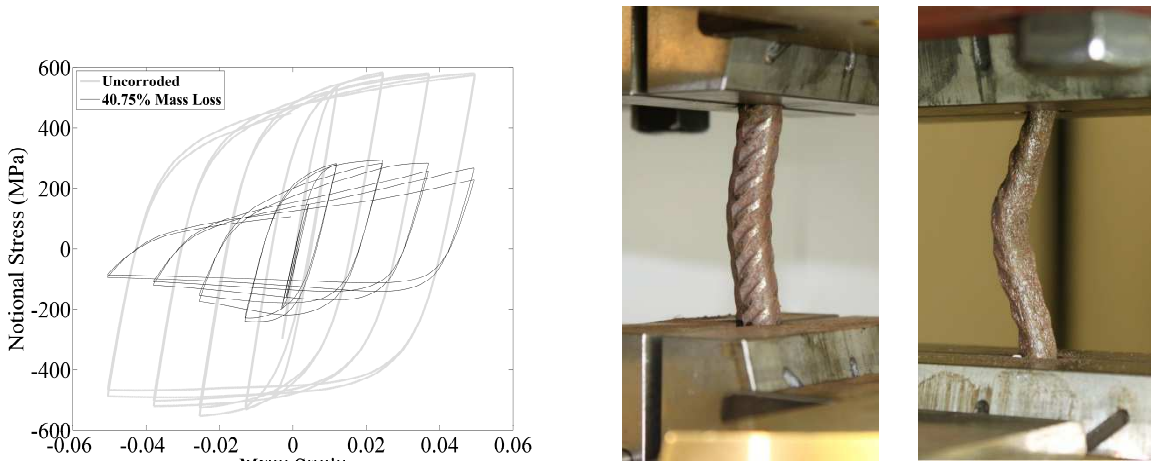

(a) **(b)** **(c)**

Fig. 3.23 Effect of corrosion on hysteresis response of corroded bars: (a) example response of bars with L/D =5; deformed shape of the bars (b) uncorroded and (c) corroded bar shown in (a) at the end of cyclic test

Furthermore, Fig. 3.24 shows the normalised (normalised to E_y) accumulated hysteretic energy versus the number of half-cycles for bars with different mass loss and slenderness ratios. Fig. 3.24 (a) shows the influence of slenderness ratio on accumulated energy dissipation of uncorroded bars and Fig. 3.24 (b-d) shows the influence of corrosion on accumulated energy dissipation of corroded bars with different slenderness ratios. Comparison of Fig 3.24 (a) and (b) shows that about 35% mass loss of a corroded bar with L/D = 5 will result in a similar accumulated energy dissipation trend to an uncorroded bar with L/D = 15. Similarly, comparison of Fig. 3.24 (c) and (d) shows that a corroded bar (originally L/D = 10) with a 16% mass loss has a similar accumulated energy dissipation trend to an uncorroded bar with L/D =15.

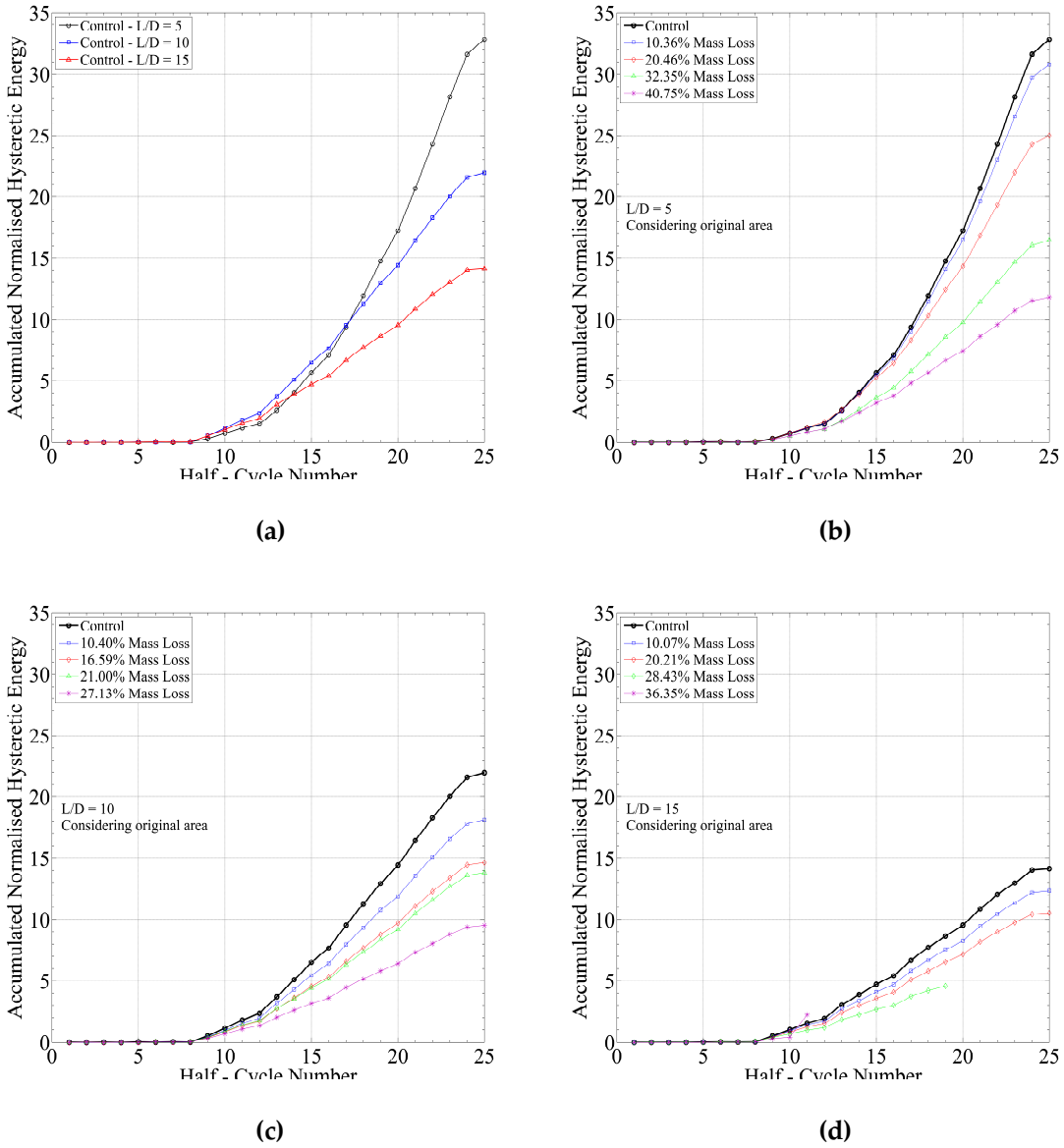

Fig. 3. 24 Accumulated normalised hysteretic energy dissipation of reinforcing bars: (a) uncorroded bars, (b) corroded bars with L/D = 5, (c) corroded bars with L/D = 10 and (d) corroded bars with L/D = 15

As discussed above, the localised pitting corrosion has a significant effect on premature fracture of bars in tension and subsequently reduces the hysteresis area. This effect was more significant in the group of bars with higher slenderness ratios (i.e. Fig. 3.24 (d) corroded bars with mass loss of 28.43% and 36.35%). Although more uniform corrosion is less likely to result in fracture of bars in tension, it still has a considerable effect on the shape of hysteresis cycles because the slenderness ratio of the bars effectively changes and therefore buckling is more likely.

Based on the results of the recent experimental studies on the cyclic behaviour of corroded beams and columns (Ou et al. 2011, Akiyama et al. 2011 and Ma et al. 2012) there is evidence that the buckling and/or fracture of corroded bars has a significant effect on the global response, plastic rotation capacity and plastic hinging mechanisms of the corroded RC elements. As a result, in the seismic assessment and evaluation of existing corroded structures, consideration needs to be given to the buckling of bars even if the structure is originally designed to have sufficient level of confinement and anti-buckling reinforcement.

3.7.2 Modelling low-cycle high amplitude fatigue degradation

As shown in the previous section, the combined effect of pitting corrosion and low-cycle high-amplitude fatigue resulted in a stress degradation of the reinforcement in tension. The stress degradation of uncorroded reinforcing steel bars due to low-cycle high amplitude fatigue has been investigated experimentally by several researchers (Higai et al. 2006, Moyer MJ and Kowalsky 2003, Mander et al. 1994, Brown and Kunnath 2004). In previous studies the well-known Coffin-Manson (Manson 1965) fatigue strain life model (Eq. (3.17)) is used to predict the bar fracture strain in tension.

$$\varepsilon_p = \Theta_f \left(2N_f\right)^{-\alpha} \tag{3.17}$$

where, ε_p is the plastic strain amplitude ($\varepsilon_p = \varepsilon_a - \varepsilon_e$ where, ε_a is the total strain amplitude and ε_e is the elastic strain), $2N_f$ is the number of half-cycles to failure and α and Θ_f are material constants (further detail is available in Kunnath et al. (2009) and Brown and Kunnath (2004)). Brown and Kunnath (2004) conducted a comprehensive set of low-cycle high amplitude fatigue tests on reinforcing bars with constant amplitudes. They calibrated the material constants based on the regression analysis of the experimental data. The reported calibrated values of Θ_f and α are 0.12 and 0.44 respectively. Hawileh et al. (2010) conducted low-cycle high amplitude fatigue tests on B500 British Standard reinforcing bars and the reported values of Θ_f and α by Hawileh et al. are 0.219 and 0.54 respectively. Given the reinforcement used in this experiment are B500 British Standard reinforcement, the latter values have been used here.

The effect of strain history and varying strain amplitudes can be included using the linear cumulative damage hypothesis known as Miner's rule (Miner 1945). According to this rule, applying n_1 half cycles with a strain amplitude ε_1 and corresponding fatigue life of $2N_{f1}$, is equivalent to consuming $n_1/\ 2N_{f1}$ of the fatigue resistance. The same assumption applies to any subsequent block of load cycles. Accordingly, the cumulative low-cycle fatigue damage (Δ_f) can be estimated using the Eq. (3.18) as follows:

$$\Delta_f = \frac{1}{\sum_{i=1}^{n}\left(2N_f\right)_i} \tag{3.18}$$

where, $(2N_f)_i$ is the number of half cycles to failure at the plastic strain amplitude ε_p corresponding to cycle i. The value of Δ_f is 1.0 for an undamaged bar and is 0 for a bar at fracture. Kunnath et al. (2009) used the Coffin-Manson formulation to model stress degradation due to low-cycle fatigue. The stress loss at each cycle can be estimated using the Eq. (3.19) below:

$$\varepsilon_p = \Theta_d \left(\delta_{sr}\right)^{\beta} \tag{3.19}$$

where, Θ_d and β are the material constants (Θ_d=0.2, β=α) and δ_{sr} is the stress reduction factor corresponding to plastic strain amplitude at cycle i. Then the cumulative stress degradation factor χ_{sd} for any strain history (assuming a simplified linear relationship between δ_{sr} and number of cycles) can be calculated as follows:

$$\chi_{sd} = \sum_{i=1}^{n}\left(\delta_{sr}\right)_i = \zeta_d\, \Delta_f \tag{3.20}$$

where, ζ_d is the cumulative damage constant as below:

$$\zeta_d = \left(\frac{\Theta_f}{\Theta_d}\right)^{\frac{1}{\alpha}} \tag{3.21}$$

Further details and derivation of the above equations are available in Kunnath et al. (2009).

3.7.2.1 Modelling the influence of corrosion on fatigue degradation

In order to have a realistic prediction model two main features need to be considered. The first one is the influence of corrosion on the tension envelope of corroded bars in the absence of fatigue and the second is the influence of non-uniform pitting corrosion on the fatigue life of corroded bars. These issues are discussed in the following sections.

3.7.2.1.1 Modelling the influence of corrosion on the tension envelope

The effect of corrosion damage on the mechanical properties of reinforcing bars has been investigated by several researchers (Almusallam 2001, Du et al. 2005a,b, Cairns at al. 2005, Apostolopoulos et al. 2006 and Apostolopoulos 2007). Most have come to the conclusion that non-uniform pitting corrosion affects the average stress-strain response of corroded bars. More recently, Apostolopoulos et al. (2006) have investigated the influence of pitting depth on the mechanical properties of corroded bars. They concluded that stress concentrations at the pitting locations cause significant degradation in mechanical properties of corroded bars. Therefore, in the modelling of the cyclic behaviour of corroded bars consideration needs to be given to the modified tension envelope. Du et al. (2005a,b) provides a detailed description of the effect of corrosion damage on residual capacity of corroded bars in tension. They concluded that the effect of corrosion on tension stress-strain curve of corroded bars can be modelled by employing a pseudo stress-strain curve with modified yield stress (Fig. 3.25).

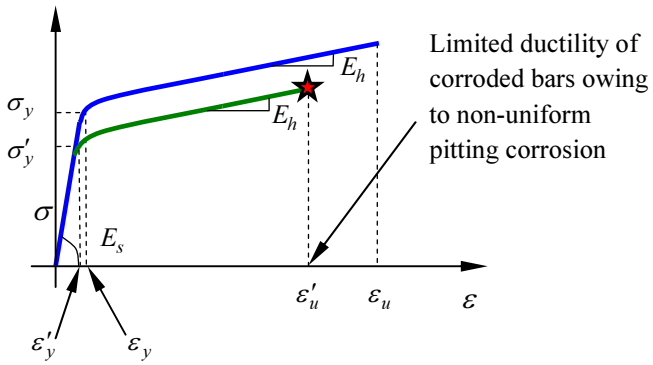

Fig. 3.25 Modified Pseudo stress-strain curve of corroded bars

The modified yield stress of the corroded reinforcement can be calculated using Eq. (3.22) below:

$$\sigma'_y = \sigma_y(1-\rho\psi) \tag{3.22}$$

where, σ'_y is the yield stress of corroded bar in tension, σ_y is the corresponding yield stress of the uncorroded bar and ψ is the percentage mass loss, $\psi = 100\gamma$, with γ taken from Eq. (3.3). The value of ρ is 0.015 for Notional Stress (stress based on original cross section area) and 0.005 for Mean Stress (stress based on average reduced cross section area) (Du et al. 2005a). The loss of cross section area due to corrosion is calculated using Eq. (3.4) as discussed in the previous sections.

3.7.2.1.2 Modelling the influence of corrosion on fatigue life

Apostolopoulos (2007) conducted a series of low-cycle fatigue tests on corroded bars with constant strain amplitudes. The experimental data reported in Apostolopoulos (2007), is used in this study to calibrate the effect of corrosion on the material constants Θ_f and α of the corroded bars. The total strain amplitudes reported are ±1%, ±2.5% and ±4% (further detail is available in Apostolopoulos (2007)). Based on the regression analysis of the reported data, it was found that the effect of corrosion on the material constant Θ_f is negligible. However, corrosion does change the material constant α. The relationship between percentage mass loss and the material constant α, based on the reported experimental data, is shown in Eq. (3.23) below ($R^2 = 0.62$):

$$\frac{\alpha_{corr}}{\alpha} = 1 + 0.004\psi \tag{3.23}$$

where, α_{corr} is the material constant of corroded bars and ψ is the percentage mass loss (ψ=100γ). Accordingly the value of α in Eq. (3.17) to Eq. (3.21) can be replaced with α_{corr} to account for non-uniform pitting on fatigue life. A schematic of the proposed corrosion extended Kunnath et al. (2009) cyclic degradation model for corroded bars is shown in Fig. 3.26.

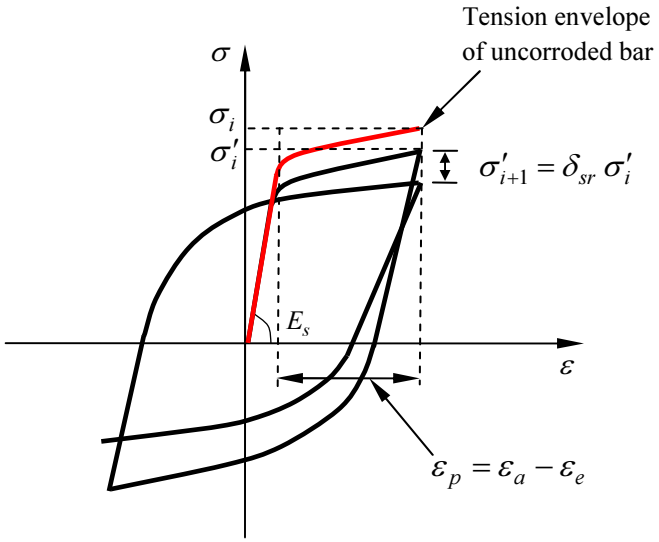

Fig. 3.26 Low-cycle high amplitude fatigue degradation model of corroded bars

The influence of buckling in the proposed model is included within the cumulative damage constant. This is done by modifying the material constant Θ_d in Eq. (3.19) based on a regression analysis of the experimental results. The calibration graphs are presented

in Fig. 3.27 and show the comparison of the proposed model with and the experimental results. Two levels of total strain amplitude (ε_a) of 0.025 and 0.0375 are considered. The influence of considering either the average reduced cross section area or the original cross section area is considered separately. The computed values in Fig 3.27 are the predicted stress values at ε_a and the experimental values are the corresponding observed tension stress at ε_a in cyclic tests. It should be noted that all the values in the Fig. 3.27 are normalised to the corresponding pricewise stress value on the tension envelope of uncorroded reinforcement at ε_a. The graphs presented in Fig. 3.27 are based on $\Theta_d = 0.6$.

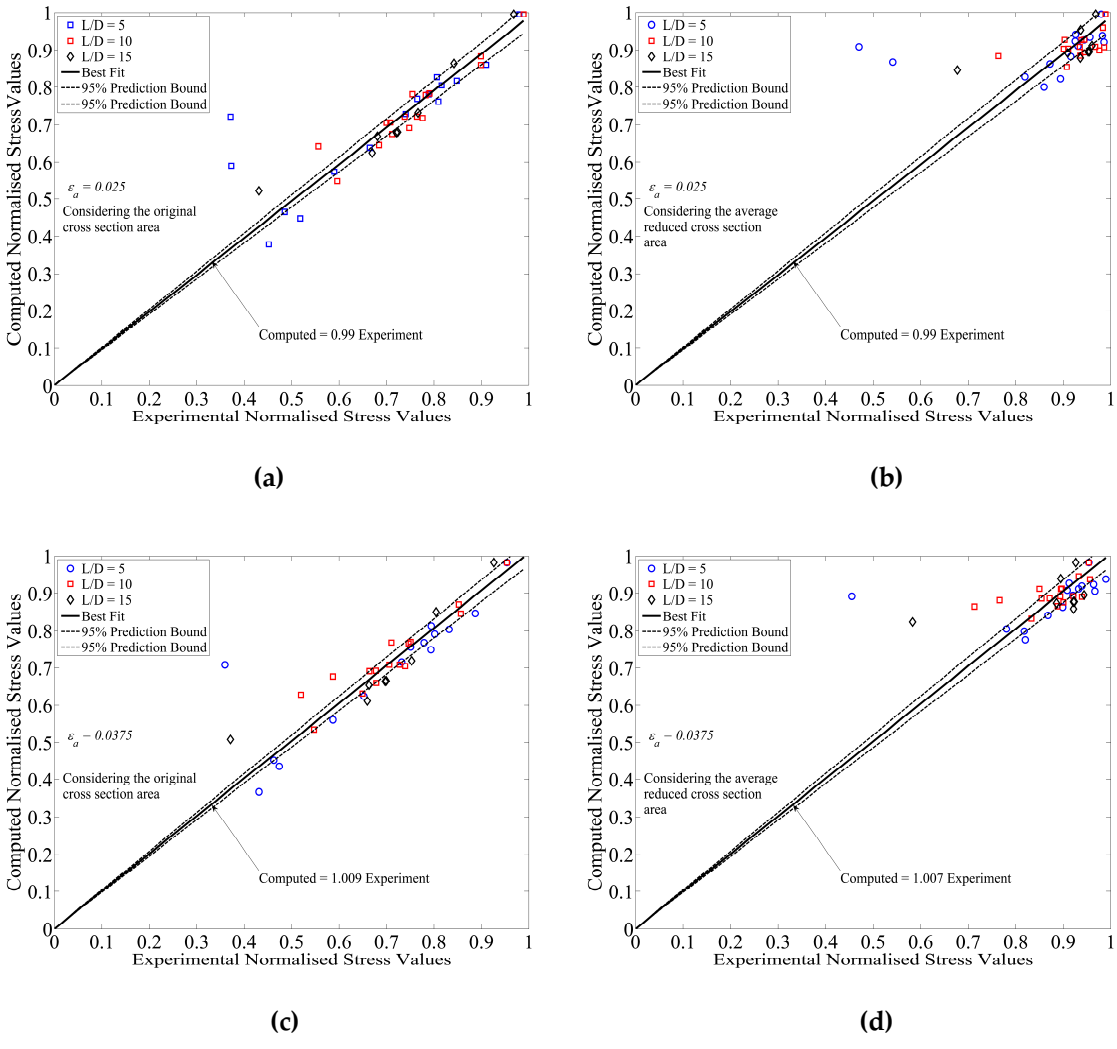

Fig. 3.27 Comparison of the proposed analytical fatigue degradation model with experimental results: (a) ε_a = 0.025, stress based on original area (b) ε_a = 0.025, stress based on average corroded area (c) ε_a = 0.0375, stress based on original area (d) ε_a = 0.0375, stress based on average corroded area

The reinforcing steel model developed by Kunnath et al. (2009) has already been incorporated into OpenSees (OpenSees 2012). This model consists of a low-cycle fatigue degradation model in tension and Dhakal-Maekawa buckling (Dhakal and Maekawa 2002a) in compression. It also includes the Giuffre–Menegotto–Pinto (GMP) (Menegotto

and Pinto 1973) cyclic rules to model the Bauschinger effect (Bauschinger 1887). The combined effect of low-cycle fatigue degradation and the buckling model developed in this chapter is used to modify the Kunnath et al. model in the OpenSees. A qualitative comparison between the experimental and simulated mean stress-strain response of a corroded bar with *L/D* = 5 and 10.36% mass loss is shown in Fig 3.28. The original GMP model with modified yield stress based on Eq. (3.22) without buckling and low-cycle fatigue is shown in Fig 3.28 (a) and the Kunnath et al. model including the corrosion extended inelastic buckling and low-cycle fatigue models is shown in Fig 3.28 (b).

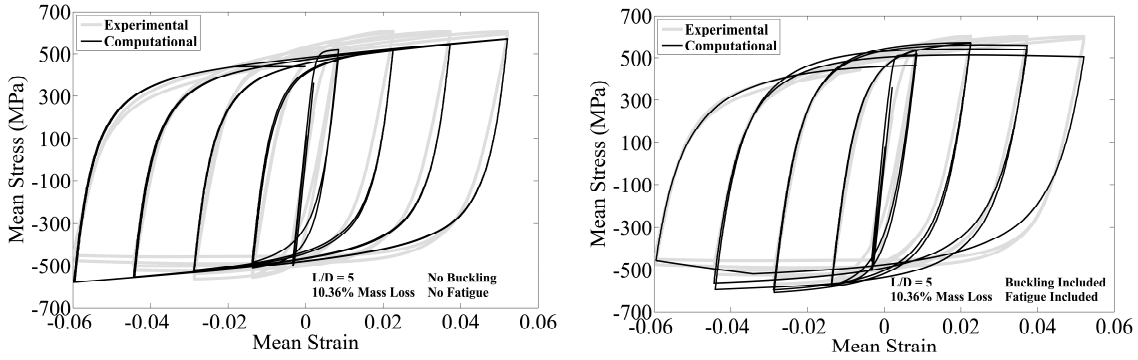

Fig. 3.28 Comparison of computed and experimentally observed response of a corroded: (a) GMP model (b) the corrosion extended Kunnath et al. model.

Figs. 3.27 and 3.28 show that the proposed corrosion extended analytical model developed in this chapter (Eq. (3.17) to (3.21)) is generally in good agreement with experimental results up to about 25% mass loss. However, when the mass loss exceeds about 25%, more disagreement is seen between the proposed model and the observed response. This is due to the combined effect of low-cycle fatigue in tension and inelastic buckling of bars in compression which increases the total strain amplitude at the maximum pit location. This problem is very important in seismic assessment of old RC bridges/structures where there is not enough anti-buckling reinforcement to tie the vertical bars. There is currently very limited experimental data available for calibration of the material constants accounting for the combined effect of low-cycle fatigue degradation and inelastic buckling. This is an area for further research and requires experimental investigation of the influence of localised pitting corrosion on low-cycle high amplitude fatigue of corroded bars with the effect of inelastic buckling.

3.8 Conclusions

The effects of corrosion on the stress-strain behaviour of reinforcing bars in tension, compression and cyclic loading have been studied experimentally. The parameters investigated in this study are the residual capacity of corroded bars in tension, the effect of corrosion on the buckling mechanism and the buckling capacity of corroded bars, and the effect of corrosion on the post-yield behaviour. A new constitutive material model for modelling the post-yield buckling response of corroded bars using Dhakal-Maekawa buckling model is also presented. Moreover, an analytical methodology for quantification of cyclic fatigue degradation of corroded bars is also proposed. The results of the analytical modelling show a good agreement with the data from the physical tests. The key outcomes of this chapter can be summarised as follows:

1. The results of this experiment showed that non-uniform pitting corrosion has a significant effect of the plastic deformation of corroded bars in tension. Based on these experiments a 20% mass loss would appear to result in approximately a 50% reduction in the total plastic deformation of the corroded bars in tension. This result agrees with the results observed by other researchers (Du et al. 2005b).
2. The inelastic buckling mechanism of bars is affected by non-uniform pitting corrosion. The observed buckling modes showed that the buckling mechanism of corroded bars is a function of the mass loss due to corrosion and the distribution of pits along the bar length.
3. It was found that the distribution of pits along the length of corroded bars is the most important parameter affecting the stress-strain response in both tension and compression. This is more critical in compression where any load eccentricity and imperfections have a significant influence on the buckling capacity of bars.
4. The results of the experiments showed good agreement with the proposed corrosion extended Dhakal-Maekawa buckling model. However, there is need for further research for more accurate estimation of the residual buckling capacity of corroded bars.
5. The proposed corrosion extended Dhakal-Maekawa buckling model can easily be incorporated into computer programmes for section analysis and nonlinear seismic analysis of corrosion damaged RC structures using a fibre-based section decomposition technique.
6. The hysteresis behaviour of bars with $L/D>10$ under high compression strain demand is similar to the behaviour of slender beam-column elements. This is due to the effects of large deformations and buckling. There is a need for further research to develop a phenomenological material model to capture this behaviour.
7. Low-cycle high amplitude fatigue results in a severe degradation to the tension envelope of corroded bars.

8. The buckling capacity of bars under cyclic loading is greatly influenced by the previous plastic strain history in tension. This phenomenon (for uncorroded reinforcement) has been reported by other researchers (Moyer and Kowalsky 2003). This is a particularly important parameter when the corroded bars have highly localised pitting corrosion. The experimental results from this study showed that corroded bars with pitting will fracture in tension after fewer cycles of stress reversal. This is due to the combined effect of low-cycle fatigue, premature yielding and inelastic buckling of bars at pitting locations.
9. The results from the corrosion extended Kunnath et al. material model generally showed good agreement with the experimental results up to about 25% mass loss. However, as the level of mass loss increased the localised pitting corrosion increased, therefore, the analytical model became less accurate. Nevertheless, the proposed model is currently the only available material model which is able to simulate the combined effect of inelastic buckling and low-cycle high amplitude fatigue degradation on nonlinear cyclic response of corroded reinforcing bars.

This page is intentionally left blank.

CHAPTER 4

Stochastic Corrosion Pattern Analysis and Finite Element Investigation

4.1. Introduction

The nonlinear stress-strain behaviour of corroded bars under monotonic tension, compression and cyclic loading with the effect of buckling was discussed in Chapter 3. It was found that failure and necking of a corroded bar in tension normally occurs at the location of the maximum pit (minimum cross section area). However, when corroded bars are subject to compression, where inelastic buckling is critical, the buckling mechanism is significantly affected by the distribution of pits along the bar. This is because the distribution of pitted areas along a corroded bar creates variable major and minor axes as well as load eccentricity which are challenging to quantify. Moreover, for inelastic buckling analysis other cross sectional properties of the corroded bars such as the minimum second moment of area and maximum load eccentricity are also required.

Previously, several researchers have investigated, both experimentally and analytically, the time and spatial variability of the maximum pitting depth of corroded reinforcing bars, prestressing wires and steel pipelines (Gonzalez et al. 1995, Darmawna and Stewart 2007, Caleyo et al. 2009, Kim 2009 and Darmawna 2010). The outcomes of these studies are a set of time-variant probabilistic distribution models of the maximum pitting depth. These models have made a major contribution towards the structural safety and reliability analysis of RC beams and slabs (Val and Melchers 1997, Darmawan and Stewart 2007, Stewart and Al-Harthy 2008, Stewart and Suo 2009 and Stewart 2009).

However, for capacity loss estimation of corrosion damaged columns subject to earthquakes i.e. bridge piers; buckling of vertical bars is one of the most important performance parameters that limit the plastic rotation capacity of columns. Therefore, there is a need for probabilistic models that can capture the time-dependent distribution of pitted areas along the length of corroded bars. This has a significant influence on the seismic reliability analysis of corroded RC structures. This chapter addresses these issues using a novel corrosion pattern analysis of corroded reinforcing bars. The corroded bar specimens were produced using an accelerated corrosion technique in the laboratory. Using an advanced 3D optical scanning technique the surface corrosion pattern of bars was then measured. Based on the statistical analysis of corrosion pattern data, a set of time-variant probabilistic models have been developed for the geometrical properties of corroded bars. These models are the input parameters of a probabilistic platform for future research in spatial-time-dependent seismic reliability analysis of deteriorating systems.

The influence of the pattern of corrosion along the length of a reinforcing bar on inelastic buckling and cyclic response in also explored. Data from a previously presented experimental study reported in Chapter 3 are reviewed with the objectives of establishing the response of corroded bars under monotonic and cyclic loading and characterising the pattern of corrosion along the length of the reinforcing bar. A computational model, employing co-rotational beam-column elements with fibre-type cross-section models and nonlinear material models, is proposed for simulating the response of a corroded reinforcing bar. The model is validated through comparison with experimental data. The model and experimental data are used to investigate the impact of the corrosion pattern on the buckling strength, tensile yield strength and cyclic response of a reinforcing bar. Finally, experimental data are used to evaluate existing one-dimensional constitutive models for reinforcing steel, which simulate compressive strength loss due to buckling and the impact of buckling and low-cycle fatigue on cyclic response.

4.2. Investigation of corrosion patterns using an advanced optical measurement technique

4.2.1. 3D optical measurement procedure

As mentioned in section 2.3, 23 corroded reinforcing bars were taken out of the total of 120 samples for more refined geometrical surface analysis of corrosion patterns. The reinforcing bars varied in length (from 220mm to 400mm) and had a range of mass loss ratios (8.93% to 55.94%).

The surface pitting pattern of the corroded bars was measured using a structured light scanner with 5.0 MP resolution. The accuracy of the measurement was set to 20μm which was the highest resolution for the instrument. Given the high accuracy of the measurement technique it was very sensitive to any vibration during the scanning process. Therefore, the corroded bars were securely fixed to a turntable to facilitate the scanning process. The direction and coordinate system of the measurement is shown in Fig. 4.1 This coordinate system has been used throughout this chapter for the analysis of the scanned data.

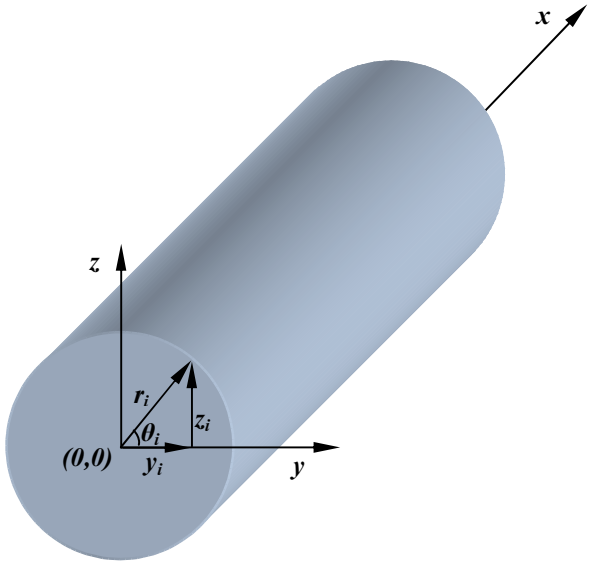

Fig. 4.1 Coordinate system of the 3D surface measurement

The outcome of the scanning process was a set of 3D solid models of the corroded bars that were identical to the real bars including the very fine details of pitting pattern. Fig. 4.2 (a-c) shows examples of the 3D solid elements created using the optical measurement data.

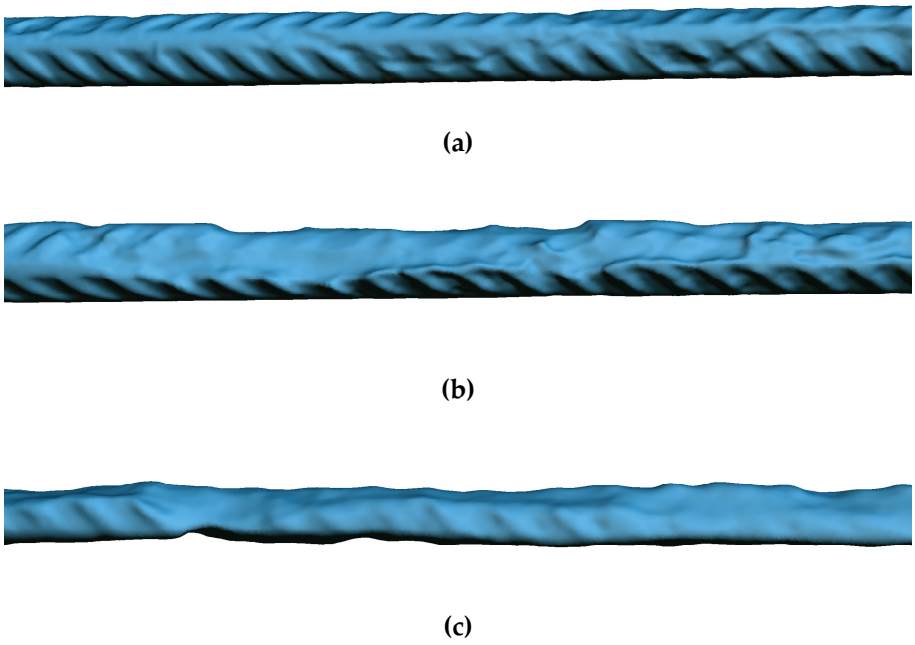

Fig. 4.2 Three solid models generated using 3D scans of corroded bars: (a) 10.37% average mass loss (b) 30.87% average mass loss (c) 55.94% average mass loss

The software associated with the scanner is capable of generating 3D meshes and generating cross sections and profiles through the solid element. For processing the data a 3D polygon mesh was generated for each solid element. In order to explore the corrosion patterns and distribution of pits, for each bar cross sections were taken through the 3D solid mesh at 0.5mm intervals along the whole length of the solid elements. The cross sections were transformed to data points (x, y, z coordinates) and each cross section included data points at 0.03mm intervals around the perimeter. The raw data points were then exported to MATLAB (MTLAB R2012b) for post-processing and data analysis. Fig. 4.3 shows an example of cross sections extracted from the 3D model.

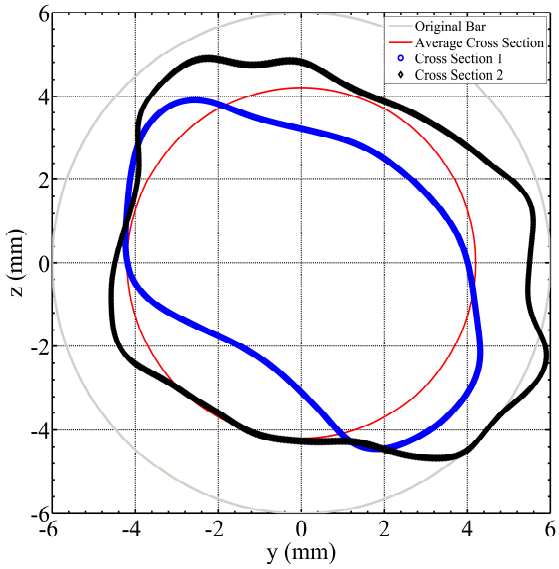

Fig. 4.3 Cross section of a corroded bar with 54.34% average mass loss taken from the 3D solid model

With reference to Fig. 4.3, the cross sections taken from two different locations along the same bar are different in shape and area. As expected, the change in the cross section shape and geometrical properties of the bar are not captured considering a uniform corrosion and an average reduced cross section area.

It should be pointed out that there is one section on the plot of Cross Section 2 in Fig. 4.3 which is larger than the nominal diameter of the original bar. This is due to the presence of ribs on the bar. This will influence the cross sectional area and geometrical properties of corroded bars taken from the scanned data. Therefore, the raw data needs some processing to filter out the influence of the ribs. This is discussed in detail in section 4.3 of this chapter.

To better understand the corrosion patterns, the cross section of the bars can be unwrapped ($-\pi \leq \theta \leq \pi$) and the data presented in the format of r and θ in polar coordinates (Fig. 4.4). This also helps with investigating the influence of ribs on the corrosion patterns. Fig. 4.4 (a) shows a typical 3D surface plot of an unwrapped cross section of a corroded bar and Fig. 4.4 (b) shows the contour plot of the same bar. The contour plot is a topographical map of the corrosion pattern over the entire length of the bar. A localised pitting corrosion pattern and the ribs on the bar can be seen in Fig. 4.4.

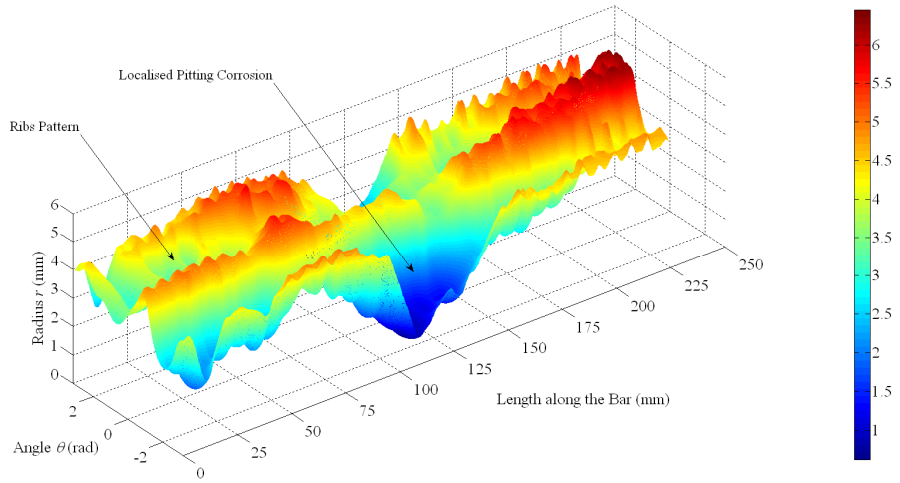

(a)

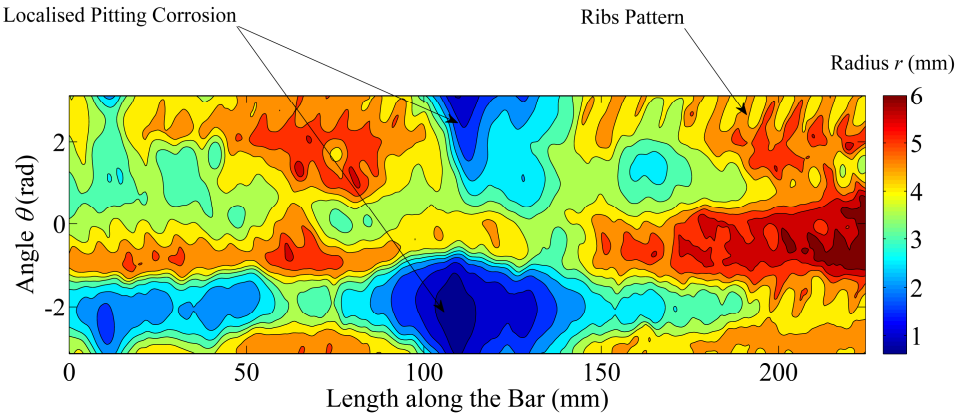

(b)

Fig. 4.4 Corrosion pattern of a corroded bar with 54.23% mass loss: (a) 3D surface plot of corrosion pattern (b) contour plot of corrosion pattern

From the values of r and θ all the geometrical properties of each cross section can be calculated over the length of each bar. The method that was used for calculation of geometrical properties of bars is discussed in the following section.

4.2.2. Calculation of the geometrical properties of corroded bars using the 3D optical measurement data

As shown in Fig. 4.4 (a) the cross section shape of corroded bars is a simple polygon (a non-self-intersecting polygon). The area of a simple polygon with n vertices can be calculated using Eq. (4.1) which is based on Green's Theorem.

$$A = \tfrac{1}{2}\sum_{i=0}^{n-1}\left(y_i z_{i-1} - y_{i+1} z_i\right) \tag{4.1}$$

where y and z are the coordinate of the vertices.

Subsequently by taking moments about the centre (0,0 coordinate) the centroid and second moment of area of the polygon about y and z axis can be calculated using Eq. (4.2) to Eq. (4.6):

$$C_y = \tfrac{1}{6A}\sum_{i=0}^{n-1} a_i\left(y_i + y_{i+1}\right) \tag{4.2}$$

$$C_z = \tfrac{1}{6A}\sum_{i=0}^{n-1} a_i\left(z_i + z_{i+1}\right) \tag{4.3}$$

$$I_y = \tfrac{1}{12}\sum_{i=0}^{n-1} a_i\left(z_i^2 + z_i z_{i+1} + z_{i+1}^2\right) \tag{4.4}$$

$$I_z = \tfrac{1}{12}\sum_{i=0}^{n-1} a_i\left(y_i^2 + y_i y_{i+1} + y_{i+1}^2\right) \tag{4.5}$$

$$a_i = \left(y_i z_{i-1} - y_{i+1} z_i\right) \tag{4.6}$$

Using the equations above all of the geometrical properties of the corroded cross sections can be calculated. The correlation between the geometrical properties of pitted sections, original section and mass loss ratio can then be investigated. Using the geometrical properties of the corroded bars the pitted cross sections could be transformed into an idealised arbitrary section for buckling analysis using a fibre technique with the geometrical properties equivalent to the pitted section. Load eccentricity can also be quantified which is very important in inelastic buckling analysis.

4.3. Frequency analysis and signal processing of corrosion pattern data

4.3.1. Power spectral density estimate

A Power Spectral Density (PSD) is normally used to characterise the frequency content of a time-series random signal (Cryer and Chan 2008). The purpose of estimating the PSD is to determine if there is any periodic pattern in the data by observing peaks at the frequencies corresponding to these periodicities. The Fast Fourier Transform (FFT) is one of the well-known methods for frequency analysis of time-series signals. This algorithm transforms the signal from time domain to frequency domain to evaluate the periodic

pattern of the signal and estimate the PSD. Welch (1967) has developed an efficient algorithm based on the FFT for estimation of the PSD. This algorithm involves sectioning the time series, taking modified periodograms of these sections, and averaging these modified periodograms. This is computationally more efficient than other methods and is very useful for testing and measuring nonstationarity in random data, further details are available in (Welch 1967). In this research the Welch method is employed for PSD estimation of the measured data. It should be noted that the data in this chapter are represented in spatial domain series. Therefore, the unit of frequency is mm^{-1}.

The radius data of each corroded bar r, calculated from the measured data (shown in Fig. 4.3 and Fig. 4.4), were saved in a 2D matrix. The rows of the matrix represented the angles (θ_i) of each r_i around the perimeter of section and columns of the matrix represented the position of each r_i along the length of the bar. The PSD of all radii along the bar for each θ_i was estimated for each bar. Fig. 4.5 shows an example of the PSD calculated for two different bars at $\theta = \pi/2$. As shown in Fig. 4.5 the frequency at $0.1292mm^{-1}$ is identified as the frequency of ribs and the next peak at $0.2701mm^{-1}$ as the second harmonic of that frequency. This was validated by testing the coherence of several PSDs of different bars. In addition, as an extra check the frequency of ribs was calculated by physical measurement of rib spacing on the bars. The physical measurement showed that the ribs were at 7.85mm intervals which gives a frequency of $1/7.85 = 0.1274mm^{-1}$. This rib frequency can be considered as noise along, what would otherwise be a smooth circular bar. Therefore, it needs to be filtered from the data to leave just the influence of corrosion on the bars.

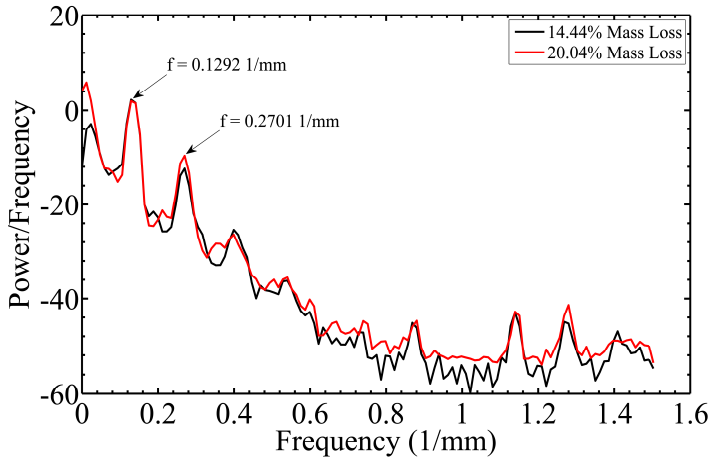

Fig. 4.5 Welch PSD estimate of the radius r at $\theta = \pi/2$ for two bars with different mass loss ratios

4.3.2. Design of band-stop filter

In order to better distinguish the locations of the corrosion along the bars the repeating rib pattern has been removed by filtering the raw profile data. A pair of 2nd order band-

stop butterworth filters were employed, one centred at 0.13mm^{-1} with a width of 0.03mm^{-1}, the other centred at 0.27mm^{-1} with a width of 0.03mm^{-1}. Two filters were used to remove both the main repeat period of the ribs and also the 2nd harmonic. Use of band-stop filters meant that only the rib pattern was targeted by the filtering. Therefore, both lower and higher frequency corrosion components were maintained. Once the rib pattern was removed from the data the radius data was then processed to give the geometrical properties of the bars at each location down their length based on the method explained in section 4.2.2 of this chapter. Fig. 4.6 visualises the band-stop filter designed for this analysis.

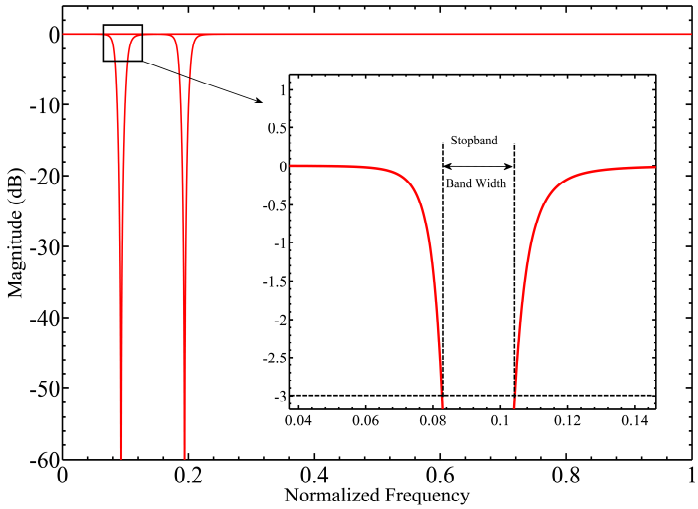

Fig. 4.6 Butterworth band-stop filter visualisation

4.3.2.1. Result of band-stop filtering process

Fig. 4.7 (a) and (b) shows a comparison of the contour plot of the profile data of a corroded bar with 8.93% mass loss before and after the filtering process. As it is evident from Fig. 4.7 that the rib pattern has been removed from the raw data and the pattern of pitting corrosion with all the fine details is left unaffected.

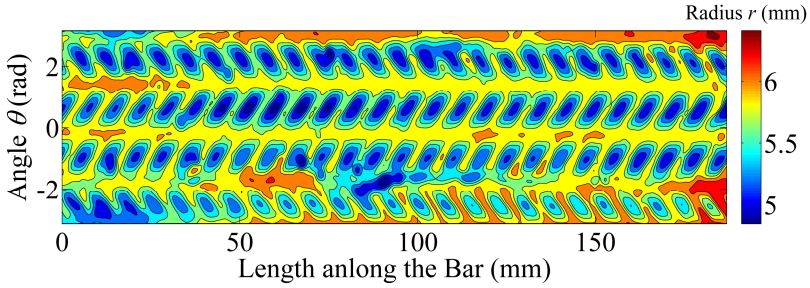

(a)

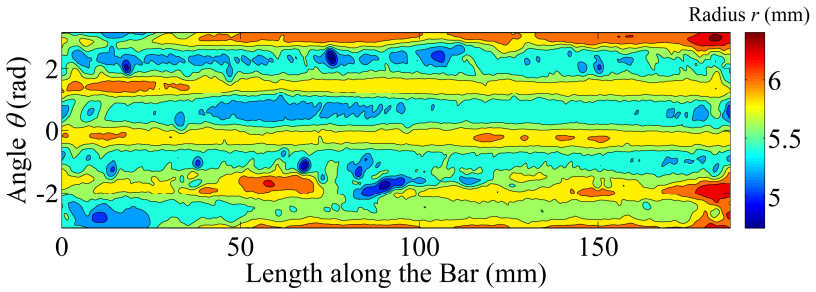

(b)

Fig. 4.7 Comparison of the contour plot of a corroded bar with 8.93% mass loss before and after filtering the ribs pattern: (a) before filtering (b) after filtering

Fig. 4.8 (a) also shows a longitudinal profile of a slice through the length of another corroded bar with a 54.23% mass loss at θ = 2.631rad. Fig. 4.8 (b) shows the PSD estimation of the same profile before and after the filtering process. It should be noted that the 3D surface and contour plot of this corroded bar are previously shown in Fig. 4.4. This bar had one of the most complex corrosion patterns but the band stop filtering successfully kept the corrosion pattern while removing the rib frequency.

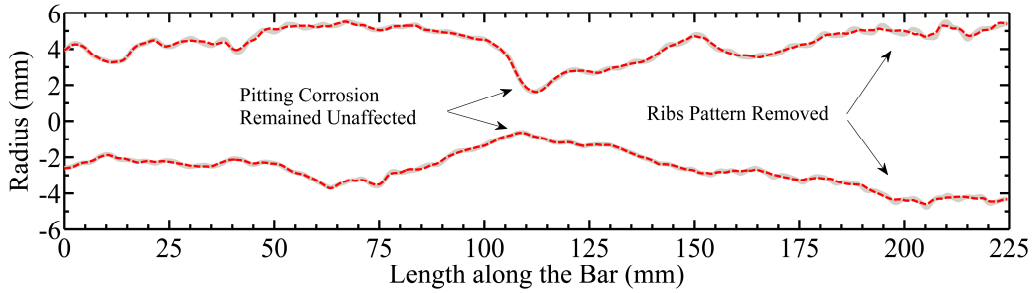

(a)

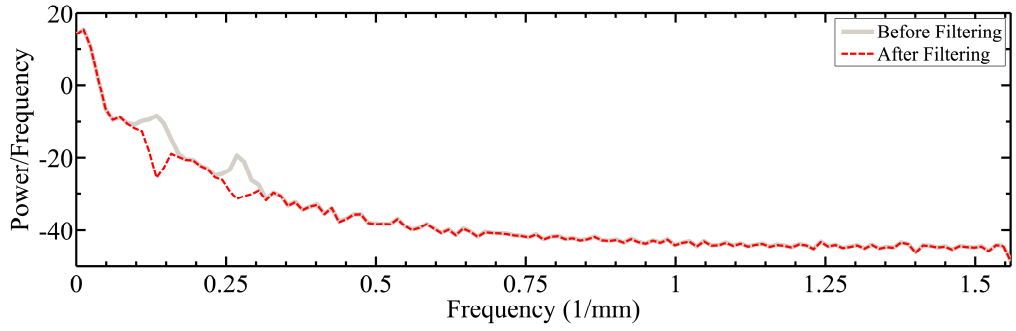

(b)

Fig. 4.8 Pitting corrosion pattern of a corroded bar with 54.23% before and after filtering process: (a) longitudinal profile through the length at θ = 2.631rad (b) PSD of the profile shown in (a)

From the filtered data the geometrical properties of each corroded bar were calculated. Fig. 4.9 (a) shows examples of the variation, along the length of the bars, of the residual

cross section areas (A') of three corroded bars normalised to the original uncorroded cross section area (A_0). Fig. 4.9 (b) and (c) show the variation of residual second moment of areas (I'_y and I'_z) normalised to the original second moment of area (I_0) and Fig. 4.9 (d) shows an example orbit of centroid movement of a corroded bar with 54.23% mass loss in relation to the original bar diameter. Fig. 4.9 shows that non-uniform corrosion results in a significant variation in the geometrical properties of corroded bars along their length.

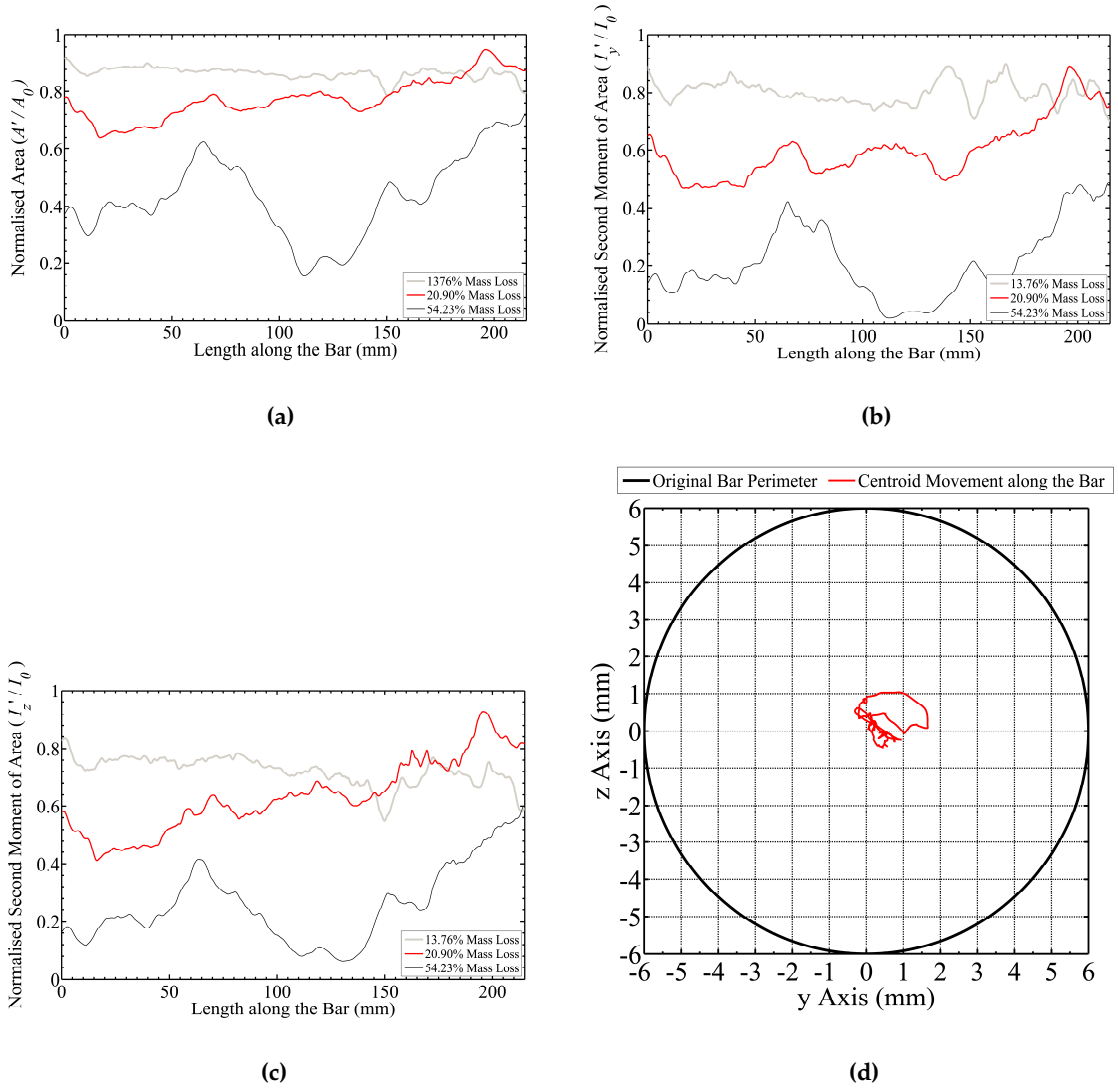

Fig. 4.9 Geometrical properties of corroded bars at section level: (a) normalised A′ (b) normalised I′y (c) normalised I′z (d) orbit of centroid movement along the whole length of a corroded bar with 54.23% mass loss

Fig. 4.10 shows the relationship between the ratio of minimum cross section area A'_{min} and the average reduced cross section area A_{ave} (i.e. the pitting coefficient of the minimum area) and the percentage mass loss ψ.

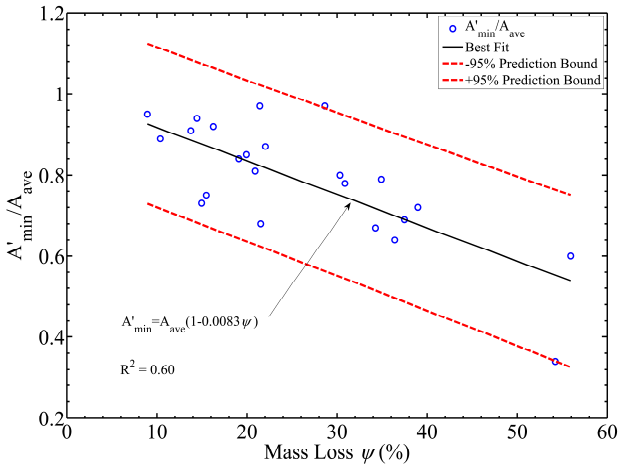

Fig. 4.10 Regression analysis of the pitting coefficient of the minimum cross section area

As shown in Fig. 4.10 there is a linear relationship, with a negative slope, between A'_{min} / A_{ave} and the percentage mass loss. This shows that the pitting coefficient is not constant but decreases with an increase in the percentage mass loss. In other words, the area loss due to pitting increases with an increasing mass loss. The slope of the regression line (0.0083 as shown in Fig. 4.10) is the rate of change of the pitting coefficient. Fig. 4.10 only shows the pitting coefficient for the minimum area (maximum area loss). However, the pitting coefficient also varies (randomly distributed) over the length of a corroded bar with a known percentage mass loss. Accordingly, a probabilistic platform is developed in this chapter to model the uncertainties associated with pitting distribution. The details of this methodology are explained in the following sections.

4.4. Probabilistic-based modelling of time-variant distribution of pitting corrosion

4.4.1. Probability distribution functions for geometrical properties of corroded bars

Hawn (1977) and Sheikh et al. (1990) investigated the distribution of maximum pitting depth of corroded steel pipelines. They suggested that a Gumbel distribution can be used to model the distribution of maximum pits. Darwaman and Stewart (2007) studied the probabilistic distribution of maximum pitting depth of corroded prestressing wires. Stewart and Al-Harthy (2008) investigated the probabilistic distribution of the maximum pitting depth of corroded reinforcement. Darwaman and Stewart (2007) and Stewart and Al-Harthy (2008) both adopted a Gumbel distribution function to model the statistical distribution of the maximum pit depth.

In this section a set of probabilistic models are developed that account for: a) the change of cross section area over the length of corroded bars, b) the change in second moment of area of cross sections over the length of corroded bars and c) the influence of corrosion on load eccentricity. These parameters are defined below:

a) Area pitting coefficient:

$$\beta(x) = \frac{A'(x)}{A_{ave}} \tag{4.7}$$

where $A'(x)$ is the cross section area including the pitting effect as a function of length x, A_{ave} is the average reduced cross section area calculated assuming a uniform volumetric mass loss and $\beta(x)$ is the area pitting coefficient as a function of length x.

b) Residual second moment of area coefficient:

In the calculation of the residual second moment of area consideration needs to be given to the axis rotation. This is due the irregular shape of the corroded cross section and the movement of the section centroid. As a result each cross section has three component second moment of areas i.e., the second moment of areas at the origin (0,0), the second moment of areas at the centroid, and the second moment of areas about the principal axis. Given that the minimum second moment of area is critical; it was decided to investigate the probabilistic distribution of this variable. To account for the axis rotation, the minimum second moment of area about the principal axes was considered in the calculations. The coefficient of the residual minimum second moment of area is then defined in Eq. (4.8) below:

$$\eta(x) = \frac{I'_{min}(x)}{I_0} \tag{4.8}$$

where, $I'_{min}(x)$ is the minimum residual second moment of area of corroded section including the axis rotation and pitting effect as a function of length x, I_0 is the second moment of area of the original uncorroded cross section and $\eta(x)$ is the coefficient of the residual minimum second moment of area as a function of length x.

c) Load eccentricity coefficient:

The load eccentricity is considered as the ratio of the product of the centroid in y and z axes to the original bar diameter of uncorroded bar as Eq. (4.9) below:

$$\upsilon(x) = \frac{e(x)}{r_0} \tag{4.9}$$

$$e(x) = \sqrt{c_y(x)^2 + c_z(x)^2} \tag{4.10}$$

where, $e(x)$ is the coefficient of load eccentricity ratio as a function of length x, r_0 is the original bar radius, $c_y(x)$ and $c_z(x)$ are the section centroid in the y and z axes respectively.

The probability distribution is an important component in uncertainty modelling and selection of a particular distribution may significantly affect the characteristic values based on the selected distribution model. The modelling strategy that Sriramula and Chryssanthopoulos (2009) used for uncertainly modelling of the mechanical properties of GFRP panels is employed here for uncertainty modelling of the random variables (β, η and ν).

Several distribution models have been fitted to the observed random variables (β, η and ν). The goodness of fit was investigated using Chi-square (C-S) and Kolmogorov-Smirnov (K-S) hypothesis tests (Massey 1951). It was found that the two parameter lognormal distribution is supported by both tests at a significance level of 0.05 (95% confidence) for all three random variables (β, η and ν). In order to visualise the goodness of fit for demonstrative purposes, a comparison between representative probability graphs of the random variables and a Weibull, normal and lognormal fit is presented in Fig 14 (a,c,e). Fig. 14 (b,d,f) shows example cumulative probability graphs of the random variables presented in Fig 4.11 (a,c,e) and predicted values using the lognormal fit together with 95% prediction bounds.

From Fig. 4.11 it is evident that the predicted values based on a lognormal fit are generally within the 95% prediction bounds. Therefore, based on null hypothesis tests it can be concluded that a lognormal distribution model can represent the distribution of the random variables (β, η and ν).

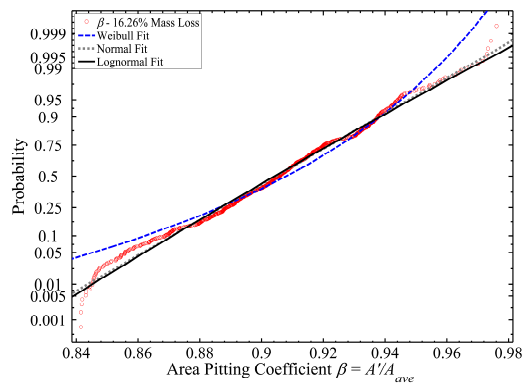

(a)

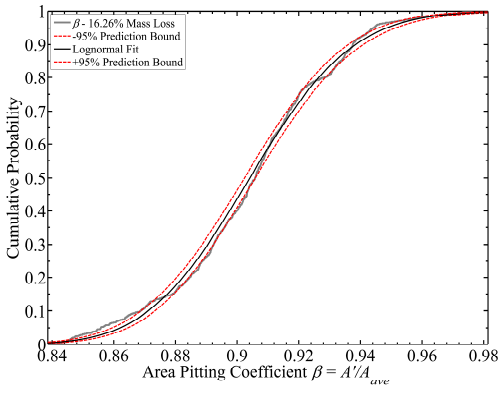

(b)

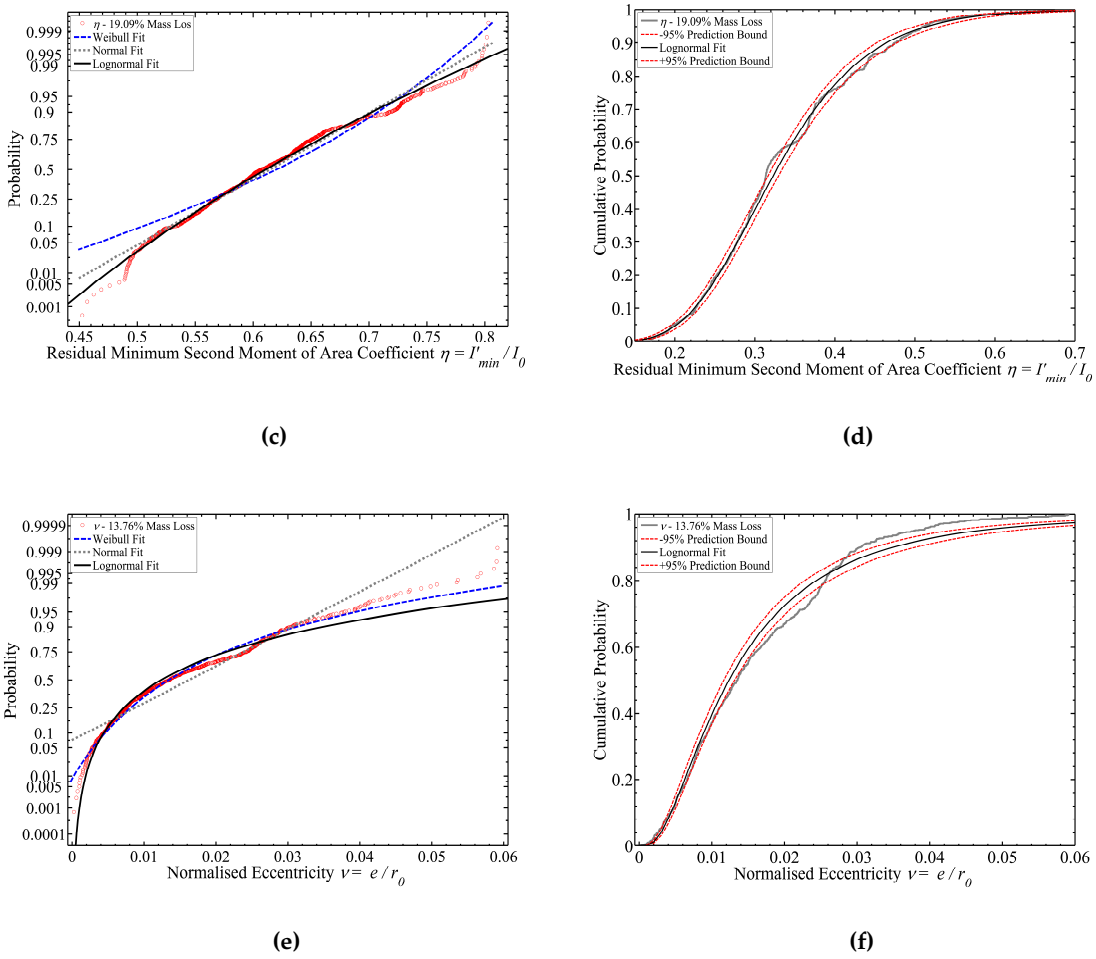

Fig. 4.11 Probability and cumulative probability graphs of the random variables

4.4.2. Correlation between the parameters of the probabilistic models and the mass loss ratio

As shown in the previous section the lognormal distribution model can represent the distribution of the corrosion pattern over the length of corroded bars. However, it should be noted that the values of the lognormal parameters are different in bars with different mass loss ratios. Therefore, it is important to find the correlation between the model parameters and mass loss ratio.

The general form of the lognormal distribution model is defined in Eq. (4.11) below:

$$f\left(g \mid \mu_g, \sigma_g\right) = \frac{1}{g\,\sigma_g\sqrt{2\pi}} \exp\left(\frac{-\left(\ln g - \mu_g\right)^2}{2{\sigma_g}^2}\right) \qquad g > 0 \tag{4.11}$$

where, g is the random variable (either of β, η and ν), and μ_g and σ_g are the corresponding lognormal model parameters. The mean (M_g) and standard deviation (V_g) of each random variable are functions of μ_g and σ_g as defined in Eq. (4.12) and (4.13) below:

$$M_g = \exp\left(\mu_g + \frac{\sigma_g^{\,2}}{2}\right) \tag{4.12}$$

$$V_g = \left(\exp\left(2\mu_g + \sigma_g^{\,2}\right)\right)\left(\exp\left(\sigma_g^{\,2}\right) - 1\right) \tag{4.13}$$

The correlation of the random variables and the mass loss ratio was investigated using Pearson's linear correlation coefficient (ρ) and nonparametric hypothesis tests such as Kendall's rank correlation coefficient (τ) and Spearman's rank correlation coefficient (ρ_{sp}) (Gibbons 2003). The calculated correlation coefficients together with *P-values* for each method at 0.05 significance are shown in Table 4.1.

Table 4.1 Statistical dependence of the lognormal distribution model parameters and mass loss ratio

Model Parameter	Pearson		Kendall		Spearman	
	ρ	*P-value*	τ	*P-value*	ρ_{sp}	*P-value*
β						
μ_β	-0.7965	9.20×10^{-6}	-0.7316	1.26×10^{-7}	-0.8961	3.35×10^{-6}
σ_β	0.496	0.0189	0.4545	0.0026	0.6002	0.0038
η						
μ_η	-0.9839	2.04×10^{-16}	-0.9134	6.87×10^{-14}	-0.9808	3.11×10^{-6}
σ_η	0.8849	4.53×10^{-8}	7.49×10^{-1}	4.91×10^{-8}	0.904	3.66×10^{-6}
ν						
μ_ν	0.6844	3.16×10^{-4}	0.6037	7.89×10^{-5}	0.823	1.43×10^{-6}
σ_ν	-0.1448	0.51	-0.0966	0.54	-0.1347	0.54

μ_β and σ_β are the lognormal model parameters related to the area pitting coefficient β.
μ_η and σ_η are the lognormal model parameters related to the residual second moment of area coefficient η.
μ_ν and σ_ν are the lognormal model parameters related to the load eccentricity coefficient ν.

The results of the correlation analysis show that there is very strong correlation between most of the model parameters and the mass loss ratio. However it was found that there is only a very weak correlation between the model parameter σ_ν and the mass loss ratio. This is clear from the corresponding *P-values* of the random variables β, η and μ_ν which are all less than the considered significance level (0.05). This shows that the dependence of the model parameters of random variables β , η and μ_ν to the mass loss ratio is statistically significant. However, the calculated *P-values* of the model parameter σ_ν for the random variable ν are all greater than the considered significance level. This shows

that there is no correlation between the model parameter σ_ν and the mass loss ratio. Therefore, the dependence of the model parameter σ_ν and the mass loss ratio is statically insignificant. It should be noted that other distribution models i.e. Weibull distribution; show the same result for the random variable ν.

In summary, the results of the correlation analysis show that as the level of corrosion increases the mean values of random variables β and η decrease (indicating an increase in the reduction of area and second moment of area) and the standard deviations increase (indicating that the variation of the data is increasing). However, the mean value of random variable ν increases as the level of corrosion increases (indicating that the load eccentricity is increasing) but, given that the variation of the centroid is numerically very small, the change in mass loss ratio does not have a significant influence on the standard deviation of variable ν.

The interrelationship between the model parameters and the mass loss ratio is modelled using regression analysis of the data. The results of the regression analysis are shown in Fig 4.12 (a-e). The relationships between the model parameters and the mass loss ratio are defined by empirical Eq. (4.14) and (4.15) which are based on the regression analysis.

$$\mu_g = a\,\psi^b \tag{4.14}$$

$$\sigma_g = c\,\psi^d \tag{4.15}$$

where, μ_g and σ_g are the model parameters of random variables (β, η and ν), a, b, c and d are the regression coefficients that are defined in Table 4.2 and ψ is the percentage mass loss ($\psi = 100\gamma$).

Table 4.2 The proposed probabilistic model parameters as a function of the mass loss ratio

Model Parameter	*a*	*b*	*c*	*d*
β				
μ_β	-0.000052	1.825		
σ_β			0.0006491	1.526
η				
μ_η	-0.008811	1.354		
σ_η			0.001768	1.495
ν				
μ_ν	-8.473	-0.304		

μ_β and σ_β are the lognormal model parameters related to the area pitting coefficient β.
μ_η and σ_η are the lognormal model parameters related to the residual second moment of area coefficient η.
μ_ν and σ_ν are the lognormal model parameters related to the load eccentricity coefficient ν.

It should be noted that, given that the model parameter σ_v is statically independent from the mass loss ratio, the average value of σ_v = 0.685 is considered in the probabilistic models.

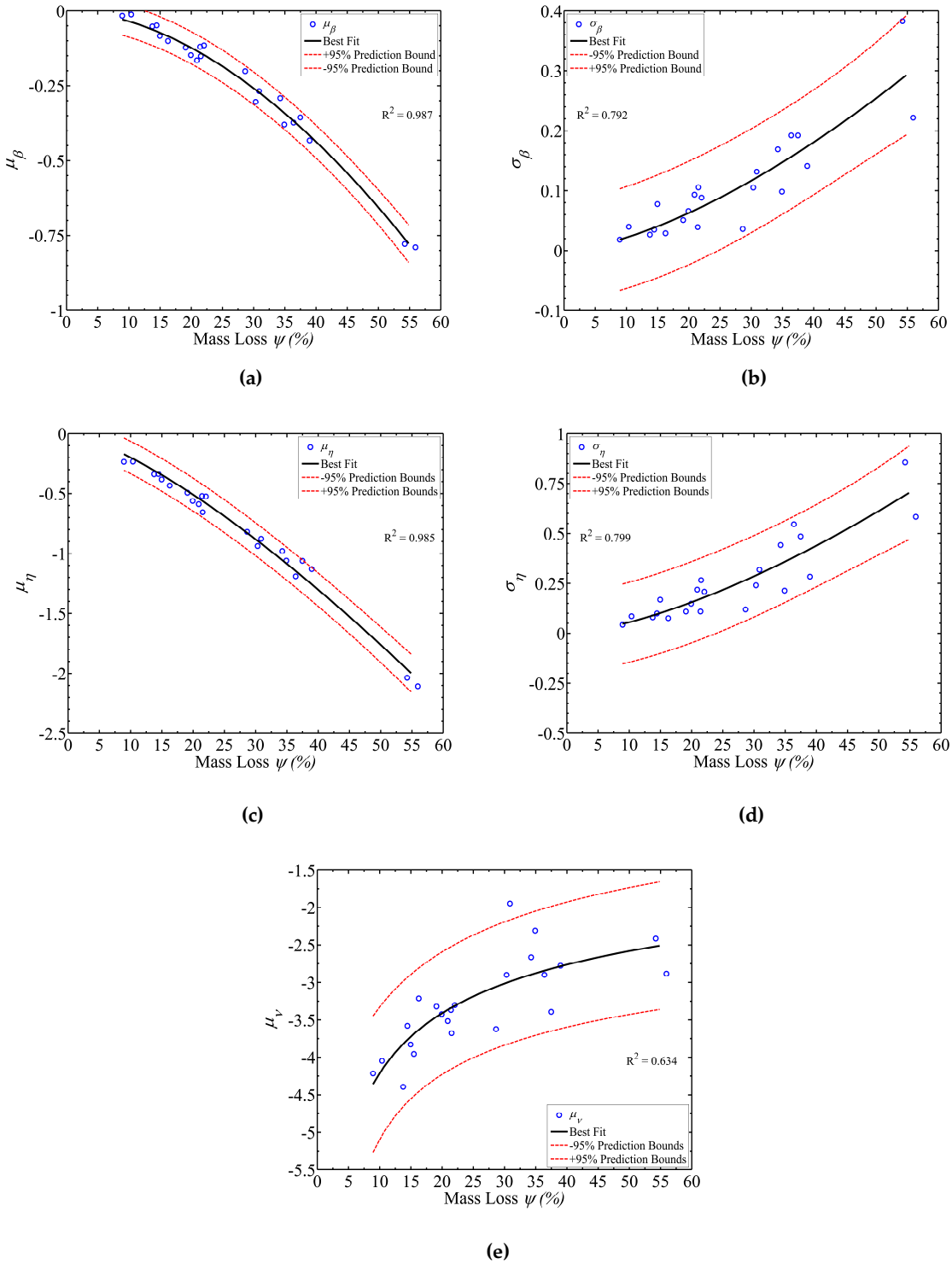

Fig. 4.12 Regression analysis of the probabilistic model parameters

Using empirical Eq. (4.14) and (4.15) it is possible to generate a set of probabilistic distribution models for the random variables (β, η and ν) for any given mass loss ratio. In other words, these models can represent the time-variant distribution of the geometrical properties of corroded bars. The results of these models with a numerical example are discussed in the section 4.6 of this chapter.

So far we have discussed the probabilistic distribution of geometrical properties of corroded bars as function of the mass loss ratio. However, an important parameter that needs to be considered in using the above probabilistic models is the length dependence of the model parameters. This is discussed in the following section.

4.5. Autocorrelation function, cross-correlation function and spatial variability of corrosion pattern

The cross-correlation function (CCF) indicates the correlation, or similarity, of two time-series random variable as function of a time-lag applied to one of them. This is widely used in signal processing i.e. searching a long signal for a shorter signal and in pattern recognition (Cryer and Chan 2008). The autocorrelation function (ACF) is a special case of the CCF being the CCF of the signal with itself. The ACF indicates the similarity/correlation between observed data as a function of the time separation between points (Cryer and Chan 2008). This is an efficient mathematical tool for finding repeating patterns, such as the presence of a periodic signal which has been hidden by noise in the time-domain. The ACF is often used in signal processing for analysing functions or series of values, such as time-domain signals.

In this research the CCF and ACF have been used to investigate the spatial variability of the cross section areas along the corroded bars as a function of length separation between the cross sections. Fig. 4.13 (a) and (b) shows example ACF graphs for two corroded bars with different lengths and mass loss ratios.

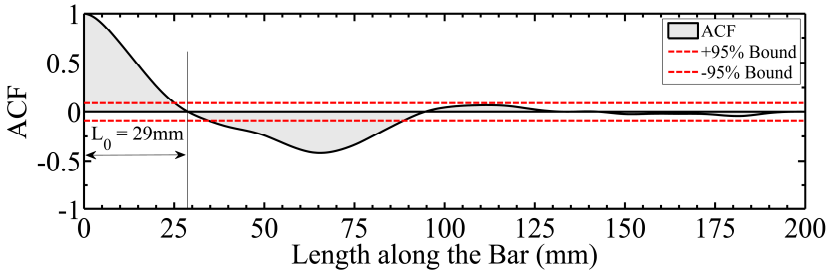

(a)

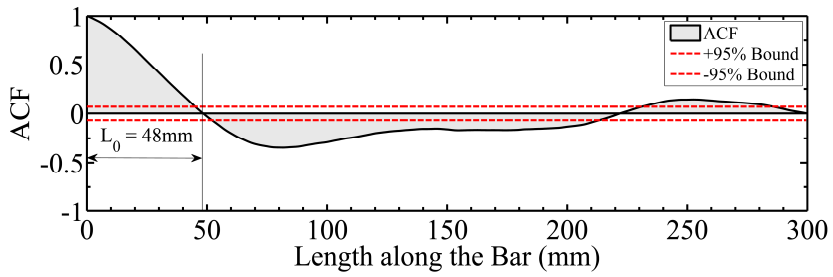

(b)

Fig. 4.13 ACF for the cross section area of two corroded bars with different lengths and mass loss ratios: (a) 36.40% mass loss (b) 19.93% mass loss

The length L_0 shown in Fig. 4.13 indicates the length lag at which there is no correlation between the cross section areas. In other words the similarity between the cross section area at length l of a corroded bar and the cross section area at length $l+L_0$ is zero. As shown in Fig. 4.13 the value of L_0 is different for bars with different lengths and mass loss ratios. Therefore, a comparison between corroded bars with the same length but different mass loss ratios was made using a CCF. Fig. 4.14 (a) and (b) shows two example CCF graphs each for a pair of corroded bars with the same length but with different mass loss ratios.

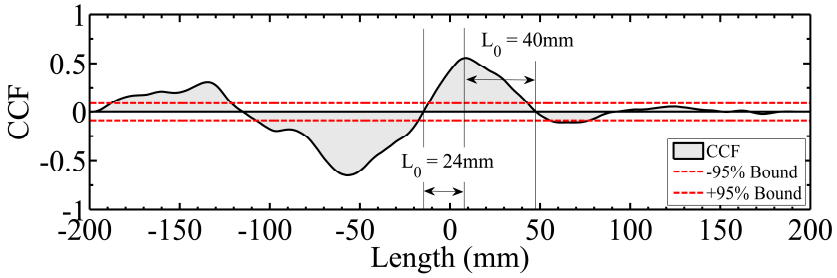

(a)

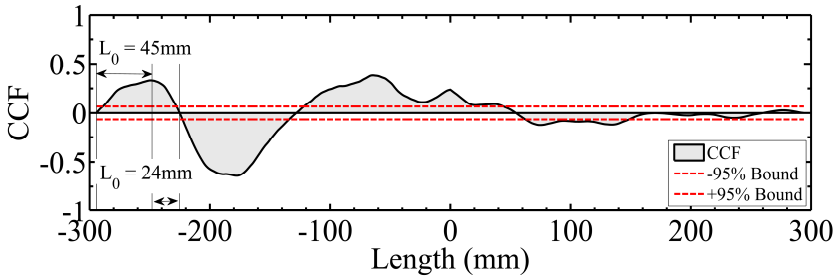

(b)

Fig. 4.14 CCF plot of two pairs of corroded bars with different mass loss ratios and lengths: (a) 200mm length with 21. 42% and 36.40% mass loss (b) 300mm length with 19.93% and 30.32% mass loss

As shown in the Fig. 4.13 and Fig. 4.14 the length L_0 generally varied between 20mm and 50mm in all bars. The ACF and CCF analysis showed that, in most cases, within a length (l) 10mm ≤ l ≤ 20mm the variation in correlation coefficient is low, while if l ≥ 20mm the

variation in correlation coefficient can be large and hence the variation between cross section areas is significant. It was found that within a critical length (L_c) equal or less than 10mm the AFC is always above 0.7 and CCF is always above 70% of the maximum calculated CCF. In other words, the variation of cross section areas within 10mm of any given point along the bar is relatively small. The value of L_c is important in spatial-variant probabilistic modelling of pitting distribution in corroded bars. For example, if a corroded bar is 100mm long it can be idealised by 10mm segments. The above probabilistic models can then be considered separately for each 10mm segment of the whole bar. It should be pointed out that if a smaller L_c ($L_c \leq 10$mm) is considered, more accurate results can be obtained, however the analysis process will be computationally more expensive. On the other hand, if a larger critical length ($L_c \geq 10$mm) is considered, there is always a possibility that we lose some of the variation in the corrosion pattern data.

Further analytical and experimental research is required to investigate the influence of L_c on the mechanical response prediction of corroded bars. There are other factors that might influence the length L_c such as corrosion rate, concrete mix (cement and aggregate types) and exposure type (chloride induced corrosion or carbonation induced corrosion). Given that all of the test specimens in this research were corroded at the same corrosion rate and were taken from concrete specimens with the same concrete mix, these parameters could not be investigated in this experiment. This is an important area for further research and the methodology developed in this work will allow researchers to analyse the corrosion patterns of any corroded reinforcement in the future. Nevertheless, a suggested conservative value of L_c = 10mm can be taken based on the correlation analysis of the various corrosion patterns found in this work. Therefore, the probabilistic models developed in this research combined with the suggested L_c can safely be used in uncertainty modelling of corrosion pattern.

4.6. Results of probabilistic models

In order to demonstrate the utilisation of the probabilistic models that were developed in section 4.4 some of the results of these models are presented in this section.

Consider a RC bridge pier that is subject to chloride attack due to the splashing of de-icing salts from the adjacent road. Assume the cover concrete C = 50mm, the water cement ratio w/c = 0.4 and the diameter of main reinforcement is 20mm. The deterioration mechanism has two main stages which are (a) the corrosion initiation period and (b) the corrosion propagation period (Vu and Stewart 2003, and Rafiq and Chryssanthopoulos 2004). Several researchers have investigated the critical time to corrosion initiation, caused by diffusion of chloride ions through the cover concrete to the reinforcement, and as a result of their effort several probabilistic models have been

developed (Vu and Stewart 2003, and Rafiq and Chryssanthopoulos 2004). Other researchers studied the corrosion propagation period i.e. crack initiation and crack propagation due to the penetration of corrosion products into concrete (Ozbolt et al. 2011, Zhao et al. 2011a, Zhao et al. 2011b, Zhao et al. 2012, Zhao et al. 2013). In this example we only consider the corrosion propagation period to demonstrate the application of the proposed models. Once corrosion is initiated, using Eq. (4.16) to (4.19) the average reduced area and the mass loss ratio can be calculated.

The average reduced diameter of a corroded bar assuming a uniform mass loss can be calculated using Eq. (4.16):

$$D_{corr}(t) = D_0 - 2P_{ave}(t) \tag{4.16}$$

where, $D_{corr}(t)$ is the average reduced diameter of a corroded reinforcing bar at time t after corrosion initiation, D_0 is the original bar diameter and $P_{ave}(t)$ is the average corrosion penetration depth based on the uniform volumetric mass loss at time t after corrosion initiation. $P_{ave}(t)$ can be calculated using Eq. (4.17) below (Stewart and Suo 2009):

$$P_{ave}(t) = \kappa \int_{T_{cr}}^{t} i_{corr}(t)\,\mathrm{d}t \tag{4.17}$$

where, $i_{corr}(t)$ is the corrosion current density at time t after corrosion initiation in $\mu A/cm^2$ and $\kappa = 0.0116$ is the conversion factor from $\mu A/cm^2$ to mm/year and T_{cr} is the critical corrosion initiation time.

The time dependent corrosion current density can be estimated using Eq. (4.18) and (4.19):

$$i_{corr}(t) = 0.85\, i_{corr0}\left(t - T_{cr}\right)^{-0.3} \tag{4.18}$$

$$i_{corr0} = \frac{27\left(1 - w/c\right)^{-1.64}}{C} \tag{4.19}$$

where, i_{corr0} is the corrosion current density at corrosion initiation time T_{cr}, w/c is the water cement ratio of concrete and C is the thickness of cover concrete. Eq. (4.18) shows that corrosion current density decreases after corrosion initiation time. This is due to the formation of corrosion products around the surface of reinforcement. This reduces the diffusion of the iron ions away from the reinforcement surface which will result in reduction of corrosion rate with time (Vu and Stewart 2000).

Subsequently, using the probabilistic models described in section 4.4, the time-variant distribution models of the geometrical properties of corroded bar can be generated. Fig

4.15 (a-f) shows the results of the time variant probabilistic models for the given example.

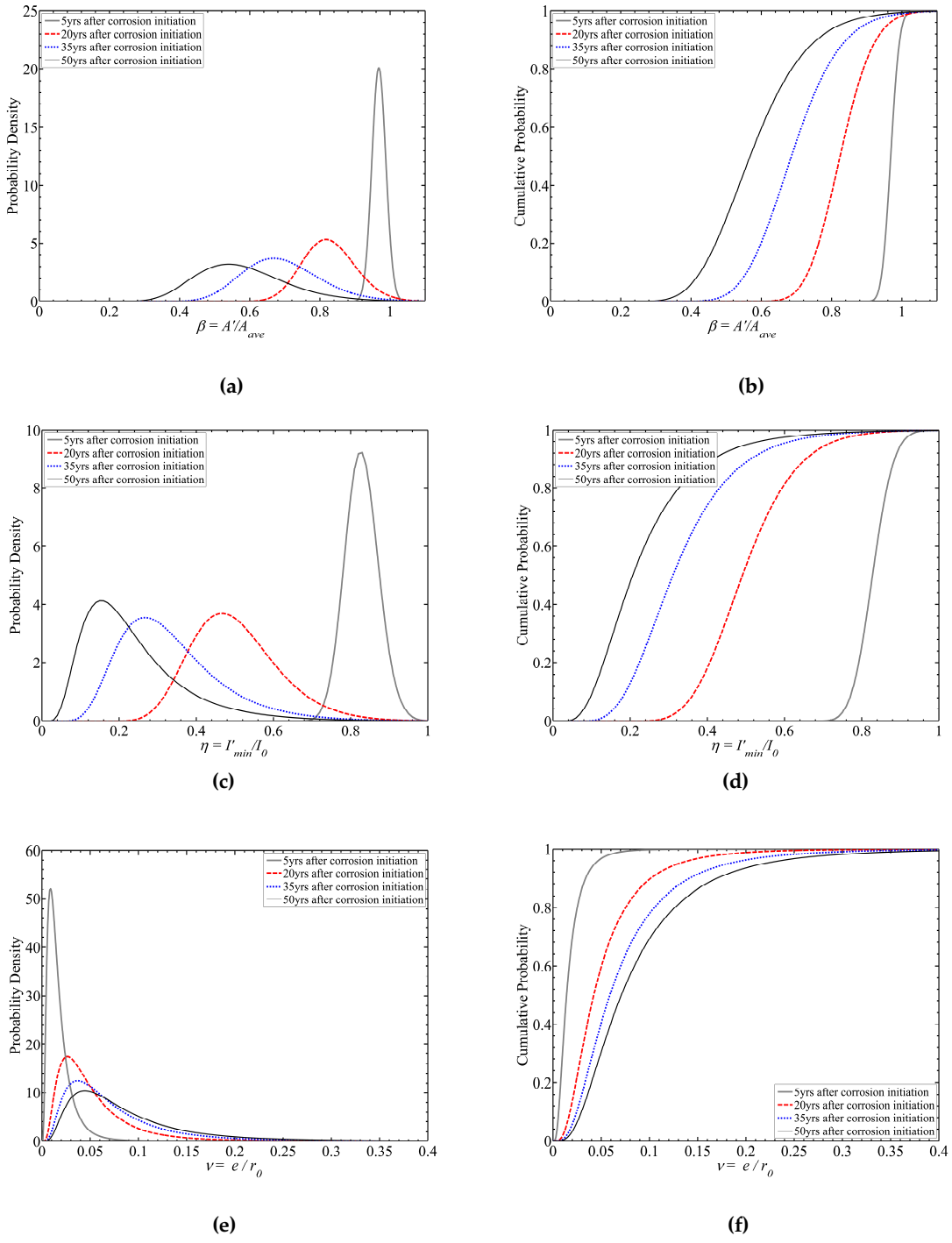

Fig. 4.15 Results of time-variant probabilistic models: (a) and (b) variation of area pitting coefficient with time, (c) and (d) variation of residual minimum second moment of area with time and (e) and (f) variation of load eccentricity coefficient of corroded reinforcement with time

The results of probabilistic models shown in Fig. 4.15 can then be used in a structural safety and reliability analysis of the bridge pier in this example.

The current standards for the assessment of corroded structures such as BA 51/95 and BA 38/93 in the UK provide simplified approaches for estimation of the cross section loss of corroded reinforcement which requires destructive sampling from the structure. However, the models developed in this chapter can predict the cross section loss as well as other geometrical properties of the corroded bars based on a non-destructive predictive method. This will significantly improve the maintenance optimisation techniques for the entire bridge network. Furthermore, if the bridge network is located in an earthquake prone region where the response of structure is severely affected by corrosion of reinforcement (Ou et al. 2011, Ma et al. 2012) the time-dependent seismic performance of the network is very important. Therefore, in recent years, other researchers have investigated the time-dependent seismic performance of corroded bridges using finite element analysis assuming a uniform corrosion (Choe et al. 2008, Berto et al. 2009, Ghosh, and Padgett 2010, and Alipour et al. 2011). The result of this research provides a probabilistic platform allowing researchers to create more realistic uncertainty modelling for seismic reliability analysis of corroded RC bridges and other structures.

4.7. Micro-fibre nonlinear finite element analysis of reinforcing bars

Nonlinear finite element analysis has been used by other researchers to study the behaviour, including buckling, of reinforcing bars without corrosion under monotonic and cyclic loading. Mau and El-Mabsout (1989) developed a special beam-column element for nonlinear finite element analysis of inelastic buckling of reinforcing bars. Using a fibre-type model of the bar cross section, Dhakal and Maekawa (2002a,b) conducted a nonlinear finite element analysis of individual reinforcing bars, with different L/D and yield strengths, to investigate their buckling response. Nakamura and Higai (2002) performed nonlinear finite element analyses studying the stress-strain behaviour of reinforcing bars under monotonic and cyclic loading. In all cases, analyses and experiments considered isolated bars (i.e. bars were not embedded in concrete); in all cases, good agreement between the experimental data and finite element results was observed. Here nonlinear finite element analysis was employed to investigate the impact of corrosion on the behaviour of reinforcement under monotonic and cyclic loading. An approach similar to that employed by Dhakal and Maekawa (2002a) for analysis of bars without corrosion was employed.

4.7.1. The finite element model

The open-source three-dimensional nonlinear finite element analysis platform OpenSees (Open System for Earthquake Engineering Simulation) (OpenSees 2012) and the force-

based distributed plasticity beam-column (FBBC) element formulation (Spacone et al. 1996a,b) available in the OpenSees platform were used for the analyses. This element formulation assumes a linear moment distribution and constant axial force distribution along the length of the element. Nonlinear material response under flexural-type loading is simulated at the section level. For this study, a fibre-type model of the reinforcing bar cross section was used; fibre response was defined using a nonlinear constitutive model. Moment and axial load at a section of the beam-column element are determined by integrating the fibre stresses over the section. Using the FBBC element formulation, generalised nodal displacements are determined from section deformations using a Gauss-Labotto integration scheme. For this study, geometric nonlinear was simulated using the co-rotational formulation (Neuenhofer and Filippou 1998, Souza 2000).

A series of preliminary analyses were conducted to determine model parameters for use in the subsequent analyses. A mesh refinement study was conducted at the section and component levels. It was found that a section mesh comprising 6 fibres in the radial direction and 35 fibres in the circumferential direction resulted in a converged section response. It was found that use of 10mm long elements with three Gauss-Lobatto integration points per element resulted in a converged component response. An initial imperfection of 0.001mm (1.0×10^{-5} to 4.16×10^{-6} of L) was introduced at mid height of the bar to initiate buckling (the initial imperfect shape was linear). To emulate the boundary conditions during the laboratory tests, the rotations and displacements of the bottom node of the bars were fully restrained in the model. The axial displacement history applied in the laboratory experiments was applied in the analyses.

4.7.2. Steel material model

Dhakal and Maekawa (2002b) modelled the path-dependent behaviour of isolated reinforcing bars exhibiting buckling. They concluded that the average stress-strain and buckling behaviour of bars in compression and the unloading/reloading behaviour of cyclic loops are greatly influenced by the accuracy of the basic steel model used for the analysis. Therefore, to model the cyclic behaviour of bars correctly, an accurate steel model must be used that is able to simulate the unloading/reloading behaviour of reinforcing steel including the Bauschinger effect. In this study the Giuffre–Menegotto–Pinto (GMP) model (Menegotto and Pinto 1973) implemented in OpenSees as the *Steel02* material model is used to model the uniaxial stress-strain response of steel. The GMP model employs a smooth transition curve that asymptotically approaches bilinear tension and compression response envelopes (Fig. 4.16); this enables simulation of the Bauschinger effect. The variables in Fig. 4.16 are defined in Table 4.3. Table 4.3 also provides the values used in the analyses, which were determined from coupon tests

conducted per ASTM E8/E8M-09. It should be noted that the ultimate strain (ε_u) is the strain at the ultimate strength (σ_u).

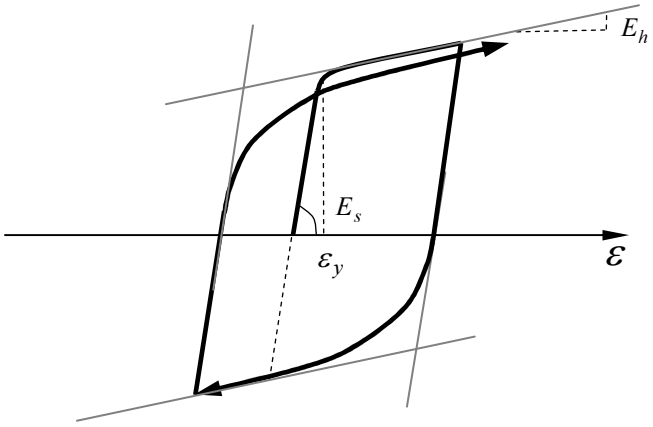

Fig. 4.16 The Giuffre–Menegotto–Pinto model

Table 4.3 Mechanical properties of uncorroded reinforcement

Reinforcement Type		**12mm (B12)**
Yield Strength	σ_y (MPa)	540
Modulus of Elasticity	E_s (Mpa)	210000
Hardening Ratio	E_h/E_s	0.008
Ultimate Strength	σ_u (MPa)	616
Strain at ultimate strength	ε_u	0.06
Strength Ratio	σ_u/σ_y	1.14

4.7.3. Model validation

For validation of the computational model, computed and experimental average stress versus strain results for uncorroded bars were compared. Fig. 4.17 (a-d) shows a comparison between the computed and observed experimental response during monotonic tests for uncorroded bars with L/D = 8, 10, 15 and 20 respectively. Fig. 4.18 (1-c) shows a comparison between the computed and observed experimental response of cyclic tests for uncorroded bars with L/D = 5, 10 and 15 respectively. As shown in Fig. 4.17 and 4.18 the numerical model accurately simulates the monotonic and cyclic response of reinforcing bars out to relatively large strain demands. The simulation results show that the computational model is able to capture the pinching effect seen in the bars with L/D > 10 under the large displacement demand. Furthermore, the compressive strength degradation of bars under cyclic loading due to the influence of tension history that was observed in the experiment is also captured accurately in the computational simulation. For bars with L/D = 10 and 15 subjected to cyclic loading, crack propagation caused by low-cycle fatigue in bars resulted in degradation of the

tension envelope and ultimate tensile strength; the numerical model was not able to capture this response as strength degradation due to low-cycle fatigue is not incorporated in the *Steel02* material model.

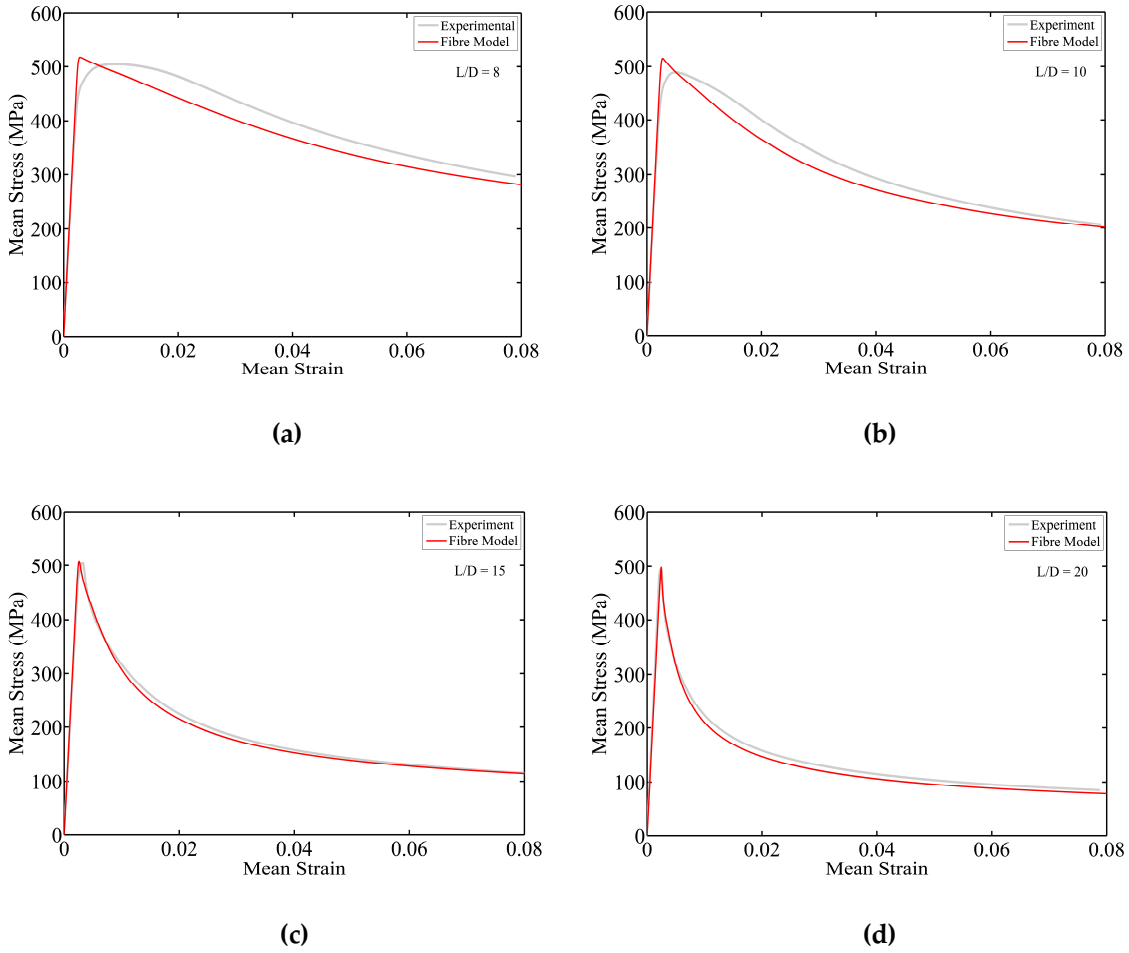

Fig. 4.17 Comparison of fibre model simulation with monotonic test results: (a) L/D = 8 (b) L/D = 10 (c) L/D = 15 and (d) L/D = 20

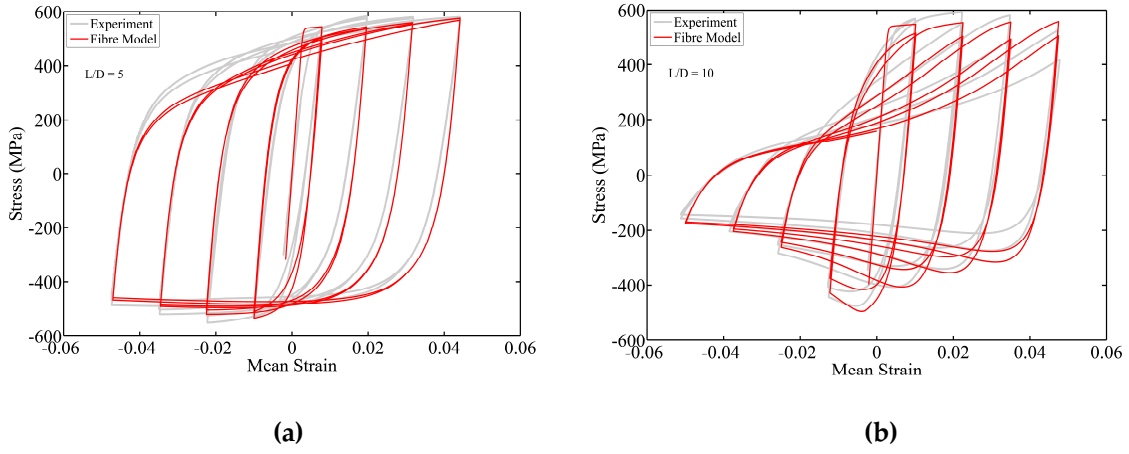

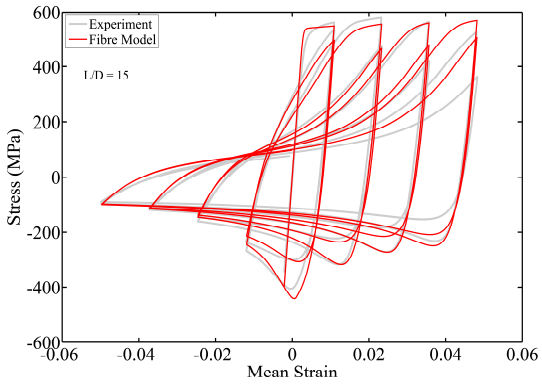

(c)

Fig. 4.18 Comparison of fibre model simulation with cyclic test results: (a) L/D = 5 (b) L/D = 10 and (c) L/D = 15

4.7.4. Modelling the effect of corrosion pattern

As was shown in Fig 4.3 and Fig. 4.4, pitting corrosion creates irregular cross section shapes along the length of corroded bars. This irregularity creates strong and weak axes, for which the second moments of area are reduced from the uncorroded state, and creates load eccentricity at the cross section. These factors must be included in analysis of isolated corroded reinforcing bars.

4.7.4.1. Modelling the cross section with equivalent rectangular

As was discussed in previous sections, nonunifrom corrosion affects both area of cross section and second moment of area due to the change in the cross section shape. A circular section has only one parameter (radius), so it is not possible to fit two parameters (area and second moment of area) to a circular section. Therefore, to model the impact of corrosion on both area and second moment of area, an equivalent rectangular cross section was used in the fibre model of a corroded bar. The equivalent section had the same area and the minimum second moment of area as calculated from the optical measurement data. To validate this assumption, initially, equivalent circular and rectangular cross section shapes were considered for an uncorroded bar. It was observed that the cross section shape has no effect on the computational response (Fig. 4.19).

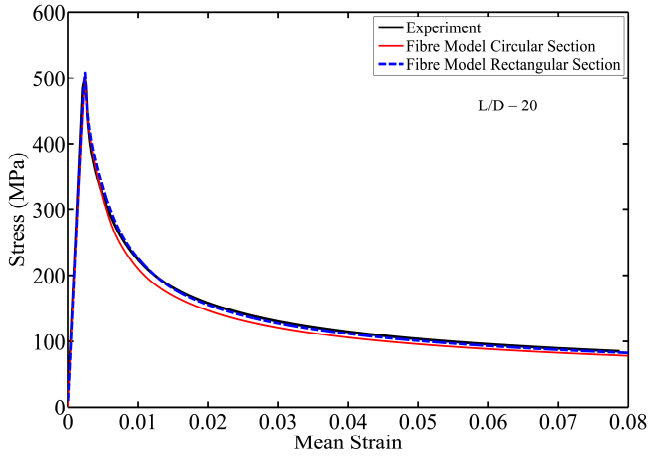

Fig. 4.19 Comparison of the nonlinear response of beam-column element models with circular and equivalent rectangular fibre sections

4.7.4.2. Modelling the load eccentricity

Pitting corrosion also results in a shifting of the centroid of the section along the length of the bar. Since load is applied through the average centroid of bar, at any location along on the length of the bar, the axial load may be locally applied eccentrically. This load eccentricity creates an imperfection in the corroded bars and significantly affects the inelastic buckling response.

To simulate the shifting centroid of the corroded bar, the nodes of the nonlinear beam-column elements were located at the measured centroid of the section and elastic beam-column elements were used as rigid link elements (RGE) to connect the nonlinear elements. Fig. 4.20 shows an idealised view of the finite element model in the OpenSees including the RGEs arrangement. The elastic beam-column elements were defined to have an axial and flexural stiffness (EA and EI) twenty times higher than the axial and flexural stiffness of the original uncorrodeded reinforcing bars (a 12mm diameter bar).

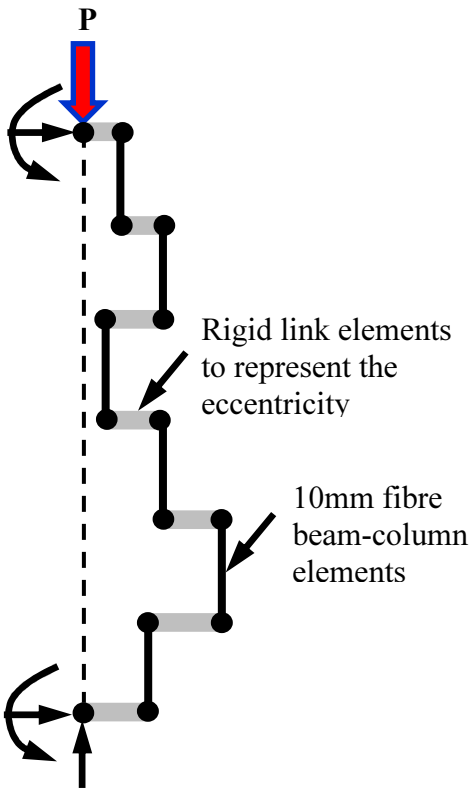

Fig. 4.20 Schematic representation of fibre beam-column model of a corroded bar with eccentricity

4.7.4.3. Mesh sensitivity and averaging length

The optical measurement data defined the corroded bar cross sections at 0.5 mm intervals along the bar. However, the results of stochastic corrosion pattern analysis using autocorrelation and cross correlation functions showed that averaging the data over 10 mm segments yields a correlation factor above 70% (discussed in Section 4.5). This suggests that the variation of the cross section within 10 mm of any given point along the bar is relatively small and that meshing the corroded bar using 10mm long elements with constant cross sections could be expected to yield accurate results. Since the computational demand of modelling with 0.5 mm long elements is significantly greater than modelling using 10 mm long elements, the impact of mesh refinement was investigated. The nonlinear buckling responses of two finite element models, one with 10 mm and one with 5 mm elements, was compared (Fig. 4.21). In both models, a constant cross section was assumed for the entire element length, cross section geometric properties (area, centroid and second moment of area) were defined as the average over the element length, and three Gauss Lobatto integration points per element were used. As shown in Fig. 4.21, reducing the element length from 10 mm to 5 mm did not significantly affect the nonlinear buckling response of a corroded bar with L/D = 20 and 34.91% mass loss. It was also found that very small element lengths results in numerical

instability during the post-buckling response (Fig. 4.21). Therefore, using 10 mm long elements is reasonably accurate and also computationally efficient.

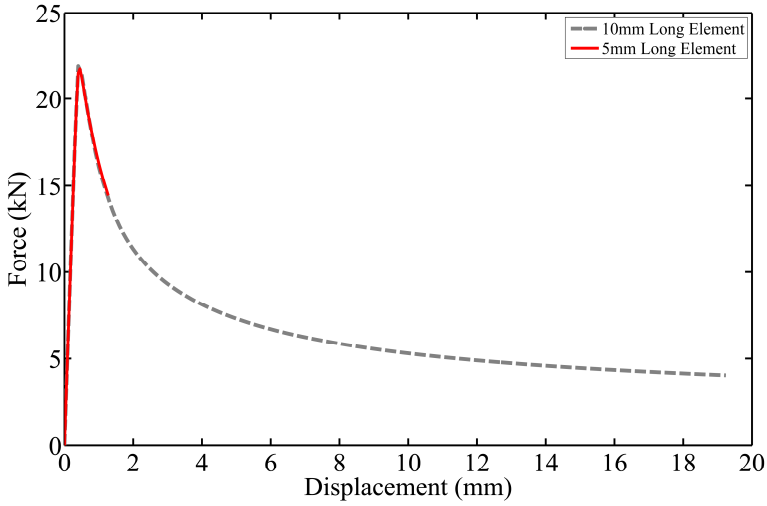

Fig. 4.21 Comparison of the nonlinear response of fibre models with 5 mm and 10 mm elements

4.7.4.4. Reference model

Preliminary analyses resulted in the development of a reference model used for all subsequent analyses. This reference model employed *i*) geometric properties (area, centroid and second moment of area) averaged over a 10mm length, *ii*) 10 mm long force-based beam-column elements with three Gauss-Lobatto integration points, and *iii*) RGEs to link element end nodes and represent the eccentricity of the corroded section.

4.8. Discussion of analysis results and comparison with observed experimental results

4.8.1. Buckling response under monotonic loading

To investigate the factors that affect the buckling strength of corroded bars, experimental and simulation data were compared for specimens with different L/D ratios and mass loss ratios and for models with and without representation of section eccentricity resulting from corrosion. The models varied only in the representation of eccentricity; all the numerical models represented the loss in section area and second moment of area resulting from corrosion.

The data in Fig. 4.22 (a) shows the load-displacement response for a bar with L/D = 20 and a mass loss ratio of 34.91%. These data show that if the reduction in cross section area and second moment of area are included in the simulation, a 46% reduction in peak buckling load is predicted; if these factors, as well as load eccentricity, are included in

the simulation, a 73% reduction in peak buckling strength is predicted. The data also show that even with load eccentricity included in the model, the predicted buckling strength is 18% greater than the measured strength. This is attributed to the irregular cross sectional shape of the pitted sections. This results in stress concentration at pitted sections and subsequently premature yielding of the section. This phenomenon then results in an additional imperfection in the bar under compression which affects the buckling load capacity. As expected, it was observed that the influence of cross section shape is a function of the mass loss and slenderness ratio. Finally, the data in Fig. 4.22 (a) show that while the model over-predicts the maximum buckling strength, the post-buckling response is accurately predicted using the model with or without simulation of load eccentricity.

Fig. 4.22 (b) and (c) show simulated and experimental response for bars with L/D = 15 and 10, respectively. In these figures, simulation results include consideration of the impact of corrosion on area, second moment of area and load eccentricity. For these tests, the maximum simulated strength exceeds the measured strength by 16% for L/D = 15 and 10% for L/D = 10. This shows that the difference between the simulated and experimental results becomes smaller with a reduction in the slenderness ratio of the corroded bars. However, as the slenderness ratio of bars reduces the contribution of cross section shape to the overall reduction of buckling load increases. In other words, as the slenderness ratio of the bars increases the impact of imperfections (induced by the combined effects of changes to the cross sectional shape and second moment of area) on the buckling load increases.

Comparison of Fig. 4.22 (b) and (c) with Fig. 4.22 (a) shows that a bigger mass loss ratio results in more severe localised pitting corrosion and subsequently degrades the geometrical properties of pitted sections more significantly. This will increase the imperfection in the bar as changes to the second moment of area and cross section shape have a more significant effect on the bars with a bigger slender ratio. Whereas in the shorter bars, the influence of second moment of area is less visible and the main parameter governing the buckling load reduction is the premature yielding of pitted sections due to stress concentration. Finally, the data in Fig. 4.22 (a), (b) and (c) show that while corrosion reduces buckling strength, it does not significantly affect the shape of the post-peak response curve and that the numerical model, with or without simulation of eccentricity, accurately simulates post-peak response.

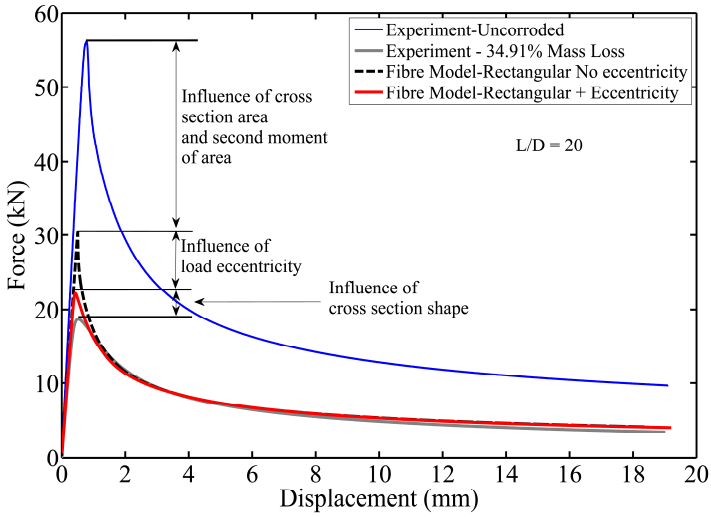
Experiment-Uncorroded
Experiment - 34.91% Mass Loss
Fibre Model-Rectangular No eccentricity
Fibre Model-Rectangular + Eccentricity
Influence of cross section area and second moment of area
L/D = 20
Influence of load eccentricity
Influence of cross section shape
Force (kN)
Displacement (mm)

(a)

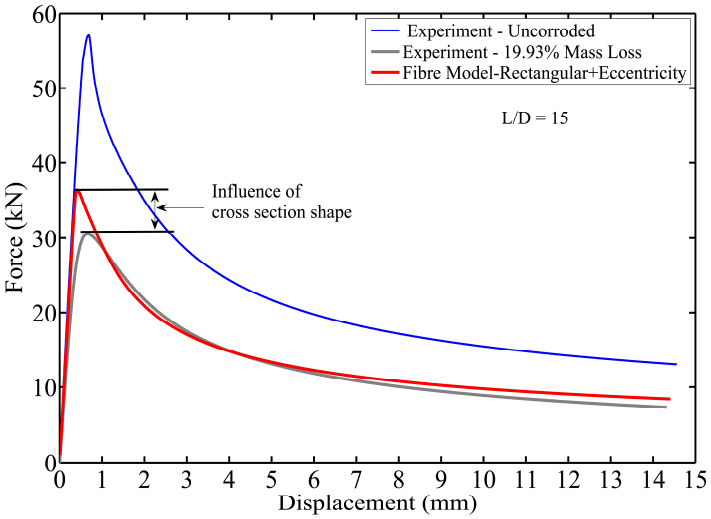
Experiment - Uncorroded
Experiment - 19.93% Mass Loss
Fibre Model-Rectangular+Eccentricity
L/D = 15
Influence of cross section shape
Force (kN)
Displacement (mm)

(b)

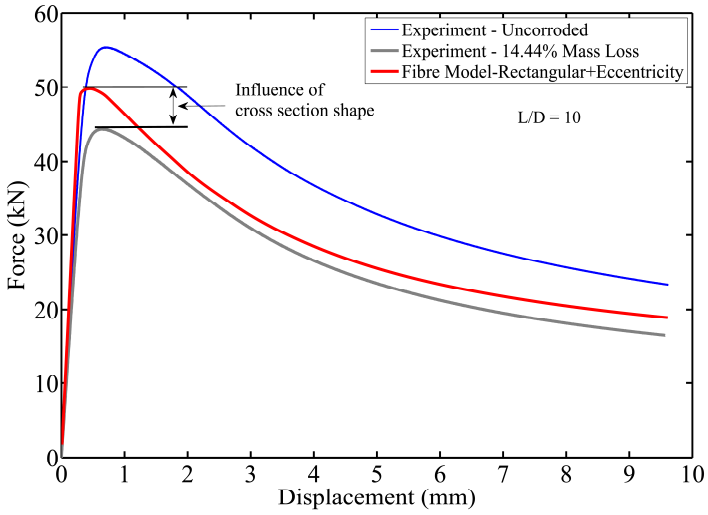

(c)

Fig. 4.22 Comparison of the simulated and experimental results of corroded bars: (a) corroded bar with *L/D* = 20 and 34.91% mass loss (b) corroded bar with *L/D* = 15 and 19.93% mass loss (c) corroded bar with *L/D* = 10 and 14.44% mass loss

4.8.2. Buckling response under cyclic loading

Experimental and computational results are compared for corroded bars with different corrosion patterns along the length of the corroded bars. Here the uniformity of the corrosion pattern is quantified by considering the ratio of the minimum cross section area to the maximum cross section area along the gauge length defined in Eq. (4.20).

$$\zeta = \frac{\text{Minimum Cross Section Area } \left(A_{\min}\right)}{\text{Maximum Cross Section Area } \left(A_{\max}\right)} \tag{4.20}$$

It is possible if $\zeta > 0.8$, the specimen can be considered to be uniformly corroded and if $\zeta < 0.8$, the specimen can be considered to have localised pitted section(s). This assumption is in good agreement with the observed experimental results and the results reported by other researchers (Du et al. 2005a,b, Palsson and Mirza 2002). Fig. 4.23 shows the variation of the cross section area of two specimens with relatively similar mass loss ratios and different corrosion patterns. Fig. 4.23 (a) shows a uniformly distributed area loss with $\zeta = 0.80$ and Fig. 4.23 (b) shows a specimen with localised pitting with $\zeta = 0.67$.

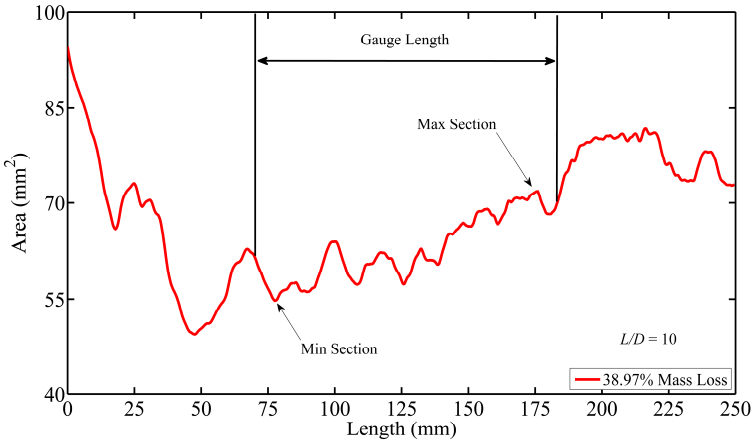

(a)

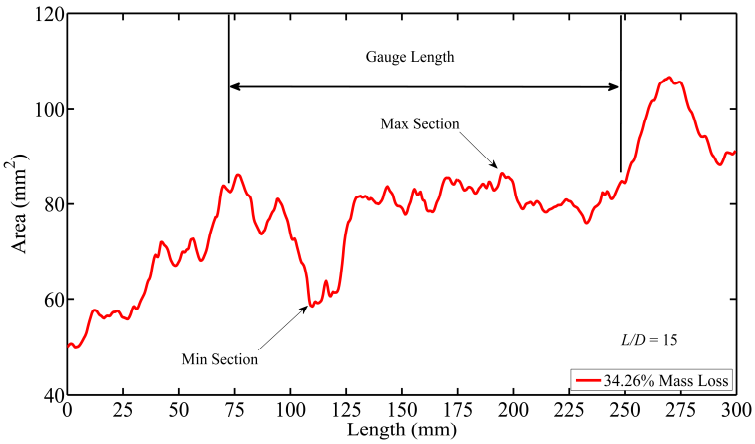

(b)

Fig. 4.23 Comparison of the uniform and localised pitting: a) corroded bar with L/D = 10 and 38.97% mass loss, b) corroded bar with L/D = 15 and 34.26%

Fig. 4.24 (a) shows the experimental and simulation results for the cyclic loading of a corroded bar with a relatively uniform pattern of pitting corrosion, (specimen in Fig. 4.23 (a)); Fig. 4.24 (b) shows results for a corroded bar with a relatively non-uniform pattern of pitting corrosion, (specimen in Fig. 4.23 (b)). Fig. 4.24 shows that for a bar with a relatively uniform pattern of corrosion, the model provides reasonably accurate simulation of response, with two exceptions. The numerical model overestimates the compressive strength by as much as 10%; as with monotonic loading, this is attributed to the irregular cross section shape effect. As the cyclic displacement demands increases, the experimental data show deterioration in the tensile strength and, ultimately, complete strength loss due to bar fracture. Strength loss is attributed to low-cycle fatigue with the experimental results showing that corrosion reduces the low-cycle fatigue life of

the reinforcement. Strength degradation due to low-cycle fatigue is not captured by the numerical model; thus degradation of tensile strength is not simulated.

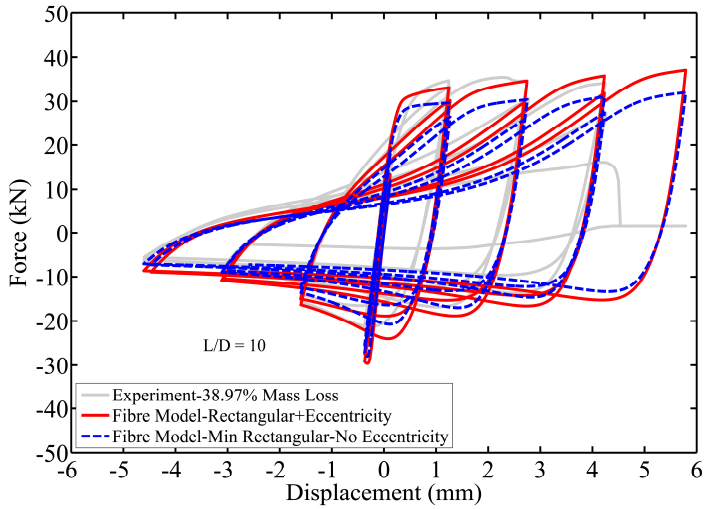

(a)

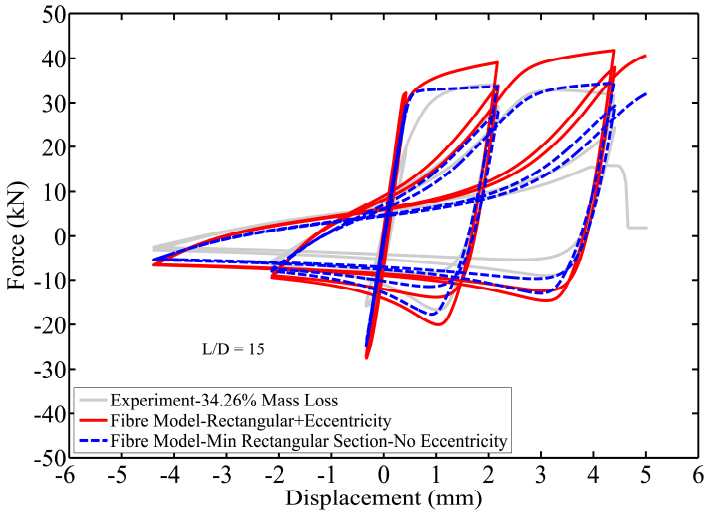

(b)

Fig. 4.24 Comparison of the simulated and experimental results of a corroded bar under cyclic loading: (a) L/D = 10 with 38.97% mass loss and (c) L/D = 15 with 34.26% mass loss

When the irregularity of corrosion along the bar increases, the differences between the computed and experimental responses increase. Fig. 4.24 (b) shows the computed and experimental response for a bar with severe localised pitting corrosion (ζ = 0.67). Simulation data are provided for the reference model described above as well as for a model in which the cross section of the bar is constant over the length of the bar and the minimum measured bar area and second moment of area are used. Using the reference

model, the tensile and compressive strength are overestimated. Using the minimum-section model, the computed response is in very good agreement with the observed experimental response. This supports the conclusion of Chapter 3, that the nonlinear cyclic behaviour of corroded bars with localised pitting corrosion is mainly governed by the inelastic response of the minimum pitted section.

It is evident from Fig. 4.24 (a) and Fig. 4.23 (a) that the plastic hinging mechanism of the bar starts at the location of the minimum pitted section which is then followed by severe inelastic buckling in compression. This mechanism results in a significant stress concentration at the minimum pitted section which subsequently increases the total strain amplitude at this location during the cyclic tests. This will cause the premature fracture of bar in tension due to a reduced low-cycle high-amplitude fatigue life.

It should be noted that the location of the minimum section is also very important. In the test specimen shown in Fig. 4.24 (b), the minimum section is located very close to the mid height of the bar. This resulted in initiation of the buckling at that location. Another example is shown in Fig 4.25 where $\zeta = 0.70$ and the minimum section is located very close to one of the test machine grips. Even though this specimen has significant localised pitted the response is not governing by the minimum section (Fig. 4.25 (a)). It is clearly shown in Fig. 4.25 (b) and (c) that a plastic hinge has formed at the location of the minimum section but the bar didn't fracture at that location. This corrosion pattern resulted in an unsymmetrical buckling mode shape as reported previously in Chapter 3. Due to the increase in the local strain amplitude at the buckling location the low-cycle fatigue life of this specimen is shortened. As a result, the specimen fractured at the buckling location instead of at the minimum section. It is evident from Fig. 4.25 (a) that, in this case, the numerical model using the minimum cross section is underestimating the capacity and predicts more of a pinching effect in the response. However, the detailed model shows a very good fit to the observed experimental response.

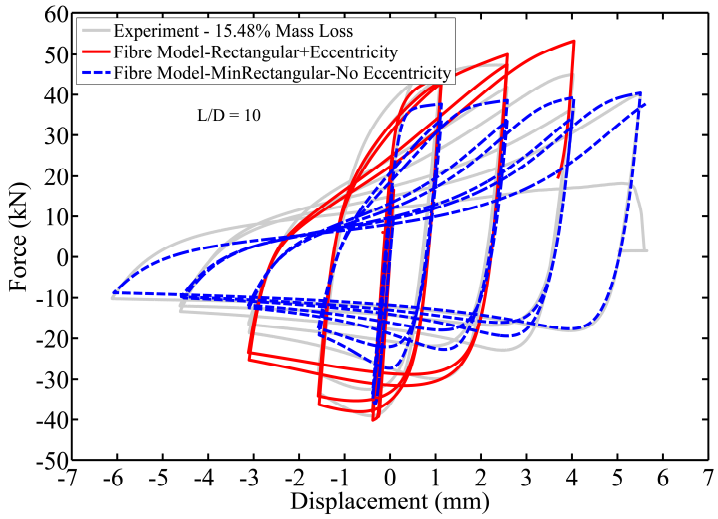

(a)

(b)

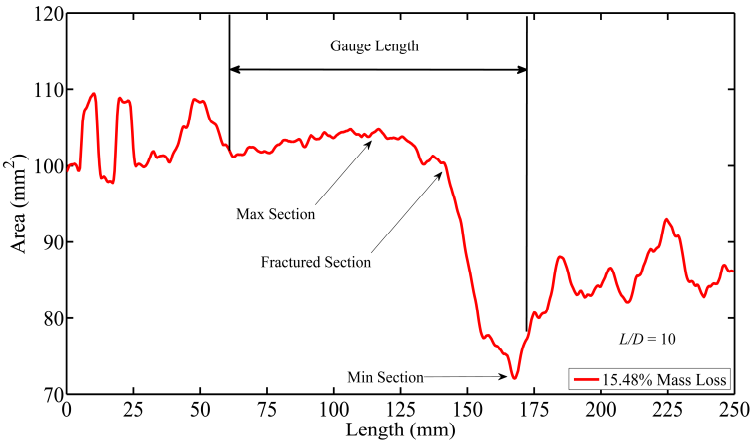

(c)

Fig. 4.25 Comparison of the simulated and experimental results of a corroded bar under cyclic loading: (a) L/D = 10 with 15.48% mass loss (b) fractured bar at the end of the cyclic test (c) variation of the cross section area along the bar

4.9. Critical review of the existing analytical models and comparison with the experimental and computational results

In this section a comprehensive review of the existing analytical models of reinforcing bars with the effect of buckling and low-cycle fatigue is conducted. A comparison between the observed experimental response, detailed FE analysis and the empirical analytical models is conducted and critical issues are reported.

4.9.1. Analytical modelling of cyclic behaviour of corroded bars including buckling and low-cycle fatigue

There are currently a number of analytical models available in the literature for cyclic stress-strain response of uncorroded reinforcing steel with and without buckling (Monti and Nuti 1992, Dodd and Restrepo 1995, Gomes and Appleton 1997, Balan et al. 1998, Rodriguez et al. 1999, Bae et al. 2005, Hoehler and Stanton 2006 and Kunnath 2009). The effect of corrosion on the behaviour of uncorroded and corroded reinforcing bars subject to low-cycle fatigue loading has also been studied by other researchers (Chang and Mander 1994, Higai 2006 and Apostolopoulos and Papadopoulos 2007). The combined effect of low-cycle fatigue degradation and inelastic buckling of corroded reinforcing bars subject to cyclic loading is studied and a modelling methodology is devopled.

In the low-cycle fatigue model (developed in Chapter 3 of this thesis) the experimental data reported by Apostolopoulos and Papadopoulos (2007) is used for model calibration. To model the cyclic behaviour of corroded bars the reinforcing steel model developed by Kunnath et al (2009), which is currently available in the OpenSees, has been modified. The original model consists of a low-cycle fatigue degradation model in tension and the Dhakal-Maekawa buckling model in compression. It also includes the GMP cyclic rules to model the Bauschinger effect. In this research the combined effect of low-cycle fatigue degradation and the corrosion extended buckling model (also developed in Chapter 3) is incorporated and simulated in OpenSees. A qualitative comparison between the experimental and analytical cyclic mean stress-strain response of a corroded bars with L/D = 10 is shown in Fig 4.26. Previously in Fig. 3.28 (b) of the Chapter 3 is shown that the Kunnath et al (2009) model can accurately predict the response of a corroded bar with $L/D = 5$ where the buckling of bar does not have a significant influence on the degradation of the hysteretic cycles. However, as the slenderness ratio of the bars increases the accuracy of the proposed corrosion extended model based on Kunnath et al (2009) reduces. Fig. 4.26 is an example comparison of this model with the observed experimental response of a corroded bar with L/D = 10.

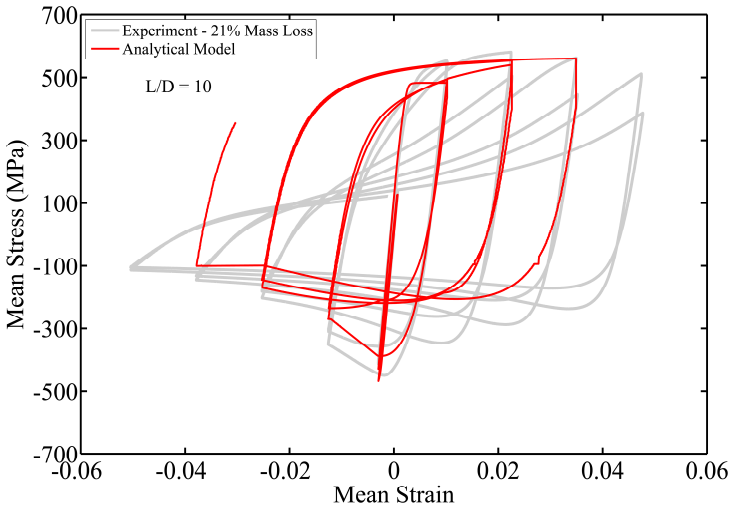

(b)

Fig. 4.26 Comparison of the corrosion extended Kunnath et al. model and experimentally observed response of a corroded bar with L/D = 10 and 21% mass loss

As discussed in Section 4.7 the pinching effect in the cyclic stress-strain curve of the reinforcing bars is due to inelastic buckling and geometrical nonlinearity. In other words, as the slenderness ratio of the reinforcing bars increases the hysteretic response changes towards a nonlinear beam-column element type response (e.g. concentric steel bracing). This has also been reported by other researchers (Nakamura and Higai 2002) and their conclusions are in a good agreement with the results of this study. This phenomenon is more critical in corroded bars where non-uniform pitting corrosion can result in a significant change to the effective slenderness ratio of reinforcing bars and subsequent degradation of the hysteretic response.

In this chapter the influence of different parameters on the inelastic behaviour of corroded bars under monotonic and cyclic loadings are discussed. As discussed in the previous sections, the irregularity in shape and the distribution of pitted sections along the bars has a significant impact on the buckling and fracture mechanism of corroded bars. Due to the random nature of the corrosion phenomenon and significant uncertainties associated with the corrosion pattern, it is almost impossible to quantify the irregularity of pitted sections with a deterministic approach. Moreover, it the real world, it is very challenging to measure the area loss and the locations of maximum/minimum pitted sections in an inspection of bridges using a non-destructive method; i.e. in a bridge pier. However, with the help of recent new technologies in bridge inspection, it is possible to measure the corrosion rate at any given location in a RC component (Broomfield 2007). Using the corrosion rate measurement data it is very simple to calculate the average mass loss of reinforcing bars. Therefore, it is very useful to relate all the models to a single measurement parameter such as the percentage mass

loss. To do this, an empirical approach using the experimental results should be used to model the average behaviour of corroded bars. Using this method it is possible to adopt a pseudo stress-strain curve which is a function of the average percentage mass loss of the corroded bars. In this method the yield and ultimate strengths are adjusted empirically to account for pitting effects. This is sufficient to investigate the global structural response of bridges/structures under vehicle and/or earthquake loading. If further detailed modelling is required, (for example a detailed model of a corroded RC bridge pier) it is then possible to model the spatial variability of the corrosion pattern probabilistically using the models developed in Section 4.4

However, with reference to Fig. 4.26, it is evident that there is need for further analytical research to develop a new uniaxial material model for reinforcing bars that accounts for the influence of inelastic buckling on degradation of the hysteretic cycles. Therefore, a new phenomenological model is developed in Chapter 5 and implemented into the OpenSees.

4.10. Conclusions

The non-uniform pitting corrosion pattern of reinforcement subjected to accelerated corrosion has been measured using a 3D optical scanning technique. The data generated by the optical measurement has been used in spatial-domain stochastic corrosion pattern analysis and uncertainty modelling of the corroded sections.

Moreover, the influence of corrosion patterns on the inelastic buckling and cyclic behaviour of corroded bars has been investigated computationally. The key parameters affecting the inelastic buckling and hysteresis behaviour of corroded bars have been identified. A critical review of the existing analytical material models and a comparison with the results of computational modelling and physical testing has been conducted.

The key outcomes from this chapter can be summarised as follows:

1. It was found that the frequency of the corrosion pattern ranges from 0.0071mm^{-1} to 0.0055mm^{-1} and is independent from the mass loss ratio and the length of the bars. This shows that the corrosion frequency is a time-invariant variable. In other words the frequency of corrosion depends on the nature of corrosion not the duration of corrosion. However, this conclusion is drawn based on the results of this experimental programme. Further research is required for investigation of the influence of other parameters such as corrosion rate, exposure type and concrete mix on the frequency of the corrosion pattern.

2. Based on the regression analysis of the maximum cross section loss, it was found that the pitting effect is function of the mass loss ratio. Therefore, this is a time-variant phenomenon.

3. A statistical analysis, based on null hypothesis tests, showed that the lognormal distribution model can represent the non-uniform distribution of geometrical properties of corroded bars including the pitting effect.

4. The probabilistic models developed in this chapter are based on accelerated corrosion tests and there is a need for further model calibration and comparison of these models with naturally corroded bars. Nevertheless the results of previous experimental studies (Palsson and Mirza 2002, Zhang et al. 2012) showed that the response of accelerated and naturally corroded bars with similar mass loss ratios is similar in tension tests.

5. A nonlinear fibre beam-column element can accurately simulate the nonlinear behaviour of reinforcing bars subject to monotonic and cyclic loading. It should be noted that the basic *Steel02* model is not able to capture the low-cycle fatigue degradation of the reinforcing bars. Apart from this, the qualitative fit of the numerical and experimental models are very good. This method can be used as a computational tool in the future research to generate further data for development and calibration of new analytical models.

6. It was observed in both experimental and computational responses that the cyclic degradation of the compressive strength of reinforcing bars with $L/D > 8$ is a function of the previous strain history in tension. This conclusion agrees with the results obtained by others (Prota et al. 2009, Moyer and Kowalsky 2003).

7. The correlations between the change in geometrical properties and the length of the bars were investigated by calculation of the ACF for each corroded bar and the CCF for pairs of corroded bars. It was found that the correlation coefficient is always more than 0.7 over a critical length L_c = 10mm. Therefore, this can be used in probabilistic modelling of corroded bars using the probabilistic models developed in this chapter. The results of mesh sensitivity and averaging length analysis showed that considering L_c = 10mm provides the desired accuracy of the nonlinear finite element analysis of corroded bars and is computationally very efficient.

8. As the slenderness ratio of bars increased, the contribution of changes to the combined cross section area and the second moment of area to the overall buckling load reduction increased. It was found that the influence of cross irregular cross sectional shape is not significant in these cases. However, it was found that by

reducing the slenderness ratio the irregular cross sectional shape has more significant influence on the overall buckling load.

9. It was observed that the cyclic response of corroded bars with severe localised pitting is mainly governed by the premature yielding of the minimum pitted section.

10. The analytical buckling model that is developed based on Dhakal-Maekawa model in Chapter 3 can accurately predict the post-yield buckling behaviour of corroded bars under monotonic compression. However, the pinching effect and cyclic degradation of the compressive strength of reinforcing bars with $L/D > 8$, due to the influence of geometrical nonlinearity, is not included in this model. Therefore, there is a need for further analytical study and development of a new phenomenological hysteretic model to account for these effects. This is discussed in the Chapter 5 of this thesis where a new phenomenological hysteretic model is developed that is able to capture this behaviour.

This page is intentionally left blank.

CHAPTER 5

A New Phenomenological Material Model for Reinforcing Bars

5.1 Introduction

Nonlinear analysis of reinforced concrete (RC) structures subject to seismic loading often employs fibre-type section models to simulate the flexural response of beams, columns and walls. These fibre-type section models are typically used within a plastic hinge or a lumped-or distributed-plasticity beam-column element (Spacone et al. 1996a,b). Examples include implementations in OpenSess, SeismoStruct and SAP2000 (OpenSees 2012, SeismoStruct 2013, SAP2000 2013). Using a fibre-type section model, the member cross section is decomposed into a number of steel and concrete fibres. The material nonlinearity is represented through uniaxial constitutive models for steel and confined and unconfined concrete. Therefore, the accuracy of the model is highly dependent on the accuracy of the uniaxial constitute models.

Previous research shows that fibre-type section models and lumped or distributed plasticity elements can provide highly accurate simulation of the stiffness, strength and cyclic response of RC members under moderate deformation demands (Berry and Eberhard 2003, Berry et al. 2008). However, few studies have addressed simulation of response due to loss of lateral and, ultimately, axial load carrying capacity; and few studies have demonstrated accurate simulation of drift capacity (i.e. the drift at onset of significant lateral strength loss) (Pugh 2012).

For RC members responding in flexure, strength loss typically results from buckling of longitudinal reinforcement, fracture of longitudinal reinforcing due to low-cycle, high-amplitude fatigue and/or crushing of the confined core concrete. The research presented here focuses on simulating the behaviour of reinforcing steel with the objective of enabling accurate simulation of component failure.

In previous decades, a number of researchers developed models to simulate the cyclic behaviour of reinforcing steel with and without buckling (Monti and Nuti 1992, Chang and Mander 1994, Apleton and Gomes 1995, Dodd and Restrepo 1995, Pantazopolou 1998, Balan et al. 1998, Rodruiguez 1999, Bayrak and Sheikh 2001, Dhakal and Maekawa 2002a,b,c, Bae et al. 2005, Hoehler and Stanton 2006, Cosenza and Prota 2006, Kunnath et al. 2009). Some of these models simulate the impact of low-cycle high-amplitude fatigue (Chang and Mander 1994, Kunnath et al. 2009) on the steel response. Most of these models were developed using data from bare-bar tests (i.e. tests of isolated reinforcing bars not embedded in RC). For these models, buckling strength and post-buckling strength loss is defined as a function of L/D, where L is the buckling length and D is the diameter of the longitudinal bars. However, as these models were developed using bare-bar data, they do not capture the impact of the concrete and transverse reinforcement on the stress-strain behaviour of reinforcing bars embedded in RC. Among the previously proposed models, only the Dhakal and Maekawa (2002a,b,c) model relates the behaviour of bare bars to that of embedded bars. Specifically, Dhakal and Maekawa provide recommendations for the definition of L, the effective buckling length of a bar embedded in RC, which is a function of the transverse reinforcement configuration. This L is used to determine the buckling strength and post-buckling strength loss.

The models noted above address simulation of uncorroded reinforcement; however, there are many critical structures that are located in regions of high seismicity and that are exposed to corrosive environments. Recent experimental studies of the cyclic behaviour of RC elements with corroded reinforcement show that corrosion has a significant impact on the response of these structures (Ou et al. 2011, Ma et al. 2012). The experimental results showed that corrosion will change the failure mode of flexural RC components. In some cases severe buckling were observed due to the combined effect of nonuniform pitting corrosion along the longitudinal reinforcement and corrosion of the

horizontal ties. Corrosion reduces the stiffness of the horizontal ties that are very important elements for preventing the buckling of the longitudinal bars. Once corroded bars buckle under cyclic loading, they fracture much faster at lower drift demands. This is due to the combined effect of buckling and nonuniform pitting corrosion that results in a significant reduction in low-cycle fatigue life corroded RC elements. Accordingly, a comprehensive experimental and computational study of the inelastic behaviour of corroded reinforcing bars, including the impact of corrosion on inelastic buckling and degradation due to low-cycle fatigue is conducted in Chapters 3 and 4 of this thesis.

In this chapter a new phenomenological hysteretic model is proposed to provide improved simulation of the buckling response of reinforcing steel with and without corrosion damage. The model accounts for the combined effect of inelastic buckling and low-cycle fatigue. In addition, the proposed model accounts for the influence of corrosion damage on inelastic buckling and low-cycle high-amplitude fatigue degradation of reinforcing bars. The model is calibrated and validated against an extensive experimental and computational dataset. This constitutive model has been implemented in OpenSees to enable the earthquake engineering community to use it in the nonlinear seismic analysis of uncorroded and corroded RC structures. Finally, the model implemented in OpenSees is validated against an experimental dataset for RC columns (UW-PEER 2004). A comparison is made between the new phenomenological material model and the other uniaxial material models for reinforcing steel available in the OpenSees. Furthermore, a comprehensive parametric study is conduced and optimum buckling parameters are quantified.

5.2 Modelling the cyclic buckling response of reinforcement without corrosion damage

Several researchers have studied the nonlinear cyclic behaviour of reinforcing bars experimentally and numerically (Monti and Nuti 1992, Dodd and Restrepo 1995, Gomes and Appleton 1997, Rodriguez et al. 1999, Nakamura and Higai 2002, Prota et al. 2009). In Chapter 4 a parametric study of the nonlinear cyclic behaviour of reinforcing bars with and without corrosion damage was conducted. The results of computational modelling showed that increasing the L/D ratio beyond 8 in reinforcing bars with yield strength between 400MPa and 500MPa results in a complex pinching effect in the hysteretic cycles. This is the influence of geometrical nonlinearity on the cyclic response. Other researchers have also come to the same conclusion based on the experimental results (Nakamura and Higai 2002, Prota et al. 2009). This shows a stable pattern in cyclic behaviour of reinforcing bars including the effects of buckling. Chapter 4 made a comparison between the existing analytical models and the computational results. They

demonstrated that the pinching effect due to the geometrical nonlinearity is not included in the existing analytical models.

Fig. 5.1 (a-c) shows the experimental cyclic response of reinforcing bars with L/D = 5, 10 and 15 as reported in Chapter 3. These data show that buckling has a limited impact on the cyclic response of reinforcing bars with L/D = 5 but that cyclic buckling degrades strength and energy dissipation for bars with L/D = 10 and 15. Specifically, cyclic loading with increasing strain demand results in, (a) significantly reduced compressive (i.e. buckling) strength, (b) significantly reduced unloading and reloading stiffness for unloading from compression and going into tension, (c) somewhat reduced unloading and reloading stiffness for unloading from tension and going into compression, and (d) reduced tensile strength.

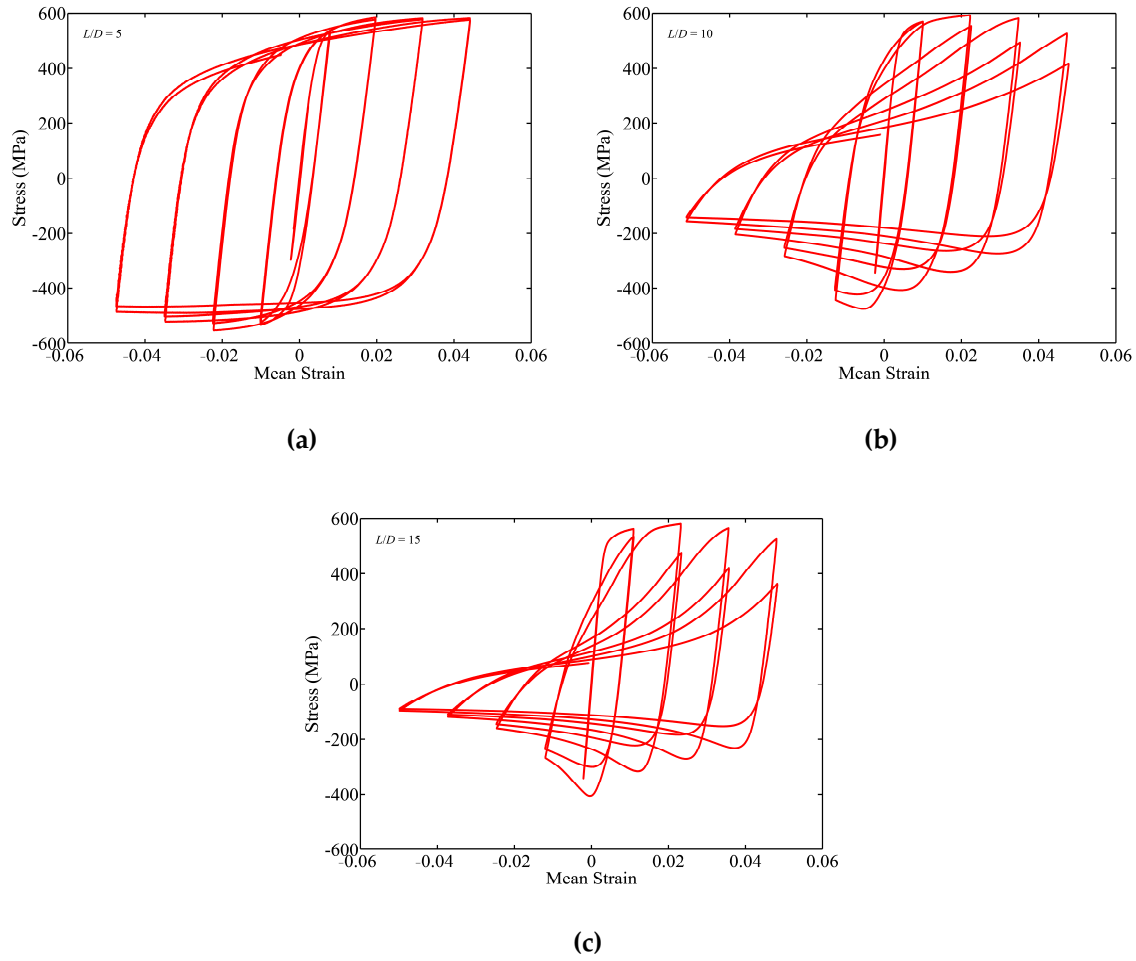

Fig. 5.1 Experimentally observed nonlinear cyclic response of reinforcing bars: (a) L/D = 5, (b) L/D = 10, (c) L/D = 15

The pinching effect in hysteretic cycles of longitudinal reinforcement has a significant influence on the cyclic degradation of the RC elements subject to seismic loading. Therefore, it needs to be considered in the material model of reinforcement in nonlinear

analysis of RC structures under cyclic loading. A set of cyclic rules have been developed in this chapter to capture this phenomenon.

5.2.1 Overview of the proposed model

The proposed model consists of eight main states. (1) tension envelope (TE), (2) compression envelope (CE), (3) unload-reload response for compression to tension (URCT), (4) unload-reload response for tension to compression (URTC), (5) incomplete unload-reload cycles (IURC), (6) degradation in buckling strength due to cyclic loading (BUCKDEG), (7) degradation in tension strength due to low-cycle fatigue/cyclic loading (FATDEG). An overview of the proposed model is shown in Fig. 5.2.

Table 5.1 summarises the analytical equations and calibration methods used for each of the states. A mixture of experimental and numerical data has have been used to calibrate the model parameter. The relevant references are also provided in Table 5.1.

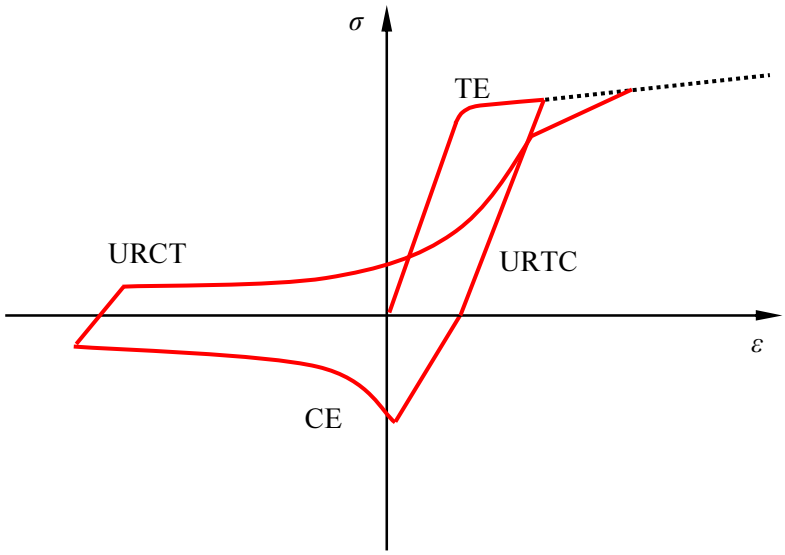

Fig. 5.2 Proposed phenomenological hysteretic model

To calibrate the model parameters in the proposed model a comprehensive set of experimental and numerical dataset, as reported by in Chapters 3 and 4, are used. The material data and mass loss ratios for both monotonic bucking and cyclic loading are available in Chapters 3. The numerical data used to calibrate the post-buckling behaviour is available in Chapter 4.

Table 5. 1 Summary of model states and calibration methods

State	Type of data used in calibration	Reference	Equation number in this chapter
TE	Experimental	(Chapter 3)	Eq. (5.1)
CE	Experimental and numerical	(Chapters 3 and 4)	Eq. (5.2) to (5.6)
URCT	Experimental	(Chapter 3)	Eq. (5.10) to (5.16)
URTC	Experimental and numerical	(Chapters 3 and 4)	Eq. (5.7) to (5.9)
IURC	Experimental	(Chapter 3)	Eq. (5.17)
BUCKDEG	Numerical	(Chapter 4)	Eq. (5.7)
FATDEG	Experiential	(Kunnath et al. 2009 and Chapter 3)	Eq. (5.24)

5.2.2 Modelling tension response

Several models available in the literature define the tension envelope for reinforcing steel (Menegotto and Pinto 1973, Dodd and Restrepo 1995, Balan et al. 1998, Hoehler and Stanton 2006, Kunnath et al. 2009). Here the equation developed by Balan et al. (1998), as shown in Fig. 5.3, is used:

$$\sigma_s = \sigma_y \frac{(1-\mu)}{2}\left[1+\frac{(1+\mu)}{(1-\mu)}\frac{\varepsilon_s}{\varepsilon_y}-\sqrt{\left(\frac{\varepsilon_s}{\varepsilon_y}\right)^2+\delta}\right] \tag{5.1}$$

where $\mu = E_h/E_s$ is the hardening ratio with E_s and E_h equal to the elastic modulus and hardening modulus for the steel, σ_y is the yield stress, and δ is a shape parameter. Eq. (5.1) represents a hyperbola with two asymptotes, one with slope E_s and one with slope E_h. This model is a continuous function that provides a smooth transition from linear elastic to strain hardening region. The shape parameter, δ, defines the curvature radius of the transition between linear elastic to hardening region of the curve. This will improve the numerical stability of nonlinear finite element analysis. Further details of this model are available in Balan et al. (1998).

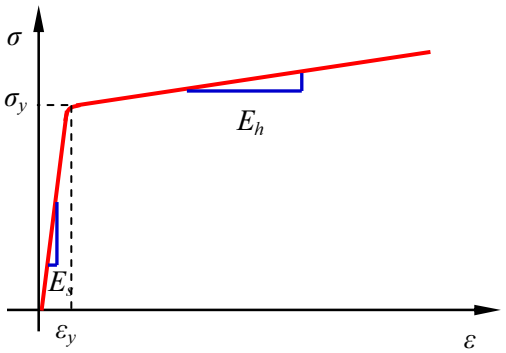

Fig. 5.3 Tension envelope model (Balan et al. 1998)

5.2.3 Modelling compression and buckling response

5.2.3.1 Previous research

Mau and El-Mabsout (1989) developed a special beam-column element for nonlinear finite element analysis of the inelastic buckling of reinforcing bars. This model can correctly simulate the inelastic buckling of a single reinforcement bar but it is computationally expensive for use in nonlinear analysis of RC structures. Monti and Nuti (1992) developed an analytical model based on experimental tests on reinforcing bars. This model is simple and suitable for incorporation into the computational section analysis that is found within a nonlinear analysis of RC structures and it uses a fibre-based section decomposition method. Bae et al. (1998) also developed an analytical model for inelastic buckling of reinforcing bars based on an experimental study of a number of single reinforcing bars with different *L*/*D* ratios and load eccentricities. In this model the post-yield buckling behaviour of the reinforcement is governed by the *L*/*D* ratio, the transverse displacement (horizontal displacement due to buckling) and yield stress σ_y. Dhakal and Maekawa (2002a,b) conducted nonlinear finite element analyses on single reinforcing bars with different *L*/*D* ratios using a fibre-based technique. They found that the post-yield buckling behaviour of reinforcing bars is governed by the combined influence of *L*/*D* ratio and the yield stress σ_y of the reinforcement. Considering this assumption, they have developed a trilinear analytical model to represent the post-yield buckling behaviour of reinforcing bars. In this model, the compression response of reinforcement is defined as a function of a single variable called the non-dimensional slenderness ratio λ_p as defined in Eq. (5.2) below:

$$\lambda_p = \sqrt{\frac{\sigma_y}{100}}\frac{L}{D} \tag{5.2}$$

where σ_y has units of MPa.

The yield stress of the most commonly used reinforcing bars in construction of RC structures around the world ranges between 400 MPa to 500 MPa. The experimental results and computational modelling of reinforcing bars for these bars showed that buckling is not critical for the groups of bars with $L/D \leq 6$ (Chapters 3 and 4). Therefore, they can be described in a similar manner to their tension behaviour. The group of bars with $6 < L/D < 8$ buckle under compression, however, given the buckling length is very small the influence of buckling on post-yield buckling doesn't result in a softening type behaviour. The behaviour of this group of bars in compression can therefore be described with an elastic perfectly plastic model. However, once the slenderness ratio exceeds $L/D \geq 8$ the inelastic buckling results in a post-buckling softening response. Accordingly, the proposed model in this paper is an extension to the Dhakal-Maekawa buckling model for reinforcing bars with $L/D \geq 8$. The parameters defining the post-yield buckling curve are similarly a function of the λ_p. Therefore, the methodology proposed by Dhakal-Maekawa (2002c) can be used to calculate the buckling length considering the influence of the stiffness of horizontal tie on buckling of vertical reinforcement.

5.2.3.2 Proposed model

The model proposed in this paper employs an exponential function to describe the post-yield bucking response of reinforcing bars as shown in Fig. 5.2. This approach has been used previously by others to model the inelastic buckling behaviour of concentric steel bracing (Hill et al. 1989, Thai and Kim 2011); here the post-buckling curve is defined by a smooth exponential curve as a function of compressive plastic strain (ε_p):

$$for \quad 8 \leq \frac{L}{D} \leq 30$$

$$\sigma = \begin{cases} E_s\,\varepsilon & \varepsilon \leq \varepsilon_y \\ \sigma^* + \left(\sigma_y - \sigma^*\right) \exp\left(-\left(\rho_1 + \rho_2\sqrt{\varepsilon_p}\right)\left(\varepsilon_p\right)\right) & \varepsilon > \varepsilon_y \end{cases} \tag{5.3}$$

where ρ_1 is the initial tangent of the post-buckling response curve, ρ_2 is the rate of change of the tangent, $\varepsilon_p = \varepsilon - \varepsilon_y$ is the plastic strain, σ^* is the asymptotic lower stress limit of the post-buckling curve, and all other variables are as previously defined. The parameters ρ_1, ρ_2 and σ^* are defined by the yield strength and geometrical slenderness ratio of the reinforcing steel, as discussed in the following section.

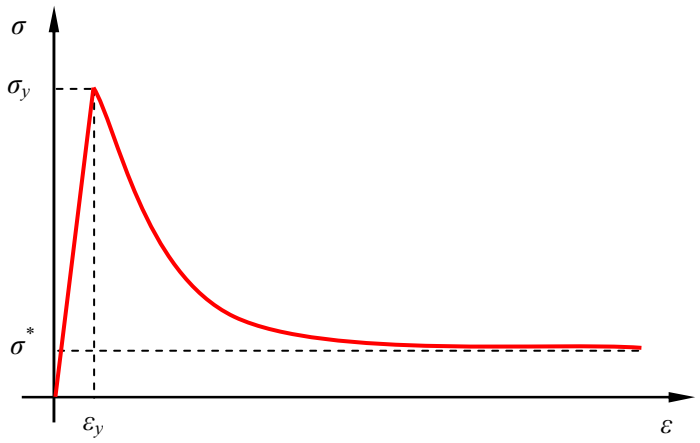

Fig. 5.4 Proposed analytical post-yield buckling envelope model

5.2.3.3 Calibration of the post-yield buckling response parameters

Nonlinear finite element analysis of isolated reinforcing bars subjected to monotonic compressive displacement histories was used to develop models defining the parameters ρ_1, ρ_2 and σ^* as a function of reinforcement yield strength and geometric slenderness ratio. Research by the author of this thesis and others validates this approach to model calibration (Dhakal and Maekawa 2002a,b, Nakamura and Higai 2002, Mau and El-Mabsout 1989). In this research, the OpenSees software platform and the co-rotational force-based fibre-type beam-column element were used; Chapter 4 provides a detailed discussion of the model. Approximately forty analyses were conducted for reinforcing bars with L/D varying from 8 to 30 and yield strengths ranging from 100 MPa to 600 MPa. The analysis data related to the post-buckling branch of each case was exported to MATLAB (MATLAB 2012). Using the CFT (curve fitting toolbox) available in MATLAB, Eq. (5.3) was fitted to each post-buckling response analysis curve. Using this approach the parameters ρ_1, ρ_2 and σ^* in Eq. (5.3) were optimised to provide the best fit to the simulated post-buckling response of the bar (Fig. 5.5 (a)). The optimised model parameters (ρ_1, ρ_2 and σ^*) for each analysis case from the curve fitting procedure were stored in a vector. Finally, regression analysis was used to determine the correlation between the model parameters and bar yield strength and geometrical slenderness ratio (λ_p). Ultimately, it was found that *i*) ρ_1 is strongly, positively correlated with λ_p, *ii*) ρ_2 is strongly negatively correlated with λ_p, *iii*) σ^* is minimally correlated with λ_p, and *iv*) σ^* is strongly positive correlation with σ_y /L/D. Fig. 5.5 (b-d) shows the model parameters determined from the simulation data as well as the models resulting from the regression analyses and correlation coefficients.

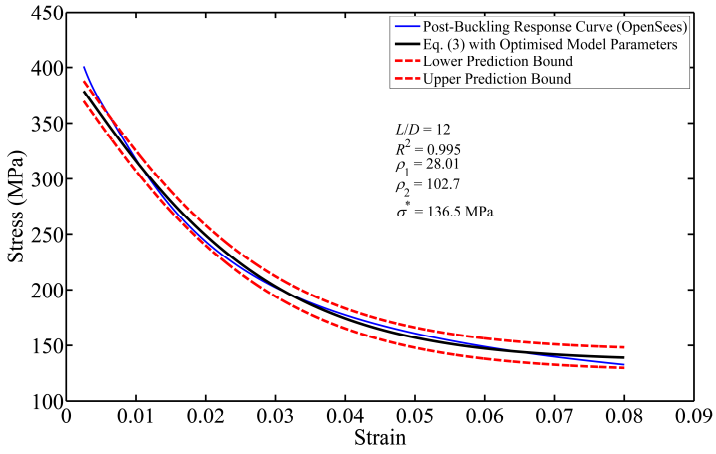

(a)

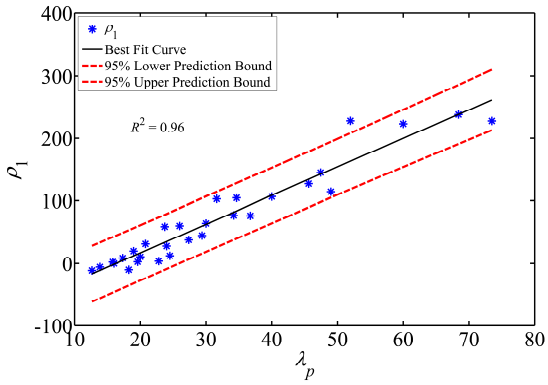

(b)

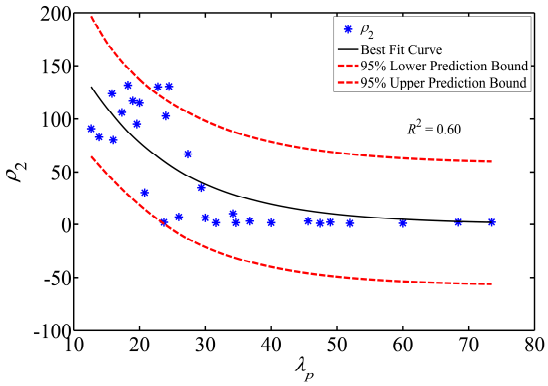

(c)

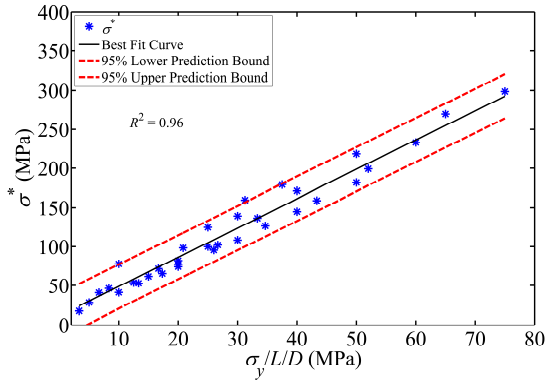

(d)

Fig. 5.5 Post-buckling model calibration: (a) best of Eq.(3) to post-buckling response of a reinforcing bar with L/D = 12 and σ_y = 400MPa and (b) ρ_1 c) ρ_2 d) σ^*

The regression analyses resulted in the following equations defining the buckling model parameters:

$$\rho_1(\lambda_p) = 4.572\lambda_p - 7443 \tag{5.4}$$

$$\rho_2(\lambda_p) = 31840\exp(-0.071\lambda_p) \tag{5.5}$$

$$\sigma^* = 3.75\ \frac{\sigma_y}{\frac{L}{D}} \tag{5.6}$$

The data in Fig. 5.6 show the influence of L/D ratio and σ_y on the model. The data in Fig. 5.6 (a) show that as L/D increases the initial slope of the post-yield buckling curve becomes increasingly negative and stress loss increases with strain. The data in Fig. 5.6 (b) show that as σ_y increases, strength loss due to buckling increases substantially at large strain demands.

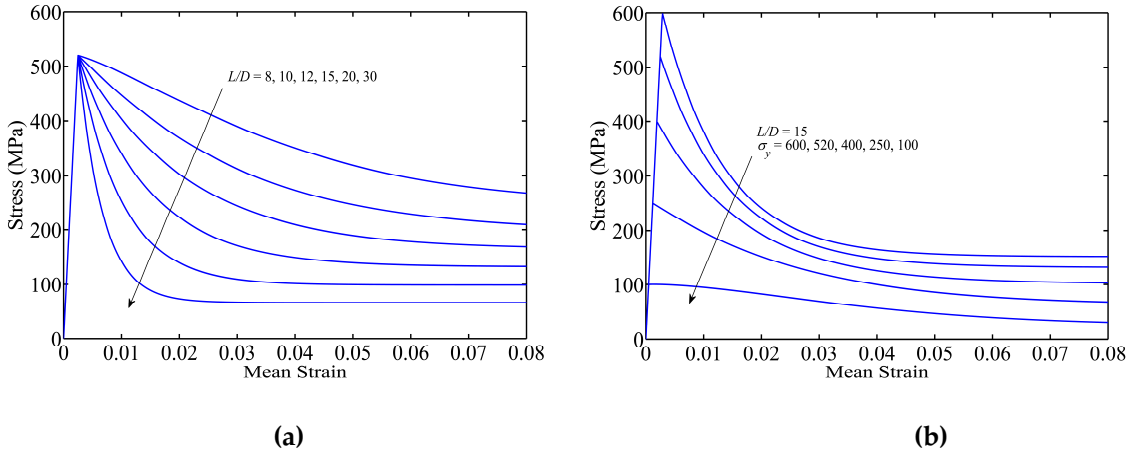

Fig. 5.6 Result of calibrated model: (a) influence L/D ratio on the model (b) influence of σ_y on the model

5.2.3.4 Model validation

Data from numerical simulations were used to calibrate the model parameters. The model was then validated using data from the experimental tests of isolated reinforcing bars reported in in Chapter 3 of this thesis. Fig. 5.7 (a-d) shows comparisons of the calibrated model, numerical simulation data and experimental data.

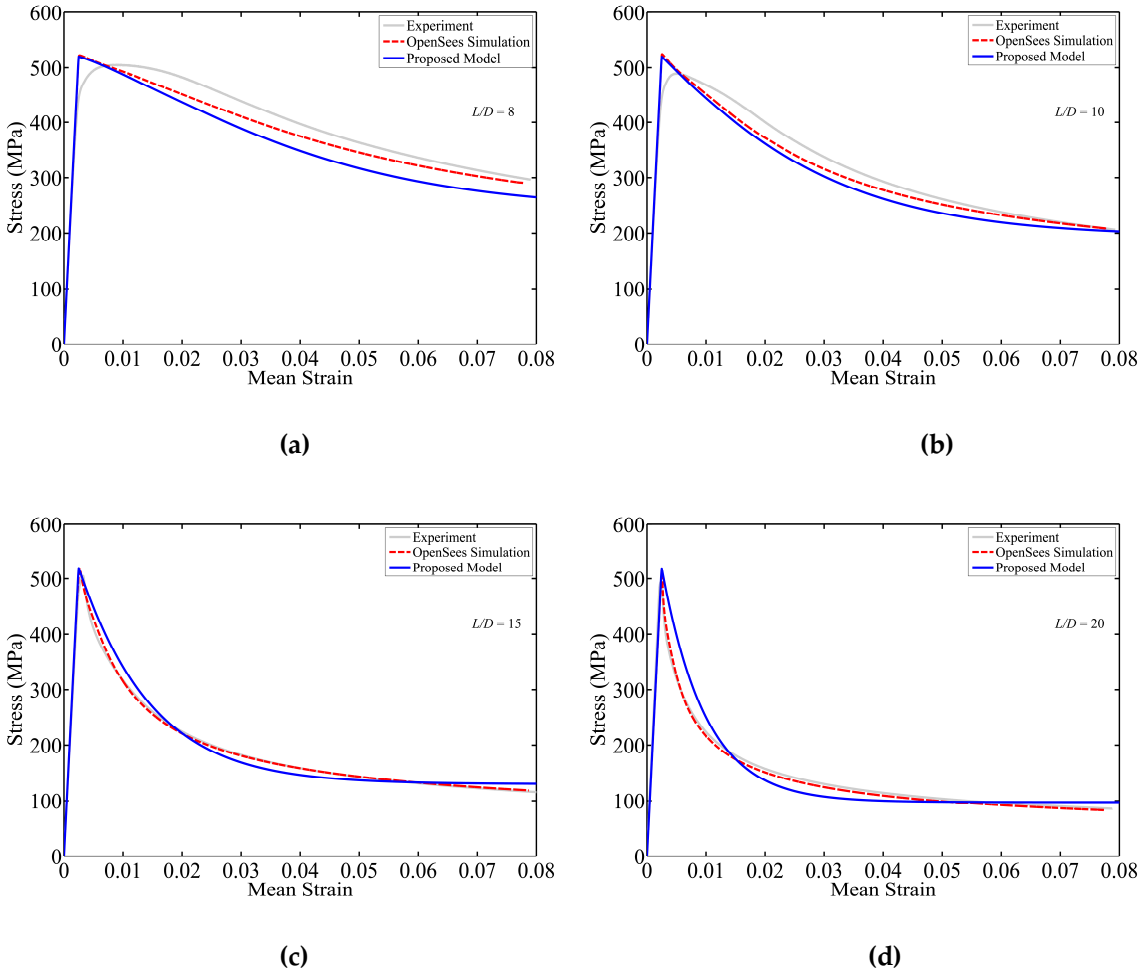

Fig. 5.7 Verification of the proposed analytical model: (a) L/D = 8 (b) L/D = 10 (c) L/D = 15 (d) L/D = 20

It should be noted that the experimental graphs shown in Fig. 5.7 were not included in the calibration process. Therefore, it is evident form Fig. 5.7 that the proposed model can accurately predict the post-yield buckling response of reinforcing bars.

5.2.4 Modelling nonlinear cyclic response

5.2.4.1 Degradation of buckling strength and unloading-reloading stiffness from tension to compression under cyclic loading

Previous research shows that under cyclic loading the buckling strength and unloading-reloading response from tension to compression of reinforcing bars is a function of the strain history. Experimental data show that the buckling strength of bare bars (Prota 2009) and bars embedded in RC columns (Moyer and Kowalsky 2003) is a function of the plastic tension strain history as well as the slenderness ratio. Dodd and Restrepo (1995) use data from bare bar tests to develop an empirical equation defining unloading stiffness, from tension to compression, as a function of plastic tension strain. Despite the

results of these previous research efforts, the impact of cyclic loading on buckling strength and unload-reload stiffness has not been incorporated in constitutive models for reinforcing steel.

For the current study, the results of nonlinear finite element analyses of bare reinforcing bars were used to develop data relating strain history to degradation of the buckling strength and unloading–reloading stiffness. A series of analyses were conducted for reinforcing bars with varying λ_p (Eq. (5.1)) and varying strain history. See Chapter 4 and for a description of the model and the analyses. Fig. 5.8 shows example simulation results for a reinforcing bar with $L/D = 20$ and $\sigma_y = 500$.

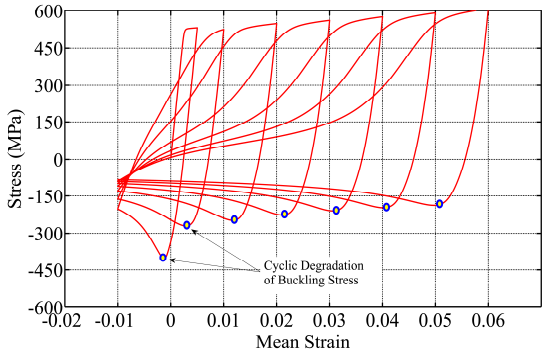

Fig. 5.8 Numerical simulation of cyclic degradation of buckling stress ($L/D = 20$)

Fig. 5.9 (a) shows the model parameters defining buckling strength and unload-reload stiffness. Simulation data and regression analysis were used to develop a model defining the degradation in buckling strength as a function of plastic strain demand in tension, ε_p, and the non-dimensional slenderness ratio, λ_p. Fig. 5.9 (b) shows buckling strength reduction under cyclic loading versus ε_p λ_p as determined from numerical simulation (blue data points) as well as the model resulting from regression analysis of the data (black line):

$$\frac{\sigma_{yc}}{\sigma_y} = \frac{1}{1+0.7\,\varepsilon_p\,\lambda_p} \qquad \sigma_{yc} \geq 0.25\,\sigma_y \tag{5.7}$$

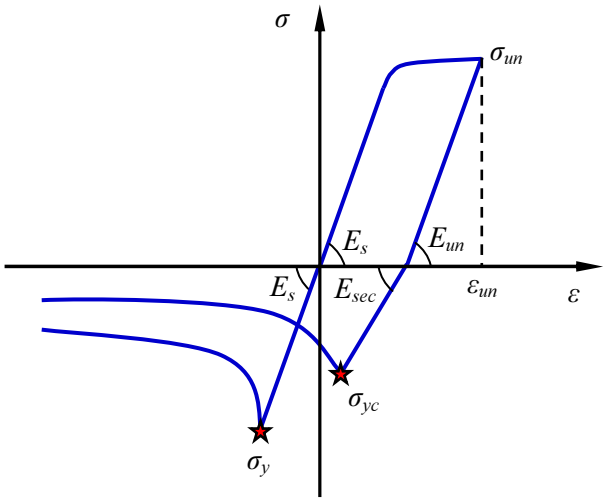

(a)

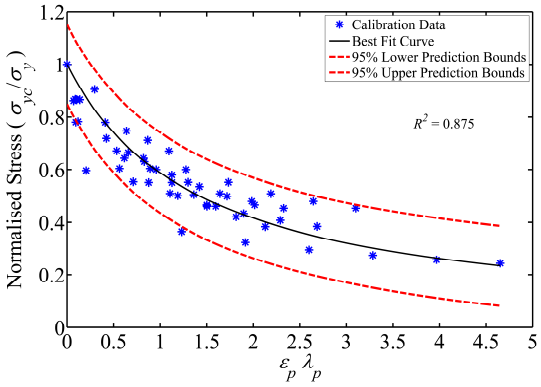

(b)

Fig. 5.9 Modelling tension unloading and compression reloading branch: (a) schematic view of model and (b) calibration of cyclic degradation of buckling stress

where σ_{yc} is the buckling strength under cyclic loading, σ_y is the buckling strength under monotonic loading (Eq. (5.7)), ε_p is the plastic strain in tension defined as $\varepsilon_p = \varepsilon_{un} - \varepsilon_y$ with ε_{un} equal to the maximum historic tension strain and ε_y equal to the yield strain, and λ_p is defined in Eq. (5.1).

The empirical equation proposed by Dodd and Restrepo (1995) (Eq. (5.8)) is used to define the unloading stiffness, E_{un}, and data from numerical simulations of bare bars were used to define the reloading stiffness, E_{sec}, for unloading from tension to compression (Eq. (5.9)). It was found that the following relationships provided a good fit to the numerical data.

$$\frac{E_{un}}{E_s} = 0.82 + \frac{1}{5.55 + 1000\varepsilon_p} \tag{5.8}$$

$$\frac{E_{sec}}{E_s} = \frac{1}{1+\left(\frac{\varepsilon_p}{0.005}\right)^{0.5}} \qquad E_{sec} \geq 0.2\,E_s \tag{5.9}$$

where, E_s is the elastic modulus and all other parameters are as previously defined.

5.2.4.2 Cyclic stiffness degradation of compression unloading and tension reloading

Fig. 5.1 shows experimental stress versus strain histories for isolated reinforcing bars with varying slenderness ratios. These data show that for slender bars ($L/D \geq 8$), unloading-reloading from compression to tension changes significantly with increasing strain demand. At small strain demands, the unloading-reloading branch is convex in shape. However as strain demand increases, the unloading-reloading response curve becomes concave and pinched. To capture this behaviour in the model, different equations are used for unloading at small and large stain demands. Similar behaviour was observed by other researchers (Nakamura and Higai 2002, Prota et al. 2009).

In the proposed model two types of curves are introduced at low and high strain demands. If unloading occurs at low strain demand ($\varepsilon \leq 9\varepsilon_y$) a trilinear curve, as shown in Fig. 5.10, is used.

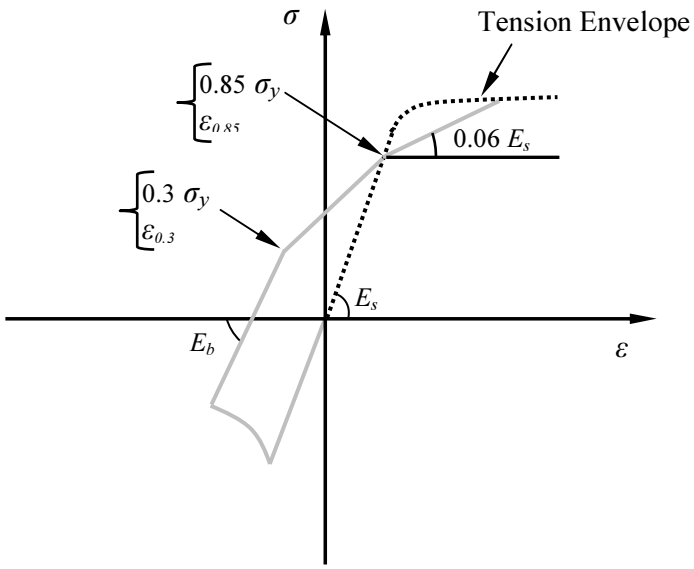

Fig. 5.10 Multi-linear curves to model compression unloading branch at small strain demand ($\varepsilon \leq 9\varepsilon_y$)

The concave shape of the compression unloading branch at large strain demand ($\varepsilon > 9\varepsilon y$) is modelled using linear-hyperbolic curves (Fig. 5.11). The initial unloading stiffness E_b can be calculated using Eq. (5.10).

$$\frac{E_b}{E_s} = \left(\frac{\sigma_{\min}}{\sigma_{t\min}} \right)^{1.5} \tag{5.10}$$

Where, σ_{min} is the minimum compressive stress at unloading and σ_{tmin} is the stress in the tension envelope corresponding to the strain at σ_{min} (Fig. 5.11 (a)).

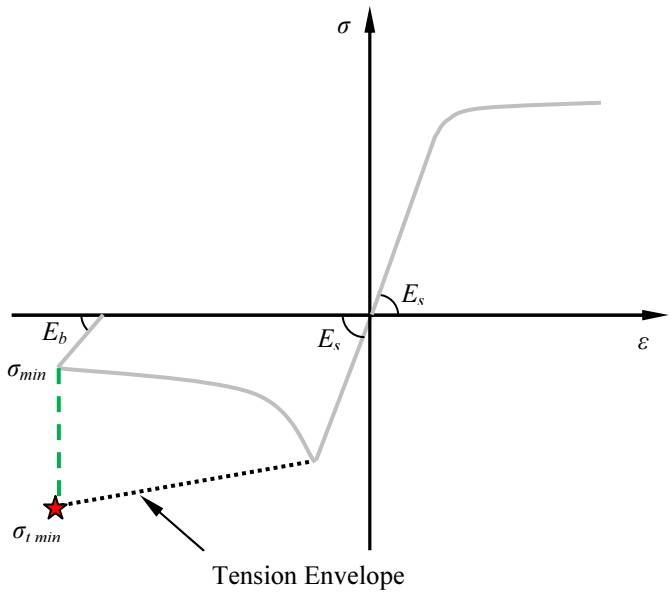

(a)

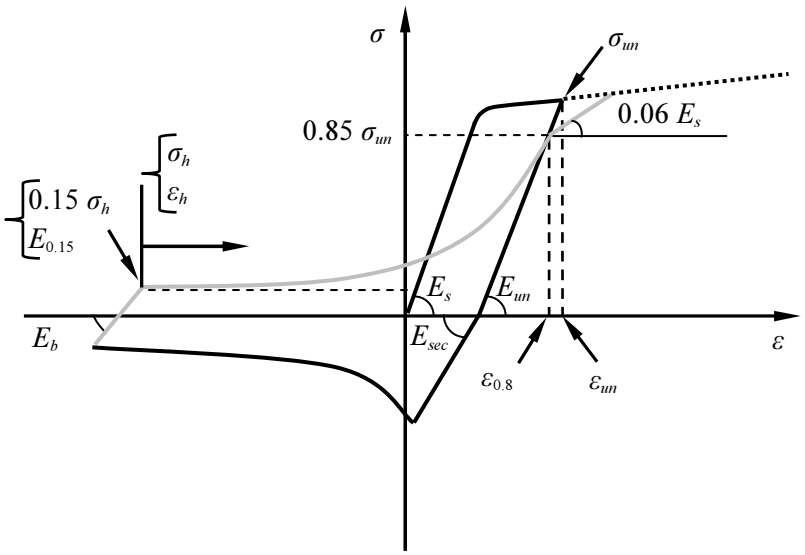

(b)

Fig. 5.11 Linear-hyperbolic curves to model compression unloading branch at large strain demand ($\varepsilon > 9\varepsilon_y$) : a) definition of the initial stiffness E_b and b) unloading-reloading rule

The hyperbolic curve between the point at 0.15 σ_y and 0.85 σ_y (Fig. 5.11 (b)) is defined in the following Eqs. (5.11) to (5.16) (Thai and Kim 2011).

$$\sigma_h = \frac{\varepsilon_h}{\eta_1 + \eta_2 \varepsilon_h} \tag{5.11}$$

$$\begin{cases} \eta_1 = \dfrac{1}{0.03 E_s} & \lambda_p \le 45 \\ \eta_1 = \dfrac{1}{0.015 E_s} & \lambda_p > 45 \end{cases} \tag{5.12}$$

$$\eta_2 = \frac{1}{0.15\sigma_y - 0.85\sigma_y} - \frac{\eta_1}{\varepsilon_{0.15} - \varepsilon_{0.85}} \tag{5.13}$$

$$\varepsilon_{0.85} = \varepsilon_{un} - \frac{\sigma_{un} - 0.85\sigma_y}{E_{un}} \tag{5.14}$$

$$\sigma = \sigma_h + 0.15\sigma_y \tag{5.15}$$

$$\varepsilon = \varepsilon_h + \varepsilon_{0.15} \tag{5.16}$$

5.2.4.3 Unloading rules from URCT and URTC states

To enable response simulation for general displacement histories, it is necessary to define behaviour for the case of a strain reversal that occurs on an unload-reload path prior to reaching the compression or tension envelope. Here a strain reversal is defined by

$$\left(\varepsilon_{i-1} - \varepsilon_{i-2}\right)\left(\varepsilon_i - \varepsilon_{i-1}\right) < 0 \tag{5.17}$$

where ε_i is the total strain at the current time step, i, and ε_{i-1} and ε_{i-2} are the total strains at previous time steps. If the bar experiences a strain reversal prior to buckling, the unload-reload path is linear with a stiffness equal to the E_{un} of the previous tension unloading path until it intersects with the tension envelope (Fig. 5.12 (a)). If the bar experiences a strain reversal while unloading from compression to tension, the unloading path is linear with stiffness equal to the E_{sec}, previously defined in Eq. (5.9), until it intersects with the post-buckling envelope (Fig. 5.12 (b)).

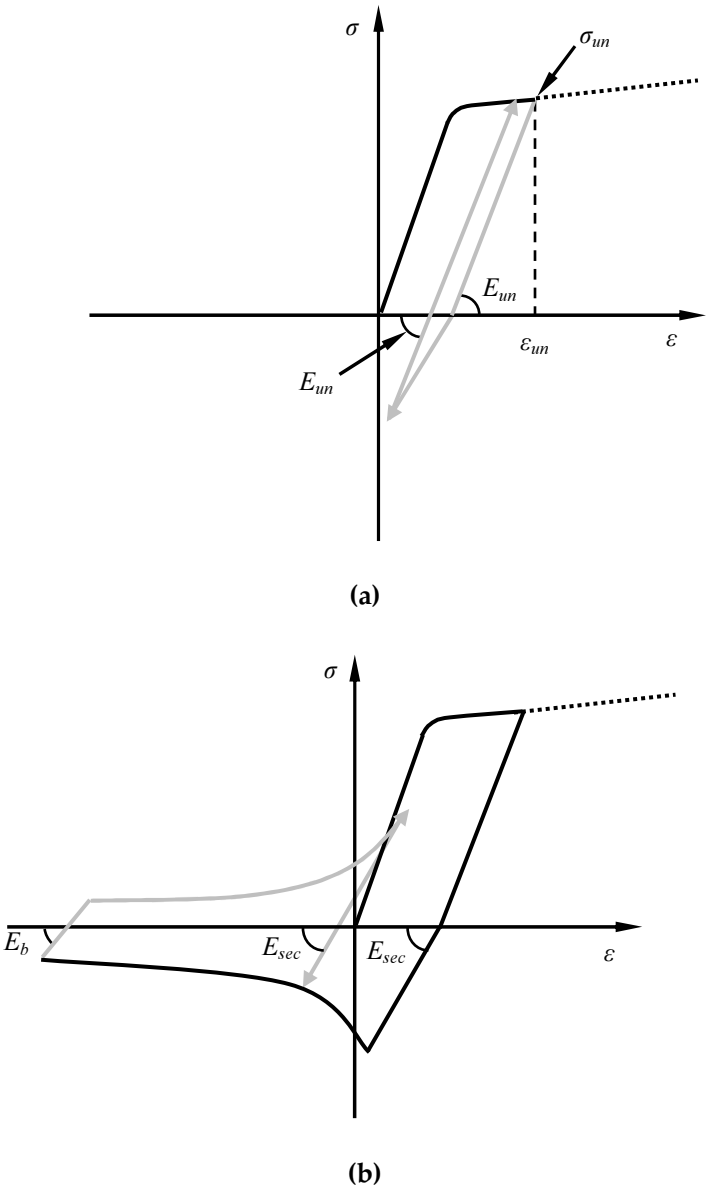

Fig. 5.12 Unloading rules from incomplete cycles: (a) pre-buckling state (b) post-buckling state

5.3 Modelling the influence of corrosion on monotonic envelope curves

5.3.1 Influence of corrosion on tension envelope

The effect of corrosion damage on the mechanical properties of reinforcing bars has been investigated by several researchers (Almusallam 2001, Du et al. 2005a,b, Cairns et al. 2005, Apostolopoulos 2006). Most have come to the conclusion that non-uniform pitting corrosion affects the average stress-strain response of corroded bars. More recently, Apostolopoulos et al.(2013) investigated the influence of pitting depth on the mechanical properties of corroded bars. They concluded that stress concentrations at the pitting

locations result in a significant degradation in mechanical properties of corroded bars. Therefore, in the modelling of the cyclic behaviour of corroded bars consideration needs to be given to the modified tension envelope. Du et al. (2005a,b) provides a detailed description of the effect of corrosion damage on residual capacity and ductility of corroded bars in tension. In this section the proposed methodology suggested by Du et al. is adopted to account for the influence of pitting corrosion on stress-strain behaviour of reinforcing bars in tension. They concluded that the effect of corrosion on tension stress-strain curve of corroded bars can be modelled by employing a pseudo stress-strain curve with modified yield stress as discussed in Chapter 3 (section 3.7.2.1.1)

The influence of corrosion on cross section loss is taken into account by considering an average reduced cross section area assuming a uniform mass loss using Eq. (5.18) below:

$$D' = \frac{D_0}{10}\sqrt{100-\psi} \tag{5.18}$$

where, ψ is the percentage mass loss due to corrosion and D_0 is the initial diameter of uncorroded reinforcement.

5.3.2 Influence of corrosion on post-yield buckling response

The influence of corrosion on the inelastic buckling behaviour of corroded reinforcing bars has been investigated experimentally and computationally and reported in chapters 3 and 4. Computational studies show that there are three main parameters that influence the buckling behaviour of corroded bars. These parameters are (a) irregular loss of cross section area and second moment of area along the length of the bar and (b) shifting of the centroid of the bar cross section along of the length of the bar that results in load eccentricity, that causes stress concentrations and exacerbates imperfections, and, as a result, reduced buckling strength. Due to the complexity of the problem and the random nature of corrosion, it is difficult to develop a mechanistic model equation defining the impact of corrosion on the parameters that determine buckling response. Here, the empirical equations developed in Chapter 3 are used to modify the compression response curve for corroded reinforcement. The proposed modifications to the post-yield buckling response of corroded bars are shown in Fig. 5.13.

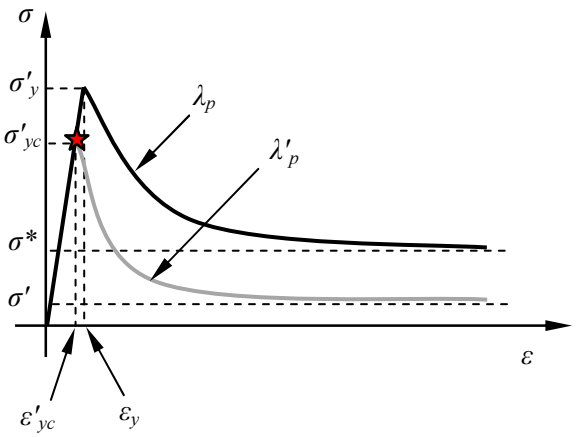

Fig. 5.13 Modified post-yield buckling envelope curve of corroded bars

The effect of corrosion on the compressive yield strength is defined using the observed experimental results as discussed in section 3.5.3 of Chapter 3:

For uncorroded reinforcement, the buckling response model is a function of the non-dimensional slenderness ratio, λ_p, and the minimum stress limit asymptotic σ^* per Eqs. (5.3) to (5.6). The impact of corrosion on these parameters is defined as follows (detailed discussion is available in Chapter 3):

$$\lambda'_p = \sqrt{\frac{\sigma'_{yc}}{100}}\frac{L}{D'} \tag{5.19}$$

$$\sigma' = 3.75\ \frac{\sigma'_{yc}}{\frac{L}{D'}} \tag{5.20}$$

Fig. 14 (a-d) shows buckling response predicted by the proposed model and experimental data for corroded bars with different percentages mass loss and slenderness ratios. The model is defined using Eqs. (5.3) to (5.6), with λ'_p and σ'. The data in Fig. 5.14 show the proposed model is in good agreement with the experimental results.

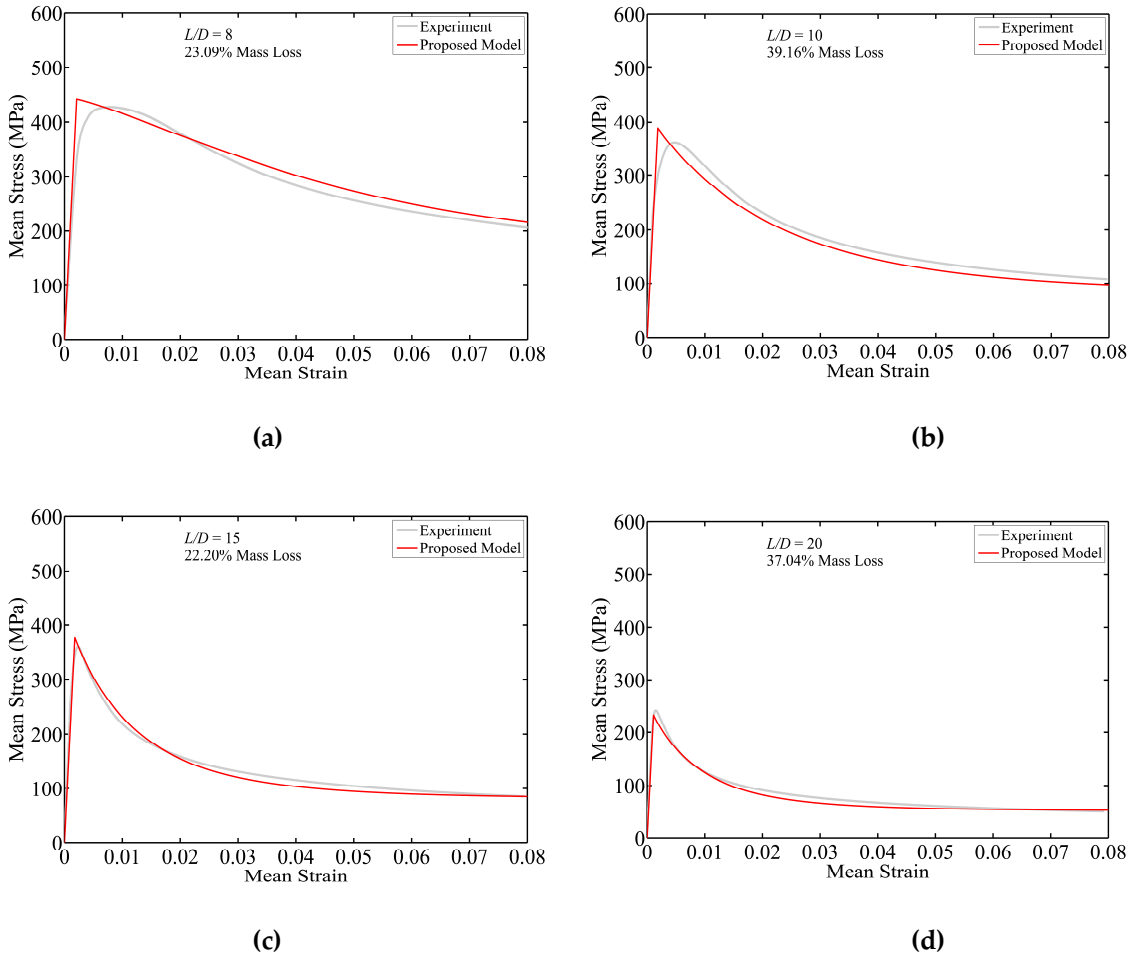

Fig. 5.14 Verification of the proposed model with observed experimental response of corroded bars: (a) L/D = 8 (b) L/D = 10 (c) L/D = 15 (d) L/D = 20

5.4 Modelling the influence of combined low-cycle fatigue and corrosion degradation

As discussed in chapter 3, the experimental data showed that the combined effects of pitting corrosion and low-cycle high-amplitude fatigue result in degradation of tension strength. Strength degradation for uncorroded reinforcing bars due to low-cycle fatigue has been investigated experimentally by other researchers (Mander et al. 1994, Brown and Kunnath 2004, Higai et al. 2006, Hawileh et al. 2010). The Coffin-Manson (Manson 1965) fatigue-life model (Eq. (5.24)) is widely used to predict the bar fracture strain in tension (Mander et al. 1994, Brown and Kunnath 2004, Higai et al. 2006, Hawileh et al. 2010).

The effect of strain history and varying strain amplitudes can be included using the linear cumulative damage hypothesis known as Miner's rule (Miner 1945). Based on Miner's rule, applying n_1 half cycles with a strain amplitude ε_1 and corresponding

fatigue life of $2N_{f1}$, is equivalent to consuming $n_1/2N_{f1}$ of the fatigue resistance. The same assumption applies to any subsequent block of load cycles. Accordingly, the cumulative low-cycle fatigue damage can be estimated. Further details and derivation of the equations are available in Kunnath et al. (2009) and Chapter 3. Brown and Kunnath (2004) investigated the low-cycle high-amplitude fatigue behaviour of reinforcing bars and calibrated material parameters α and Θ_f using data from tests of uncorroded bars subjected to constant amplitude cyclic loading. The reported calibrated values of Θ_f and α are 0.12 and 0.44 respectively.

The low-cycle fatigue behaviour for corroded bars using data from tests in which bars were subjected to cyclic loading with increasing strain amplitude is investigated in Chapter 3. They found that corrosion doesn't influence the material constant Θ_f. However, corrosion does change the material constant α. The relationship between percentage mass loss and the material constant α, based on the reported experimental data, is shown in Eq. (5. 22) below:

$$\frac{\alpha_{corr}}{\alpha} = 1 + 0.004\,\psi \tag{5.21}$$

where, α_{corr} is the material constant of corroded bars and ψ is the percentage mass loss. Accordingly the value of α in the fatigue life model can be replaced with α_{corr} to account for the influence of non-uniform pitting on fatigue life. A schematic of the cyclic degradation model for reinforcing bars is shown in Fig. 5.15.

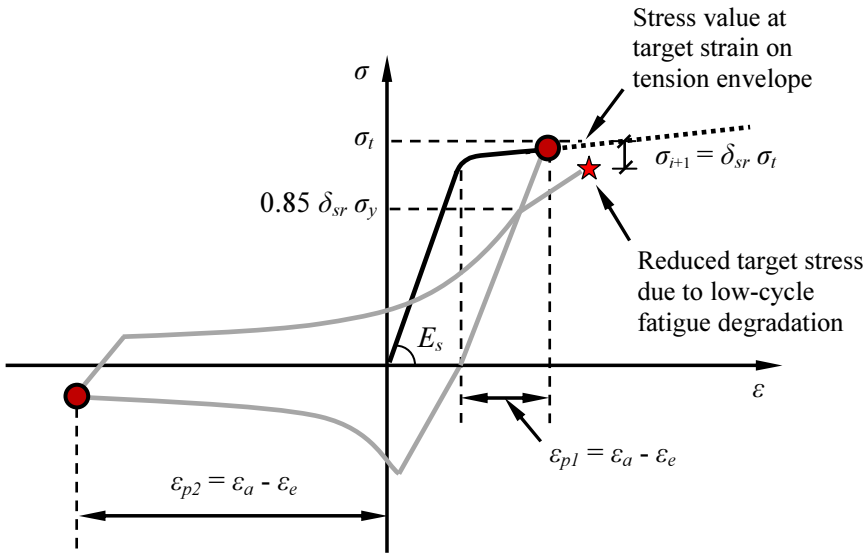

Fig. 5.15 Low-cycle high amplitude fatigue degradation model of reinforcing bars

5.5 Model verification

5.5.1 Nonlinear cyclic response of uncorroded reinforcing bars

Fig. 5.17 shows cyclic response histories for uncorroded reinforcing bars as determined from laboratory testing (chapter 3) and as simulated using the proposed model. The bars have relatively high slenderness ratios and exhibit buckling under compressive loading as well as strength deterioration due to low-cycle high-amplitude fatigue. The error in total hysteretic energy dissipation is used to quantify the accuracy of the model (Eq. (5.22)).

$$\Omega = \frac{\left| E_{model} - E_{exp} \right|}{E_{exp}} \tag{5.22}$$

Ω is the error in the model, E_{model} is the total hysteretic dissipated energy in the model and E_{exp} is the total hysteretic dissipated energy in experiment. It was found the error in Fig. 5.16 (a) and (b) was 0.007 and 0.006 respectively with the model under predicting the total dissipated energy.

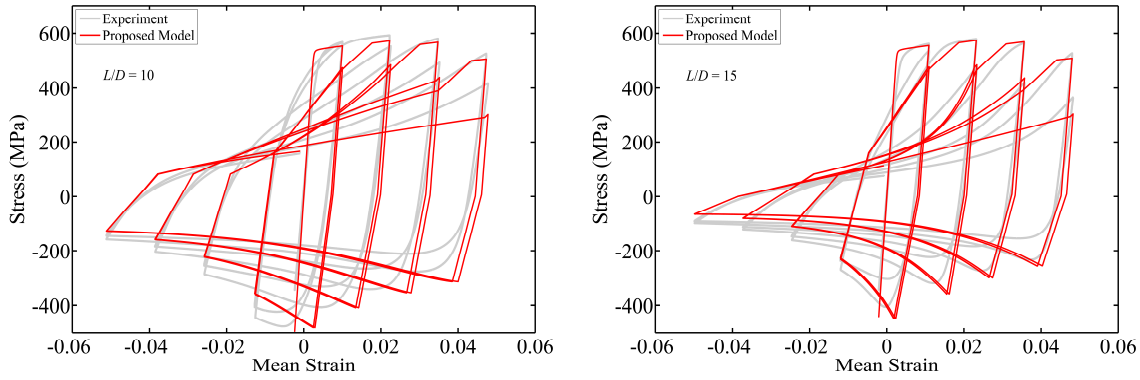

Fig. 5.16 Comparison of the proposed model with physical testing of uncorroded reinforcement: (a) L/D = 10 and (b) L/D = 15

5.5.2 Nonlinear cyclic response of corroded reinforcing bars

Fig. 5.17 (a-d) shows cyclic response histories for four corroded reinforcing bars as determined from laboratory testing and as simulated using the proposed model. The bars have relatively high slenderness ratios and exhibit buckling under compressive loading as well as strength deterioration due to low-cycle high-amplitude fatigue. The bars have moderate mass-loss due to corrosion with mass-loss ratios ranging from 10% to 27%.

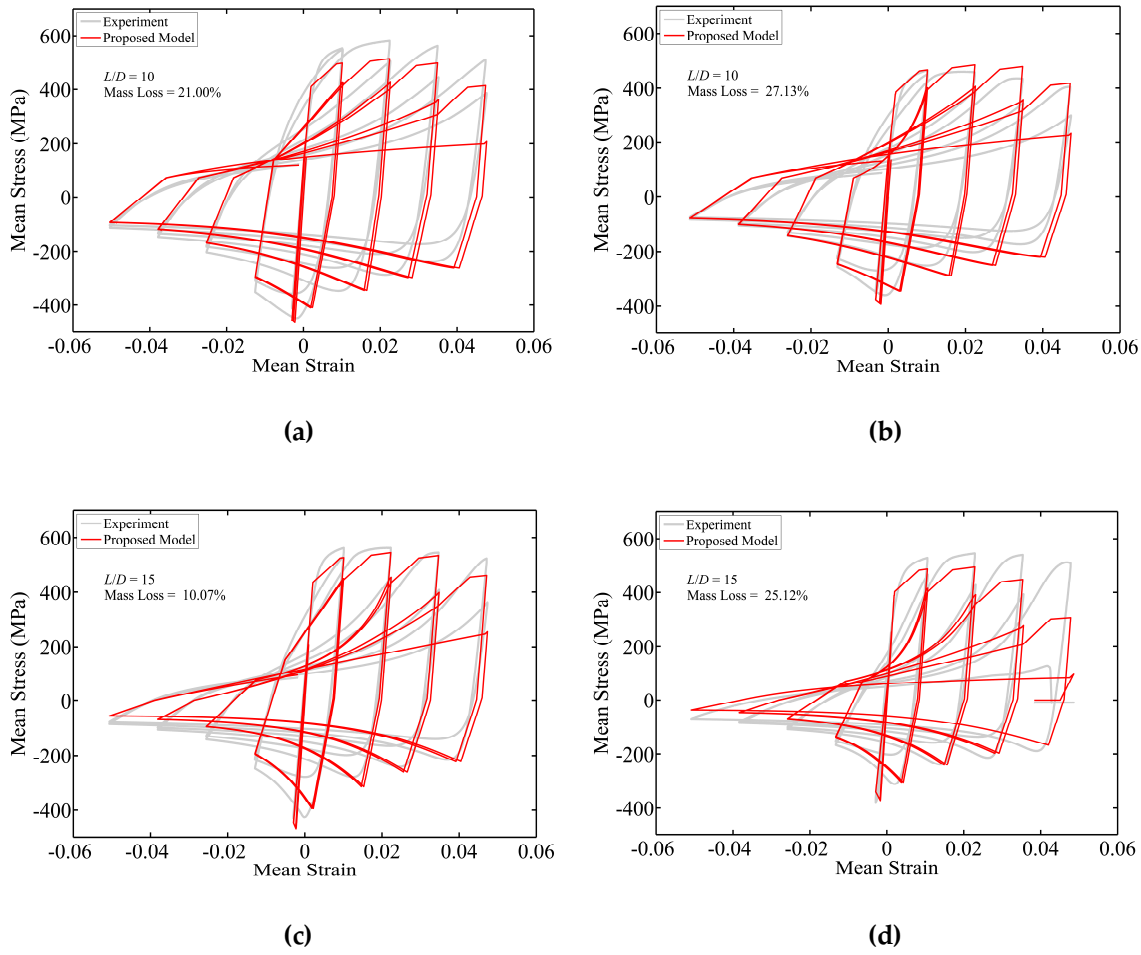

Fig. 5.17 Comparison of the proposed model with physical testing of corroded reinforcement: (a) L/D = 10 and 21% mass loss, (b) L/D = 10 and 27.13% mass loss, (c) L/D = 15 and 10.07% mass loss and d) L/D = 15 and 25.12% mass loss

As with the uncorroded bars, experimental and simulation results for corroded bars were compared on the basis of the response envelope for tension, the response envelope for compression, and hysteretic energy dissipation. The error in hysteretic energy dissipation in the model varied from 5% to about 15%. The complete list of calculated errors for the entire dataset is tabulated in the Table 5.2 and 5.3. It should be noted that the difference between the simulated and observed dissipated energy was found to be higher for bars with severe localised pitting corrosion. This could be expected given that the cyclic buckling response of corroded reinforcement is controlled by the section with the minimum area, the minimum second moment of area, and the maximum eccentricity. Fig. 5.18 (a) shows the proportionality of the dissipated energy in the model and experiment for the entire experimental dataset. Chapter 4 provides data characterising the variation in geometric properties for corroded reinforcement; future research will seek to use these data to develop *effective* mass loss ratios that capture the potential for localised pitting corrosion to result in degraded response.

Fig. 5.18 (b) shows the mean (μ) and standard deviation (σ) of the ratio of dissipated energy in the model to the dissipated energy in the experimental dataset. The calculated μ and σ for the entire dataset are 0.9774 and 0.0805 respectively. The μ and σ of the error in dissipated energy in the model together with the ratio of the calculated and experimental dissipated energy for each group of experimental data are shown in Table 5.2 and 5.3.

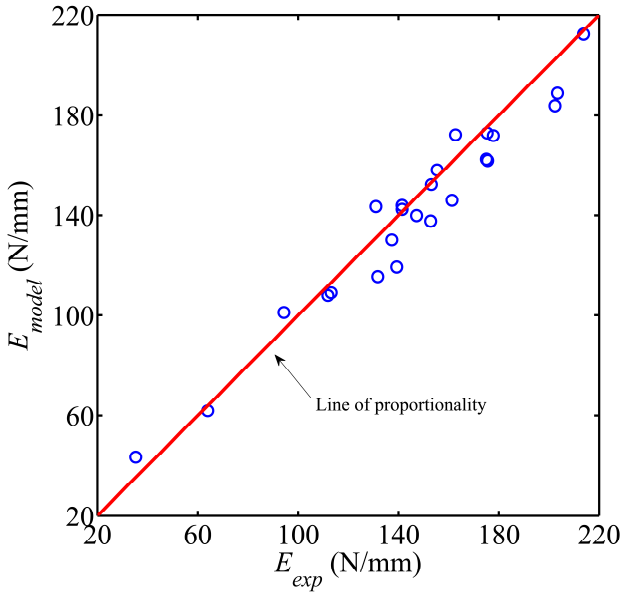

(a)

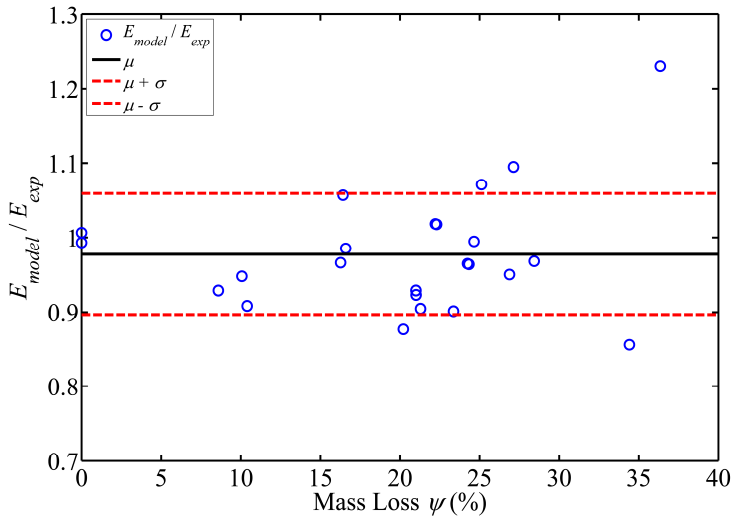

(b)

Fig. 5.18 Comparison of the total hysteretic energy dissipation ion the model and experimental data set: (a) Proportionality of dissipated energy in the model and experiment (b) mean and standard deviation

Table 5. 2 Model Error for group of bars with L/D = 10

Mass Loss (%)	E_{exp} (N/mm)	E_{model} (N/mm)	E_{model} / E_{exp}	$\Omega = \lvert E_{model} - E_{exp} \rvert / E_{exp}$
0.00	213.79	212.32	0.993	0.007
8.59	203.39	188.76	0.928	0.072
10.40	202.38	183.81	0.908	0.092
16.27	177.81	171.78	0.966	0.034
16.42	162.73	172.11	1.058	0.058
16.59	175.37	172.79	0.985	0.015
21.00	175.05	162.47	0.928	0.072
21.01	175.55	161.93	0.922	0.078
21.29	161.34	145.94	0.905	0.095
22.22	155.39	158.20	1.018	0.018
22.30	141.42	143.88	1.017	0.017
23.36	152.83	137.75	0.901	0.099
24.65	153.11	152.29	0.995	0.005
26.88	147.21	139.90	0.950	0.050
27.13	131.00	143.45	1.095	0.095
34.41	139.31	119.33	0.857	0.143
36.31	4.16	7.73	1.859	0.859
Mean (μ)			0.9642	0.0593
Std. deviation (σ)			0.0635	0.0406

Table 5. 3 Model Error for group of bars with L/D = 15

Mass Loss (%)	E_{exp} (N/mm)	E_{model} (N/mm)	E_{model} / E_{exp}	$\Omega = \lvert E_{model} - E_{exp} \rvert / E_{exp}$
0.00	141.44	142.34	1.006	0.006
10.07	137.34	130.21	0.948	0.052
20.21	131.75	115.55	0.877	0.123
24.24	111.88	107.94	0.965	0.035
24.33	113.18	109.09	0.964	0.036
25.12	94.34	101.11	1.072	0.072
28.43	63.97	61.92	0.968	0.032
36.35	35.27	43.42	1.231	0.231
Mean (μ)			0.9812	0.1408
Std. deviation (σ)			0.1068	0.0726

For further validation, the model is compared against a set of experimental data that were not included in the model calibration process. Fig. 5.19 (a) shows the comparison of the proposed model with a corroded bar with L/D = 15 and 19.93% mass loss under monotonic loading and Fig. 5.19 (b) shows the comparison of the proposed model with a corroded bard with L/D = 10 and 15.48% mass loss under cyclic loading.

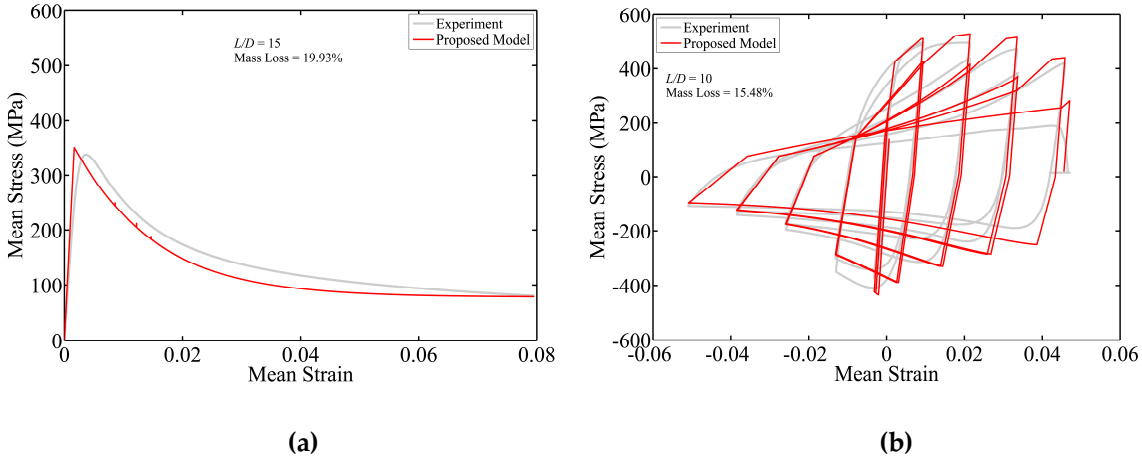

(a) **(b)**

Fig. 5.19 Comparison of the proposed model and experimental tests that were not included in model calibration: (a) L/D = 15 and 19.93% mass and (b) L/D = 10 and 15.48% mass loss

With reference to Figs. 5.16-5.19, it is evident that the proposed model can accurately predict the nonlinear cyclic response of uncorroded and corroded reinforcing bars including the effects of inelastic buckling and low-cycle high-amplitude fatigue degradation. The proposed model is simple and can be readily implemented in any finite element programme for nonlinear analysis of RC structures subject to earthquake loading.

5.6 Implementation and application of the proposed model

To facilitate community use of the model presented in this thesis, the model has been implemented in OpenSees, an open-source software framework for simulating the earthquake response of structures. OpenSees was originally developed by researchers at the Pacific Earthquake Engineering Research Centre (PEER) (OpenSees 2012). An executable version of OpenSees that includes this model is available at http://opensees.berkeley.edu. OpenSees is an object-oriented software framework written primarily in C++. Implementation of the new cyclic buckling model comprised creation of a new *UniaxialMaterial, CorrodedReinforcingSteel* in OpenSees. Specifically a *.cpp file was created that defines the response logic described in this thesis and a *.h file was created that defines all the history variables to be used in the nonlinear solution procedure. Fig. 5.20 shows a simplified version of the OpenSees abstract class structure

including the new *CorrodedReinforcingSteel* class. In Fig. 5.20 (Archer 1996, McKenna 1997, Archer et al. 1999), the *Domain* maintains the information necessary to describe and represent the state of the model throughout the analysis. The *Domain* class controls multiple subclasses including the Material subclass, and the *Material* class controls multiple subclasses including the *UniaxialMaterial* subclass.

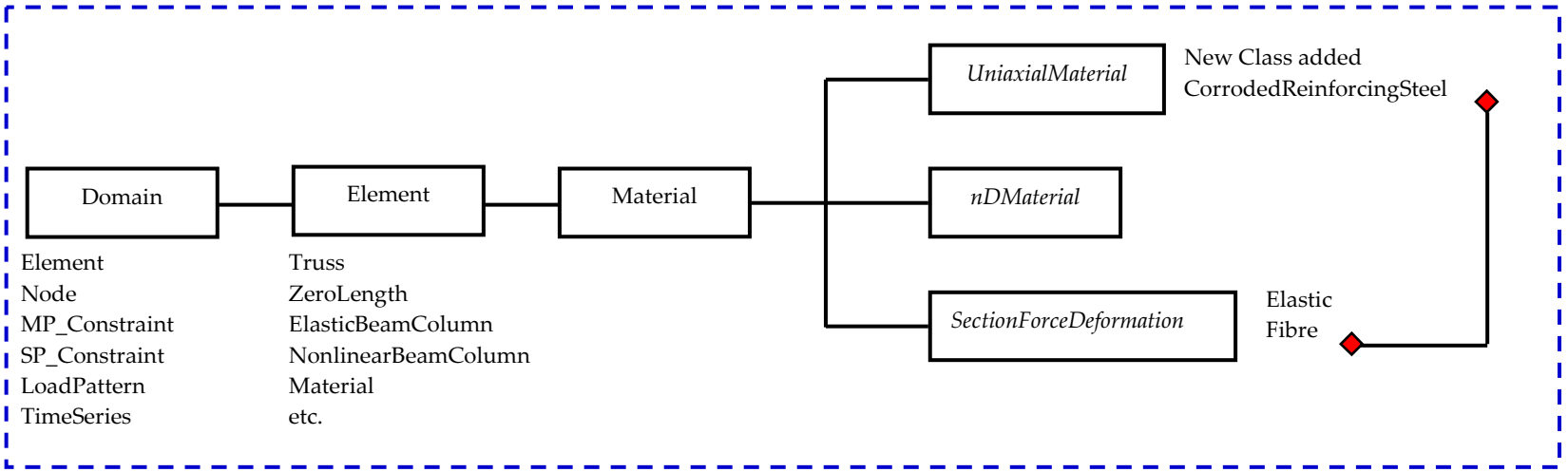

Fig. 5.20 Partial OpenSees abstract classes map representing the new implemented class

5.7 Model validation and calibration

Modern bridge design practice has improved the seismic response of bridges under earthquake loading when compared to older bridges. Nevertheless earthquake damage can still be expected and has been observed in recent large earthquakes. Even bridges which suffer minor damage after an earthquake incur a significant cost to bridge owners. To this end, it is very important for bridge owners and managers to be able to predict the likely extent of earthquake damage to their bridges. This will help to improve the whole life cycle cost (WLCC) analysis of bridges. Existing performance-based earthquake engineering (PBEE) helps bridge engineers and managers achieve these goals. PBEE relates the economic impact to the structural damage under the given hazard level. Therefore, it requires response models that predict the seismic demand on reinforced concrete (RC) bridge piers under multiple hazard levels and damage models that predict the damage state. Finally a PBEE framework links the seismic demands with damage state to estimate the economic loss. Accordingly, several researchers have put significant effort into determining the trends between the demand parameters such as drift ratio or strain at critical sections and the damage parameters such as cover concrete spalling or bar buckling (Berry and Eberhard 2003, Lehman et al. 2004, Berry and Eberhard 2005).

Moreover, recent advances in computational tools have significantly improved the ability of researchers to use refined modelling and perform nonlinear analysis of structures and bridges subject to earthquake loading. Among these recent advanced methods, the fibre-based finite element technique is the most popular method for nonlinear analysis of framed structures (Taucer et al. 1991, Spacone at al. 1996a,b). In this method element cross sections are discretised into a number of fibres at the selected locations along the length of element, known as "integration points". The behaviour of each fibre is modelled by a uniaxial constitutive model. Steel, unconfined and confined concrete are treated as separate material models. Therefore, the component response is primarily controlled by inelastic response of cross section. Accordingly, several researchers have developed uniaxial material models to be used in fibre-based finite element models.

As it is well known to researchers, buckling of vertical reinforcement in RC columns is the most common type of observed failure mechanism (Berry and Eberhard 2003, Lehman et al. 2004, Berry and Eberhard 2005). Despite significant effort over the past two decades or so in the development of buckling models for reinforcing bars and in the simulation of buckling of reinforcing bars in RC columns (Scribner 1986, Papia et al. 1988, Papia and Russo 1989, Mau and El-Mabsout 1989, Mau 1990, Monti and Nuti 1992, Apleton and Gomes 1995, Pantazopolou 1998, Rodruiguez 1999, Bayrak and Sheikh 2001, Dhakal and Maekawa 2002a,b,c, Bae et al. 2005, Cosenza and Prota 2006, Kunnath et al. 2009, Zong et al. 2013), there is still not a precise model that has been extensively

validated against experimental datasets. To this end, there are two major concerns about the existing models: *i*) all of the existing models are calibrated based on either experimental and/or numerical stress-strain behaviour of isolated bars that may or may not represent the actual behaviour of embedded reinforcing bars inside concrete, *ii*) the stress-strain behaviour of reinforcing bars is averaged over the buckling length. Therefore, consideration needs to be given to the element mesh size that will affect the integration scheme of fibre model. Ignoring this will result in strain localisation at the critical section (Coleman and Spacone 2001, Pugh 2012).

A new phenomenological uniaxial material model that accounts for the effect of inelastic buckling, low-cycle fatigue degradation and long-term corrosion damage on hysteretic behaviour of isolated reinforcing bars is developed in this chapter. This model (described in the first half of this chapter) has been implemented in OpenSees (OpenSees 2012) as a new uniaxial material class, called *CorrodedReinforcingSteel* material model. If the percentage mass loss (measure of corrosion damage) in the material input parameters is taken as zero the model represents stress-strain behaviour of uncorroded reinforcement.

This half of the chapter presents a comparison between the new *CorrodedReinforcingSteel*, *Steel02* and existing *Hysteretic* uniaxial material models available in OpenSees. The objectives of this section are

i) to determine whether the material models calibrated for isolated reinforcing bars represent the behaviour of embedded reinforcing bars inside concrete,
ii) to predict the impact of bar buckling on cyclic degradation, strength loss and failure mode of flexural govern RC columns,
iii) to develop a performance modelling strategy for simulation of bar buckling in RC columns to avoid strain localisation issues.

5.7.1 Experimental RC bridge column dataset

The UW-PEER, RC column test database (Berry et al. 2004) provides a unique opportunity to evaluate and calibrate column modelling strategies. The database documents the geometry, material properties, and reinforcement details for a set of columns. It also includes the digital force-displacement histories and the observed displacements at the onset of multiple damage states. For this study ten of the buckling critical column experiments are considered for model validation and calibration. Table 5.4 summarises the details of the selected columns and their references. In Table 5.4, L is the column length, D is the column diameter, L/D ratio is column length to column diameter ratio, ρ_l is the ratio of longitudinal reinforcement area to total cross sectional area , ρ_h is the volumetric ratio of horizontal reinforcement and P / ($A_g f_c$) is the axial force ratio, where P is the axial force on the column, A_g is the gross section area of column

section and f_c is the compressive strength of concrete. The details of the material properties can be found in either the UW-PEER column database or the relevant reference shown in Table 5.4.

Table 5. 4 Details of column dataset

	Reference	L (mm)	L/D	ρ_l (%)	ρ_h (%)	Axial Force ratio, $P/(A_g f_c)$
(1)	Kunnath et al. A2 (1997)	1372	4.5	2.04	0.01	0.09
(2)	Lehman et al. 415 (1998)	2438.4	4	1.49	0.01	0.07
(3)	Lehman et al. 815 (1998)	4876.8	8	1.49	0.01	0.07
(4)	Lehman et al. 1015 (1998)	6096	10	1.49	0.01	0.07
(5)	Lehman et al. 407 (1998)	2438.4	4	0.75	0.01	0.07
(6)	Lehman et al. 430 (1998)	2438.4	4	2.98	0.01	0.07
(7)	Henry 415p (1998)	2438.4	4	1.49	0.01	0.12
(8)	Henry 415s (1998)	2438.4	4	1.49	0.00	0.06
(9)	Moyer and Kowalsky 1 (2001)	2438.4	5.33	2.08	0.01	0.04
(10)	Hamilton UCI1 (2002)	1854.2	4.6	1.17	0.01	0.00
	Mean	2882.9	5.24	1.65	0.01	0.07
	Standard Deviation	1372.1	1.97	0.57	0.00	0.03
	Max	6096.0	10.00	2.98	0.01	0.12
	Min	1372.0	4.00	0.75	0.00	0.00

5.8 Finite element model of RC bridge piers using nonlinear fibre beam-column element

In modelling the nonlinear behaviour of structures using distributed plasticity frame models, there are typically two methods for element formulation in i.e. displacement-based and force-based formulations (Taucer et al. 1991). In the displacement-based formulation, the displacement fields along the element are expressed as functions of the nodal displacements. The assumed displacement fields are approximations of the actual displacement fields and therefore, several elements per member are is required to obtain a good approximation of the exact response. In the force-based formulation, the internal force fields are expressed as functions of the nodal forces (Taucer et al. 1991, Spacone et al. 1996).

A fibre beam-column element is a line element in which the moment-curvature response at selected locations (along the element known as integration points) is determined from the fibre section assigned to that integration point. Currently, forced-based (also known as flexibility-based) fibre elements are the most advanced 1D models for nonlinear

analysis of RC components. In the flexibility-based formulation a moment-distribution along the length of the column is considered. The curvatures at each integration point are subsequently estimated for the given moment at that section. Finally, the column response is obtained through weighted integration of the sections' response (Taucer et al. 1991). Therefore, selection of the location of integration points is crucial for realistic prediction of the nonlinear response. In RC columns the most inelastic behaviour occurs near the base of the column. Therefore, a Gauss-Labotto integration scheme, in which the integration points are placed at the ends of the element, as well as along the column length, is recommended (Berry and Eberhard 2008).

Force-based elements are well suited for nonlinear analysis of framed structures because they allow the spreading of plasticity over the length of the member using only one element that has multiple integration points. However, it is well known that forced-based elements can lose their objectivity at local and/or global level depending on section hardening/softening behaviour (Coleman and Spacone 2001, Pugh 2012). Coleman and Spacone (2001) proposed a simple material regularization technique to solve this problem. The proposed material regularization technique is based on the observed failure mode of concrete cylinders in compression tests. In compression tests the damage is a localized phenomenon and there is experimental evidence that the energy dissipated by concrete crushing in compression failure (fracture energy) is constant and independent of the length of the specimen (Jansen and Shah 1997; Lee and William 1997). Pugh (2012) successfully employed this method to predict the nonlinear cyclic response of RC shear walls using force-based fibre beam-column elements. Using this concept the constitutive material model must be modified based on the integration length for the critical section to avoid localization problems. In RC columns where the failure mode is buckling of vertical reinforcement, softening response of the critical section is controlled by the post-buckling softening response of the reinforcing steel. Therefore, post-buckling response of reinforcing steel has significant impact on strain localization at the critical section.

In this research a different method is employed to avoid the strain localization due to the post-buckling response of reinforcing bars. We know that the uniaxial material model including the post-buckling response of reinforcing bars is averaged over a known buckling length. Given it is expected that the buckling will occur at the first critical section of the column, the integration length of this section should be considered to be equal to the buckling length. Using this approach the fracture energy under the post-buckling response of the material model for reinforcing steel remains unchanged.

The Gauss-Lobatto integration scheme doesn't allow adjusting the length of the first integration point to be equal to the buckling length using one force-based element for the entire column. Therefore, two force-based elements are used to model the RC column.

Consider a force-base element with a Gauss-Labotto integration scheme and three integration points. The length of the first integration point is $l/3$ where $-1 \leq l \leq 1$ (Abramowitz and Stegun 1972). Therefore, if three integration points are chosen for the first element with the total length of 6 L_{eff}, where L_{eff} is the buckling length (L_{eff} is defined in the following section), the length of the first integration point will be equal to L_{eff}. Using this method the length of the first element at the bottom of the column is adjusted based on the buckling length for each column. Based on the recommendations reported by Berry and Eberhard (2008) a forced-based element with five integration points is considered for the second element to model the top part of the column. A schematic view of the fibre model and fibre sections is shown in Fig. 5.22 below. The numbers of fibres and the section and decomposition method are based on the recommendations reported by Berry and Eberhard (2008). To model the strain penetration and the slippage of reinforcement anchored to the foundation a zero length section element that is available in OpenSees is used. A detailed discussion of the zero length section is available in the uniaxial material models Section 5.7.2.3.

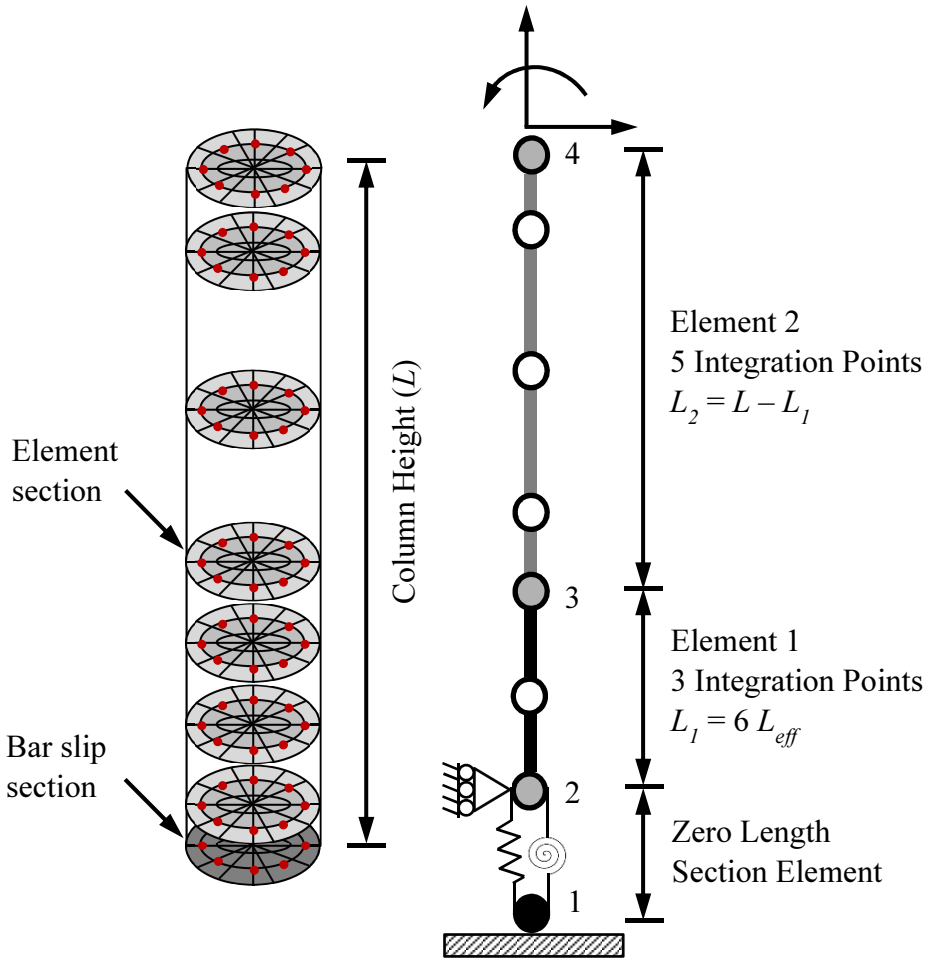

(a)

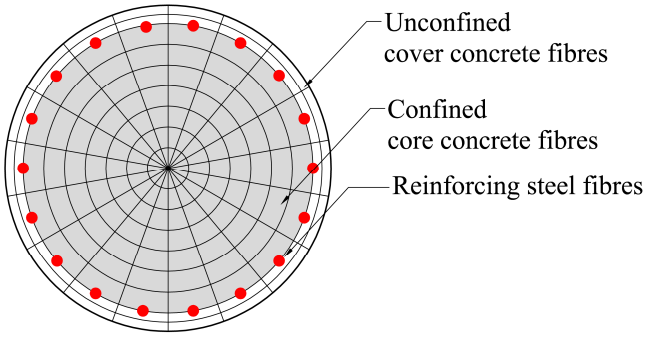

(b)

Fig. 5. 21 Implementation of fibre beam-column element with bar buckling and bar slip model

5.8.1 Calculation of buckling length of the vertical reinforcement in circular columns

Pantazopoulou (1998) studied a database of column tests to identify the parameters that influenced bar buckling. They concluded that the interaction between tie stiffness, tie spacing and bar diameter of the reinforcement influences the instability of the vertical reinforcement in columns. Based on this study Pantazopoulou derived an empirical equation to calculate the buckling length of reinforcement as a function of tie stiffness.

Dhakal and Maekawa (2002c) studied the buckling behaviour of vertical reinforcement in rectangular columns. Using energy methods, they derived the buckling mode shape accounting for the influence of tie stiffness on buckling length. This model was used in the finite element analysis of a cantilever column that was subjected to lateral and axial loads. The results of this model agreed fairly well with the experimental results. However, the Dhakal-Maekawa model has not been validated for circular columns. In this research, the proposed Dhakal-Maekawa model is used to calculate the buckling length of the vertical reinforcement in the experimental dataset presented in Table 5.4 and the results of the analyses are compared with the observed experimental results.

The proposed Dhakal-Maekawa model is shown in Fig. 5.22. The longitudinal reinforcing bar is considered as a beam fixed at both ends of the buckling length to emulate the restraining mechanism of horizontal ties. A cosine shape function satisfying the fixed boundary condition is then employed to define the deformed configuration of buckled bar.

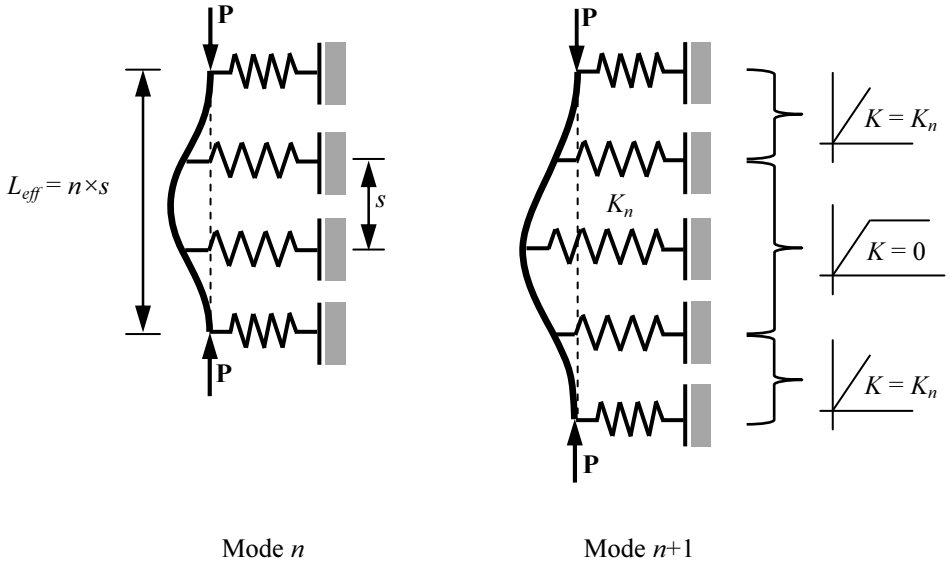

Fig. 5. 22 Proposed Dhakal-Maekawa bar buckling model

Given the buckling of reinforcing bars is an inelastic buckling phenomenon the elastic flexural rigidity E_sI cannot be used here (Timoshenko 1963). Dhakal-Maekawa suggested an average flexural stiffness EI defined in Eq. (5.23), which has been validated against an extensive set of experimental data, is used.

$$EI = \frac{E_s I}{2}\sqrt{\frac{\sigma_y}{400}} \tag{5.23}$$

Where, E_s and σ_y are the elastic modules and yield strength of the vertical reinforcement in MPa respectively.

In this research the stiffness of horizontal ties (spiral reinforcement) is computed using the empirical Eq. (5.24) suggested by Pantazopoulou (1998).

$$K_t = \frac{4E_{sp}A_{sp}}{\sqrt{\left(s^2 + d_c^2\right)}} \tag{5.24}$$

Where, E_{sp} is the elastic modulus of the spiral reinforcement, A_{sp} is the cross section area of the spiral reinforcement, s is the spiral pitch and d_c is the core diameter.

In the model, the lateral ties are simulated by discrete elastic springs. Based on the experimental observation it is evident that the lateral ties show elasto-plastic behaviour and their tangent stiffness is almost zero after yielding. Therefore, the stiffness of horizontal ties at the middle third height of the buckled length (L_{eeff} / 3) considered to be zero.

Using energy methods, Dhakal-Maekawa proposed an iterative procedure to calculate the required stiffness to sustain buckling mode n. Solving Eq. (5.25) and Eq. (5.26) simultaneously yields the required spring stiffness k_n and the corresponding load P_n.

$$\frac{2\pi^4 EI}{n^3 s^3} + \sum_{i=1}^{n} \frac{c_i K_n}{4}\left(1-\cos\frac{2i\pi}{n}\right)^2 - \frac{P_n \pi^2}{2ns} = 0 \tag{5.25}$$

$$\frac{2\pi^4 EI}{(n+1)^3 s^3} + \sum_{i=1}^{n+1} \frac{c_i K_n}{4}\left(1-\cos\frac{2i\pi}{n+1}\right)^2 - \frac{P_n \pi^2}{2(n+1)s} = 0 \tag{5.26}$$

where, EI is the averaged flexural stiffness defined in Eq. (5.23), s is the tie/spiral spacing and n is the buckling mode. The details and derivation of the equations are available in Dhakal-Maekawa (2002c). A flowchart of the iteration procedure is shown in Fig. 5.23 below.

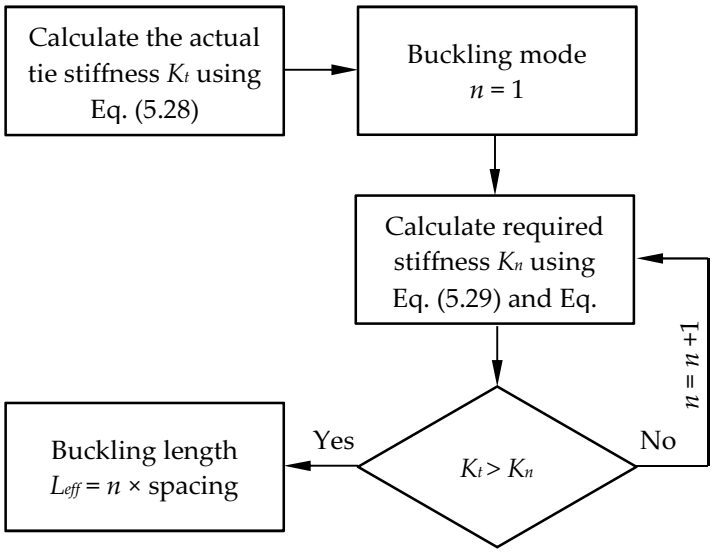

Fig. 5. 23 Iterative procedure of buckling length calculation (Dhakal-Maekawa (2002c))

5.8.1.1 Comparison of the computed buckling mode with observed experimental results

Using the procedure outlined in Section 5.8.1 the buckling lengths of the vertical reinforcement in the experimental dataset presented in Table 5.4 are computed and verified. The comparison between the computed and observed experimental results is summarised in Table 5.5.

Table 5.5 Comparison of the computed buckling mode with experimental dataset

Reference*	Bar diameter d (mm)	Yield strength σ_y (MPa)	Normalised flexural rigidity EI / E_sI	Spiral pitch s (mm)	Spiral diameter d_s (mm²)	Buckling mode computed	Buckling mode observed	s/d	L_{eff}/d
1	9.5	448.00	0.529	19	4	4	4	2	8
2	15.875	461.97	0.537	31.75	6.4	5	6	2	10
3	15.875	461.97	0.537	31.75	6.4	5	6	2	10
4	15.875	461.97	0.537	31.75	6.4	5	6	2	10
5	15.875	461.97	0.537	31.75	6.4	5	5	2	10
6	15.875	461.97	0.537	31.75	6.4	5	6	2	10
7	15.875	462.00	0.537	31.75	6.4	5	5	2	10
8	15.875	462.00	0.537	63.5	6.4	2	2	4	8
9	19.05	565.37	0.594	76.2	9.5	1	1	4	4
10	12.7	458.50	0.535	31.75	4.5	4	NA	2.5	10

* The reference number is the number allocated to the each experiment in Table 5.4.

Fig. 5.24 shows the observed buckling modes of the two experiments. Based on this comparison, it is evident that Dhakal-Maekawa buckling model is in good agreement with the experimental results. Therefore the computed buckling lengths are used in uniaxial material model of the proposed fibre section.

(a)

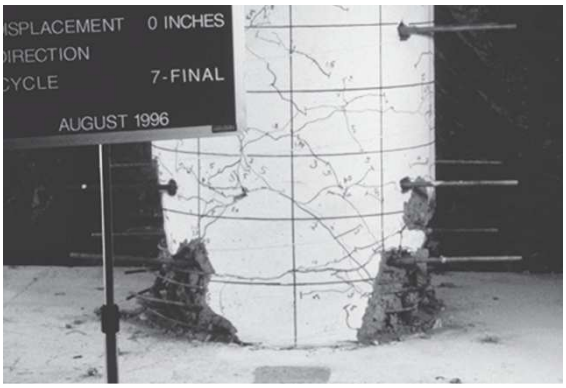

(b)

Fig. 5. 24 Comparison of the observed and computed buckling mode: (a) compute mode 1 and observed mode 1 (Moyer and Kowalsky 1) (b) computed mode 5 and observed mode 5 (Lehman 407)

5.8.2 Description of uniaxial material models

5.8.2.1 Concrete model

In this research the uniaxial material *Concrete04* is used in the analyses. This model uses Popovics curve (Popovics 1973) in compression and a linear-exponential decay curve in tension. For unloading and reloading in compression, the Karsan-Jirsa model (1969) is used to account for stiffness degradation and to determine the unloading/reloading stiffness. The secant stiffness is used to define the unloading/reloading stiffness in tension. An unconfined concrete model is used for the cover concrete and a confined concrete model is used for the core concrete. The confined concrete is defined using the confinement parameters proposed by Mander et al. (1988). Fig. 5.25 (a) shows the confined concrete model with unloading-reloading cycling rules and Fig. 5.25 (b) shows the concrete model in tension with unloading-reloading cycling rules. It should be noted that in Fig. 5.25, σ_c is the maximum concrete compressive strength, ε_{c0} is the strain at maximum compressive strength (σ_c) and ε_{ct} is the strain at concrete fracture in tension.

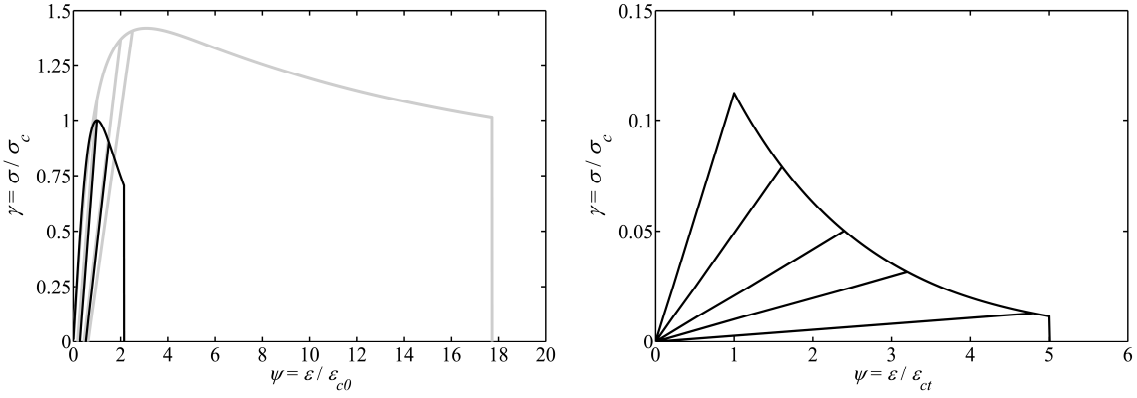

(a)

(b)

Fig. 5. 25 Cyclic response of *Concrete04*: (a) unconfined and confined concrete response in compression including cyclic degradation (b) tension response

5.8.2.2 Reinforcing steel model

5.8.2.2.1 Uniaxial *Steel02* material model

The cyclic response of the reinforcing steel is defined by the Giuffre-Menegotto-Pinto (GMP) steel model (Menegotto and Pinto 1973) and modified by Filippou (1983). The *Steel02* accounts for the Bauschinger effect (Bauschinger 1887), but does not account for cyclic strength and stiffness degradation due to bar buckling and fatigue. The cyclic response of *Steel02* is shown in Fig. 5.26. This model is used for the initial analysis and

for comparison with the proposed inelastic response prediction model which includes the influence of cyclic degradation.

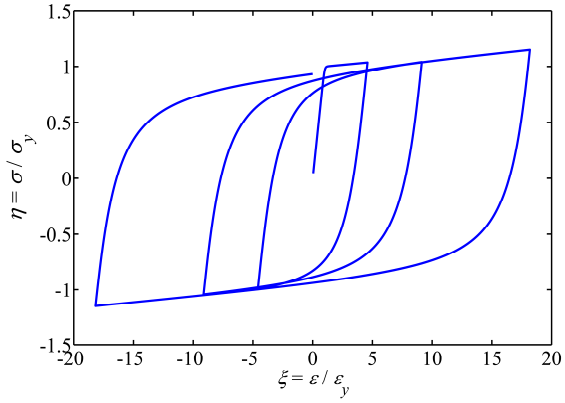

Fig. 5. 26 Cyclic response of *Steel02* material model

5.8.2.2.2 The new uniaxial *CorrodedReinforcingSteel* material model

This model has been developed and implemented in OpenSees (as discussed in Sections 5.1 to 5.5). The model parameters are calibrated using experimental and numerical modelling of uncorroded and corroded isolated reinforcing bars (as described in Chapters 3 and 4). The post-buckling envelope of this model is a function of the non-dimensional slenderness ratio λ_p (Eq. (5.27)) which is originally proposed by Dhakal-Maekawa (2002b).

$$\lambda_p = \sqrt{\frac{\sigma_Y}{100}} \frac{L_{eff}}{d} \tag{5. 27}$$

where, L_{eff} is the calculated buckling length, d is the diameter of reinforcing bar and σ_y is the yield strength.

The influence of inelastic buckling on stiffness degradation, the pinching response of the reinforcing bars in compression and the low-cycle fatigue degradation in tension is considered in the model. The unloading stiffness degradation in tension is also considered in the model using the model proposed by Dodd and Restrepo-Posada (1995). If the corrosion parameter is set to zero the model is valid for uncorroded steel. A detailed description of this model discussed in Sections 5.2 to 5.6 of this chapter. An example cyclic response of this model for a reinforcing bar with L_{eff}/d = 10 is shown in Fig. 5.27.

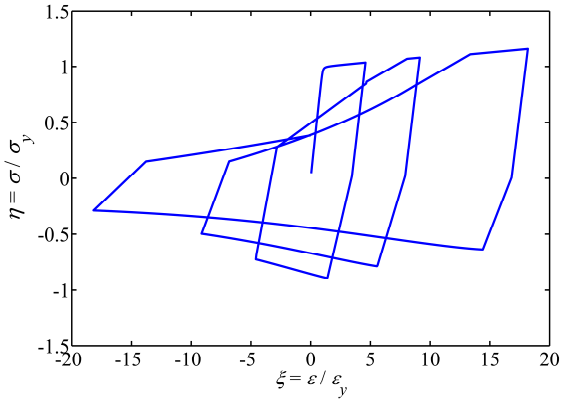

Fig. 5. 27 Cyclic response of *CorrodedReinforcingSteel* material model without corrosion

5.8.2.2.3 Uniaxial *Hysteretic* material model

The uniaxial Hysteretic material model in OpenSees is a generic hysteric model that can be used to model the stress-strain behaviour of a material or the force-displacement behaviour of a structural component. The backbone curves in tension and compression can be defined by three points. The cyclic response is defined by two pinch parameters that need to be calibrated for the proposed material or structural component. In this research this hysteretic model is used in a parametric study to calibrate the buckling parameters of the new *CorrodedReinforcingSteel* Model.

The post-buckling envelope of *CorrodedReinforcingSteel* is very similar to the Dhakal-Maekawa buckling model (Dhakal-Maekawa 2002b). The only difference is that Dhakal-Maekawa model defines the post-buckling response with a three point trilinear curve and *CorrodedReinforcingSteel* defines the post-buckling response using a smooth exponential function. The main differences between the two models are the cyclic rules including the pinching effect, fatigue degradation and the corrosion effect. Therefore, the Dhakal-Maekawa post-buckling model is used to define the compression envelope of the *Hysteretic* model using three points. Further detail of Dhakal-Maekawa model is available in Dhakal-Maekawa (2002b).

Fig 5.28 shows an example of the cyclic response of the *Hysteretic* material model. Further details and the influence of pinching parameters on the cyclic rules of *Hysteretic* model are discussed later in the parametric study section (Section 5.8.4).

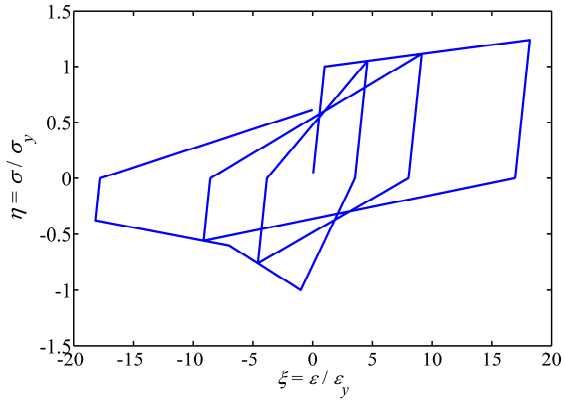

Fig. 5. 28 Cyclic response of Hysteretic material model

5.8.2.2.4 Uniaxial *Fatigue* material model

OpenSees has a generic fatigue material model that can be wrapped to any steel model without changing the stress-strain state of the parent material. This material model accounts for the effect of low-cycle fatigue. The model employs a modified rain-flow cycle counter to track strain amplitudes (Uriz 2005). The cycle counter is used in conjunction with the Coffin-Manson relationship and Miner's Rule to describe the low-cycle fatigue failure (Manson 1965, Miner 1945).

The material constants α and Θ_f are the input parameters in the *Fatigue* model. By wrapping this model to any steel model, once the *Fatigue* material reaches a damage state of 1.0, the stress of the parent material becomes zero. An example graph of the *Fatigue* material model wrapped to *Steel02* is shown in Fig. 5.29.

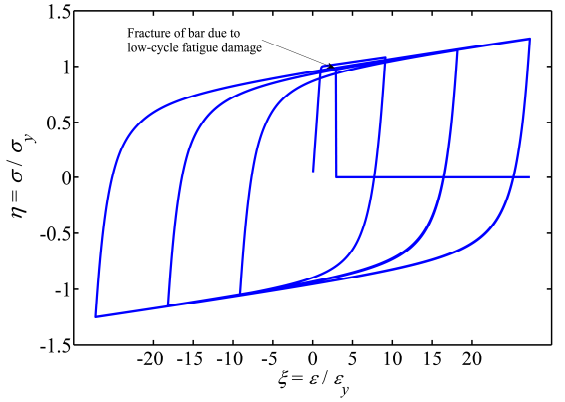

Fig. 5. 29 Fatigue material model to predicting the fracture of reinforcement due to low-cycle fatigue.

5.8.2.3 Bond-slip displacement model for zero length element

5.8.2.3.1 Tensile stress-slip model for reinforcing steel

In the seismic design of RC bridge piers, plastic hinges are designed to form at the column ends (column to foundation/capping beam connection). This will result in the slippage of longitudinal bars due to the substantial strain penetration along the bars into the foundation. This phenomenon has been observed by several researchers who studied the cyclic behaviour of RC columns experimentally (Lehman and Moehle 2000). Lowes and Altoontash (2002) employed a bar-slip model to model the end slip of longitudinal reinforcement in beam-column joints as shown in Fig. 5.31. Using the model in Fig. 5.31 the bar stress-slip relationship can be calculated using the Eqs. (5.28) to (5.32).

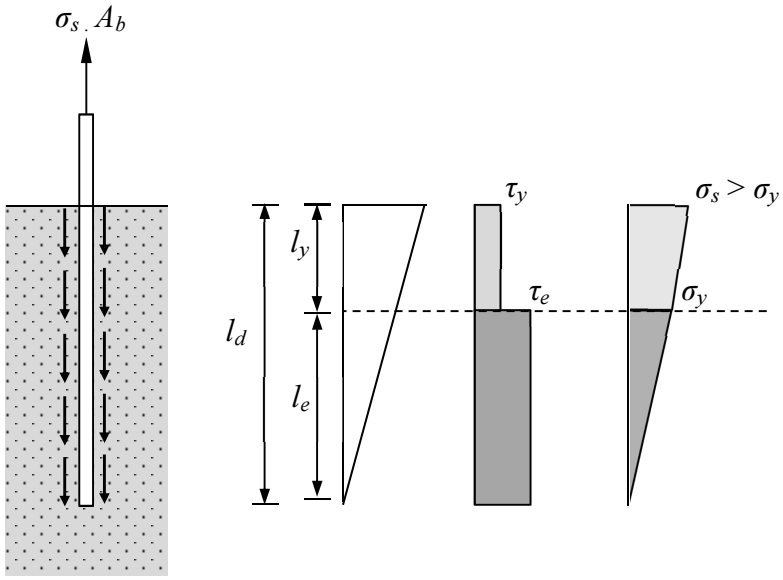

Fig. 5.30 Bar slip model (Lowes and Altoontash 2003)

$$slip = \int_0^{l_{\sigma_s}} \tau_e \frac{\pi d_b}{A_b} \frac{1}{E} x\,dx = \frac{2\tau_e l_{\sigma_s}^2}{E\,d_b} \qquad \forall \quad \sigma_s < \sigma_y \tag{5. 28}$$

$$slip = \int_0^{l_e} \frac{4\tau_e}{d_b} \frac{1}{E} x\,dx + \int_{l_e}^{l_e+l_y} \left(\frac{\sigma_y}{E} + \tau_y \frac{4\left(x - l_e\right)}{d_b E} \right) dx \qquad \forall \quad \sigma_s > \sigma_y$$

$$slip = 2\frac{\tau_e l_e^2}{E\ d_b} + \frac{\sigma_y l_y}{E} + \frac{\tau_y l_y^2}{E_h d_b} \tag{5. 29}$$

$$l_{\sigma_s} = \frac{\sigma_s}{\tau_e} \cdot \frac{A_b}{\pi d_b} \tag{5. 30}$$

$$l_e = \frac{\sigma_y}{\tau_e} \cdot \frac{A_b}{\pi d_b} \tag{5. 31}$$

$$l_y = \frac{\sigma_s - \sigma_y}{\tau_y} \cdot \frac{A_b}{\pi d_b} \tag{5. 32}$$

where, σ_s is bar stress at the column-foundation perimeter; σ_y is yield strength of reinforcing bar; E is steel elastic modulus; E_h is steel hardening modulus assuming a bilinear stress–strain response; τ_e is bond strength for elastic steel; τ_y is bond strength for yielded steel; A_b is nominal bar cross section area; and d_b is nominal bar diameter and l_e and l_y, are the lengths along the reinforcing bar for which steel stress is less than and greater than the yield stress respectively.

Berry and Eberhard (2006) conducted a comprehensive parametric study and provided recommendations for the values of bond strength to be used in the modelling of RC columns. The suggested values of average bond strengths are summarised in Table 5.6. The suggested value of steel hardening ratio (E_h/E) is suggested to be taken as 0.1.

Table 5.6 Average bond strength as a function of steel stress state

Bars stress	Average bond strength (σ_c^* in MPa)
$\sigma_s \leq \sigma_y$	$0.9\sqrt{\sigma_c}$
$\sigma_s > \sigma_y$	$0.45\sqrt{\sigma_c}$

* σ_c is the compressive strength of concrete

The material parameters of the *Steel02* are modified using Eqs. (5.28) to (5.32) and are used to model the bar stress-slip behaviour in the zero length section. Fig. 5.32 shows the normalised bar stress-slip model that is used in this study. S_y in Fig. 5.31 is the slip at onset of yielding of reinforcement.

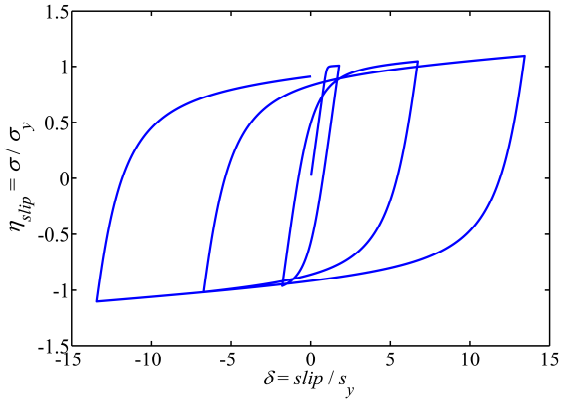

Fig. 5.31 Bar stress-slip model used in zero length section

5.8.2.3.2 Compressive stress-slip model for concrete

The slippage of the longitudinal bars in tension combined with the compression due to flexure and axial force results in a highly localised compressive stress in the concrete in the compression zone. This will cause localised damage in the confined concrete over a so-called d_{comp} depth (Berry and Eberhard 2008) as shown in Fig. 5.32.

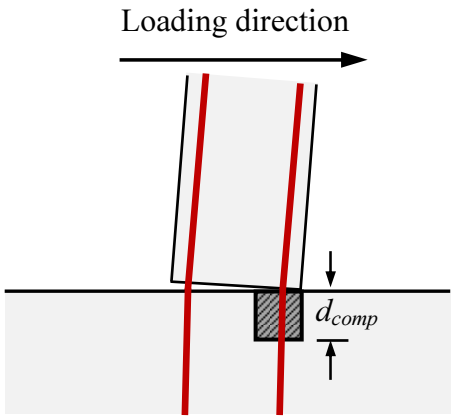

Fig. 5.32 Assumed compressive depth

Berry and Eberhard (2008) recommended a value of 0.5c for d_{ecomp} where c is the depth of the neutral axis. In this study d_{comp} = 0.3D is used in the analyses where D is the column diameter.

The uniaxial material *Concrete01*, with no tension, is used to model the concrete in the zero length section. The stress-strain behaviour of this model is modified by multiplying the strain by d_{comp}. It should be noted that the whole zero length section was considered to be confined concrete. The confinement parameters are the same parameters as the actual concrete model used in the columns. However, given the zero length section element is extremely confined in the foundation, it was assumed that the post-peak branch of the concrete model softens up to 80% of the maximum compressive strength of confined concrete and then follows a perfectly plastic plateau (Zhao and Sritharan 2007).

The stress-slip model of confined concrete model used in zero length section is shown in Fig. 5.33.

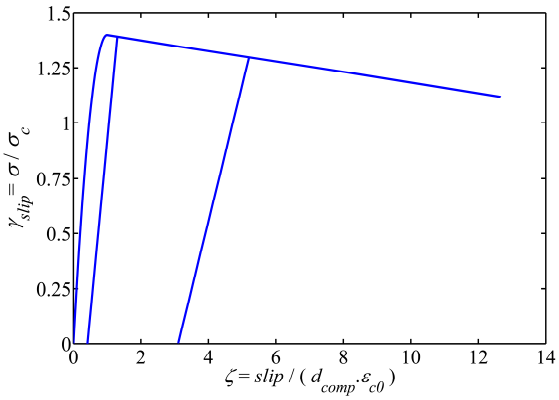

Fig. 5.33 concrete stress-slip model used in zero length section

5.8.3 Initial analysis and comparison of the Steel02 and the new *CorrodedReinforcingSteel* material models

The main objective of this part of research is to investigate the influence of steel material models with and without the effect of buckling and low-cycle fatigue degradation on the cyclic response of RC columns. Therefore the material models for the concrete and zero length elements are kept unchanged throughout the analyses based on the recommendations suggested by Berry and Eberhard (2008).

To validate the basic model, the computed responses of the fibre model using *Steel02* are compared with the experimental results (Fig. 5.34).

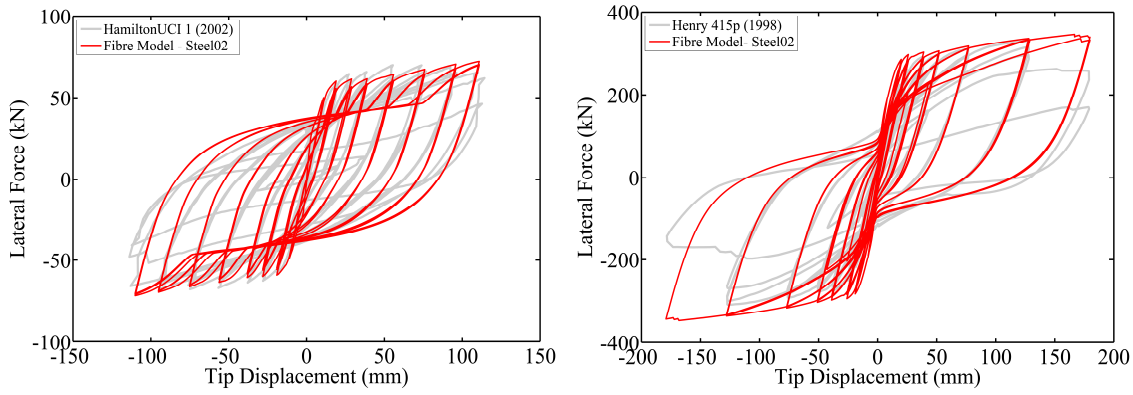

(a) **(b)**

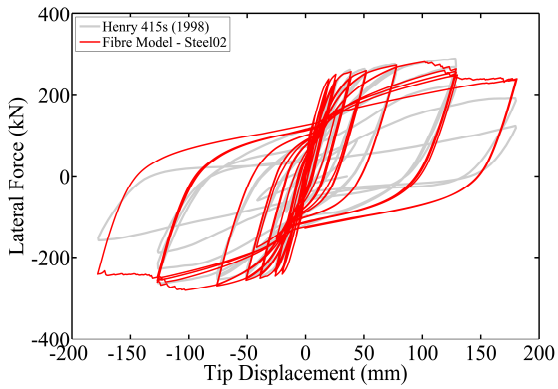
Henry 415s (1998)
Fibre Model - Steel02
Lateral Force (kN)
Tip Displacement (mm)

(c)

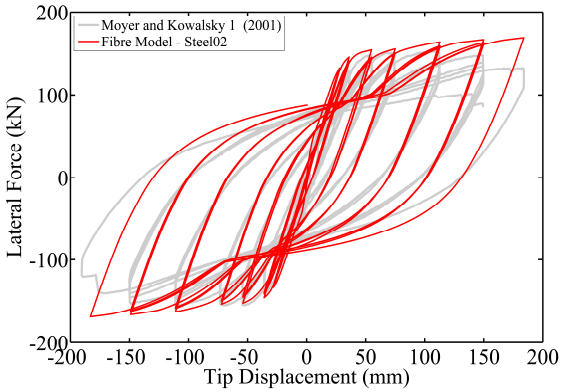
Moyer and Kowalsky 1 (2001)
Fibre Model - Steel02
Lateral Force (kN)
Tip Displacement (mm)

(d)

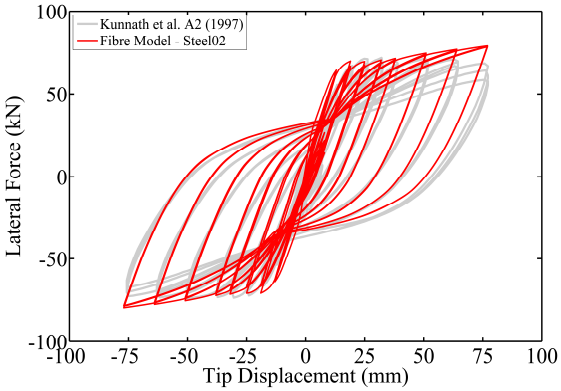
Kunnath et al. A2 (1997)
Fibre Model - Steel02
Lateral Force (kN)
Tip Displacement (mm)

(e)

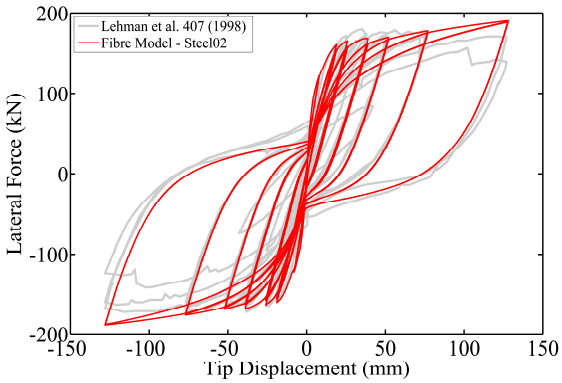
Lehman et al. 407 (1998)
Fibre Model - Steel02
Lateral Force (kN)
Tip Displacement (mm)

(f)

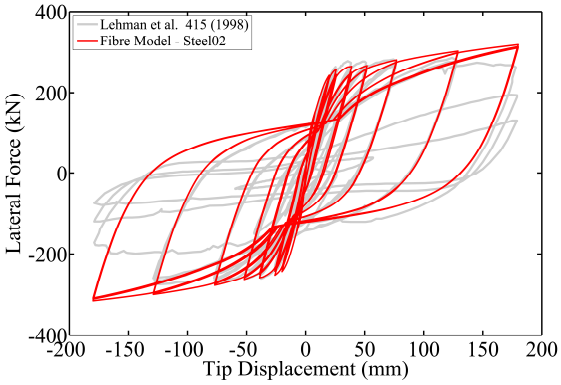
Lehman et al. 415 (1998)
Fibre Model - Steel02
Lateral Force (kN)
Tip Displacement (mm)

(g)

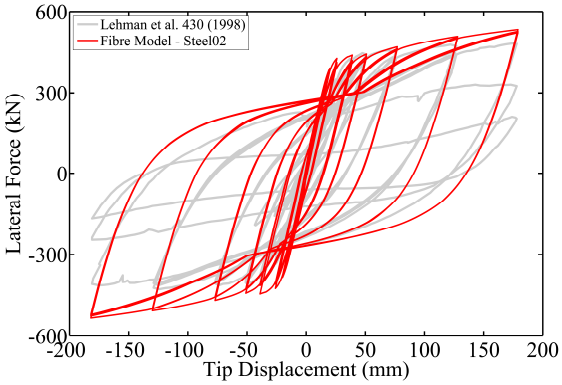
Lehman et al. 430 (1998)
Fibre Model - Steel02
Lateral Force (kN)
Tip Displacement (mm)

(h)

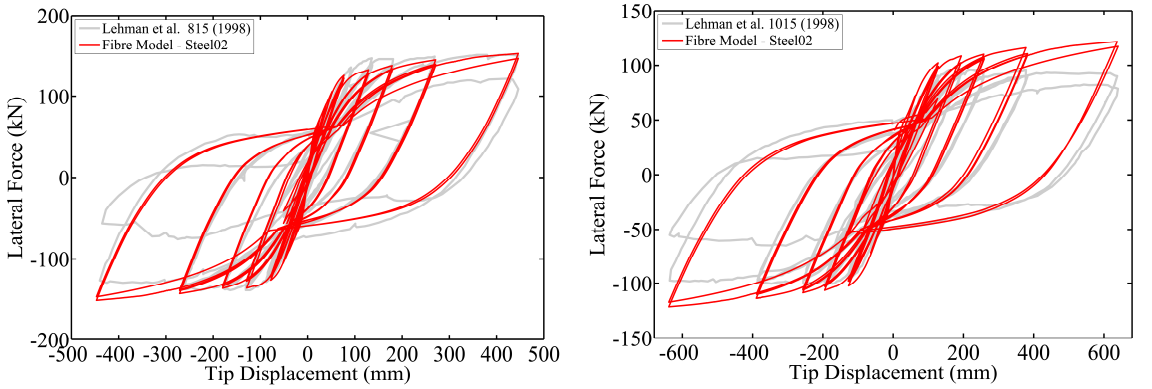

(i) (j)

Fig. 5.34 Force-displacement responses for the experimental dataset using Steel02 model

The computed responses in Fig. 5.34 are identical to those observed by Berry and Eberhard (2008). The *Steel02* model can predict the response accurately until the point that strength degradation starts due to the effect of inelastic buckling and low-cycle fatigue degradation of longitudinal bars.

In the next analyses the *Steel02* material model is replaced with the new *CorrodedReinforcingSteel* that includes inelastic buckling and low-cycle fatigue degradation. The buckling lengths used in the model are the computed values using Dhakal-Maekawa methodology (summarised in Table 5.5). The fatigue parameters used are based on the recommended values reported by Brown and Kunnath (1994). It should be noted that both buckling and fatigue parameters are calibrated for isolated bars. Fig. 5.35 shows two examples of the computed responses using *CorrodedReinforcingSteel*.

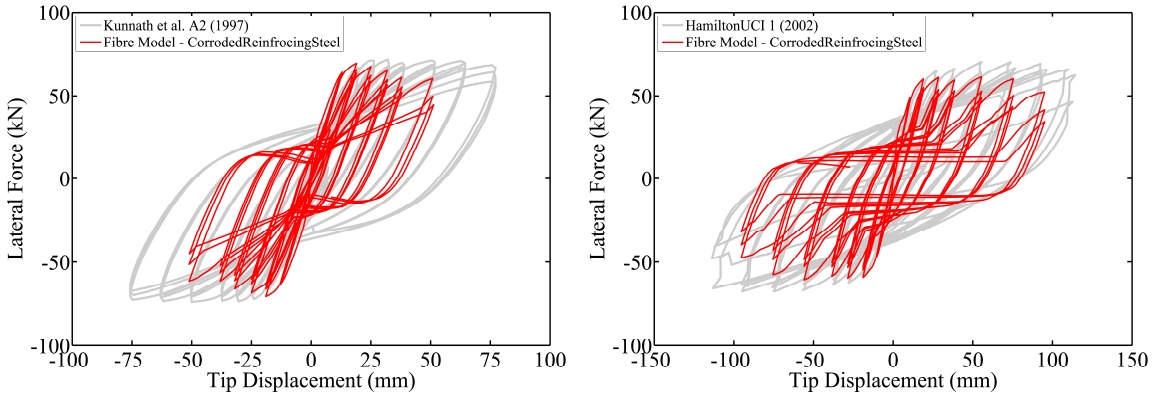

(a) (b)

Fig. 5.35 Examples of force-displacement responses using CorrodedReinforcingSteel model

It is clear from Fig. 5.35 that the computed responses using the new *CorrodedReinforcingSteel* material model are significantly different from the observed experimental responses. This shows that a buckling model of reinforcing bars calibrated using the stress-strain behaviour of isolated bars (bare bars) does not represent the real

behaviour of reinforcing bars inside concrete. The Dhakal-Maekawa methodology can accurately predict the buckling length of vertical bars. However, from comparison of the numerical and experimental results it is clear that the stiffness of ties not only affects the buckling mode and length but also affects the cyclic stress-strain behaviour of bars. In other words the interaction of tie reinforcement and vertical reinforcement under cyclic loading must be considered in the cyclic rules of the reinforcing steel.

The experimental and numerical studies on the nonlinear cyclic response of reinforcing bars showed that buckling results in a severe pinching effect in the cyclic response of isolated reinforcing bars (Chapters 3 and 4). This effect is due to the influence of geometrical nonlinearity on the stress-strain behaviour of isolated bars. However, when reinforcing bars are inside concrete and restrained by horizontal ties, the cyclic response and strength degradation of the bars are influenced by tie stiffness. Therefore, the pinching effect in cyclic response of reinforcing bars inside the concrete is not as severe as for isolated bars.

Solving this problem is a very challenging task, because the *CorrodedReinforcingSteel* model represents the material nonlinearity (due to inelastic behaviour of material), the geometrical nonlinearity (due to buckling and large deformation) and the low-cycle fatigue degradation in one uniaxial material model. Therefore, a systematic way of calibration is required to optimise this model. Accordingly, a parametric study was conducted to find an optimum uniaxial material model for reinforcing bars that provides an accurate prediction of the cyclic response of RC columns considering the inelastic buckling of vertical bars. The procedure of the parametric study is discussed in following sections.

5.8.4 Parametric study using *Hysteretic* material model

5.8.4.1 Selection of pinching parameters

The *Hysteretic* material model in OpenSees has two pinching parameters (pinch x and pinch y). Pinch x is the pinching factor for strain, ranging from 0 to 1 and pinch y is the pinching factor for stress, ranging from 0 to 1. Using these parameters it is possible to control the pinching response of a material model. In the parametric study, nine combinations which consisted of three types of pinching responses were considered (Fig. 5.36). The pinching combinations used in the parametric study are summarised in Table 5.7.

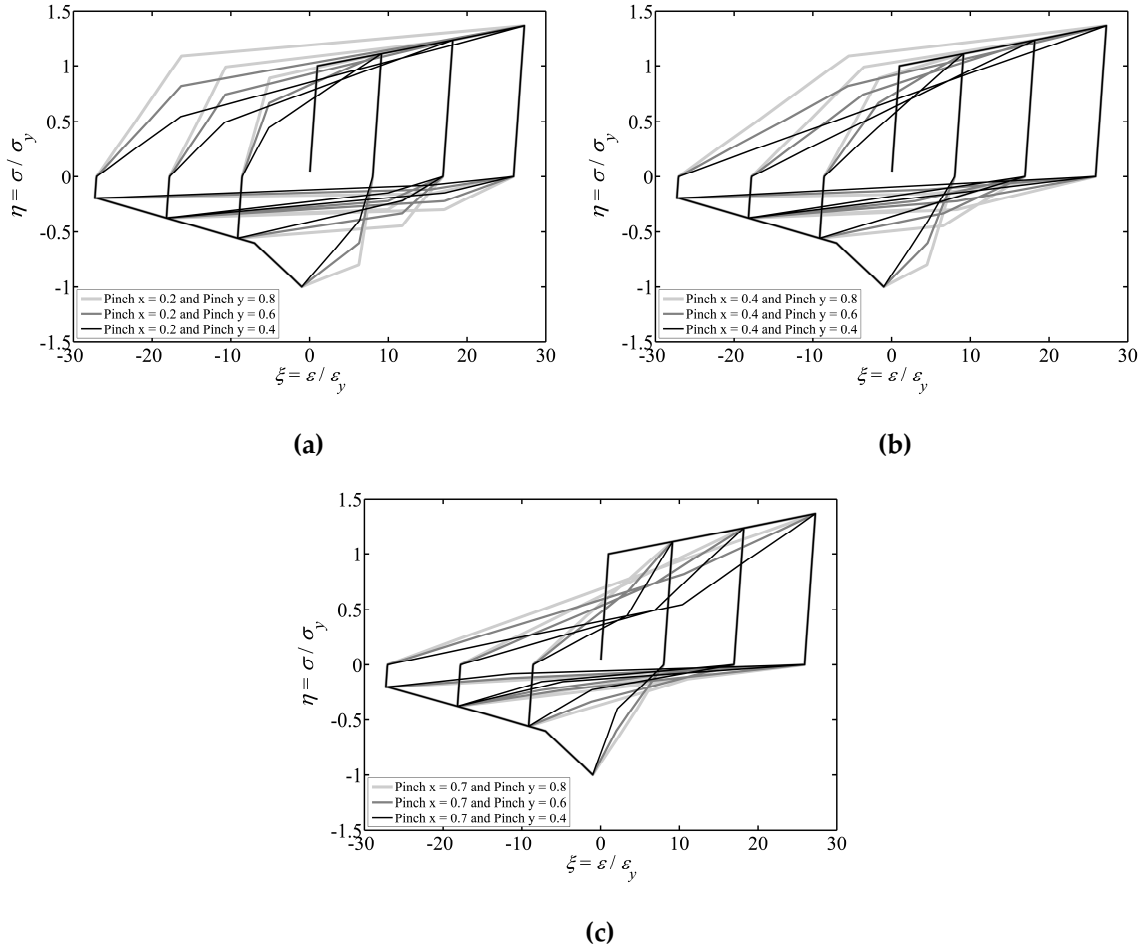

Fig. 5.36 Cyclic responses of reinforcing bar using Hysteretic material model with Leff/d = 10 and different pinching parameters: (a) small pinch (b) moderate pinch (c) severe pinch

Table 5.7 Pinch combination used in the parametric study

Combination	1	2	3	4	5	6	7	8	9
pinch *x*	0.2	0.2	0.2	0.4	0.4	0.4	0.7	0.7	0.7
pinch *y*	0.8	0.6	0.4	0.8	0.6	0.4	0.8	0.6	0.4

The error in hysteretic energy dissipation (Eq. (5.33)) is used as a measure of accuracy in the parametric study.

$$\Omega_E = \frac{\left| E_{meas} - E_{comp} \right|}{E_{meas}} \tag{5. 33}$$

where, Ω_E is the energy error, E_{meas} is the measured dissipated energy in experiment and E_{comp} is the computed dissipated energy in fibre model.

It should be noted that for calculation of the hysteretic energy only hysteretic cycles before severe strength loss in the cyclic response are considered. In this study when the drift capacity falls below 80% of the maximum drift capacity it is considered to be severe strength loss. Given that low-cycle fatigue degradation is normally considered to occur after severe strength loss due to buckling, the *Fatigue* model is not considered in the parametric study.

Fig. 5.37 shows the error in hysteretic energy dissipation (Ω_E) of each column test experiment for all the pinching parameters. It is clear from Fig. 5.37 that the errors for pinching combinations numbered 1 to 4 and numbered 8 to 10 are quite large. However, the error in combinations 5 to 7 is generally below 10% for most columns. It was found that among these three combinations, combination 6 has the smallest average error in the predicted responses. As a further check, the correlation between the pinch parameters (pinch x and pinch y) and design parameters (ρ_l, s/d etc.) was investigated and it was found that there no correlation between these parameters. Therefore combination 6 was taken as the optimum model for further analyses.

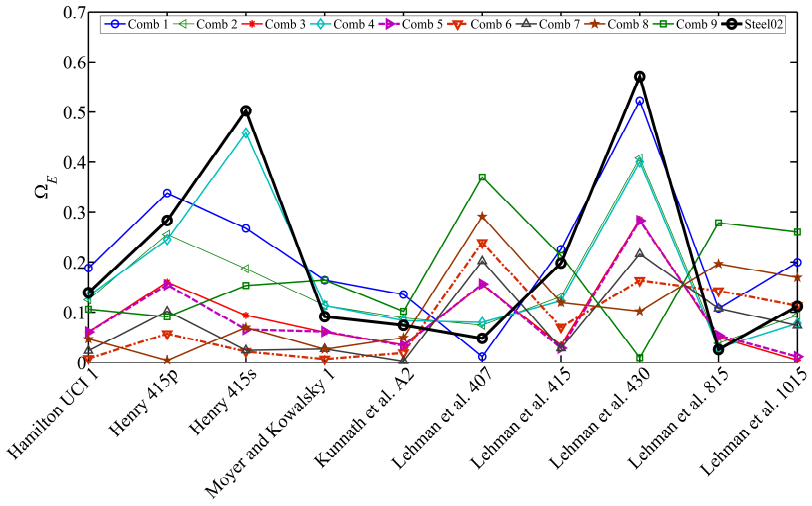

Fig. 5.37 Error in hysteretic energy dissipation of each pinch combination for all the columns

5.8.5 Comparison and discussion of the numerical results of calibrated model with the experimental column dataset

5.8.5.1 Discussion of results without low-cycle fatigue of bars

Fig. 5.38 shows a qualitative comparison between the OpenSees model with the optimised buckling model of reinforcement and the experimental dataset.

It is clear from Fig. 5.38 that the predicted responses of the optimised model are in very good agreement with the observed experimental responses. For example, consider Fig. 5.38 (b) and (c) which show the Henry's columns 415p and 415s. All the details of these two columns are identical apart from the s/d ratio. The difference in s/d resulted in a change in buckling length. Therefore, the response of column 415p with $L_{eff}/d = 10$ is more pinched compared to the response of column 415s with $L_{eff}/d = 8$. This observation is consistent with the observed experimental response.

The buckling of vertical bars in columns results in strength loss in the post-buckling branch of the stress-strain response of reinforcement. This strength loss in reinforcing steel increases the stress in the confined core concrete. Moreover, the horizontal deformation of the vertical bars due to buckling results in yielding and subsequent fractures in the horizontal reinforcement. As a result the core confined concrete crushes. This mechanism results in severe strength loss and degradation in the cyclic response of the column. This can be seen in Fig. 5.38 (b, c, g, h, and i). By comparing the computational responses using *Steel02* and the optimised buckling model, it is clear that the strength degradation cannot be captured using *Steel02*.

It was observed that if vertical bars buckle over a short length the buckling of the vertical bars does not have a significant influence on the cyclic response of the column. For example Fig. 5.38 (d) shows the Moyer and Kowalsky's column 1. The vertical reinforcement in this column buckled over one tie spacing, therefore $L_{eff}/d = s/d = 4$. In this case, the numerical responses using *Steel02* and the optimised buckling model are almost identical and both are in good agreement with the observed experimental response. This is because the compression response of buckling model for $L_{eff}/d < 6$ is identical to the tension envelope. As discussed in Chapters 3 and 4, for ordinary high yield reinforcing bars with yield strength ranging from 400MPa to 500MPa, if $L_{eff}/d < 6$, buckling does not significantly influence the cyclic stress-strain behaviour of reinforcement. Moreover, given the buckling length is very short the horizontal deformation is smaller than for bars with longer buckling lengths. Therefore, horizontal ties do not fracture quickly following the buckling of the vertical bars. As a result the column can sustain a much larger drift without crushing of the confined core concrete in compression.

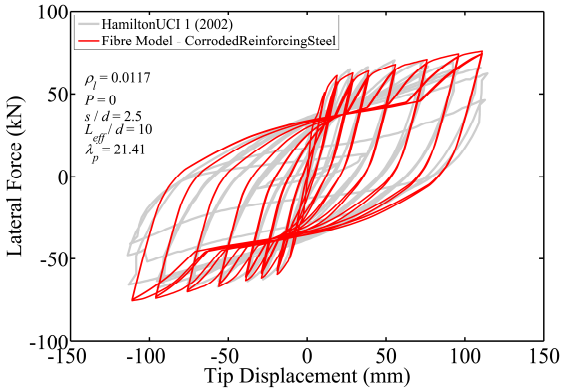
HamiltonUCI 1 (2002)
Fibre Model – CorrodedReinforcingSteel
$\rho_l = 0.0117$
$P = 0$
$s/d = 2.5$
$L_{eff}/d = 10$
$\lambda_p = 21.41$
Lateral Force (kN)
Tip Displacement (mm)

(a)

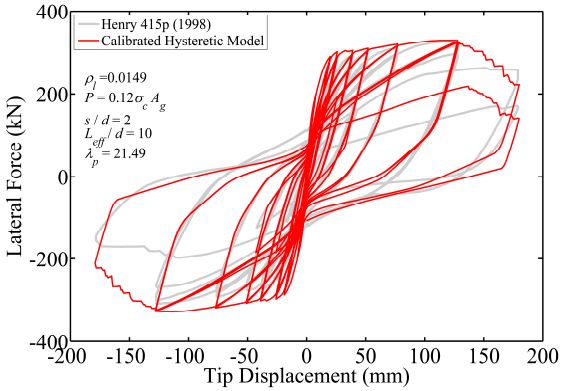
Henry 415p (1998)
Calibrated Hysteretic Model
$\rho_l = 0.0149$
$P = 0.12\sigma_c A_g$
$s/d = 2$
$L_{eff}/d = 10$
$\lambda_p = 21.49$
Lateral Force (kN)
Tip Displacement (mm)

(b)

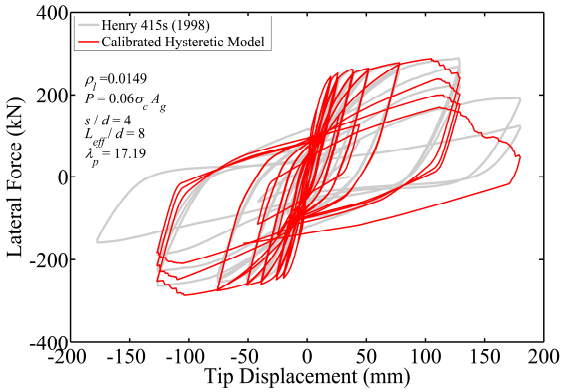
Henry 415s (1998)
Calibrated Hysteretic Model
$\rho_l = 0.0149$
$P = 0.06\sigma_c A_g$
$s/d = 4$
$L_{eff}/d = 8$
$\lambda_p = 17.19$
Lateral Force (kN)
Tip Displacement (mm)

(c)

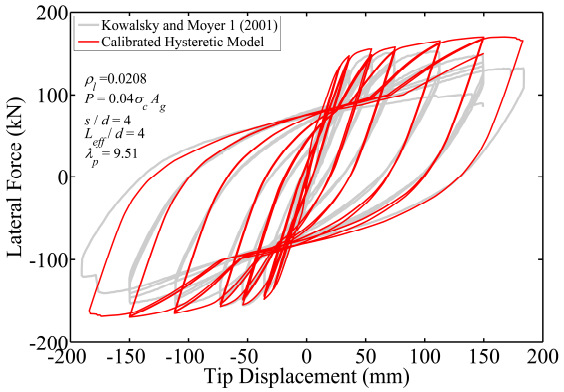
Kowalsky and Moyer 1 (2001)
Calibrated Hysteretic Model
$\rho_l = 0.0208$
$P = 0.04\sigma_c A_g$
$s/d = 4$
$L_{eff}/d = 4$
$\lambda_p = 9.51$
Lateral Force (kN)
Tip Displacement (mm)

(d)

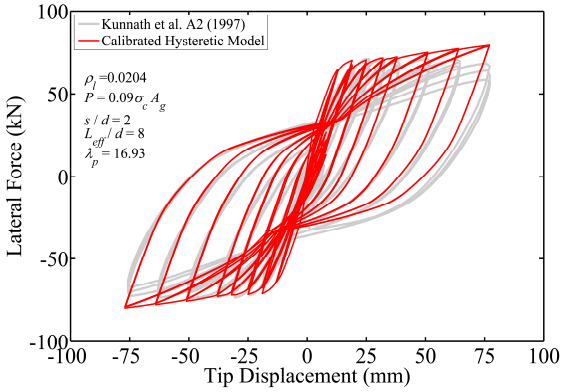
Kunnath et al. A2 (1997)
Calibrated Hysteretic Model
$\rho_l = 0.0204$
$P = 0.09\sigma_c A_g$
$s/d = 2$
$L_{eff}/d = 8$
$\lambda_p = 16.93$
Lateral Force (kN)
Tip Displacement (mm)

(e)

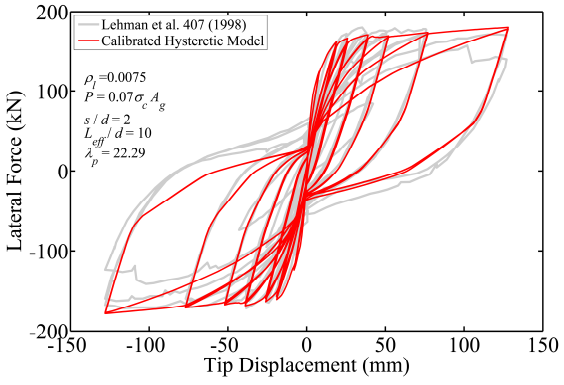
Lehman et al. 407 (1998)
Calibrated Hysteretic Model
$\rho_l = 0.0075$
$P = 0.07\sigma_c A_g$
$s/d = 2$
$L_{eff}/d = 10$
$\lambda_p = 22.29$
Lateral Force (kN)
Tip Displacement (mm)

(f)

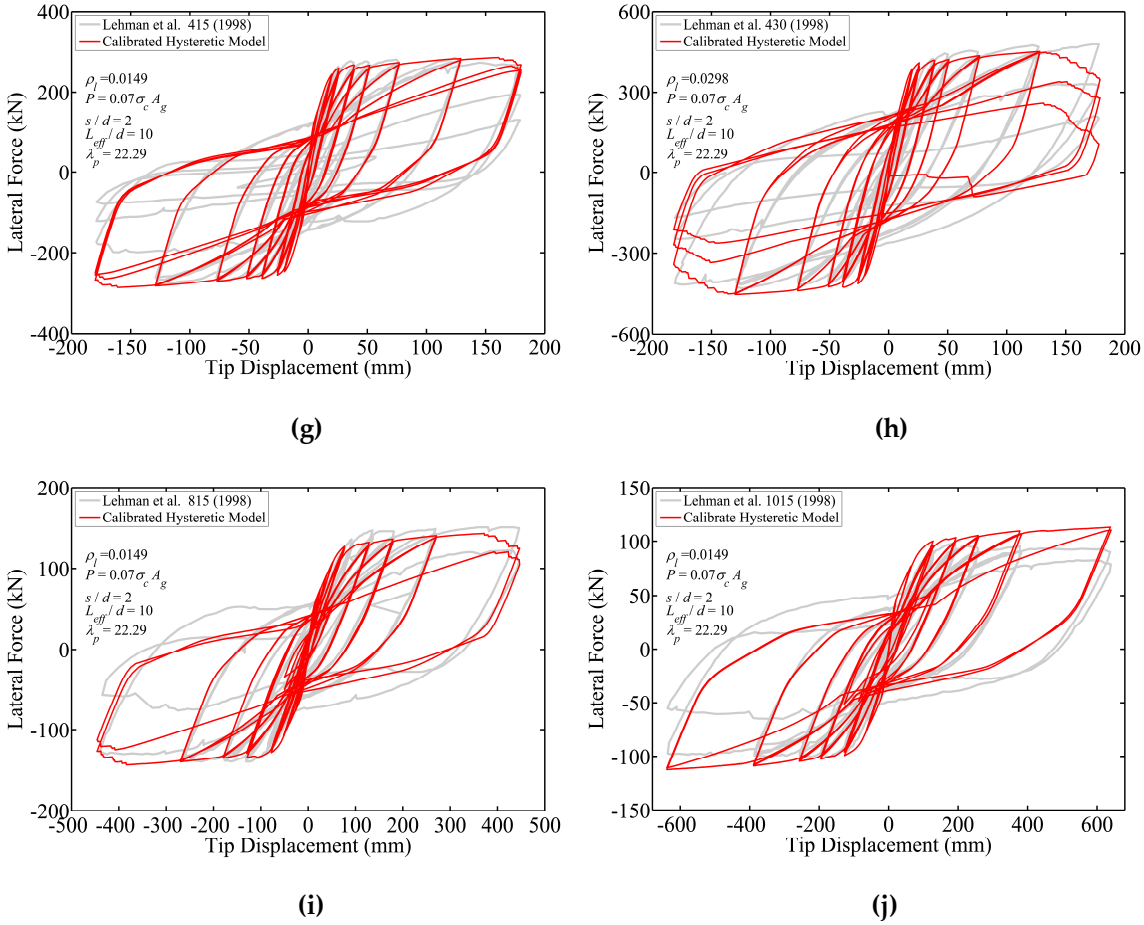

Fig. 5.38 Force-displacement responses for the experimental dataset using calibrated Hysteretic model

In order to quantify the accuracy of the numerical model the errors in predicting the responses at critical stages are compared. The stages considered are the initial stiffness ($K_{initial} = F_y/\Delta_y$ where the F_y is the force at first yield of reinforcement and Δ_y is the corresponding displacement), the prediction of the 1% drift capacity (F_1) and the prediction of the maximum drift capacity (F_{max}). F_{max} is the force at the maximum drift, that column experienced in the physical test. Table 5.8 shows the result of this comparison including the statistics of the error data. Eq. (5.34), below, is used to calculate the error.

$$\Psi_\eta = \left| \frac{\eta_{experiment} - \eta_{computed}}{\eta_{experiment}} \right| \tag{5.34}$$

Where, $\eta_{experiment}$ is the experimental value of the considered variable ($K_{initial}$, F_1 and F_{max}) and $\eta_{computed}$ is the computed predicted value of the considered variable ($K_{initial}$, F_1 and F_{max}).

Table 5.8 Quantitative comparison of the error in the optimized model and experimental dataset

Experiment	$\Psi_{Kinitial}$	Ψ_{F1}	Ψ_{Fmax}
Kunnath et al. A2 (1997)	0.236	0.175	0.083
Lehman et al. 415 (1998)	0.059	0.012	0.004
Lehman et al. 815 (1998)	0.131	0.132	0.167
Lehman et al. 1015 (1998)	0.246	0.295	0.222
Lehman et al. 407 (1998)	0.018	0.011	0.029
Lehman et al. 430 (1998)	0.260	0.188	0.038
Henry 415p (1998)	0.404	0.169	0.000
Henry 415s (1998)	0.366	0.110	0.120
Kowalsky & Moyer 1 (2001)	0.275	0.268	0.245
Hamilton UCI1 (2002)	0.238	0.045	0.127
Mean Value	0.223	0.140	0.104
Standard Deviation	0.117	0.094	0.084
Max	0.404	0.295	0.245
Min	0.018	0.011	0.000

5.8.5.2 Discussion of results considering low-cycle fatigue of bars

The observed experimental results show that some of the columns experienced bar fracture in tension shortly after buckling. The point at which bar fracture occurred during the cyclic test for each column is reported in the relevant references. In this research the *Fatigue* model in OpenSees is warped to the optimised buckling model to model the fracture of bars due to low-cycle fatigue. The fatigue material constants (α and Θ_f) are set to predict the bar fracture at the same point as was observed in the experiment. Fig. 5.39 shows some typical cyclic responses considering the fracture of reinforcing bars due to fatigue.

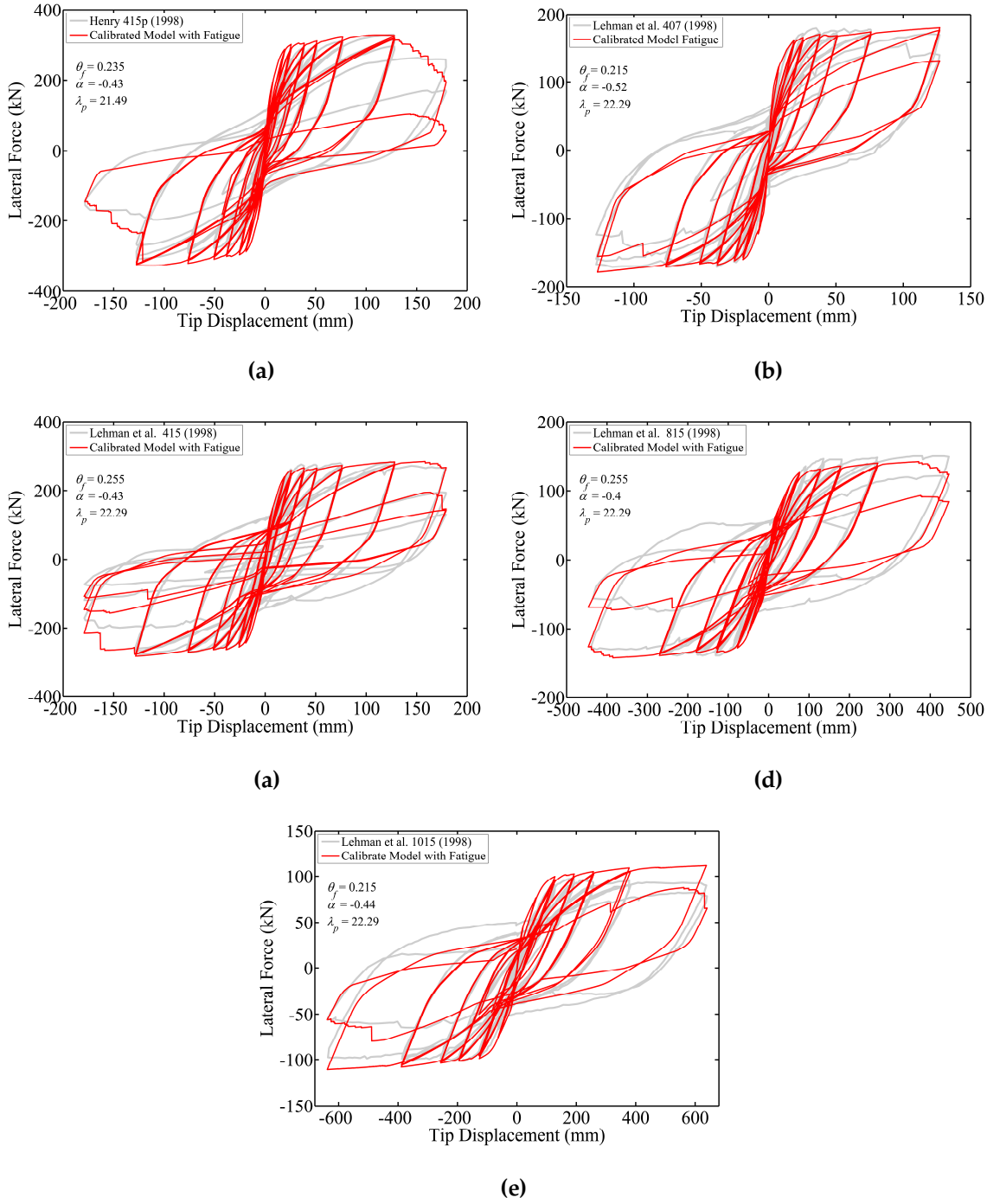

Fig. 5.39 Force-displacement responses for the experimental dataset using calibrated Hysteretic model combined with Fatigue model

It was found that the fracture of bars in tension and the fatigue material constants are both sensitive to λ_p. All the columns with λ_p < 18 did not experience bar fracture in tension. However, as λ_p increased the low-cycle fatigue life of the bars reduced. This shows that the low-cycle fatigue life of reinforcing bars is a function of the non-dimensional slenderness ratio λ_p. This can be seen by comparing Henry column 415p where λ_p = 21.49 with column 415s where λ_p = 17.19. Fig. 5.39 (a) shows the response of

Henry column 415p that experienced bar fracture in tension. However, bar fracture in tension was not observed in Henry column 415s.

This shows that the combined effect of inelastic buckling and low-cycle fatigue degradation has a significant influence on the inelastic response of RC columns. Fig. 5.40 shows a comparison between the normalized accumulated energy dissipation in the two columns. Fig. 5.40 (a) shows Henry column 415p with $\lambda_p = 21.49$ and Fig. 5.40 (b) shows Moyer and Kowalsky column 1 with $\lambda_p = 9.5$.

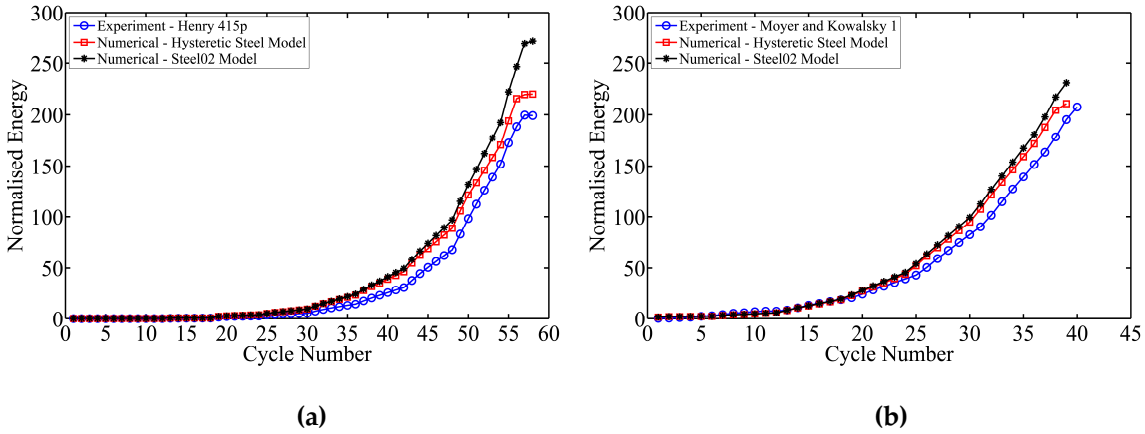

(a) **(b)**

Fig. 5.40 Influence of material model on accumulated energy dissipation: (a) Henry 415p and (b) Moyer and Kowalsky 1

Fig. 5.40 (a) shows that as the number of cycles increases there is a cumulative error in the numerical model which uses *Steel02*. However, Fig. 5.40 (b) shows that the predicted response using Steel02 and the optimized buckling model with fatigue are almost identical. This is another observation which suggests that the bar buckling parameter, λ_p, has a significant influence on the inelastic response of RC columns. This is an area for further research to develop a methodology to calibrate the fatigue material constants as a function of λ_p.

For further validation of the calibrated model a set of cyclic analyses of the Kunnath et al. (1997) columns with random displacement history was conducted. These columns were not included in the calibration process. Fig. 5.41 shows a comparison between the simulated and experimental results of the Kunnath et al (1997) column A11. Fig. 5.41 (a) shows the simulated response using the calibrated buckling model without considering fatigue and Fig. 5.41 (b) shows the simulated response using calibrated buckling model with a fatigue wrapper. It is evident from Fig. 5.41that the calibrated model is capable of predicting the inelastic response of the RC column under an arbitrary random load history. Moreover, the model is able to account for cyclic degradation due to the combined effect of buckling and low-cycle fatigue degradation of the vertical reinforcement.

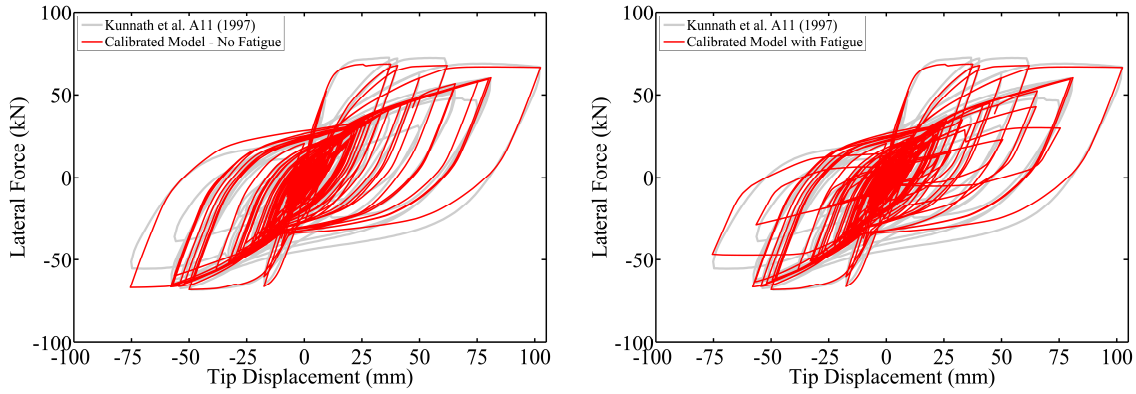

(a) **(b)**

Fig. 5.41 Force-displacement responses for Kunnath et al column A11 under earthquake loading pattern: (a) calibrated buckling model without considering fatigue (b) calibrated buckling model with fatigue

5.9 Conclusions

A new phenomenological model is presented that simulates the inelastic buckling response of uncorroded and corroded reinforcing steel subjected to cyclic loading. The model was developed using data from laboratory testing and from nonlinear finite element analysis of bare reinforcing bars subjected to monotonic and cyclic loading. The model simulates inelastic buckling, the impact of low-cycle high-amplitude fatigue degradation on the nonlinear response, and the impact of mass loss due to corrosion. Response is defined on the basis of *i*) steel material properties, *ii*) nominal reinforcement area, *iii*) the reinforcement slenderness ratio, which may be computed from the bar diameter and spacing of horizontal reinforcement using the model proposed by Dhakal and Maekawa, and *iv*) mass loss due to corrosion. To facilitate use of the model, it has been implemented in OpenSees, an open-source software framework for nonlinear finite element analysis of structures. Furthermore, a new modelling strategy for fibre element modelling of RC bridge piers considering inelastic buckling and low-cycle fatigue of reinforcing bars is presented. The numerical model was calibrated using the UW-PEER experimental RC column dataset. The main conclusions and outcome of this chapter can be summarised as below:

1. Based on the numerical simulation, it was observed that the non-dimensional slenderness ratio, λ_p, is the main parameter influencing the post-yield buckling response of reinforcing bars. This conclusion is in agreement with the outcome of a previous study by Dhakal and Maekawa 2002a,b,c and the experimental results discussed in Chapters 3 and 4.

2. The proposed model, in most cases, can accurately simulate the inelastic buckling and low-cycle fatigue degradation of corroded bars. However, severe localised pitting corrosion might result in an inaccurate simulation. As discussed in Chapters 3 and 4, the stress-strain behaviour of these bars is mainly governed by the minimum section. Given the complexity and high uncertainty associated with localisation of corrosion, this problem should be solved probabilistically. This is an area for further research.
3. The localisation issue in force-based elements in systems with softening response due to buckling can be resolved by using two elements. As suggested the integration length of the first section of first element must be the same as the buckling length in the uniaxial model of reinforcing steel.
4. The methodology developed by Dhakal and Maekawa (2002c) for calculation of the buckling length showed a very good agreement with the observed experimental results. Therefore, this is an accurate and reliable model to be used in calculation of the buckling length of reinforcing bars in RC column accounting for the tie stiffness.
5. It was found that the new *CorrodedReinfrocingSteel* material in OpenSees which was calibrated using experimental and numerical data from isolated bars cannot accurately represent the cyclic behaviour of reinforcing bars inside concrete. This is an area for further research aimed at improving this material model to account for the influence of tie stiffness on the nonlinear cyclic stress-strain behaviour of reinforcing bars.
6. The observed experimental and numerical results showed that fracture of bars due to low-cycle fatigue is very sensitive to the non-dimensional slenderness ratio of the bars (λ_p). This is an area for further research to investigate the influence of buckling on low-cycle fatigue life of reinforcing bars.
7. The final calibrated model was very effective at predicting the nonlinear cyclic response of circular RC columns. The model was also validated against a column experiment with an applied random displacement history which was not included in calibration process. The modelling strategy developed in this chapter can be used in the nonlinear seismic analysis of RC bridges with circular piers as a reliable tool for both researchers and practicing engineers.

This page is intentionally left blank.

CHAPTER 6

Multi-Mechanical Nonlinear Fibre Model for Corroded RC Bridge Piers

6.1. Introduction

In this chapter a numerical model is presented that enables simulation of the nonlinear flexural response of RC components with corroded reinforcement. The model employs the force-based beam-column element and the fibre-type section model that are available in OpenSees (as described in Chapter 5). The new constitutive model for corroded reinforcing steel developed in Chapter 5 is also used. This model simulates the buckling of longitudinal reinforcement under cyclic loading and the impact of corrosion on buckling strength. The basic buckling steel model is validated through comparison of simulated and observed response for RC columns with uncorroded reinforcement (Chapter 5). Typical concrete constitutive models are employed to simulate the response of components with corroded reinforcement. The cover concrete strength is adjusted to account for corrosion induced damage, while the core concrete strength and ductility are adjusted to account for corrosion induced damage to the transverse reinforcement. This model is used to explore the impact of corrosion on the nonlinear response of two hypothetical corroded RC columns under monotonic and cyclic loading.

In recent years several researchers have put significant effort into studying the seismic vulnerability and fragility analysis of RC bridges (Choe et al. 2008, Berto 2009, Ghosh and Padgett 2010, Alipour et al. 2011, Alipour et al. 2013, Ou et al. 2013, Biondini et al. 2013). However, due to a significant paucity in availability of uniaxial material and damage models, in all of the previous studies only very simple material models are considered. Therefore, the aim of the numerical exploration study in this chapter is to explore the impact of different corrosion damage models on the nonlinear response of corroded RC columns. Furthermore, it provides comprehensive modelling guidelines that other researchers can employ to improve the existing numerical models for seismic vulnerability and fragility analysis of corroding systems in future research.

6.2. The proposed nonlinear fibre beam-column element model

The force-based nonlinear fibre beam-column model developed in Chapter 5 is use here. The detailed discussion and validation of the proposed modelling methodology are available in Chapter 5. Therefore, only the relevant uniaxial material models to be used in fibre section are discussed here. Fig. 6.1 shows the fibre section assigned to the beam-column element. The relevant sections discussing the material models are also noted in Fig. 6.1. The implementation of the corrosion damage models that are developed in this thesis into the OpenSees abstract classes is shown in Fig. 6.2. The calculation of buckling length of the corroded vertical reinforcement, uniaxial material models and corrosion damage models are discussed in the following sections.

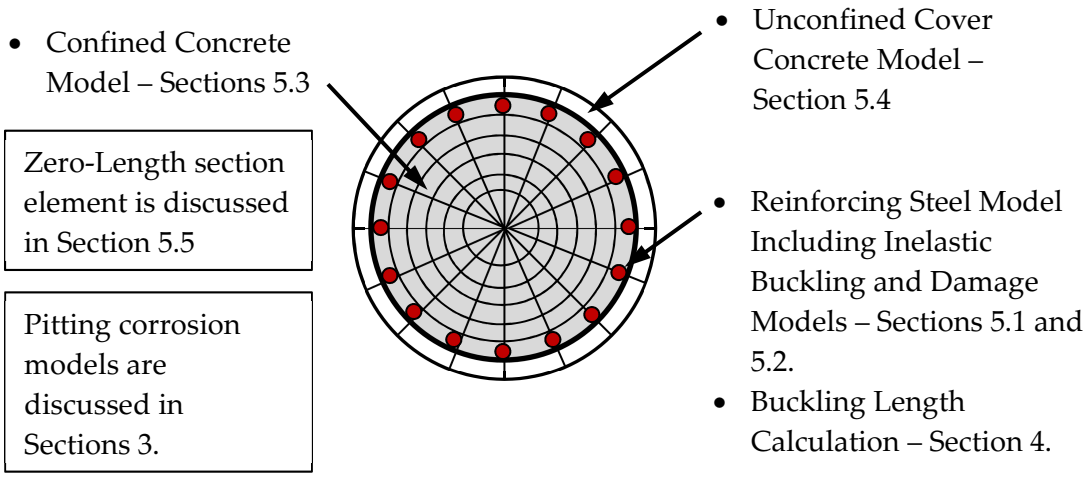

Fig. 6.1 Proposed fibre section model

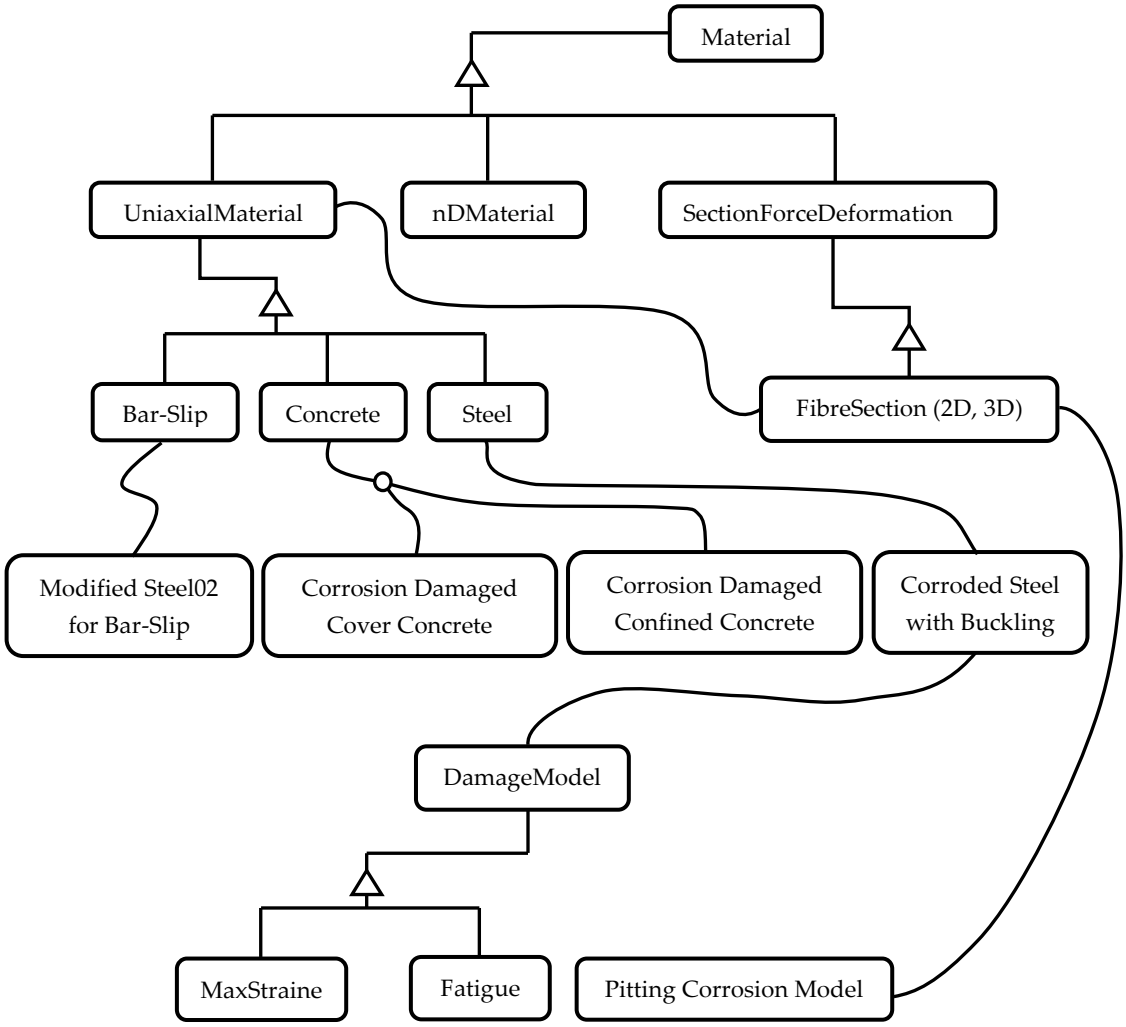

Fig. 6.2 Implementation of the corrosion models within the OpenSees abstract classes

6.3. Influence of corrosion on geometrical properties of corroded bars

Chloride induced corrosion results in irregular loss of the cross section of reinforcing steel known as pitting corrosion. Several researchers studied the impact of nonuniform corrosion on cross section loss of reinforcing bars (Val and Melchers 1997). Chapter 4 conducted a 3D optical measurement on corroded bars to explore the spatial variability of corrosion pattern. As a result they developed a set of probabilistic distribution models to predict the geometric properties of corroded bars. They found that the geometric properties of corroded bars can be modelled using a lognormal distribution model. In this study, the mean value of the lognormal distribution model is used to model the effect of pitting corrosion on the geometric properties of corroded bars.

The Eq. (6.1) can be used to calculate the average reduced cross section area of reinforcement considering a linear reduction in area as function of percentage mass loss ψ.

$$A_{ave} = A_0\left(1-0.01\psi\right) \tag{6.1}$$

where, A_{ave} is the average reduced cross section area of corroded reinforcement and A_0 is the corresponding original uncorroded cross section area.

Once the average reduced cross section area is calculated, the cross section area considering pitting effect (A') can be calculated using the Eq. (6.2).

$$A' = \Upsilon A_{ave} \tag{6.2}$$

where, Υ is the mean value of area pitting coefficient that is derived by assuming a lognormal distribution.

It was found that the irregular cross section shape of corroded bars results in axis rotation (as described in Chapter 4). Therefore, in probabilistic models they considered the minimum principal second moment of area which is very important to model the buckling behaviour of reinforcing bars. The minimum second moment of area of corroded bars ($I'_{\min}$) can be calculated by introducing a pitting coefficient for second moment of area as defined in Eq. (6.3) below:

$$I'_{\min} = \mathrm{K}\, I_0 \tag{6.3}$$

where, K is the mean value of pitting coefficient of minimum second moment of area of the corroded bars considering a lognormal distribution and I_0 is the second moment of area the original uncorroded bar.

The mean values of the pitting coefficients (Υ and K) can be calculated using the Eq. (6.4).

$$M_{(\Upsilon or \mathrm{K})} = \exp\left(\mu + \frac{\sigma^2}{2}\right) \tag{6.4}$$

where, μ and σ are defined in Eqs. (6.5) and (6.6) below:

$$\mu = a\psi^b \tag{6.5}$$

$$\sigma = c\psi^d \tag{6.6}$$

Definitions of the coefficients a, b, c and d are available in Chapter 4.

6.4. Calculation of the buckling length using Dhakal-Maekawa proposed model

The detailed discussion and validation of the Dhakal-Maekawa buckling model is available in Chapter 5. Here the same model is used for calculation of buckling length of corroded reinforcement.

Fig. 6.3 shows a schematic overview of the extent of corrosion damage on a hypothetical corroded RC column. The pattern of damage at section level shown in Fig. 6.3 is based on the observed experimental tests by (Lee et al. 2000, Aquino 2001). The corrosion of vertical reinforcement results in longitudinal cracks at the surface of column parallel to vertical reinforcement. This will reduce the cross sectional area and flexural rigidity of vertical reinforcement which is very important in buckling. Corrosion of horizontal (spiral) reinforcement reduces the volumetric ratio of confinement which is very important for strength and ductility of core concrete. Furthermore, this will result in splitting of the core and cover concrete by creation of horizontal cracks around the perimeter of column section. Horizontal ties (spiral reinforcement in circular columns) also restrain the vertical bars against buckling and corrosion reduces the stiffness of these ties. Therefore, these parameters need to be considered in prediction/calculation of the buckling length of corroded bars.

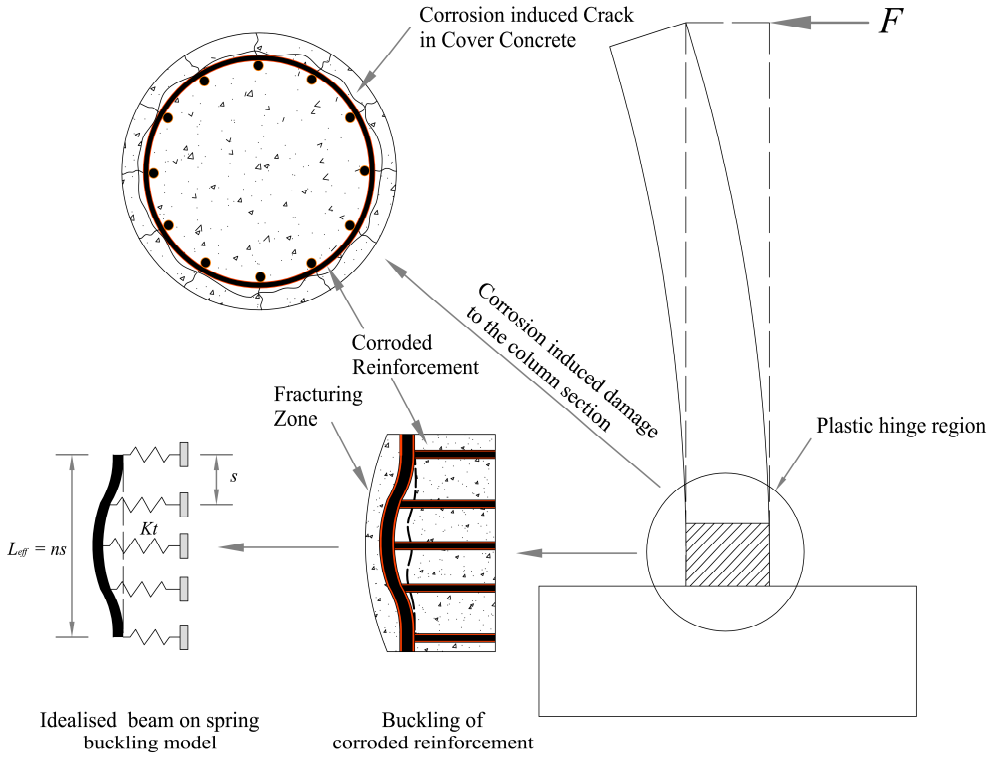

Fig. 6.3 Schematic overview of corrosion induced damage to RC column

As explained in Chapter 5, the Dhakal-Maekawa buckling model is used to calculate the buckling length of vertical reinforcement. To account for the effect of corrosion on Dhakal-Maekawa equations the flexural rigidity of vertical reinforcement *EI* and Stiffness of spiral reinforcement are adjusted. This is discussed in the following sections.

6.4.1. Influence of corrosion on flexural rigidity of corroded bars

The average flexural rigidity (*EI*) in Dhakal-Maekawa model is a function of yield strength and second moment of area of reinforcement. Therefore, by adjusting the second moment of area and yield strength of corroded bars the same equation can be used for calculating the average flexural rigidity of corroded reinforcement as defined in Eq. (6.7).

$$EI = \frac{E_s I'_{\min}}{2}\sqrt{\frac{\sigma'_y}{400}} \tag{6.7}$$

Where, E_s and σ'_y are the elastic modules and yield strength of the corroded vertical reinforcement in MPa respectively and I'_{min} is defined in Eq. (6.3).

As discussed in Chapter 3, corrosion of reinforcing bars affects the yield strength of reinforcement. The yield strength can be modified based on the empirical Eq. (6.8) suggested by Du et al. (2005a).

$$\sigma'_y = \sigma_y\left(1 - 0.005\psi\right) \tag{6.8}$$

where, ψ is the percentage mass loss of the reinforcement.

6.4.2. Influence of corrosion on stiffness of tie reinforcement

In this study the stiffness of spiral (tie) reinforcement is computed using the empirical Eq. (6.9) suggested by Pantazopolou (1998).

$$K_t = \frac{4E_{sp}A'_{sp}}{\sqrt{\left(s^2 + d_c^2\right)}} \tag{6.9}$$

Where, E_{sp} is the elastic modules of the spiral reinforcement, A'_{sp} is the cross section area of the corroded spiral reinforcement as defined in Eq. (6.2), s is the spiral pitch and d_c is the core diameter.

The focus of this chapter is on circular columns, however, In the case of rectangular section the axial stiffness of tie reinforcement can be computed using Eq. (6.10).

$$K_t = \frac{E_{st}A'_{st}}{l_t} \tag{6.10}$$

where, E_{st} is the elastic modules of the tie reinforcement, A'_{st} is the cross section area of the corroded tie reinforcement as defined in Eq. (6.2) and l_t is the length of the rectangular tie reinforcement.

6.5. Description of uniaxial material models including corrosion damage

6.5.1. Reinforcing steel model – tension and compression envelopes

The uniaxial material model developed in Chapter 5 is used to model the reinforcing steel. The impact of corrosion on tension envelope and compression envelope (including the post-buckling behaviour) are discussed in Chapter 3 and 5. To implement the buckling model in the OpenSees the uniaxial *Hysteretic* model available in OpenSees is used (The detailed discussion is available in Chapter 5). Fig. 6.4 shows the implemented tension and compression envelope curves of corroded bars in OpenSees.

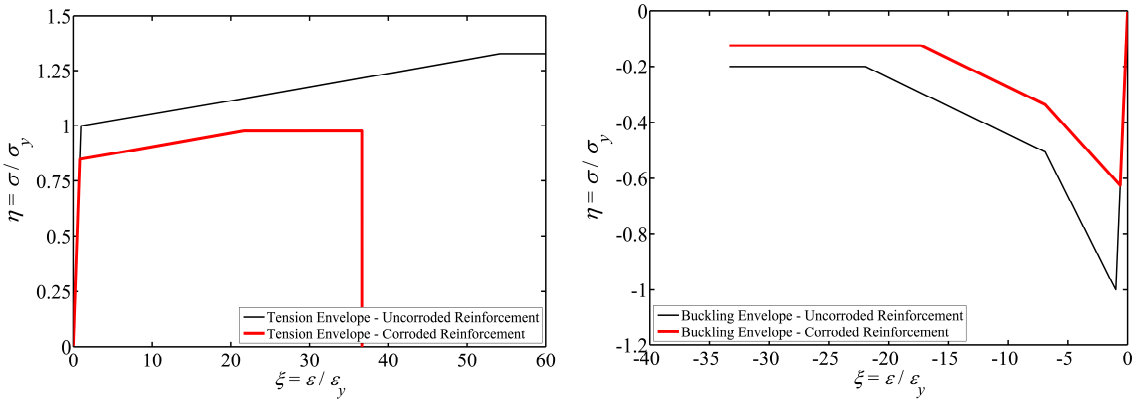

(a) **(b)**

Fig. 6.4 Implemented material model of corroded bars in the OpenSees: (a) tension envelopes, (b) compression envelope

6.5.2. Reinforcing steel model – cyclic response and low-cycle fatigue behaviour

As explained in section 6.5.1 the *Hysteretic* material model in OpenSees is used to define the reinforcing steel model. The cyclic response of the *Hysteretic* model is defined by two pinch parameters (pinch x and pinch y). The pinching effect in cyclic response of reinforcing bars is affected by the stiffness of horizontal ties. The optimum values of pinch parameters have been obtained in Chapter 5 (pinch x = 0.4 and pinch y = 0.6). The *Uniaxial Fatigue* model is wrapped to the steel material model to model the low-cycle fatigue degradation of corroded reinforcement. The low-cycle fatigue material constants are modified to account for the impact of corrosion on the low-cycle fatigue life of

corroded bars based on the model developed in Chapter 3. Fig. 6.5 shows an example cyclic response of the implemented *Hysteretic + Fatigue* model for the uncorroded and corroded reinforcing bars. Further detailed discussion about modelling combined fatigue and buckling of reinforcing bars inside RC columns is available in Chapter 5.

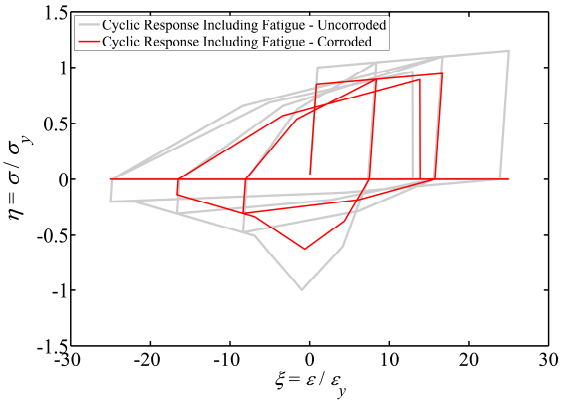

Fig. 6.5 Cyclic response of the *Hysteretic + Fatigue* model in the OpenSees

6.5.3. Corrosion-damaged confined concrete model

The compressive behaviour of confined concrete is a function of the volumetric ratio and the yield strength and fracture strain of the tie reinforcement (i.e. spiral or hoop reinforcement) (Mander et al. 1988, Mander et al. 1989). Since tie reinforcement is the outmost reinforcement to be exposed to chloride attach, it starts corroding prior to the corrosion initiation of the vertical reinforcement. As a result the volumetric ratio of the tie reinforcement decreases due to cross section loss and the yield strength and fracture strain are reduced due to the pitting effect. Therefore, the internal confinement pressure of the core concrete results in premature fracture of tie reinforcement.

To date, there have not been any experimental studies to quantify and model the effect of corrosion on nonlinear behaviour of confined concrete under monotonic compression and cyclic loading. Further research is required for understanding and modelling the extent of corrosion damage on confined concrete behaviour. However, a simplified methodology is used in this research to modify the confined concrete model as a function of percentage mass loss to account for the effect of corrosion damaged.

The uniaxial *Concrete04* material model that was described in Chapter 5 is used to model the concrete. The parameters proposed by Mander et al. (1989) are used to model the effect of confinement on concrete in compression. The maximum compressive stress of the concrete (σ_{cc}) and the strain at the maximum compressive stress (ε_{cc}) can be calculated using the following Eqs. (6.11) to (6.16).

$$\sigma_{cc} = \sigma_c \left(2.254\sqrt{1+7.94\frac{\sigma_{pl}}{\sigma_c}} - 2\frac{\sigma_{pl}}{\sigma_c} - 1.254 \right) \tag{6.11}$$

$$\varepsilon_{cc} = 0.002\left(1+5\left(\frac{\sigma_{cc}}{\sigma_c}-1\right)\right)$$

$$\sigma_{pl} = \frac{1}{2}\rho_{sc}\sigma_{ytie}k_e \tag{6.12}$$

(6.13)

$$k_e = 1-\frac{\frac{s'}{2d_c}}{1-\rho_l} \tag{6.14}$$

$$s' = s - d_{trans} \tag{6.15}$$

$$\rho_{sc} = 4\left(\frac{A_{tie}}{d_c\, s}\right) \tag{6.16}$$

where, σ_c is the compressive strength of the concrete, d_c is the diameter of the core, ρ_l is the ratio of the longitudinal reinforcement, and A_{tie}, d_{trans}, s and σ_{ytie} are the area, diameter, spacing and yield strength of the tie/spiral reinforcement respectively. Further detail is available in Mander et al. (1989).

The maximum crushing strain of the confined concrete is defined by the fracture of the first horizontal tie/spiral reinforcement. Here the model proposed by Scott et al. (1982) is used to predict the concrete crushing strain as defined in Eq. (6.17).

$$\varepsilon_{cc} = 0.004 + 1.4\left(\frac{\rho_{sc}\,\sigma_{ytie}\,\varepsilon_{utie}}{\sigma_c}\right) \tag{6.17}$$

where, ε_{utie} is the fracture strain of the tie/spiral reinforcement.

It is clear that the confined concrete model is function of the volumetric ratio, yield strength and fracture strain of tie/spiral reinforcement. Therefore, the same method that was adopted to modify the tension envelope of reinforcing bars can be used to modify the cross section area, yield strength and fracture strain of tie/spiral reinforcement as a function of percentage mass loss. Using this method the influence of corrosion on confined concrete model is accounted as shown in Fig. 6.6.

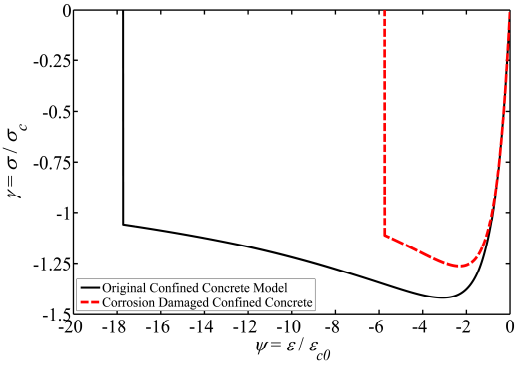

Fig. 6.6 Corrosion damaged confined concrete model

6.5.4. Corrosion-damaged cracked cover concrete model

Once corrosion initiates, the corrosion products accumulate around the reinforcement. Given the volume of the corrosion products are bigger than the original reinforcing steel, this generates a radial pressure/expansion on the concrete surrounded the reinforcement. This behaviour is like a thick cylinder under internal pressure that eventually results in fracture of the cover concrete. This cracking of cover concrete results in loss of compressive strength and ductility of the concrete in the compressive zone of RC sections. Therefore consideration needs to be given to modelling the influence of cracking on the response of concrete in compression.

The response of cracked concrete in compression is described in detail by Vecchio and Collins (1986) and is known as Compression Field Theory (CFT). Based on CFT the compressive strength of cracked concrete in compression depends on the magnitude of the average tensile strain in the transverse direction, which causes longitudinal microcracks. Coronelli and Gambarova (2004) employed this method in nonlinear finite element analysis of corrosion damaged RC beams with a modified constitutive model for cracked cover concrete as a function of the percentage mass loss. Therefore, the following Eq. (6.18) to Eq. (6.21) suggested by Coronelli and Gambarova (2004) are used in this study to modify the uniaxial material model used in unconfined cover concrete.

$$\sigma_c' = \frac{\sigma_c}{1 + K\dfrac{\varepsilon_1}{\varepsilon_{c_0}}} \tag{6.18}$$

where, σ'_c is the residual compressive strength of cracked cover concrete, σ_c is the compressive strength of the original cover concrete, K is the coefficient related to bar roughness and diameter which can be taken as K = 0.1, ε_{c0} is strain at the peak compressive stress σ_c; and ε_1 is average (smeared) tensile strain in the cracked concrete at right angles to the direction of the applied compression. ε_1 can be calculated as follows:

$$\varepsilon_1 = \frac{(P_{corr} - P_0)}{P_0} \tag{6.19}$$

$$P_{corr} - P_0 = n_{bars} w_{cr} \tag{6.20}$$

$$w_{cr} = 2\pi (v_{rust} - 1) X \tag{6.21}$$

where, where P_0 is the perimeter of the original column section (uncorroded with no cracks), P_{corr} is the perimeter of the column section increased by corrosion cracking, n_{bars} is the number of bars in column section, w_{cr} is the total crack width for a given corrosion level X. v_{rust} is ratio of the volumetric expansion of the corrosion products with respect to the original steel, and X is depth of the corrosion attack (pitting depth). Molina et al. (1993) suggested the value of $v_{rs} = 2$. Fig. 6.7 (a) shows the compression envelope and Fig. 6.7 (b) shows the tension envelope of the corrosion damaged unconfined cover concrete model used in the fibre model. Further detail is available in Coronelli and Gambarova (2004).

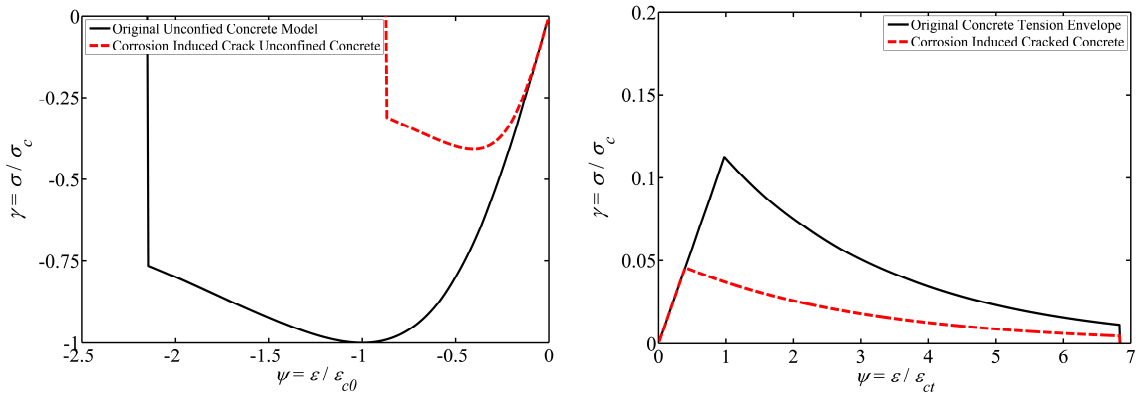

(a) **(b)**

Fig. 6.7 Corrosion damaged cracked cover concrete model: (a) compression (b) tension

6.5.5. Bond-slip model and zero length element

In seismic design of RC structures and bridges, plastic hinges are formed at the column/beam ends. This induces a substantial strain penetration along the longitudinal bars into the joint that eventually results in slippage of the longitudinal bars. This phenomenon has been observed by other researchers experimentally (Lehman and Moehle 2000). Lowes and Altoontash (2003) adopted a bar-slip model for the end slip of longitudinal reinforcement in beam-column joints. This model was employed in Chapter 5 to model the cyclic behaviour of RC columns and was validated against an experimental dataset.

It is well known to researchers that corrosion affects the reinforcing bars near the surface of concrete due to diffusion of chloride ions from the surface and/or carbonation of cover concrete. In bridge piers, the longitudinal bars are anchored to the foundation well below the foundation surface. Therefore, the longitudinal bars don't corrode at this depth and the bar-slip behaviour of bars at the anchorage zone remains the same as uncorroded column. This has been observed experimentally by other researchers (Ou et al. 2011, Ma et al. 2012).

It should be pointed out that corrosion does affect the bond strength of corroded longitudinal bars above the foundation level (internal bond-slip within the column itself). However, based on the observed experimental results the reduced bond-strength does not govern the failure of the columns. Ou et al. (2011) and Ma et al. (2012) reported that the failure of corroded columns and beams under cyclic loading is mainly governed by fracture of bars in tension due to low-cycle fatigue and buckling of the longitudinal bars and crushing of the confined concrete in compression. Kallias (2011) conducted a comprehensive detailed nonlinear finite element analysis of corroded RC beams and validated them against experimental results. They reported that reduced bond strength only changes the crack pattern and affects the serviceability of corroded beams. They concluded that reduce bond strength does not affected the ultimate capacity of corroded beams. Therefore, bond-slip of corroded longitudinal bars within the element is not considered in this research.

The detailed discussion and implementation of the zero length section in modelling the cyclic behaviour of RC columns is available in Chapter 5.

6.6. Impact of corrosion damage models on nonlinear response of corroded RC bridges piers

In this section the impact of different corrosion models on the inelastic response of RC columns is explored. A comparative study on two hypothetical corroded RC columns with different buckling lengths of vertical bars is conducted. The columns are taken from the UW-PEER (Berry et al. 2004) experimental RC column database. These columns were also used to validate and calibrate the basic numerical model for the uncorroded columns (Chapter 5).

To investigate the impact of corrosion on drift capacity and strength loss of RC columns a series of nonlinear pushover analysis with varied corrosion levels were conducted. To explore the impact of cyclic degradation, nonlinear cyclic analyses were conducted using the actual load histories that were used in the experiments. For each analysis type three scenarios are considered:

(a) Reinforcing steel is corroded, but cover and core concrete are not affected by corrosion.
(b) Reinforcing steel is corroded and cover concrete is cracked due to corrosion, but core concrete is not affected.
(c) Reinforcing steel is corroded, cover concrete is cracked and core concrete is affected due to corrosion of confining reinforcement.

The Lehman column 415 and Moyer and Kowalsky column 1 are considered in this study. The geometrical detail, material properties and detailed experimental results of these columns are available in (Lehman and Moehle 2000, Moyer and Kowalsky 2003). Fig. 6.8 shows a comparison of the numerical model and experimental response of these columns. It should be noted that the Lehman column 415 has L_{eff}/d = 10 and Moyer and Kowalsky column 1 has L_{eff}/d = 4. The detailed discussion of the numerical model validation is available in Chapter 5.

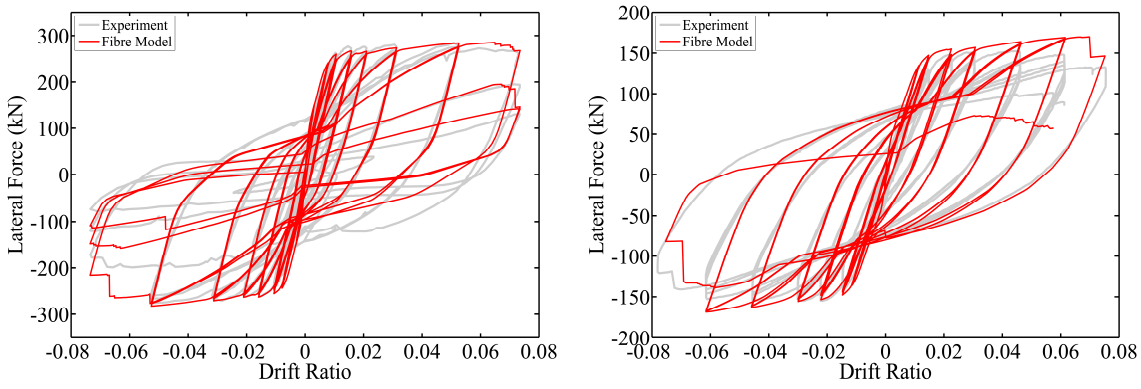

(a) **(b)**

Fig. 6.8 Geometry of columns in the experimental data for the original uncorroded columns: (a) Lehman 415 (b) Moyer and Kowalsky 1

The buckling lengths of corroded bars are calculated using the methodology described in Section 6.4. The corrosion of horizontal ties is considered in the buckling length calculation. As discussed previously, the buckling length of the vertical bars is a function of the horizontal reinforcement stiffness and the flexural stiffness of the vertical reinforcement. Corrosion results in a reduction in the flexural rigidity of vertical bars. Therefore, the required stiffness from tie reinforcement to restrain the vertical bars against buckling is reduced. However, corrosion also reduces the stiffness of tie reinforcement. For example in Moyer and Kowalsky's column, vertical reinforcement buckled between two ties (mode 1). In this case, it was found that corrosion doesn't affect the buckling length. In Lehman's column 415, vertical reinforcement buckled over five ties (mode 5), However, once corrosion level exceeded 10% the buckling mode changed to mode 4 and therefore, buckling length reduced. It should be noted that,

although buckling length reduced, the L_{eff}/d' is not necessarily reduced where L_{eff} is the buckling length and d' is the diameter of corroded reinforcement. This is because corrosion reduces the diameter of vertical bars.

In the real world, tie reinforcement corrodes earlier than vertical bars and therefore, the corrosion level in the tie reinforcement is higher than in the vertical bars. In this research, in the absence of any experimental data, the same corrosion level is considered for both vertical and tie reinforcement. This is an area for future research.

It should be noted that calculation of the time to corrosion initiation and time-dependant corrosion propagation is out of the scope of this research. There are mathematical models available in the literature that enable an estimation of the time to corrosion initiation and corrosion propagation based on the environmental conditions (Vu and Steward 2000, Val 2007). The corrosion rate can also be measured on site using electrical equipment (Broomfield 2007) which then can be turned into a mass loss ratio using Faraday's law of electrolysis (Broomfield 2007). The aim of this research is to explore the impact of different mass loss ratios on seismic performance of RC columns. Therefore, corrosion level is considered as percentage mass loss throughout this research.

6.6.1. Impact of corrosion models on nonlinear response of bridge piers

6.6.1.1. Monotonic and cyclic response considering corrosion of longitudinal reinforcement only

In this scenario, it is assumed that the corrosion damage is limited to the vertical reinforcement; i.e. the cover concrete is uncracked and corrosion of the confining reinforcement doesn't affect the confined concrete behaviour. It should be noted that this considering scenario is only for comparison of the impact of damage models. In this case the steel model described in Sections 6.5.1 and 6.5.2 is used, which includes the impact of corrosion on buckling and post-buckling behaviour in compression; strength and ductility loss in tension.

Fig. 6.9 shows the results of monotonic pushover analyses. Fig 6.9 (a) shows that the failure mode of Lehman column 415 is bar buckling and concrete crushing up to 10% mass loss. However, for a corrosion level beyond 10%, mass loss changes the failure mode from bar bucking and concrete crushing in compression to fracture of vertical bars in tension. Fig 6.9 (b) shows that the Moyer and Kowalsky column has also failed via bar buckling and concrete crushing in compression. However, because the L_{eff}/d = 4, the strength loss is not as significant as the Lehman column 415 with L_{eff}/d = 10 under monotonic loading. However, corrosion results in a change in this column behaviour.

For corrosion level between 10% and 20% mass loss the Moyer and Kowalsky column shows a combination of bar buckling and concrete crushing in compression and fracture of vertical bars in tension. However when the corrosion level is greater than 20% mass loss the column just experiences premature fracture of vertical bars in tension.

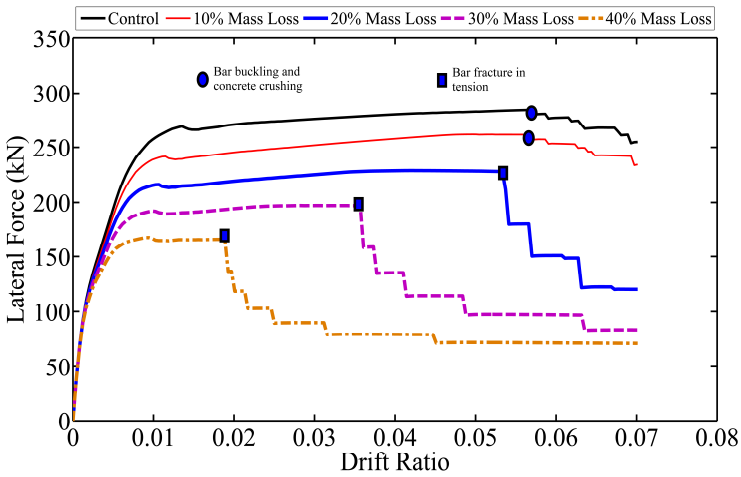

(a)

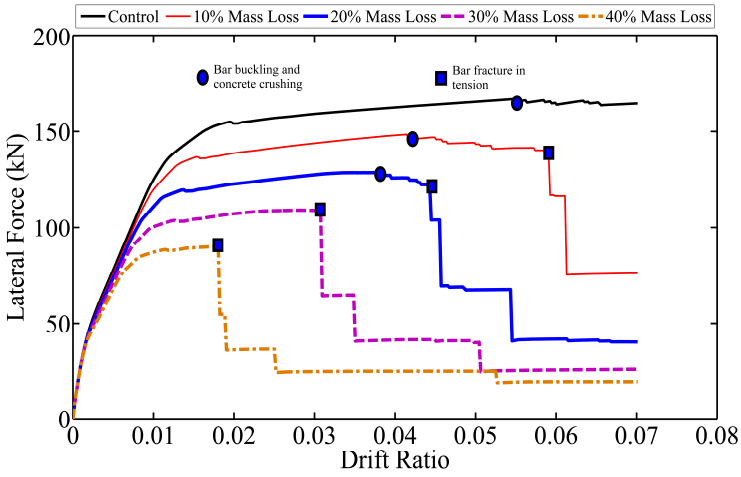

(b)

Fig. 6.9 Pushover analyses considering corrosion induced damage in reinforcing steel: (a) Lehman 415 (b) Moyer and Kowalsky 1

Fig. 6.10 (a) and (b) show the Lehman's column 415 with hypothetical 10% and 20% mass loss respectively. Comparison of the monotonic and cyclic responses (the same cyclic load protocol as the experiment) shows that low-cycle fatigue has a significant impact on the corroded columns. The monotonic analysis showed that 10% mass loss did not result in bar fracture in tension and the failure was governed by bar buckling and concrete crushing. However, in the cyclic analysis, the failure mode is combined bar buckling and

concrete crushing in compression followed by bar fracture in tension due to low-cycle fatigue. It was found that a mass loss ratio greater than 10% has a significant impact on nonlinear response of corroded columns due to reduced low-cycle fatigue life. Fig 6.10 (b) shows that 20% mass loss results in bar fracture at 0.05 drift ratio in pushover analysis but it results in bar fracture at 0.03 drift ratio under cyclic loading due to low-cycle fatigue failure. Fig. 6.10 (c) and (d) show a similar results for the Moyer and Kowalsky column 1. The Moyer and Kowalsky column 1 has slightly less pinched cyclic response; this is due to the influence of the buckling length of the vertical bars and cyclic degradation due to bar buckling (Chapter 5).

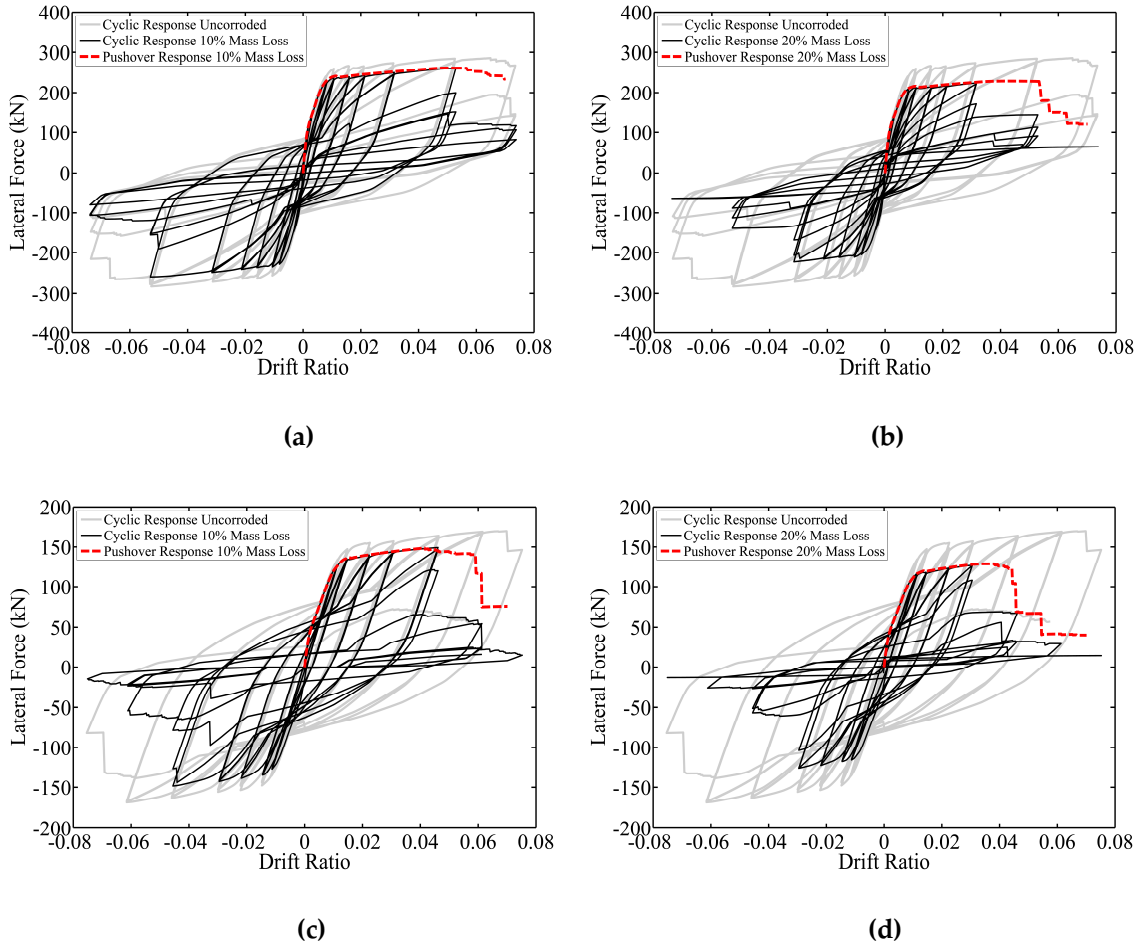

Fig. 6.10 Cyclic analyses considering corrosion induced damage in reinforcing steel: (a) and (b) Lehman 415, (c) and (d) Moyer and Kowalsky 1

6.6.1.2. Monotonic and cyclic response considering corrosion of longitudinal reinforcement and cracked cover concrete

In this scenario, it is assumed that the corrosion damage affects the steel reinforcement and the cracked cover concrete. Fig. 6.11 and Fig. 6.12 show the results of the pushover and cyclic analyses. The results in this case are almost identical to the previous case

where the damage in cover concrete was not considered. Therefore considering the corrosion induced cracking of cover concrete does not appear to have a significant impact on the nonlinear response of corroded columns.

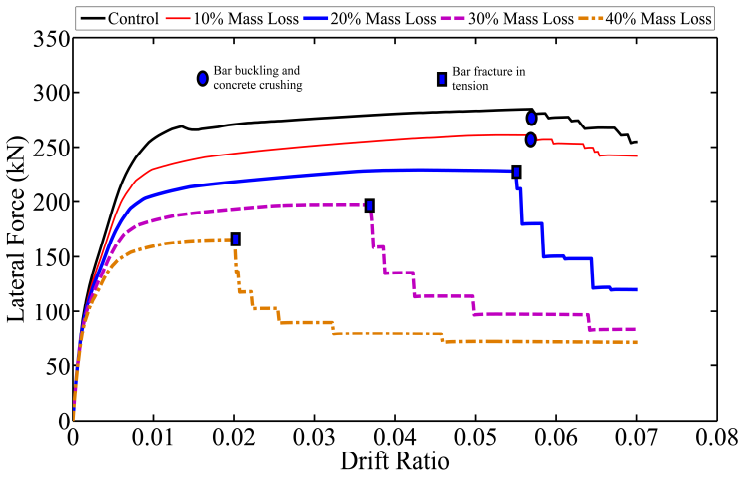

(a)

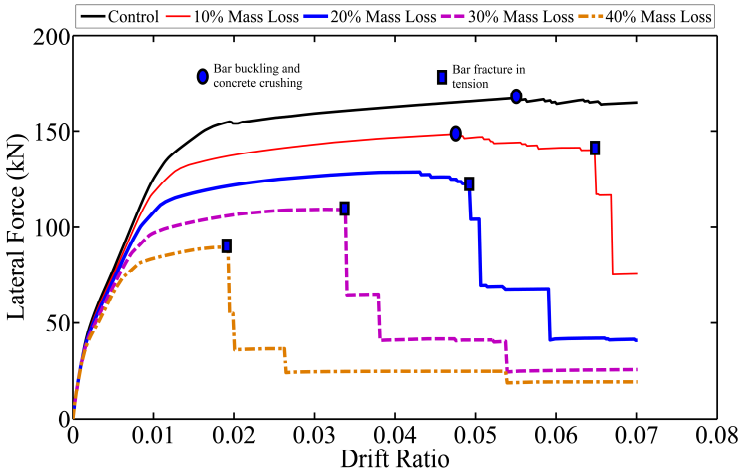

(b)

Fig. 6.11 Pushover analyses considering corrosion induced damage in reinforcing steel and cracked cover concrete: (a) Lehman 415, (b) Moyer and Kowalsky 1

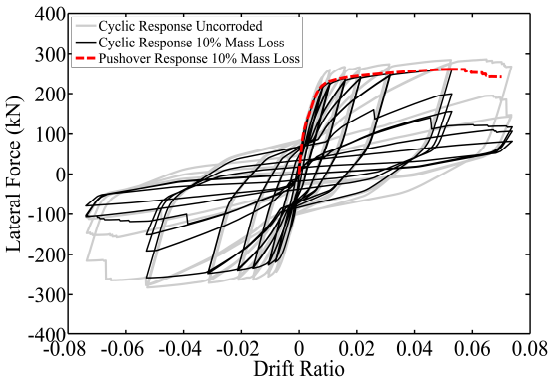

(a)

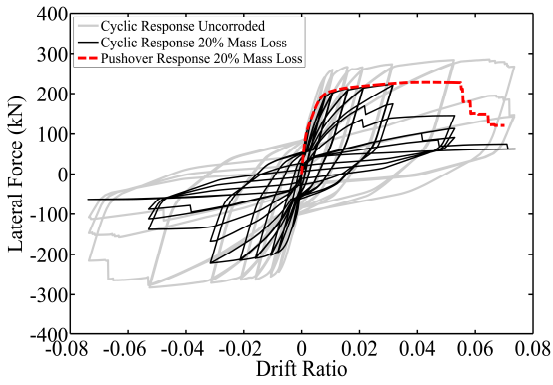

(b)

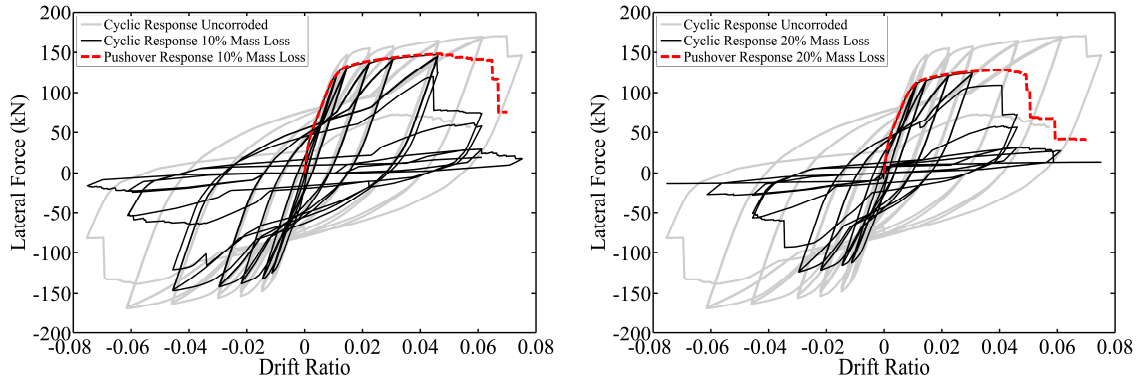

(c) **(d)**

Fig. 6.12 Cyclic analyses considering corrosion induced damage in reinforcing steel and cracked cover concrete: (a) and (b) Lehman 415, (c) and (d) Moyer and Kowalsky 1

6.6.1.3. Monotonic and cyclic response considering corrosion of longitudinal reinforcement, confining reinforcement and cracked cover concrete

In this scenario, it is assumed that the corrosion damage affects the reinforcing steel model, the cover concrete is cracked and the core confined concrete is affected (as described in Section 6.5.3). Fig. 6.13 (a) shows the results of monotonic pushover analyses of Lehman column 415. The results show that the failure mechanism of the column for up to 10% mass loss is bar buckling and concrete crushing in compression. However, for corrosion levels beyond 10% the failure mode changes. The drift capacity loss starts with bar buckling and concrete crushing in compression and followed by bar fracture in tension. The analyses show that consideration of the impact of corrosion damage on confined concrete results in a rapid reduction in strength and ductility of corroded columns compared to the previous cases where the confined concrete was considered to be undamaged. Fig. 6.13 (b) shows the results of pushover analyses of Moyer and Kowalsky column 1. In this case, the failure mode was mainly bar buckling and concrete crushing followed by fracture of bars in tension for up to 20% mass loss. However, corrosion levels beyond 20% mass loss have changed the failure mode to premature fracture of bars in tension. This difference between the behaviour of two columns is due to the buckling behaviour of vertical bars. Given Moyer and Kowalsky's column has a much smaller buckling length, the strength degradation in compression is much smaller than the Lehman column 415. Therefore, corrosion has a more significant impact in terms of ductility loss for the bars in tension whereas in the Lehman column 415 only 10% corrosion results in severe bar buckling and concrete crushing which is then followed by fracture of bars in tension.

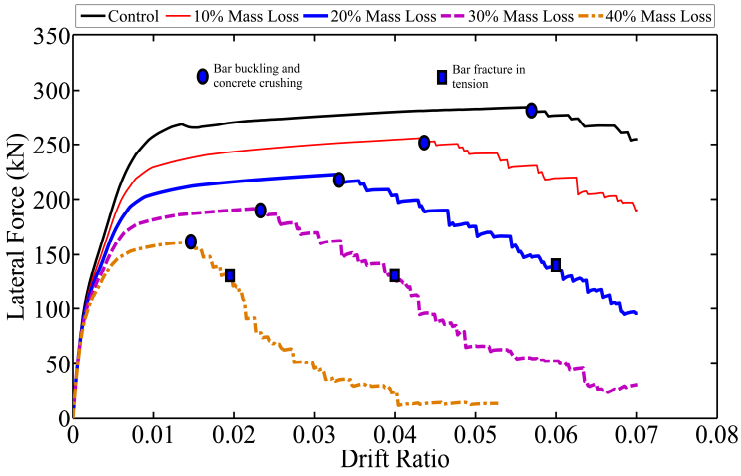

(a)

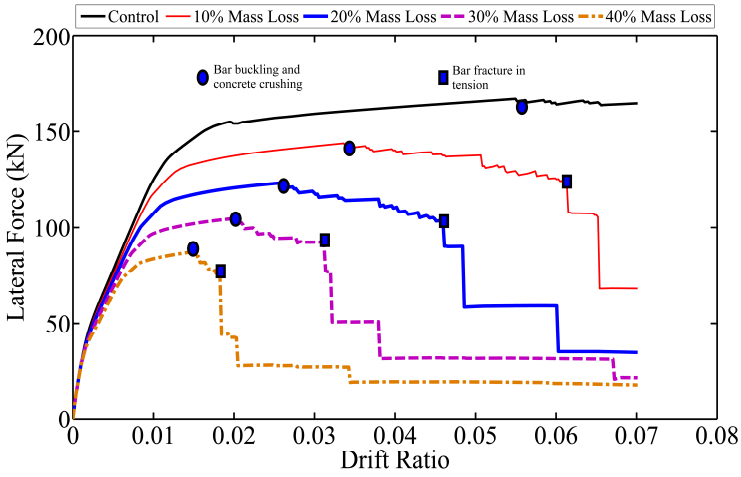

(b)

Fig. 6.13 Pushover analyses considering corrosion induced damage in reinforcing steel, cracked cover concrete and confined concrete: (a) Lehman 415, (b) Moyer and Kowalsky 1

Fig. 6.14 shows the results of the cyclic analyses. It shows the cyclic analysis of Lehman column 415 and Moyer and Kowalsky column 1 with 10% and 20% mass loss together with the corresponding pushover envelopes. Fig 6.14 shows that the extent of corrosion damage under cyclic loading is more severe than under monotonic loading. The results of monotonic analyses showed that considering ductility loss of both the corroded bars in tension and of the confinement reinforcement in compression has a big impact in bar buckling and fracture of reinforcement. However, cyclic analysis results show that considering cyclic degradation due to low-cycle fatigue is crucial if we are to have a realistic evaluation of the seismic performance of existing corroded bridges. For example in Fig. 6.14 (a) and (b), the failure of Lehman column 415 was governed by bar buckling and concrete crushing for corrosion level up to 10% under monotonic loading. However,

the same corrosion level results in a much more severe ductility loss under cyclic loading due to reduced low-cycle fatigue life. Similarly in Fig. 6.14 (c) and (d) the failure of the Moyer and Kowalsky column was governed by concrete crushing in compression followed by bar fracture in tension. However, low-cycle fatigue degradation due cyclic loading results in premature fracture of bars resulting in severe loss of drift capacity in the column.

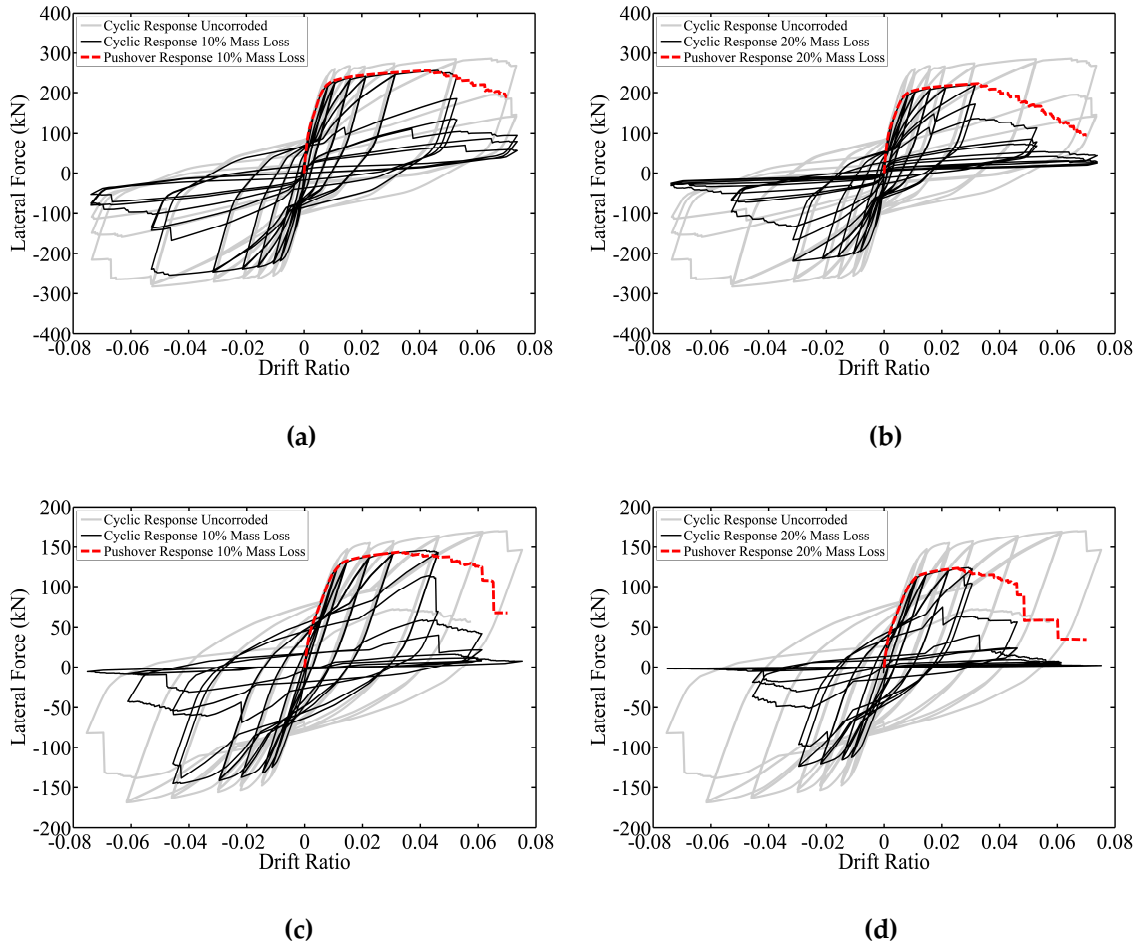

Fig. 6.14 Cyclic analyses considering corrosion induced damage in reinforcing steel, cracked cover concrete and confined concrete: (a) and (b) Lehman 415 (c) and (d) Moyer and Kowalsky 1

Ou et al. (2011) conducted a series of experimental study on cyclic behaviour of large scale corroded RC beams. They found that as the level of corrosion increases the flexural failure initiates with premature buckling of longitudinal bars. This conclusion is in good agreement with the numerical results of the present study. In another study Ma et al. (2012) conducted a series of experimental studies on the cyclic behaviour of corroded RC columns with varying axial force. They have reported that once corrosion levels increase beyond about 14% a rapid strength and ductility reduction and cyclic degradation in hysteretic loops is seen. This conclusion is also in good agreement with the failure modes predicted using the present numerical model.

The modelling technique developed in this thesis can accurately model the nonlinear behaviour of corroded RC columns subject to cyclic loading. However, further experimental study on corroded RC columns is required for further validation and calibration of the model parameters.

6.7. Conclusions

The impact of corrosion on reinforcing steel and concrete is modelled. The influence of cyclic degradation due to low-cycle fatigue is also modelled. The main outcome of this study can be summarised as follows:

1. Corrosion has a more significant impact on ductility loss of RC columns than on strength loss.
2. It was found that flexural failure is initiated by buckling of vertical bars and crushing of core concrete which then followed by fracture of bars in tension.
3. The analysis results showed that for seismic performance and evaluation of existing corroded bridges monotonic pushover analysis is not adequate. The cyclic degradation due to low-cycle fatigue has a significant influence on the response of corroded RC columns.
4. The results of this study show that it is inadequate to assume that corrosion only affects the reinforcing bars. It was found that the confined concrete with corroded reinforcement starts crushing much faster than uncorroded undamaged concrete. This results in premature buckling of vertical reinforcement. This change in the failure mode cannot be predicted if the damage in core confined concrete due corrosion is ignored. This is in good agreement with observed experimental results reported by other researchers (Ou et al. 2011, Ma et al. 2012).
5. Further experimental study is required for validation and calibration of the present numerical model. Moreover, the basic uncorroded model is only validated against experimental data from circular columns. Therefore, further parametric studies for rectangular columns are required. Nevertheless the modelling guidelines shown in this chapter can be used in the future research to improve the assessment of seismic vulnerability and fragility of corroded RC bridges.

This page is intentionally left blank.

CHAPTER 7

Conclusions and Future Work

7.1. Conclusions

Computational tools for the simulation of nonlinear behaviour of corrosion damaged RC bridge piers, divided into component, section and material levels are developed. Previous studies in modelling the corrosion-induced structural degradation of RC structures and bridges are reviewed (Chapter 2). The impact of corrosion on stress-strain behaviour of reinforcing steel under monotonic and cyclic loading with the effect of inelastic buckling is explored experimentally (Chapter 3). The impact of corrosion pattern on nonlinear behaviour of corroded bars using a novel 3D stochastic analysis of corrosion pattern and finite element modelling of corroded bars is explored (Chapter 4). Using the experimental and numerical data generated in Chapters 3 and 4 a new phenomenological hysteretic material model is developed for corroded reinforcing bars (Chapter 5). The new constitutive material and damage models at material and section levels are implemented into a nonlinear fibre beam-column element in OpenSees for calibration of the material parameters (Chapters 5). The basic uncorroded material model is validated against UW-PEER experimental RC column database (Chapter 5). Finally, an algorithm for the implementation of the corrosion damage models into the fibre model is developed and implemented in OpenSees (Chapter 6).

These corrosion damage models are used to explore the impact of material deterioration on the nonlinear behaviour of two hypothetical RC bridge piers with varied corrosion and confinement levels (Chapter 6).

The outcome of this thesis resulted in a significant improvement to the existing models for the seismic assessment and evaluation of corrosion damaged RC bridge piers. The new uniaxial material models have enhanced the accuracy of the fibre beam-column models for predicting the nonlinear response of RC columns. The modelling technique that is specifically developed for buckling critical (buckling of reinforcement) RC columns is available for other researchers and practicing engineers to use for nonlinear seismic analysis of RC bridges.

Prior to the work conducted in this thesis there was no rigorous modelling technique that could model the nonlinear behaviour of corrosion damaged flexural RC bridge piers. To this end, the most significant contribution of this thesis is that it will improve the nonlinear models to be used in fragility and vulnerability analysis of corroded RC bridges. This will enable bridge managers and owners to develop a more accurate maintenance strategy (compare to the previous models) to evaluate and predict the performance of their bridge network. As a result the critical bridges among the entire network can be identified and prioritised to be repaired / retrofitted.

The major detailed technical findings of this thesis are summarised below. It should be noted that these conclusions are limited to the specific cases studied in this thesis:

1) The results of the experimental testing showed that non-uniform pitting corrosion has a significant effect on the stress-strain behaviour of corroded bars under monotonic loading.

Based on these experiments a 20% mass loss would appear to result in approximately a 50% reduction in the ductility of corroded bars in tension. This result agrees with the results observed by other researchers (Du et al. 2005b). The inelastic buckling mechanism of bars is also affected by non-uniform pitting corrosion. The observed buckling modes showed that the buckling mechanism of corroded bars is a function of the mass loss due to corrosion and the distribution of pits along the bar length. It was found that the distribution of pits along the length of corroded bars is the most important parameter affecting the stress-strain response in both tension and compression. This is more critical in compression where any load eccentricity and imperfections have a significant influence on the buckling capacity of bars.

2) It was found that buckling has a significant impact on the hysteresis behaviour of bars with L_{eff}/d >10 under high compression strain demand (where L_{eff} is the effective bucking length and d is the bar diameter).

This is due to the effect of geometrical nonlinearity. It was found that the combined effect of buckling and low-cycle high amplitude fatigue results in a severe degradation to the tension envelope of corroded bars. The buckling capacity of bars under cyclic loading is greatly influenced by the previous plastic strain history in tension. This phenomenon (for uncorroded reinforcement) has been reported by other researchers (Moyer and Kowalsky 2003). This is a particularly important parameter when the corroded bars have highly localised pitting corrosion. The experimental results from this study showed that corroded bars with pitting will fracture in tension after fewer cycles of stress reversal. This is due to the combined effect of low-cycle fatigue, premature yielding and inelastic buckling of bars at pitting locations.

3) The 3D corrosion pattern analysis showed that the distribution and the cross section shape of pitted sections have a significant impact on the stress-strain behaviour of corrodes bars.

Based on the regression analysis of the maximum cross section loss, it was found that the pitting effect is function of the mass loss ratio. Therefore, it is a time-variant phenomenon. The statistical analysis based on null hypothesis tests showed that the lognormal distribution model can represent the non-uniform distribution of geometrical properties of corroded bars including the pitting effect. The probabilistic models developed in this thesis are based on accelerated corrosion tests and there is a need for further model calibration and comparison of these models with naturally corroded bars. Nevertheless the results of previous experimental studies (Palsson and Mirza 2002, Zhang et al. 2012) showed that the response of accelerated and naturally corroded bars with similar mass loss ratios is similar in tension tests.

4) The new phenomenological hysteretic model developed in this thesis, in most cases can accurately simulate the inelastic buckling and low-cycle fatigue degradation of corroded bars.

However, severe localised pitting corrosion might result in an inaccurate simulation. As discussed in Chapters 3 and 4, the stress-strain behaviour of these bars is mainly governed by the minimum section. Given the complexity and highly uncertainty associated with localisation of corrosion, this problem should be solved probabilistically. This is an area for further research. The localisation issue in force-based elements in structural systems with softening response due to buckling can be resolved by using two elements. As suggested, the integration length of the first section of first element must be the same as the buckling length considered in the uniaxial material model of reinforcing steel. It was found that the new *CorrodedReinforcingSteel* material in OpenSees which is calibrated using the experimental and numerical data of isolated bars cannot represent the cyclic behaviour of reinforcing bars inside concrete. This is an area for further

research to improve this material model to account for the influence of tie stiffness on the nonlinear cyclic stress-strain behaviour of reinforcing bars. The observed experimental and numerical results of the cyclic response of RC columns showed that fracture of bars inside columns due to low-cycle fatigue is very sensitive to the non-dimensional slenderness ratio of bars (λ_p). This is an area for further research to investigate the influence of buckling on low-cycle fatigue life of reinforcing bars. The final calibrated model is very good at predicting the nonlinear cyclic response of circular RC columns. The model is also validated against column experiments with random displacement history which were not included in calibration process. Although there is need for further model calibration, the modelling strategy developed in this thesis can be used in nonlinear seismic analysis and evaluation of RC bridges as a reliable tool for both researchers and practicing engineers.

5) The current codes of practice for seismic design and detailing of RC bridges (EC8 2010, Caltrans 2013) have no requirement for the minimum volumetric ratio of confinement reinforcement to satisfy bar buckling (relative stiffness of tie reinforcement to flexural rigidity of vertical reinforcement).

The experimental results of RC bridge piers that were designed according to the Caltrans detailing requirements (Lehman et al. 2000) showed severe buckling of vertical bars. This is because the code requirements do not account for the influence of tie stiffness on buckling behaviour of vertical reinforcement. There is need for an additional requirement in the current design practice to provide sufficient confinement reinforcement against buckling of vertical reinforcement based on the cross section shape of the column and λ_p.

7.2. Future Work

This research can be further pursued in the following directions:

1) Exploring the crushing failure mechanisms of the core concrete in RC columns subject to corrosion and high axial force. The aim of this research is to develop a new material model for confined concrete to be used in modelling of RC elements using a fibre technique that accounts for time dependent corrosion damage. This requires a series of experimental investigations on short RC columns with varied reinforcement details and corrosion levels under monotonic compression and cyclic loading. The issues that need to be explored are as follows:
   a) Is buckling of vertical reinforcement going to cause the section failure in uncorroded specimens?
   b) What is the extent of corrosion damage on the observed response in (a)?

c) What is the post-peak and concrete crushing behaviour after corrosion and what is the influence of corrosion on the ultimate failure modes?

2) The outcome of this thesis provides a computational platform for modelling nonlinear behaviour of corrosion damaged flexural RC bridge piers. However, further experimental studies are required for model validation and better understanding of the failure modes of corroded columns.

3) The focus of this thesis has been on the impact of corrosion on material models and the extent of damage on inelastic section and component response. There is a need for further research to investigate the impact of corrosion of bridge piers on the inelastic system response. A new collaboration has been set up between the University of Bristol and the Rice University in the US and the Trinity College Dublin in Ireland to conduct this research. The fibre model of the corroded columns developed in this thesis has been implemented in a 3D bridge model in OpenSees which was originally developed by researchers at Rice University and Trinity College Dublin using a very simple column model. The aim of this collaboration is:

a) To explore the impact of corrosion on the inelastic system response under earthquake ground motions using a detailed column model and compare the results with the earlier simplified column models.

b) Develop the fragility functions for RC bridges with corroded piers. This includes analysis of different bridge systems with varied number of spans and lengths.

4) As it is well known to researchers there are uncertainties associated with earthquake ground motions, corrosion phenomenon and RC material properties. Earlier research by Kappos et al. (1999) explored the influence of material uncertainties associated with confined concrete models on inelastic section response. A similar study is required to explore the impact of both material (corroded and uncorroded) and ground motion uncertainties on component and system response.

5) The focus of this thesis has been on flexural RC columns. However, there are a large number of bridges with shear critical corroded columns around the world that need to be structurally evaluated. Therefore, there is need for further experimental studies on shear critical columns to explore the impact of corrosion on the failure mechanism and inelastic response of shear critical RC columns. This requires the development of new modelling techniques to account for axial-flexure-shear interaction.

6) As it is discussed in Chapter 5, the nonlinear cyclic stress-strain behaviour of longitudinal reinforcing bars inside RC columns is greatly influenced by the stiffness of horizontal tie reinforcement. There is a need for additional computational modelling and parametric study for further calibration of the phenomenological

model developed in this thesis. The parameters need to be investigated are as follow:

a) The influence of internal core pressure due to expansion of confined concrete on the buckling behaviour of vertical reinforcement.
b) The influence of tie stiffness and flexural rigidity of vertical reinforcement on the buckling load capacity, buckling length and the average strain (average over the buckling length) at the onset of buckling of vertical reinforcement.
c) The influence of tie stiffness on the cyclic stress-strain behaviour of reinforcing bars. The material model should include cyclic rules to be adjusted as a function of tie stiffness.

REFERENCES AND BIBLIOGRAPHY

Abramowitz M, Stegun CA. *Handbook of mathematical functions with formulas, graphs, and mathematical tables.* 9th. New York: Dover, 1972.

Akiyama M, Frangopol DM. "Long-term seismic performance of RC structures in an aggressive environment: emphasis on bridge piers." *Struct Infrastruct E* DOI: 10.1080/15732479.2012.761246 (2013).

Akiyama M, Frangopol DM, Matsuzaki H. "Life-cycle reliability of RC bridge piers under seismic and airborne chloride hazards." *Earthquake Eng and Struct Dyn* 40 (2011): 1671–1687.

Alexopoulos ND, Apostolopoulos CA, Papadopoulos MP, Pantelakis SG. "Mechanical Performance of BStIV Grade Steel Bars with Regard to the Long-term Material Degradation Due to Corrosion Damage." *Constr Build Mater* 21 (2007): 1362-1369.

Alipour A, Shafei B and Shinozuka M. "Performance evaluation of deteriorating highway bridges located in high seismic areas." *J Bridge Eng* 6, no. 5 (2011): 597-611.

Alipour A, Shafei B, Shinozuka M. "Capacity loss evaluation of reinforced concrete bridges." *J Bridge Eng* 9, no. 1 (2013): 8-27.

Almusallam AA. "Effect of degree of corrosion on the properties of reinforcing steel bars." *Const and Build Mat* 15 (2001): 361-368.

Almusallam AA, Algahtani A, Aziz AR. "Effect of reinforcement corrosion on bond btrength." *Constr Build Mater* 10, no. 2 (1996): 123–129.

Alonso C, Andrade C, Rodriguez J, Diez JM. "Factors controlling cracking of concrete affected by reinforcement corrosion." *Mater Struct* 31 (1998): 435-441.

Al-sulaimani G, Kaleemullah M, Basunbul I, Rasheeduzzafar. "influence of corrosion and cracking on bond behavior and strength of reinforced concrete members." *ACI Struct J* 87, no. 2 (1990): 220-231.

Amleh L, Mirza S. "Corrosion influence on bond between steel and concrete." *ACI Struct J* 96, no. 3 (1999): 415–423.

Andrade C, Alonso C, Garcia D, Rodriguez J. "Remaining lifetime of reinforced concrete structures: effect of corrosion in the mechanical properties of the steel. Life Prediction of Corrodible Structures." Cambridge: NACE, 1991.

Andrade C, Alonso C, Molina FJ. "Cover cracking as a function of bar corrosion: Part 1-experimental test." *Mater Struct* 26 (1993): 453-464.

Andrade C, Kropp J. “Advances in modelling of Rilem Tc-178. Testing and modelling chloride penetration in concrete.” Lausanne: Life-cycle performance of deteriorating structures – assessment, design and management, Eds. DM Frangopol, E Bruhwiller, MH Faber and B Adey, 2003.

Ang A, Tang WH. *Probability concepts in engineering planning and design.* Volume I. New York: John Wiley and Sons, 1975.

Ang A, Tang WH. *Probability concepts in engineering planning and design.* Volume II. New York: John Wiley and Sons, 1984.

Apostolopoulos CA. “Mechanical behavior of corroded reinforcing steel bars S500s tempcore under low cycle fatigue.” *Construct and Build Mater* 21 (2007): 1447–1456.

Apostolopoulos CA. “The influence of corrosion and cross-section diameter on the mechanical properties of B500c steel.” *J Mater Eng Perfor* 18, no. 2 (2009): 190-195.

Apostolopoulos CA, Demis S, Papadakis VG. “Chloride-induced corrosion of steel reinforcement -Mechanical performance and pit depth analysis.” *Constr Build Mater* 38 (2013): 139-146.

Apostolopoulos CA, Koutsoukos PG. “Study of the corrosion of reinforcement in concrete elements used for the repair of monuments.” *Constr Build Mater* 22, no. 7 (2008): 1583–1593.

Apostolopoulos CA, Michalopoulos D. “Corrosion of reinforcing steel and low cycle fatigue behaviour.” *Mater Corr* 58, no. 6 (2007): 438–446.

Apostolopoulos CA, Papadakis VG. “Consequences of steel corrosion on the ductility properties of reinforcement bar.” *Constr Build Mater* 22 (2008): 2316-2324.

Apostolopoulos CA, Papadopoulos MP. “Tensile and low cycle fatigue behavior of corroded reinforcing steel bars S400.” *Constr Build Mater* 21 (2007): 855-864.

Apostolopoulos CA, Papadopoulos MP, Pantelakis SG. “Tensile behavior of corroded reinforcing steel bars BSt 500s.” *Construct and Build Mater* 20 (2006): 782–789.

Apostolopoulos CA, Pasialis VP. “Use of quality indices in comparison of corroded technical steel bars B500c and S500s on their mechanical performance basis.” *Constr Build Mater* 22, no. 12 (2008): 2325-2334.

Aquino W. *Long-term performance of seismically rehabilitated corrosion-damaged columns.* PhD Thesis, University of Illinois at Urbana Champaign, 2002.

Archer GC. *Object-Oriented Finite Element Analysis.* University of California Berkeley, PhD Thesis, 1996.

Archer GC, Fenves G, Thewalt C. “A new object-oriented finite element analysis program.” *Comput Struct* 70 (1999): 63-75.

Arscott EM. “Slides on the Hyogo-ken Nanbu (Kobe) Earthquake Set I: An Overview.” EERI, 1995.

Assessment Task Group. *Guidance on the Assessment of Concrete Bridges.* Concrete Bridge development Group, 2007.

ASTM G1-03. *Standard practice for preparing, cleaning, and evaluating corrosion test specimens.* ASTM Int’l, 2011.

Auyeung Y, Balaguru P, Chung L. “Bond behavior of corroded reinforcement bars.” *ACI Struct J* 97, no. 2 (2000): 214–220.

Azad A, Ahmad S, Azher S. “Residual strength of corrosion-damage reinforced concrete beams.” *ACI Struct J* 104, no. 1 (2007): 40-47.

Bae S, Mieses A, Bayrak O. “Inelastic buckling of reinforcing bars.” *J Struct Eng* 131, no. 2 (2005): 314–321.

Bae S, Mieses A, Bayrak O. “Inelastic buckling of reinforcing bars.” *J of Struct Eng* 131, no. 2 (2005): 314–321.

Baharagava K, Ghosh AK, Mori Y, Ramanujam S. “Analytical model of corrosion-induced concrete considering the stiffness of reinforcement.” *Struct Eng Mech* 16, no. 6 (2003): 749-76.

Balan TA, Filippou FC, Popov EP. “Hysteretic model of ordinary and high-strength reinforcing steel.” *J of Struct Eng* 124, no. 3 (1998): 288–297.

Bamforth PB. *Enhancing reinforced concrete durability.* Concrete Society, 2004.

Bamforth PB, Price WF, Emerson M. *An international review of chloride ingress into structural concrete.* TRL, 1997.

Bauschinger J. “Variations in the elastic limit of iron and steel.” *The J. of the Iron and Steel Institute* 12, no. 1 (1887): 442-444.

Bayrak O, Sheikh AS. “Plastic hinge analysis.” *J Struct Eng* 127, no. 9 (2001): 1092–1100.

Bažant ZP. “Physical Model for Steel Corrosion in Sea Structures Applications.” *J Struct Div* 105, no. ST6 (1979): 1155-1166.

BD 79/06. *The management of sub-standard highway structures.* DMRB, Highways Agency, 2006.

Belarbi Al, Sang-Wook B. “An experimental study on the effect of environmental exposures and corrosion on RC columns with FRP composite jackets.” *Compos Part B: Eng* 38, no. 5 (2007): 674-684.

Berry M, Eberhard MO. *Performance Models for Flexural Damage in Reinforced Concrete Columns.* Berkeley: Pacific Earthquake Engineering Research Centre, 2003.

Berry M, Parrish M, Eberhard M. *Performance Database User’s Manual, PEER, Univ. of Calif. Berkeley.* 2004. www.ce.washington.edu/~peera1 (accessed 2013).

Berry MP, Eberhard MO. “Practical performance model for bar buckling.” *J Struct Eng* 131, no. 7 (2005): 1060-1070.

Berry MP, Eberhard MO . *Performance modeling strategies for modern reinforced concrete bridge columns.* Berkeley: Pacific Earthquake Engineering Research Centre, 2006.

Berry MP, Lehman DE, Lowes LN. “Lumped-plasticity models for performance simulation of bridge columns.” *ACI Sruct J* 105, no. 3 (2008): 270-279.

Berto L, Simioni P, Saetta A. “Numerical modelling of bond behaviour in RC structures affected by reinforcement corrosion.” *Eng Struct* 30 (2008): 1375-1385.

Berto L, Vitaliani R, Saetta A, Simioni P. “Seismic assessment of existing RC structures affected by degradation phenomena.” *Struct Saf* 31 (2009): 284–297.

Bhargava K, Ghosh AK, Mori Y, Ramanujam S. “Analytical model for time to cover cracking in RC structures due to rebar corrosion.” *Nuclear Eng Design* 236, no. 11 (2006): 1123-1139.

Biondini F, Camnasio E, Palermo A. “Lifetime seismic performance of concrete bridges exposed to corrosion.” *Struct Infrastruct E* DOI: 10.1080/15732479.2012.761248 (2013).

Bousias SN, Triantafillou TC, Fardis MN, Spathis L. “Fiber-reinforced polymer retrofitting of rectangular reinforced concrete columns with or without corrosion.” *ACI sruct J* 101, no. 4 (2004).

Bresler PH, Gilbert B. “The requirements for reinforced concrete columns.” *ACI J* 58, no. 5 (1961): 555–570.

Broomfield JP. *Corrosion of steel in concrete: understanding, investigation and repair.* 2. Taylor and Francis, 2007.

Brown J, Kunnath SK. “Low-Cycle Fatigue Failure of Reinforcing Steel Bars.” *ACI Mater J* 201, no. 6 (2004): 457–466.

BS 4449-2005 +A2. *Steel for the reinforcement of concrete - Weldable reinforcing steel - bar, coil and decoiled product.* BSI, 2009.

BS-EN 10080. *Steel for the reinforcement of concrete - Weldable reinforcing steel – General.* BSI, 2005.

Cabrera J. "Deterioration of concrete due to reinforcement corrosion." *Cement Concrete Compos* 18, no. 1 (1996): 47-59.

Cairns J, Du Y, Law D. "Structural performance of corrosion-damaged concrete beams." *Mag Concrete Res* 60, no. 5 (2008): 359-370.

Cairns J, Plizzari GA, Du YG, Law DW, and Chiara F. "Mechanical properties of corrosion-damaged reinforcement." *ACI Mat J* 102, no. 4 (2005): 256–264.

Cairns J, Zhao MA. "Strength assessment of corrosion damaged reinforced slabs and beams." *Struct Build* 99 (1993): 141-154.

Caleyo F, Velázquez JC, Valor A, Hallen JM,. "Probability distribution of pitting corrosion depth and rate in underground pipelines: A Monte Carlo study." *Corros Sci* 51 (2009): 1925-1934.

Caltrans. "Seismic Design Criteria." *Caltrans* VERSION 1.7 (2013).

Capozucca R, Cerri MN. "Influence of reinforcement corrosion—in the compressive zone - on the behaviour of RC beams." *Eng Struct* 25, no. 13 (2003): 1575-1583.

CEB-FIP Model Code 90. London: Thomas Telford, 1993.

Chang GA, and Mander JB. *Seismic energy based fatigue damage analysis of bridge columns: Part I – Evaluation of seismic capacity.* NCEER-94-0006, 1994.

Chang GA, Mander JB. "Seismic energy based fatigue damage analysis of bridge columns: Part I – Evaluation of seismic capacity." Technical report NCEER-94-0006, 1994.

Choe D, Gardoni P, Rosowsky D, and Haukaas T. "Probabilistic capacity models and seismic fragility estimates for RC columns subject to corrosion." *Reliab Eng Syst Safe* 93 (2008): 383–393.

Choe D, Gardoni P, Rosowsky D, Haukaas T. "Seismic fragility estimates for reinforced concrete bridges subject to corrosion." *Struct Saf* 31 (2009): 275-283.

Chryssanthopoulos MK, Sterrit G. "Integration of deterioration modelling and reliability assessment for reinforced concrete bridge structures." Glasgow: ASRANet International Colloquium, 2002.

Clark LA, Saifullah M. “Effect of corrosion rate on the bond strength of corroded reinforcement. Corrosion and Corrosion Protection of Steel in Concrete.” Sheffield Academic Press , 1994.

Coleman J, Spacone E. “Localization issues in force-based frame elements.” *J Struct Eng* 127, no. 11 (2001): 1257–1265.

commission, European. “DARTS – Durable and reliable tunnel structures: deterioration modelling.” Grwoths 2000 project GrD1-25633, 2004.

Coronelli D. “Corrosion cracking and bond strength modelling for corroded bars in reinforced concrete.” *ACI Struct J* 99, no. 3 (2002): 265-276.

Coronelli D, Gambarova P. “Structural assessment of corroded reinforced concrete beams: modelling guidelines.” *J Struct Eng* 130, no. 8 (2004): 1214-1224.

Cosenza E, and Prota A. “Experimental behavior and numerical modeling of smooth steel bars under compression.” *J of Earthq Eng* 10, no. 3 (2006): 313-329.

Crank J. *The mathematics of diffusion.* Second Edition. Oxford: Clarendon press, 1975.

Cryer JD, Chan KS,. *Time series analysis with applications in R.* second ed. New York: Sprineger, 2008.

Darmawan MS, Stewart MG. “Spatial time-dependent reliability analysis of corroding pretensioned prestressed concrete bridge girders.” *Struct Saf* 29 (2007b): 16-31.

Darmawna MS. “Pitting corrosion model for reinforced concrete structures in a chloride environment.” *Mag Concrete Res* 62, no. 2 (2010): 91-101.

Darmawna MS, Stewart MG. “Effect of pitting corrosion on capacity of prestressing wires.” *Mag Concrete Res* 49, no. 2 (2007a): 131-139.

DE Hawn. “Extreme value prediction of maximum pits on pipelines.” *Mater Perform* 3, no. 29 (1977): 29-32.

Design Manual for Roads and Bridges 38/93. *Assessment of the fatigue life of corroded or damaged reinforcing bars.* Highways Agency, UK, 1993.

Design Manual for Roads and Bridges BA 51/95. *The assessment of concrete structures affected by steel corrosion.* Highways Agency, UK, 1995.

Dhakal RP, Maekawa K. “Modeling for postyield buckling of reinforcement.” *J of Struct Eng* 128, no. 9 (2002a): 1139–1147.

Dhakal RP, Maekawa K. “Path-dependent cyclic stress-strain relationship of reinforcing bar including buckling.” *Eng Struct* 24, no. 11 (2002b): 1383-1396.

Dhakal RP, Maekawa K. “Reinforcement stability and fracture of cover concrete in RC members.” *J of Struct Eng* 128, no. 10 (2002c): 1253–1262.

Dodd LL, and Restrepo-Posada JI. “Model for predicting cyclic behavior of reinforcing steel.” *J Struct Eng* 121, no. 3 (1995): 433–445.

Dodd LL, Restrepo-Posada JI. “Model for predicting cyclic behavior of reinforcing steel.” *J of Struct Eng* 121, no. 3 (1995): 433–445.

Du Y, Clark LA, Chan AHC. “Impact of reinforcement corrosion on ductile behaviour of reinforced concrete beams.” *ACI Struct J* 104, no. 3 (2007): 285-293.

Du YG, Clark LA, Chan AHC. “Effect of corrosion on ductility of reinforcing bars.” *Magazine of Conc Res* 57 , no. 7 (2005a): 407–419.

Du YG, Clark LA, Chan AHC. “Residual capacity of corroded reinforcing bars.” *Magazine of Conc Res* 57 , no. 3 (2005b): 135–147.

DuraCrete. *Probabilistic performance based durability design of concrete structures: statistical quantification of the variables in the limit state foundations.* BE 95-1347, 2000 .

DV Val, RE Melchers. “Reliability of deteriorating RC slab bridges.” *J Struct Eng* 123, no. 12 (1997): 1638-1644.

Eberhard MO. “Personal Communication.” 2013.

El Maaddawy T, Soudki K. “A model for prediction of time from corrosion initiation to corrosion cracking.” *Cement Concrete Compos* 29 (2007): 168-175.

El Maddawy T, Soudki K, Topper T. “Analyticalmodel to predict nonlinear flexural behaviour of corroded reinforced concrete beams.” *ACI Struct J* 102, no. 4 (2005): 550-559.

El-Maaddawy TA, Soudki KA. “Effectiveness of impressed current technique to simulate corrosion of steel reinforcement in concrete.” *J of Mat in Civil Eng* 15, no. 1 (2003): 41-47.

Eurocode 8. “Design provisions for earthquake resistance of structures - Part 2: Bridges.” *BS EN 1998-2:2005 +A1:2009*, 2010.

Fang C, Gylltoft K, Lundgren K, Plos M,. “Effect of corrosion on bond in reinforced concrete under cyclic loading.” *Cement Concrete Res* 36 (2006): 548-555.

Fang C, Lundgren K, Plos M, Gylltoft K,. “Bond behaviour of corroded reinforcing steel bars in concrete.” *Cement Concrete Res* 36 (2006): 1931-1938.

fib bulletin 34. “CEB-FIP Model code for service life design.” Lausanne, 2006.

Filippou FC, Popov EP, Bertero VV. *Effects of Bond Deterioration on Hysteretic Behavior of Reinforced Concrete Joints.* Berkeley: UCB/EERC, Univ. of Calif. Berkeley, 1983.

Fu XDDL, Chung DDL. “Effect of corrosion on the bond between concrete and steel rebar.” *Cement Conc Res* 27, no. 12 (1997): 1811-1815.

Galambos, TV, Surovek, AE. “Structural stability of steel: concepts and applications for structural engineers.” 87–131. John Wiley and Sons Inc, 2008.

GCM, Gaal. *Prediction of Deterioration of Concrete* . PhD Thesis, University of Delft, 2004.

Ghosh J, JE Padgett. “Aging considerations in the development of time-dependent seismic fragility curves.” *J Struct Eng* 136, no. 12 (2010): 1497–1511.

Gibbons JD, Chakraborti S. *Nonparametric Statistical Inference.* fourth. New York: Marcel Dekker Inc, 2003.

Glass GK, Buenfeld NR. “The presentation of the chloride threshold level for corrosion of steel in concrete.” *Corros Sci* 39, no. 5 (1991): 1001-1013.

Gomes A, Appleton J. “Nonlinear cyclic stress-strain relationship of reinforcing bars including buckling.” *Eng Struct* 19 (1997): 822–826.

Gonzalez JA, Andrade C, Alonso C, Feliu S. “Comparison of rates of general corrosion and maximum pitting penetration on concrete embedded steel reinforcement.” *Cement Concrete Res* 25, no. 2 (1995): 257-264.

Hajarali M, Hamad B, Rteil A. “Effect of confinement on bond between steel bars and concrete.” *ACI Struct J* 10, no. 4 (2004): 559-603.

Hamilton CH, Pardoen GC, Kazanjy RP. *Experimental Testing of Bridge Columns Subjected to Reversed-Cyclic and Pulse-type Loading Histories.* Irvine: University of California Irvine , 2003.

Hawileh RA, Abdalla JA, Oudah F, Abdelrahman K. “Low-cycle fatigue life behaviour of BS 460B and BS B500B steel reinforcing bars.” *Fatigue Fract Eng M* 33, no. 7 (2010): 397-407.

Hida S, Ibrahim FIS, Capers HA, Bailey GL, Friedland IM, Kapur J, Martin BT, Mertz DR, Perfetti GR, Saad T, Sivakumar B. *Assuring bridge safety and serviceability in Europe.* Technical report No. FHWA-PL-10-014: Office of International Programs Federal Highway Administration US Department of Transportation American Association of State Highway and Transportation Officials, 2010.

Higai T, Nakamura H and Saito S. “Fatigue failure criterion for deformed bars subjected to large deformation reversals.” *ACI SP 237* 4 (2006): 37-54.

Hill CD, Blandford GE, Wang ST. “Post-buckling analysis of steel space trusses.” *J Struct Eng* 115, no. 4 (1989): 900-919.

Hoehler MS, Stanton JF. “Simple phenomenological model for reinforcing steel under arbitrary load.” *J Struct Eng* 132, no. 7 (2006): 1061-1069.

Inc, Economic Development Research Group. *The economic impact of current investment trends in surface transportation infrastructure.* Americam Society of Civil Engineers, 2011.

Jansen D, Shah S. “Effect of length on compressive strain softening of concrete.” *J Eng Mech* 123, no. 1 (1997): 25–35.

Johnsen TH, Geiker MR, Faber MH. “Quantifying condition indicators for concrete structures: probabilistic modelling of indicators facilitates cost-efficient inspection and maintenance planning.” *Concrete International* 25, no. 12 (2003): 47-54.

Kallias AN. *Advanced probabilistic resistance assessment of corroding RC beams.* PhD Thesis, University of Surrey, 2011.

Kappos AJ, Chryssanthopoulos MK, Dymiotis C. “Uncertainty analysis of strength and ductility of confined reinforced concrete members.” *Eng Struct* 21, no. 3 (1999): 195-208.

Karimi A, Buenfield N. *Service life prediction of concrete structures based on automated monitoring.* Department of Civil Engineering, Imperial College London, 2007.

Karsan ID, Jirsa JO. “Behavior of concrete under compressive loading.” *J Struct Div* 95, no. ST12 (1969).

Kashani MM. *Estimating transition probabilities in markov chain-based deterioration for chloride-induced corrosion.* Master Thesis, University of Surrey, 2006.

Kemp EL, Wilhelm WJ. “Investigation of the parameters influencing bond cracking.” *ACI J* 76, no. 1 (1979).

Kim H, Tae S, Lee H, Lee S, Noguchi T. “Evaluation of mechanical performance of corroded reinforcement considering the surface shape.” *ISIJ International* 49, no. 9 (2009): 1392-1400.

Kirkpatrick TJ, Weyers RE, Anderson-Cook CM, Sprinkel MM. “Probabilistic model for the chloride-induced corrosion service life of bridge decks.” *Cement Concrete Res* 32, no. 12 (2002): 1943-1960.

Kivell A. *Effects of bond deterioration due to corrosion on seismic performance of reinforced concrete structures.* Master Thesis, University of Canterbury, 2012.

Kunnath SK, El-Bahy A, Taylor AW, Stone WC. *Cumulative seismic damage of reinforced concrete bridge piers.* Technical Report NCEER , 1997.

Kunnath SK, Heo Y, Mohle JF. "Nonlinear uniaxial material model for reinforcing steel bars." *J Struct Eng* 135, no. 4 (2009): 335-343.

Lambert P, Atkins C. "Maintaining the silver jubilee bridge- cathodic protection for a critical causeway." *Concrete international* 25, no. 5 (2007).

Lee C, Bonacci JF, Thomas MD, Maalej M, Khajehpour S, Hearn N, Sheikh S. "Accelerated corrosion and repair of reinforced concrete columns using carbon fibre reinforced polymer sheets." *Can J Civil Eng* 27, no. 5 (2000): 941-948.

Lee H, Kage T, Noguchi T, Tomosawa F. "An experimental study on the retrofitting effects of reinforced concrete columns damaged by rebar corrosion strengthened with carbon fibre sheets." *Cement Concrete Res* 33 (2003): 536-570.

Lee HS, Cho YS. "Evaluation of the mechanical properties of steel reinforcement embedded in concrete specimen as a function of the degree of reinforcement corrosion." *Int J Fracture* 157, no. 1-2 (2009): 81-88.

Lee HS, Noguchi T, Tomosawa F. "Evaluation of the bond properties between concrete and reinforcement as a function of the degree of reinforcement." *Cement Concrete Res* 32 (2002): 1313-1318.

Lee Y, William K. "Mechanical properties of concrete in uniaxial compression." *ACI Mat J* 94, no. 6 (1997): 457–471.

Lehman DE, Moehle JP. *Seismic performance of well-confined concrete bridge columns.* Berkeley: Pacific Earthquake Engineering Recerch Centre, 2000.

Lehman DE, Moehle JP, Mahin SA, Calderone AC, Henry H. "Experimental Evaluation of Seismic Design Provisions for Circular Reinforced Concrete Columns." *J of Struct Eng* 130, no. 6 (2004): 869-879.

Liu YP, Weyers RE. "Modelling the time-to-corrosion cracking in chloride contaminated reinforced concrete structures." *ACI Mater J* 95, no. 6 (1998): 675-681.

Lounis Z. "Probabilistic modelling of chloride contamination and corrosion of concrete bridge structures." Proceedings of the Fourth Int. Symposium on Uncertainty Modelling and Analysis, Computer Society, 2003.

Lounis Z, Almeh L. "Reliability-based prediction of chloride ingress and reinforcement corrosion of aging concrete bridge decks." Lausanne: Life-Cycle Performance of

Deteriorating Structures – Assessment, Design and Management, Eds. DM Frangopol, E Bruhwiller, MH Faber and B Adey, 2003.

Lowes LN. “Personal Communication.” 2013.

Lowes LN, Altoontash A. “Modeling reinforced-concrete beam-column joints subjected to cyclic loading.” J. Struct.” *J of Struct Eng* 129, no. 12 (2003): 1686-1697.

Lundgren K. “Modelling the effect of corrosion on bond in reinforced concrete.” *Mag Concrete Res* 54, no. 3 (2002): 165-173.

Ma Y, Che Y, Gong J. “Behavior of corrosion damaged circular reinforced concrete columns under cyclic loading.” *Construct and Build Mater* 29 (2012): 548–556.

Management of highway structures - a code of practice. Roads Liaison Group, 2005.

Mander JB, Panthaki FD and Kasalanat A. “Low-cycle fatigue behavior of reinforcing steel.” *J Mater Civil Eng* 6, no. 4 (1994): 453–468.

Mander JB, Priestley MJN, Park R. “Observed stress-strain behavior of confined concrete.” *J Struct Eng* 114, no. 8 (1988): 1827-1849.

Mander JB, Priestley MJN, Park R. “Theoretical stress-strain model for confined concrete.” *J Struct Eng* 114, no. 8 (1988): 1804-1825.

Manson SS. “Fatigue: A complex subject-Some simple approximations.” *Exp Mech* 5, no. 7 (1965): 193–226.

Massey FJ. “The Kolmogorov-Smirnov test for goodness of fit.” *J Am Stat Assoc* 46, no. 253 (1951): 68-78.

Matsuki S, Billington SL, Baker JW. “Impact of long-term material degradation on seismic performance of a reinforced concrete bridge.” San Francisco: Proceedings of 8th US National Conference on Earthquake Engineering, 2006.

Matthews S, Jacobs J. *Concrete Structure Management Digest G 510.* IHS BRE Press, 2009.

Mau ST. “Effect of tie spacing on inelastic buckling of reinforcing bars.” *ACI Struct J* 87, no. 6 (1990): 671–678.

Mau ST, El-Mabsout M. “Inelastic buckling of reinforcing bars.” *J of Eng Mech* 115, no. 1 (1989): 1-17.

McKenna FT. *Object-oriented finite element programming: frameworks for analysis, algorithms and parallel computing.* University of California Berkeley, PhD Thesis, 1997.

Melchers RE. *Structural reliability analysis and prediction.* John Wiley and Sons, 1999.

Melchers RE, Li C, Lawanwisut W. “Modelling deterioration of structural behaviour of reinforced concrete beams under saline environment corrosion.” *Mag Concrete Res* 58, no. 9 (2006): 575-587.

Menegotto M, and Pinto PE. “Method of analysis of cyclically loaded RC plane frames including changes in geometry and nonelastic behavior of elements under normal force and bending.” In *Preliminary Report*, 13:15–22. Zurich: IABSE, 1973.

Miner MA. “Cumulative damage in fatigue.” *J Appl Mech* 12 (1945): A159–A164.

Mishanlani RG, McCord MR. “Infrastructure condition assessment, deterioration modelling, and maintenance decision making: Methodological advances and practical consideration.” *J Infrastruct Syst* 12, no. 3 (2006): 145-146.

Molina FJ, Alonso C, Andrade C. “Cover cracking as a function of rebar corrosion: part 2 - numerical model.” *Mater Struct* 26, no. 9 (1993): 532-548.

Monti G, Nuti C. “Nonlinear cyclic behavior of reinforcing bars including buckling.” *J of Struct Eng* 118, no. 2 (1992): 3268–3284.

Moyer MJ, Kowalsky MJ. “Influence of tension strain on buckling of reinforcement in concrete columns.” *ACI Struct J* 100, no. 1 (2003): 75-85.

Moyer MJ, Kowalsky MJ. “Influence of tension strain on buckling of reinforcement in concrete columns.” *ACI Struct J* 100, no. 1 (2003): 75-85.

MTLAB R2012b. “The MathWorks lnc.” 1994-2012. www.mathworks.com.

Nakamura H, Higai T,. “Modeling nonlinear cyclic behavior of reinforcing bars.” *ACI SP 205-14* 205 (2002): 273-292.

Neuenhofer A, Filippou FC. “Geometrically nonlinear flexibility-based frame finite element.” *J Struct Eng* 124, no. 6 (1998): 704-71.

Ohtsu M, Yohsimura S. “Analysis of crack propagation and initiation due to corrosion of reinforcement.” *Construct Build Mater* 11 (1997): 437-442.

OpenSees. “The Open System for Earthquake Engineering Simulation, .” PEER, University of California, Berkeley, 2011.

Ou Y, Tsai L, Chen H. “Cyclic performance of large-scale corroded reinforced concrete beams.” *Earthquake Eng and Struct Dyn* 41 (2011): 592-603.

Ou YC, Fan HD, Nguyen ND. “Long-term seismic performance of reinforced concrete bridges under steel reinforcement corrosion due to chloride attack.” *Earthq Eng Struct D* 42, no. 14 (2013): 2113–2127.

Ozbolt J, Balabanic G, Kušter M. “3D Numerical modelling of steel corrosion in concrete structures.” *Corros Sci* 53 (2011): 4166-4177.

Palsson R, Mirza MS. “Mechanical response of corroded steel reinforcement of abandoned concrete bridge.” *ACI Struct J* 99, no. 2 (2002): 157–162.

Pantazopoulou SJ. “Detailing for reinforcement stability in reinforced concrete members.” *J of Struct Eng* 124, no. 6 (1998): 623–632.

Pantazopoulou SJ, Bonacci JF, Sheikh ST, Thomas MDA, Hearn NA. “Repair of corrosion-damaged columns with FRP wraps.” *J compos constr* 5, no. 1 (2001): 3-11.

Pantazopoulou SJ, Papolia D. “Modelling cover-cracking due to reinforcement corrosion in RC structures.” *J Eng Mech* 127, no. 4 (2001): 97-99.

Papadopoulos MP, Apostolopoulos CA, Alexopoulos ND, Pantelakis SG. “Effect of salt spray corrosion exposure on the mechanical performance of different technical class reinforcing steel bars.” *Mater Des* 28, no. 8 (2007): 2318-2328.

Papia M, Gaetano R, Gaetano Z. “Instability of longitudinal bars in RC columns.” *J of Struct Eng* 114, no. 2 (1988): 445–461.

Papia M, Russo G. “Compressive concrete strain at buckling of longitudinal reinforcement.” *J of Struct Eng* 115, no. 2 (1989): 382–397.

Park R, Paulay T,. *Reinforced concrete structures.* New York: John Wiley and Sons, 1975.

Park R, Priestley N, Gill W,. “Ductility of square-confined concrete columns.” *J Struct Div* 108, no. 4 (1982): 929-950.

Park R, Sampson A,. “Ductility of reinforced concrete column sections in seismic design.” *ACI J* 69 (1972): 543-555.

Penelis G, Kappos A. *Earthquake resistance concrete structures.* London: E & FN Spon, 1997.

Popovics S. “A numerical approach to the complete stress strain curve for concrete.” *Cem Concr Res* 3, no. 5 (1973): 583-599.

Poulsen E, Mejlbro L. *Diffusion of chloride in concrete.* Taylor & Francis, 2006.

Prota A, Cicco FD, Cosenza E. “Cyclic behavior of smooth steel reinforcing bars: experimental analysis and modeling issues.” *J Earthq Eng* 13, no. 4 (2009): 500-519.

Pugh JS. *Numerical simulation of walls and seismic design recommendations for walled buildings.* University of Washington, PhD Thesis, 2012.

Rafiq MI, Chryssanthopoulos MK, Onoufriou T. “Performance updating of concrete bridges using proactive health monitoring methods.” *Relib Eng Syst Safe* 86 (2004): 247-256.

Rafiq MI, Chryssanthopoulos MK, Onoufriou T. “Sensitivity of uncertainties in performance prediction of deteriorating concrete structures.” *Struct Infrastruct E* 2, no. 2 (2005): 117-130.

Razak HA, Choi FC. “The effect of corrosion on the natural frequency and modal damping of reinforced concrete beams.” *Eng Struct* 23, no. 9 (2001): 1126-1133.

Report of Working Party. *Diagnosis of deterioration in concrete structures.* Concrete Society, 2000.

Restrepo-Posada J, Dodd L, Park R, Cooke N. “Variables effecting cyclic behavior of reinforcing steel.” *J of Struct Eng* 120, no. 11 (1994): 3178–3196.

RM, Souza. *Force-based finite element for large displacement inelastic analysis of frames.* . Berkeley : PhD Thesis University of California, 2000.

Rodriguez J, Ortega L.M, Casal J, Diez J. “Corrosion of reinforcement and service life of concrete structures.” Sweden: Seventh International Confrence on Durability of Building Materials and Components, E&FN Spon Publisher, 1996.

Rodriguez J, Ortega LM, Aragoncillo J, Izquierdo D, Andrade C. “Methodology for the structural assessment of concrete affected by reinforcement corrosion.” *ACI Struct J* SP 229 (2005): 305-318.

Rodriguez J, Ortega LM, Casal J. “Load carrying capacity of concrete structures with corroded reinforcement.” *Constr Build Mater* 11, no. 4 (1997): 239-248.

Rodriguez ME, Botero JC, Villa J. “Cyclic stress-strain behavior of reinforcing steel including the effect of buckling.” *J of Struct Eng* 125, no. 6 (1999): 605–612.

SAP2000. “ Structural analysis and design software.” Computers and Structures Inc., 2013.

Schlune H. *Bond of corroded reinforcement: Analytical description of the bond-slip response.* Master Thesis, Chalmers University, 2006.

Scott BD, Park R, Priestley MJN. “Stress-strain behavior of concrete confined by overlapping hoops at low and high strain rates.” *ACI J* 79, no. 1 (1982): 13-27.

Scribner CF. “Reinforcement buckling in reinforced concrete flexural members.” *ACI J* 83, no. 6 (1986): 966–973.

SeismoStruct v5.2.2. “Seismosoft Earthquake Engineering Software Solutions.” 2011.

Sheikh AK, Boah JK, Hansen DA. “Statistical modelling of pitting corrosion and pipeline reliability.” *Corrosion* 46, no. 3 (1990): 190-197.

Spacone E, Filippou FC, Taucer FF. “Fibre beam-column model for non-linear analysis of R/C frames: part I: formulation.” *Earthq Eng Struct D* 25 (1996): 711-725.

Spacone E, Filippou FC, Taucer FF. “Fibre beam-column model for non-linear analysis of R/C frames: part II: applications.” *Earthq Eng Struct D* 25 (1996): 727-742.

Sriramula S, Chryssanthopoulos MK,. “Probabilistic models for spatially varying mechanical properties of in-service GFRP cladding panels.” *J Compos Constr* 13, no. 2 (2009): 159-167.

Stanish K, Hooton RD, Pantazopoulou SJ. “Corrosion effects on bond strength in reinforced concrete.” *ACI Struct J* 96, no. 6 (1999): 915–921.

Stanton JF. “Personal Communication.” 2013.

Steward MG. “Mechanical behaviour of pitting corrosion of flexural and shear reinforcement and its effect on structural reliability of corroding RC beams.” *Struct Saf* 31 (2009): 19-30.

Stewart MG, Al-Harthy A. “Pitting corrosion and structural reliability of corroding RC structures: Experimental data and probabilistic analysis.” *Relib Eng Syst Safe* 93 (2008): 373-382.

Stewart MG, Suo Q. “Extent of spatially variable corrosion damage as an indicator of strength and time-dependent reliability of RC beams.” *Eng Struct* 31 (2009): 198-207.

Tastani SP, Panatazopoulou SJ. “Behaviour of corroded bar anchorages.” *ACI Struct J* 104, no. 6 (2007): 756-766.

Tastani SP, Pantazopoulou SJ. “Experimental evaluation of FRP jackets in upgrading RC corroded columns with substandard detailing.” *Eng Struct* 26, no. 6 (2004): 817-829.

Taucer F, Spacone E, Filippou FC. *A fiber beam-column element for seismic response analysis of reinforced concrete structures.* Berkeley: EERC College of Engineering, University of California, 1991.

Thai HT, Kim SE. “Nonlinear inelastic time-history analysis of truss structures.” *J of Constructional Steel Res* 67 (2011): 1966-1972.

Thoft-Christensen P. “Corrosion and cracking of reinforced concrete.” Lausanne: Life-Cycle Performance of Deteriorating Structures – Assessment, Design and Management, Eds. DM Frangopol, E Bruhwiller, MH Faber, B Adey, 2003.

—. “Stochastic modelling of the crack initiation time for reinforced concrete structures.” Philadelphia: Structures Congress ASCE, 2000.

Thompson KJ, Park R. “Moment-curvature behaviour of cyclically loaded structural members.” *Proceeding of Institution of Civil Engineers* 69 (1980): 317-341.

Timoshenko S, Gere J. “Theory of elastic stability.” 163-182. MacGraw-Hill, 1963.

Toongoenthong K, Maekawa K. “Multi-mechanical approach to structural performance assessment of corroded members in shear.” *J of Advance Conc Tech* 3, no. 1 (2005): 107-122.

Transportation Research Board. *Highway deicing: Comparing salt and calcium magnesium acetate, special report 235.* Washington, DC: National Research Council, 1991.

Tutti K. *Corrosion of steel in concrete.* Stockholm: Swedish Cement and Concrete Research Institute, 1982.

Urix P. *Towards earthquake resistant design of concentrically braced steel structures.* University of California Berkeley,PhD Thesis, 2005.

Val DV. “Factors affecting life-cycle cost analysis of RC structures in chloride contaminated environment.” *J Infrastruct Syst* 13, no. 2 (2007): 135-143.

Val DV, Melchers RE. “Reliability of deteriorating RC slab bridges.” *J Struct Eng* 123, no. 12 (1997): 1638-1644.

Vidal T, Castel A, Francois R. “Corrosion process and structural performance of a 17 year old reinforced concrete beam stored in chloride environment.” *Cement Concrete Res* 37 (1551-1561): 2007.

Vidal T, Castel A, Francois R,. “Analysing crack width to predict corrosion in reinforced concrete.” *Cement Concrete Res* 34 (2004): 165-174.

Vu K, Steward MG. “Structural reliability of concrete bridges including improved chloride-induced corrosion models.” *Struct Saf* 22 (2000): 313-333.

Vu K, Stewart MG, Mullard J. “Corrosion-induced cracking: experimental data and predictive models.” *ACI Struct J* 102, no. 5 (2005): 719-726.

Vu KAT, Stewart MG. “Structural reliability of concrete bridges including improved chloride-induced corrosion models.” *Struct Saf* 22 (2000): 313-333.

Vu KAT, Stewart MG. “Structural reliability of concrete bridges including improved chloride-induced corrosion models.” *Struct Saf* 22 (2000): 313-333.

Wallbank EJ. “The performance of concrete in bridges: A survey of 200 highway bridges.” London, 1989.

Welch PD. “The use of fast fourier transform for the estimation of power spectra a method based on time averaging over short, modified periodograms.” *IEEE Trans. Audio Electroacoustics* 15, no. 3 (1967): 70-73.

Williamson SJ, Clark LA. “Pressure required to cause cover cracking of concrete due to reinforcement corrosion.” *Magazine of Conc Res* 52, no. 6 (2000): 455-467.

Y Zhao, Y Wu, W Jin. “Distribution of millscale on corroded steel bars and penetration of steel corrosion products in concrete.” *Corros Sci* 66 (2013): 160-168.

Yanev B. *Bridge management.* John Wiley and Sons, 2007.

Zhang PS, Lu M, Li XY. “The Mechanical behaviour of corroded bar.” *J of Indus Build* 257, no. 25 (1995): 41-44.

Zhang W, Song X, Gu X, Li S. “Tensile and fatigue behavior of corroded rebars.” *Constr Build Mater* 34 (2012): 409-417.

Zhao J, Sritharan S. “Modeling of strain penetration effects in fiber-based analysis of reinforced concrete structures.” *ACI Struct J* 10, no. 42 (2007): 133–141.

Zhao Y, Hu B, Yu J, Jin W. “Non-uniform distribution of rust layer around steel bar in concrete.” *Corros Sci* 53 (2011a): 4300–4308.

Zhao Y, Yu J, Hu B, Jin W,. “Crack shape and rust distribution in corrosion-induced cracking concrete.” *Corros Sci* 55 (2012): 385–393.

Zhao Y, Yu J, Jin W. “Damage analysis and cracking model of reinforced concrete structures with rebar corrosion.” *Corros Sci* 53 (2011b): 3388–3397.

Zong Z, Kunnath S, Monti G . “Material Model Incorporating Buckling of Reinforcing Bars in RC Columns.” *J of Struct Eng* 140, no. 1 (2014).